Accurate Ground Penetrating Radar Numerical Modeling for Automatic Detection and Recognition of Antipersonnel Landmines

DISSERTATION
zur
Erlangung des Doktorgrades (Dr. rer. Nat.)
der
Mathematisch-Naturwissenschaftlichen Fakultät
der
Rheinischen Friedrich-Wilhelms-Universität Bonn

vorgelegt von
Maria Antonia Gonzalez Huici
aus
Ordizia (Spanien)

Bonn, Dezember 2012

Angefertigt mit Genehmigung der Mathematisch-Naturwissenschaftlichen
Fakultät der Rheinischen Friedrich-Wilhelms-Universität Bonn

1. Gutachter: Prof. Dr. Andreas Hördt
2. Gutachter: Prof. Dr. Andreas Kemna

Tag der Promotion: 14.10.2013
Erscheinungsjahr: 2013

A mi familia

Acknowledgments

This research project was funded by the Federal Office of Defense Technology and Procurement (BWB), an agency of the German Ministry of Defense, and carried out in the Fraunhofer Institute for High Frequency Physics and Radar Techniques (former FGAN e.V.), Wachtberg, Germany.

This dissertation could have never been completed without the help, support and efforts of a lot of people. Firstly, I would like to express my deepest gratitude to my initial mentor and co-supervisor of this thesis, Prof. Andreas Hördt, for introducing me the methods of applied Geophysics and for his crucial support and assistance, in particular, throughout my first stage at the University of Bonn. Similarly, my most sincere thanks go to Prof. Andreas Kemna, for accepting the co-supervision of this thesis and for all his valuable comments and recommendations.

I also want to profoundly acknowledge my project director in the Fraunhofer Institute FHR, Dr. Udo Uschkerat, for giving me the opportunity of working with him in this project and for his fundamental guidance and insight during all these years. I feel in depth too with the Passive Sensor Systems and Classification department director in FHR, Dr. Joachim Schiller, for taking care every time there was a problem and for his constant disposal to help. Also my gratitude to our secretary, Ms. Winandy, always cheerful and ready to make the things more simple.

I am be very grateful to my friends in the Fraunhofer, specially, to my dear Macarena, who gave more colour to my routine inside and outside the institute, to Alfred, for making my life easier several times and for countless funny moments in the climbing wall, to Angel, for his honest friendship and so many personal and technical advices, to my friend Mariano, for our endless conversations, his help and the productive discussions about antennas and hardware during the coffee breaks; also a mention to Fernando, for his encouragement and last review reading of this thesis, to Carlos, Iole, Giulia, Diego, Robert, Mario, Chris, Omar, Jens, Christian, Thomas and all the colleagues who along these years have contributed to make me feel 'at home'.
In addition, gratitude words to some GPR and microwave colleagues who I had the luck to meet in annual conferences: to my friend Merchi Solla, who I appreciate as person and as a researcher, and with whom I feel always happy to share a post-conference trip, to Alex Novo, for your humor and sympathy and for the nice days spent traveling in China! You know I am really in depth with you...I dedicate also some words to Clemente Cobos, who I met in the best GPR workshop ever...the one in Granada!, I am very thankful for the beautiful days spent together in Andalucía and in Bonn. Sincere thanks as well to José Luis Gómez, who gave me new strength and motivation, and to my friend Sebas, for his brilliant theoretical suggestions and all the fantastic shared moments, specially during your research stay in the FHR and my visit to Murcia.
I would also like to convey sincere thanks to the colleagues in the Leibniz Institute for Applied Geophysics (LIAG) in Hannover, Dr. Jan Igel and Dr. Holger Preetz, for providing the test field for the measurement campaign and their friendly aid and assistance.

This thesis is also dedicated to my dearest friend Naroa whose continuous support and emphasis has decisively contributed to the completion of this work, eskerrik asko!, to Sandra, for your close friendship, our great girl dinners and conversations and the beautiful time spent together, to Julia, for your loyal friendship and your great help with the German language, to my dear Anne Drew, another mountain lover...thank you for the fantastic months enjoyed together practicing our favorite sport and for that nice trip to the Alps; to Alejandro Garcia, for your big encourage at the very beginning, to Peter who has shared with me many funny moments since my early times in the student dormitory, to Ricardo for several meals, parties and thrilling theoretical discussions during my first years in Bonn, to Nesrin, for the interesting conversations and pleasant walks along the Rhein, to Suni, my very first friend in Bonn, and to Jenny, Andrés, Daniel, Felix, Bram ...and all the friends who were with me throughout this long journey.

A mis companeros de carrera, Fabri, Antonio, Santi, Juan Francisco..., y en particular a Raquel, quien desde la distancia y a pesar de nuestros largos silencios, todavía mantiene un lugar muy grande en mi corazón. A mi prima Maribel, por tu constante apoyo, por tantos viajes y aventuras compartidas y porque eres como una hermana para mí, y a mi prima Noelia, que con su optimismo y vitalidad siempre fue capaz de transmitirme energía positiva.

Very warm thanks to my beloved Fabio, who has permanently motivated and accompanied me throughout the latest phase of this work. Thank you for making me smile even in the moments of more stress. Ti amo.

Finalmente, quiero expresar mi gratitud más profunda a mi familia, a los que quiero con locura. A mi hermano, que siempre ha sido un modelo y referente para mí. Especialmente, a mis padres, que desde la distancia han estado constantemente presentes apoyándome de manera incondicional y transmitiéndome todo su cariño y fuerza. Gracias por creer en mí, sin vosotros nunca habría llegado hasta donde estoy. Y finalmente a mis abuelos, allá donde estén, en particular a mi yaya, que siempre permanererá de manera especial en mi recuerdo.

Bonn, November 2012.

María A. Gónzalez Huici

Zussamenfassung

Der Bodenradar (Ground penetrating radar, GPR), der flach vergrabene Objekte mit niedrigem dielektrischem Kontrast durch non-invasive Messung des Untergrunds aufspüren kann, gilt als viel versprechende Technologie für die Abbildung wenig oder kein Metall enthaltender Landminen. Aufgrund der schwachen Radarreflexion dieser Minen und des Auftretens unerwünschter Effekte wie Antennenkopplung, System Ringing und Reflektionen der Oberflche und des Bodens, stellt sich dies als besondere Herausforderung dar. Diese Effekte können die Antwort des Zielobjektes verdunkeln und die numerische Modellierung bietet die Möglichkeit ein solch komplexes Problem Rückstreuung (Backscattering) zu analysieren.
Die Aufgabe, die sich im Rahmen der Detektierung von Landminen stellt, ist demnach nicht nur, diese zu finden, sondern auch die Rate des falschen Alarms aufgrund von weiterer Störddaten (Clutter) zu verringern, d.h., die Reflektoren zu identifizieren und eine präzise Modellierung als notwendige Grundlage für die korrekte Interpretation des durch den GPR gewonnenen Outputs zu erstellen.

In der vorliegenden Arbeit beschreiben wir den GPR Modellierungsprozess sorgfältig hinsichtlich Frequenz- und Zeitbereich und entwickeln ein vollständiges Modell eines realistischen GPR Szenarios, welches validiert und angepasst wurde, bis eine zufriedenstellende Übereinstimmung zwischen Freiraum-Messungen und Simulationen erreicht wurde. Dieses Modell beinhaltet eine genaue Aufführung des aktuellen GPR Impuls-Systems, der Schnittstelle, des Bodens und der Zielobjekte und wurde mittels der Methode der finiten Elemente (FEM) berechnet.
Das Antennenmodell wurde den Dimensionen und bekannten Charakteristika unseres GPR Systems entsprechend erstellt und zunächst dahingehend optimiert, Impedanz und Antennencharakteristik mehrerer Konfigurationen im Frequenzbereich zu analysieren, um eine passende Antenneneffizienz und -richtcharakteristik sicher zu stellen. Es vergleicht weiterhin das simulierte Übersprechen der Antenne und Signaturen einfacher Zielobjekte mit den Messungen im Zeitbereich. Bei dem Boden wird von einem nicht-streuenden verlustbehafteten Medium ausgegangen, welcher heterogen und dessen Oberfläche uneben sein kann. Die statistische Verteilung, die der Beschreibung von Topografie und Bodeninhomogenität zu Grunde liegt, wird im Detail erläutert, und kann leicht über nicht konstante elektrische Parameter und variable oberflächenhöhe in das Modell eingegliedert werden. Die Zielobjekte werden exakt durch entsprechende CAD-Modelle beschrieben.

Das oben beschriebene Modell konnte nun genutzt werden, Zeitbereichsignaturen für unterschiedliche Testminen und kleine Objekte unter mehreren Oberflächen- und Bodenbedingungen zu erhalten. Die simulierten Antworten geben uns ein weitreichendes Verständnis über die Faktoren, die die elektromagnetischen Streuungen durch kleine vergrabene Objekte kontrollieren. Sie dienen der Interpretation der Signaturcharakteristika bezogen auf Zielobjekt und Hintergrundparameter. Die daraus gezogenen Schlussfolgerungen werden zuletzt zusammengefasst und erste Betrachtungen zur Erstellung einer repräsentativen Datenbank für die existierenden Landminen werden kurz erörtert.

Schlielich wurde bewiesen, dass die berechneten Zielsignaturen zufriedenstellend als Referenzsignale für eine effiziente Clutter-Unterdrückung und verbesserte Landminendetektion/-erkennung eingesetzt werden knnen. Um dies zu tun, definieren wir eine kombinierte Strategie aus einem Energie-basierten Detektionsalgorithmus und einer Kreuzkorrelation-basierten Identifikationstechnik. Letztere kann vor dem Aufbringen der Detektion als zusätzlicher Filterschritt in Form einer Ähnlichkeitszwangsbedingung zwischen gemessenen und synthetischen Signalen umgesetzt werden. Die vorgeschlagene Methodik wird mit experimentellen Daten in einem inhomogenen Testfeld am Leibniz-Institut für Angewandte Geowissenschaften LIAG in Hannover (Deutschland) validiert, wo mehrere Minensimulanten und Testziele vergraben waren. Im Besonderen ergibt die Anwendung des kombinierten Verfahrens mit experimentellen Daten eine deutliche Verbesserung der Detektionsrate, insbesondere für die Minen, die mit alleiniger Betrachtung von rückgestreuter Energie sehr schwer zu erkennen sind. Das Potential der Methode für Zielunterscheidung wurde ebenfalls belegt.

Abstract

Ground penetrating radar (GPR) is a promising non-invasive technology for imaging shallowly buried low-metal or non-metallic antipersonnel (AP) landmines. However, the application of GPR to the landmine problem remains nowadays a complex scientific and technical task due to the weak echoes produced by the dielectric landmines and the presence of undesirable effects from antenna coupling, system ringing and interface/soil contributions (clutter). In this context, accurate simulations, which are of great help in prediction and correct interpretation of GPR output, may become crucial for an efficient detection, clutter removal and eventual classification of the mines.

This work presents a full forward model of a realistic GPR scenario which includes targets, soil, ground surface and an accurate representation and radiation characteristic analysis of the considered ultra-wideband (UWB) impulse GPR system. The modeling procedure is comprehensively described and the GPR model optimized until a good agreement between measurements and simulations is achieved. The problem is solved numerically in time and frequency domains via the Finite Element Method (FEM) and using COMSOL Multiphysics Simulation Tool.
The final model is then used to perform a parametric study of the scattering signatures (one-dimensional synthetic responses) by several buried landmine-like targets and a series of configurations (depth, soil conditions, target size and shape, etc.). The extracted conclusions are summarized together with some guidelines to build a representative target signature database.

Finally, this research demonstrates that the computed signatures can be satisfactorily employed as reference waveforms for efficient clutter suppression and enhanced landmine detection/recognition. This is done through a combined strategy consisting of an energy based detection algorithm and a cross-correlation based identification technique. The latter is implemented before conducting the detection as an additional filtering step in the form of a similarity constraint between measured and synthetic reference signals. The proposed methodology is validated using experimental data acquired in a prepared inhomogeneous test field at the Leibniz Institute for Applied Geosciences LIAG in Hannover (Germany) where diverse mine simulants were buried at different depths. In particular, the application of the combined strategy to field data yields a clear improvement in the detection sensitivity, especially for those mines which are most difficult to detect through backscattered energy considerations alone. The potential of the method for target discrimination is also evidenced and quantified via Receiver Operating Characteristic (ROC) curves.

Contents

1

Introduction

Whatever you can do, or dream you can do, do it. Boldness has genius, power and magic in it. Begin it now

Goethe

1.1 Motivation of the Study

The landmines were used for the first time during the World War I and since then, they were massively employed in warfare along the last century. They constitute one of the worst types of global pollution as they may remain active for more than 50 years after placement. Since 1975, antipersonnel (AP) landmines have killed or maimed more than 1-million people, being many of them civilians and children.

Together with the direct tragic personal consequences, the widespread use of landmines and the huge cost of demining labors, have a terrible impact on the economy of a country, in particular in underdeveloped regions. The presence of mines affects enormously the social infrastructures and the return to normal life after a conflict results seriously hindered. They make reconstruction of rail and road networks, power lines, and waterways almost impossible, prevent fertile land from being cultivated and restrict animal grazing. Commercial activities are also interrupted since farmers and other people are unable to move along mined trails and roads to transport their products to the market. Such consequences, ruin people's capacity to meet their basic needs increasing hunger and poverty.

All this has led to a worldwide effort to ban further landmine production and use and clear away existing landmines. This international effort to completely ban all AP mines was formalized in 1997 through the Ottawa Convention or the Mine Ban Treaty, formally the Convention on the Prohibition of the Use, Stockpiling, Production and Transfer of Anti-Personnel Mines and on

their Destruction. Nowadays, in 2012, there are 160 states parties to the treaty. Two states have signed but not yet ratified while 36 UN countries are non-signatories to the Convention, making a total of 39 states out of the treaty including USA, China and Russia. But even if this treaty prevents new mines to be laid, the challenge of safely detecting and removing all these devices is overwhelming. This is known as humanitarian demining, and in this context the ideal clearance program must present a very high efficiency and minimum number of casualties. The UN criterion is that nearly all mines should be cleared (99.6% is required), recognizing that in reality no detection system achieves 100%.
Conventional hand-held metal detectors (MD) employed in humanitarian clearance procedures find every piece of metal, giving rise to a large number of false alarms. Moreover, demining operations with standard MD may become particularly slow, dangerous and cost expensive, since many modern AP mines contain little or no metal.
Therefore, intensive research is being conducted to develop and improve new demining methods based on other parameters or characteristics different from the metal content. There are infrared (IR) cameras which produce images of the thermal contrast associated with the disturbed soil layer surrounding the mine or the alteration of the heat flow due to the presence of a mine. They are, however, strongly dependent on environmental conditions and they present limited penetration depth and low sensitivity to non recent mines. Other methods are for example artificial vapor sensors, which detect the odor from the explosive material within the mine, but in general they lack sensitivity, speed and portability and don't result very well suited for demining applications. The interest is also growing in techniques for detecting bulk explosives such as nuclear methods and nuclear quadrupole resonance but the operator security and system complexity are some of their drawbacks where more research need to be done. Only a few of these alternative methodologies are currently employed in real mine affected areas. Probably the most advanced of them is Ground Penetrating Radar (GPR), which is a promising non-invasive technique able to detect both metallic and dielectric buried objects in different soils. Nevertheless, to be successfully used in landmine detection, the resolution needed implies ultra wideband (UWB) signals of frequencies up to some GHz, which decreases soil penetration and raises the image clutter, making necessary further and often complex signal processing. GPR systems are also quite expensive and the challenge is to translate the potential of this technology into practical and affordable systems which should include robust signal processing algorithms for automatic detection and identification of landmines.

1.2 Objectives and Scientific Contributions

Typical environmental conditions for a GPR survey are generally neither ideal nor uniform, so that GPR antennas have to cope with changing soil parameters and topographic fluctuations. Analytical solutions are only available for unrealistic idealized scenarios, such as infinitesimal dipole sources located on or above homogeneous half-spaces.
Numerical modeling permits to analyze the scattering problem under realistic conditions and provides an important understanding about the phenomena which control the electromagnetic response.

There are several works dealing with the forward modeling of GPR problems. Many of them focus only in one element of the model, as for example the GPR antennas [Uduwawala et al., 2005], [Lampe & Holliger, 2001], [Warren & Giannopoulos, 2009] or the inhomogeneous dispersive soil [Texeira et al., 1998]. Others consider the whole system (antenna, interface, soil, targets) but most of them include approximations in one or more aspects. One of the first trials to model a complete GPR scenario in a realistic way was carried out by [Bourgeois & Smith, 1996] and afterwards by *Gürel et. al* in [Gürel, 2001], [Gürel, 2001]. However, even if they perform full 3D modeling, they still assume canonical targets without internal structure, flat ground surface and simplified models to represent soil inhomogeneity as a collection of random inclusions. Moreover, the numerical method massively employed for full GPR modeling is the Finite Difference Time Domain, which is relatively fast and easy to implement but it shows clear limitations to model irregular geometries and complex materials; hence, certain simplifications need to be done. Sometimes these approximations are very convenient to handle the numerical problem and to reduce its computational weight without introducing significant errors in the calculations; but some other times, on the contrary, they generate inaccurate results which may not be valid to interpret real measurements.
When we tackle the problem of GPR modeling for detection and classification of small buried dielectric landmines, high precision and spatial resolution are desirable in order to find all the mines and reduce the high number of false alarms produced by unwanted reflections (clutter). Then, in such a context, it becomes essential to understand and take properly into account the role played by all the elements and parameters introduced in the model. Only then, it will be possible to reach an adequate trade-off between the assumptions acquired and the accuracy required for achieving satisfactory results/interpretations.

In this thesis we accomplish satisfactorily the following major goals:

1. To present a detailed description and analysis of the full modeling process of a realistic GPR scenario in order to obtain a broad understanding about the factors which control and affect the electromagnetic scattering by small targets as well as the GPR antenna performance. Validate the results with analytical solutions when possible.

2. Carry out laboratory experiments to adjust all the modeling parameters, until good correlation between measurements and simulations is achieved: set the proper model to accurately represent the GPR scenario including the antenna, interface, soil and targets.

3. Use the obtained target responses to interpret the main features of the scattering signatures according to the object and background parameters, and develop a representative database for some typical landmines and canonical objects buried in different soil types.

4. Define a detection/recognition methodology which incorporates a minimum distance or similarity constraint between measured and synthetic reference target signatures. Test the potential of this method to eliminate the clutter and recognize the landmines using field data, i.e., study its ability to reduce the amount of false alarms in real conditions.

1.3 Thesis Outline

The following paragraphs are intended to provide a brief overview of the structure and content of this thesis.

Chapter 2 presents the demining problem and the standard methods for demining available, describing thoroughly the GPR types, operating principles and components, as well as the data acquisition methodology.

Chapter 3 concentrates on the numerical modeling of the GPR problem describing the integral and differential techniques applied in GPR simulations. The discretization scheme, the boundary conditions and the advantages and disadvantages of each method are discussed. In particular, the Finite Element Method is explained in detail and the COMSOL simulation tool is introduced.

Chapter 4 is a review of the physical and geophysical background related to the GPR modeling problem. We start from the Maxwell equations to describe the propagation of EM waves through different materials and interfaces, then we present the analytical description of the light scattering, we show the principles of electromagnetic (EM) radiation by physical antennas and introduce the bow-tie dipole, and finally we describe some methods to model the electrical parameters of soils and their spatial variability.

Chapter 5 is a compilation of frequency and time domain simulations in 2D. As a first approach we work in the far field of the source, i.e., we assume plane wave excitation. We study the scattering produced by several small objects of different shapes and materials in free space and buried in homogeneous and inhomogeneous soils.

Chapter 6 describes the development of the model for our GPR antenna system in frequency domain. The process to create the model, and how the geometry and the different elements affect to the radiation pattern, directivity and impedance of the antenna are studied comprehensively. These antenna characteristics are analyzed in both free space and material half-space.

Chapter 7 contains the description of the transient simulations and the optimization and validation of the antenna model in time domain. The antenna direct coupling signal behaviour is first analyzed for several antenna configurations, and these results are afterwards summarized and employed to adapt the antenna model until good correlation with the measured signal is obtained. Additionally, the scattering responses by different test objects are compared with measurements and the final model is so selected and validated. Finally we present some time domain snapshots for the considered models and study the behaviour of mine-like target signatures when modifications on object size, structure, depth and soil parameters are introduced.

Chapter 8 presents the experimental application of the obtained model. First, we summarize the preprocessing methodology for measured data and some postprocessing algorithms for

target focusing and energy based detection. Then, after describing the measurement campaign carried out in a testfield where different mine surrogates were buried, we use our GPR antenna model along with realistic CAD models of the testmines to simulate the target responses under different conditions. With these signatures, together with some other obtained from geometrically simple clutter objects, a database is created. In the end, we describe a correlation based filtering algorithm that applied before the energy based detection algorithm to the measured data, results in a clear reduction of the clutter, an improvement of the true detection rate of those mines most difficult to detect, and a potential way to classify the targets. A graphical user interface for visualization, detection and recognition has been written to automatize the process and make it user friendly.

Chapter 9 summarizes the most important conclusions and provides some recommendations for further research.

2

Demining Problem and the Ground Penetrating Radar

It has become appallingly obvious that our technology has exceeded our humanity
A. Einstein

The mines are cheap and easy to produce explosive devices which are designed to be activated through contact or pressure. When used by military forces they are intended to disable any person or vehicle either by the explosion or by the fragments launched at high speeds.
They are often laid in groups, called mine fields, and are usually strategically placed to slow the enemy or to prevent them from passing through a certain area. The landmines are usually buried shallow or surface laid, in regular or irregular distributions. They are deployed over large areas either manually, by aircraft or by mechanical minelayers and the variety of environments where they can be found is huge. Currently, it is estimated that around 60-100 million landmines remain uncleared in at least 62 countries around the world killing and injuring a big number of civilians every year (see Table 2.1 and Fig. 2.1).
The worst mine-affected areas are located in poor regions with few resources to face the consequences, being Afghanistan one of the countries most seriously affected by mines. According to the Mine Clearance Planing Agency, over a 15 years period an estimated 20000 civilians have been killed and 400000 wounded by landmines in this country. Africa is probably the most contaminated continent with more than 40 million of landmines spread over at least 19 countries. There are an estimated 30 millions of landmines only in Angola, Cambodia and Mozambique with a correspondingly high number of casualties. Former Yugoslavia also suffers this problem, since more than 5 million landmines were placed during the Balkan conflict.

In general, demining consists of detecting and neutralizing the landmines. Nowadays, the equipment available to mine detection teams is very similar to that used during World War II. Gener-

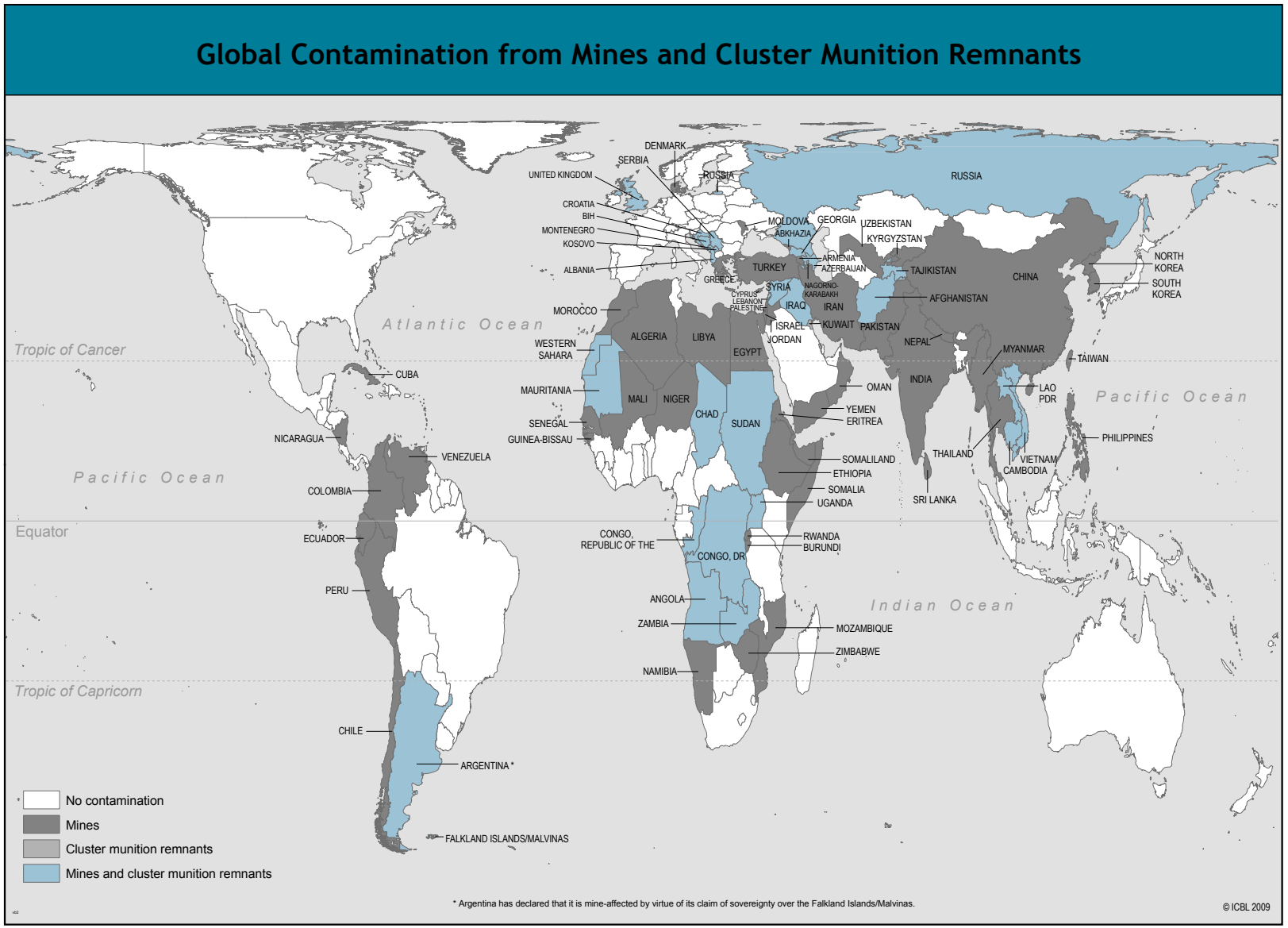

Figure 2.1 – Distribution of the AP mines and UXO in the world. Source ICBL [ICBL, 2009].

Country	Estimated number of landmines	Reported casualties (1999-2008)
Afghanistan	10,000,000	12,069
Angola	15,000,000	2,664
Bosnia and Herzegovina	1,000,000	-
Cambodia	6,000,000	7,300
China	10,000,000	-
Colombia	-	6,696
Croatia	3,000,000	-
Egypt	23,000,000	-
Eritrea	1,000,000	-
Ethiopia	500,000	1,947
China	-	2,931
Iran	16,000,000	-
Irak	10,000,000	5,184
Mozambique	1,000,000	-
Myanmar	-	2,325
Russia	-	2,795
Somalia	1,000,000	2,354
Sri Lanka	-	1,272
Sudan	1,000,000	1,748
Ukraine	1,000,000	-
Vietnam	3,500,000	1,545
Yugoslavia	500,000	-

Table 2.1 – Landmines around the world; - indicates insufficient data. Source ICBL.

ally, demining operations are conducted with a handheld MD and a prodding device, such as a pointed stick or screwdriver. The mined area is previously cleared of vegetation and divided into small lanes. Then, a deminer slowly progress down each lane while swinging the MD close to the ground. When the detector produces an acoustic alarm, the deminer probes the suspected area to determine whether a buried mine is present. Sometimes trained dogs and mechanical demining equipment are also part of the procedure.

The major limitation of the standard process is that the MD cannot differentiate a mine or any unexploded ordnance (UXO) from other metallic items (shrapnel, metal scraps, cartridge cases, etc.), which are abundant in most battlefields. This leads to many false alarms: 100-1000 false alarms for each mine detected. Tuning the sensitivity of a conventional MD to decrease the false alarm rate reduces simultaneously the probability of detection, which means that more mines remain uncleared when the demining labor is completed and under the humanitarian demining scope this is unacceptable. On the other hand, if the detector is tuned to signal even the small metal amount present in some landmines, it becomes extremely sensitive to other metallic debris present in the area, making the mine clearance a very slow and dangerous process.

The operator must achieve the best compromise between both competing goals of minimizing the false alarm and maximizing the number of mines detected. This balance can be quantified by what is known as a receiver operating characteristic (ROC) curve. A ROC curve plots the probability of finding a buried mine (the probability of detection, or PD) against the probability that a detected item is a false alarm (the probability of false alarm, or PFA). Both probabilities are represented in a curve as a function of the threshold used to make a declaration (e.g., the intensity of the tone produced by a MD). Figure 2.2 illustrates some theoretical examples of ROC curves [MacDonald & R., 2003]. The ROC curve for a perfect detector will be that approaching 100% detection at 0% false alarm, while the curve associated to a random guessing would be a diagonal line.

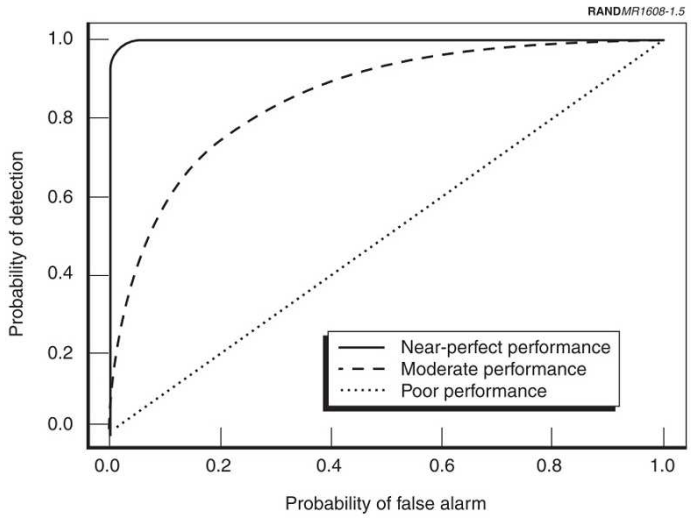

Figure 2.2 – ROC curves (Photo RAND).

There are more than 350 types of mines which can be classified into two main categories: *anti-*

Figure 2.3 – Various AP blast landmines (Photo GICHD).

personnel (AP) mines and *anti-tank* (AT) mines. The basic function of both of these varieties of landmines is the same, but there are a couple of important differences between them.
Anti-tank mines are typically larger, in order of 20-40cm and contain several times more explosive material than anti-personnel mines. They are commonly buried between 5cm and 40cm deep in soil and they contain enough explosive to destroy a tank or a truck, as well as to kill people in or around the vehicle. In addition, more pressure is usually required to detonate an anti-tank mine. Many of this type of mines are located on bridges, roads and large areas where tanks may travel. Although some classes with low metal content exist, they are in general easier to detect. They do not concern humanitarian demining, since they are usually not triggered by the weight of humans.
The AP mines can be separated into two main groups: *blast* and *fragmentation* landmines.
Blast mines are typically cylindrical shaped, 6 to 12cm in diameter and 4 to 7cm thick, and they can weight only 30gr. The casing is made of wood, plastic or metal and they usually have a small amount of explosive. They are triggered by pressure and usually just a small weight ($\sim$20kg) can activate the mechanism, causing the affected object (normally the foot/leg) to blast into fragments. As it was mentioned before, in many cases they have little or no metal content what makes these mines extremely difficult to locate using traditional MDs. Fig. 2.3 shows some examples of typical AP blast landmines and in the present work we will concentrate on the detection and recognition of this sort of mines.
The fragmentation mines throw multiple fragments upwards at high speed. They can cause several casualties at distances of up to 50m. Since all of the modern fragmentation mines employ steel, they are in principle easily found by MDs. However, they are often activated by tripwires which means that the mine can be triggered by movement at distances up to 20m before being located by the MD. These landmines, which are out of the focus of this thesis, come in diverse sizes and shapes and they normally contain more explosive than a blast mine.

2.1 Standard Methods of Demining

For 15 years several research groups have been actively investigating new detection methods for humanitarian demining applications. One aim of these methods is to lower the false alarm rate while maintaining a high probability of detection, thus saving time and reducing the chance of injury to the deminer. Table 2.2 is a compilation of most of the methods currently available. The second column depicts the detection principle on which each technology is based while the remaining columns outline the strengths and limitations of the different methods. An exhaustive description can be also found in [Acheroy, 2007]. Looking at the table and considering the different methods, we can notice that no single sensor technology is effective finding all types of mines in all conditions. Given the limitations of individual sensor technologies, only an integrated multisensor system may bring significant improvement in mine detection capability. Latest developments on GPR-based systems are hand-held dual-sensors (e.g. HSTAMIDS, MINEHOUND, ALIS), which are a combined sensor platform of a MD and a GPR; however, this kind of sensors do not make optimal use of the totality of information available since the operator receives two separate outputs and the GPR is just employed as discrimination sensor over the targets detected by the MD. Accordingly, the integration of technologies at the design level of the multisensor, and the development of algorithms for advanced signal processing and data fusion from individual sensors, is likely to yield an important gain in terms of detection rate and false alarm reduction. And even though the dual sensors are out the scope of this thesis, the investigation of the performance of the GPR alone in target detection and recognition is fundamental for its successful incorporation in such a dual sensor or its future standalone application in demining labors.

2.2 Ground Penetrating Radar

The terms ground penetrating radar (GPR), ground probing radar, subsurface radar, or surface penetrating radar (SPR) refer to a non-destructive technique which employs radio waves to probe the underground (or man-made visually opaque structures). The correct interpretation of the reflected electromagnetic (EM) field yields information on subsurface structural variations as well as changes in material properties.
GPR is used in a wide spectrum of applications in fields such as geophysics, civil engineering or archeology. Some well-developed applications are the geotechnical studies for contaminated land assessment and bedrock profiling, concrete, road and railway inspection, buried pipe and utility mapping, geological applications like ice profiling and glaciology, groundwater mapping and mineral exploration, archaeological studies for structural mapping, exploration and excavation planning, and finally military and security applications, like landmine and UXO detection. The kind of objects and features investigated can vary from a couple of centimeters to hundreds or even kilometers of meters deep. A few GPR systems have been mounted on aircrafts and satellites to sense geological structures buried beneath the Saharan desert as well as to measure the depth of the Moon or features on Mars. The range of the GPR in the ground is limited because of the absorption suffered by the signal while it travels on its two-way path through the ground

Technology	Operating principle	Strengths	Limitations
Electromagnetic			
Metal Detector	Induces eddy currents in metallic components through alternating magnetic fields	Cheap; low complexity; performs well in a variety of environments	Metal clutter; low-metal and plastic mines; slow
GPR	Emits and measures reflected radio waves from soil variations	Detects both dielectric and metallic anomalies	Natural clutter; very moist or dry environments; cost expensive
Electrical impedance tomography	Determines electrical conductivity distribution	Detects both dielectric and metallic anomalies	Dry environments; can detonate mine
Infrared/ hyperspectral	Assesses thermal, light reflectance contrasts	Operates from safe standoff distances and scans wide areas quickly	Low spatial resolution and penetration depth; presence of foliage; heavily dependent on environmental conditions
Acoustic/ Seismic	Emits and measures reflected sound/seismic waves	Low false alarm rate; not reliant on EM properties	Deep mines; presence of foliage; frozen ground
Bulk explosive detection			
Nuclear Methods: thermal neutron activation, neutron backscatter, and X-ray backscatter	Induce radiation emissions from the atomic nuclei in explosives	Identify elemental content of bulk explosives	Not specific to explosives molecule; soil topography; shallow penetration; high complexity
Nuclear Quadrupole Resonance	Induces radio frequency pulse that causes the chemical bonds in explosives to resonate	Identifies bulk explosives	TNT; liquid explosives; radio frequency interference; quartz bearing and magnetic soils
Advanced Prodders/ Probes	Provide feedback about nature of probed object and amount of force applied by probe	Could deploy almost any type of detection method	Hard ground, roots, rocks; requires physical contact with mine; slow and dangerous
Explosive Vapor: Biological (dogs, rodents, bacteria), Fluorescent, Piezoelectric, Electrochemical, Spectroscopic	Detect explosive vapors or measure changes upon exposure to explosive vapors	Confirms presence of explosives	Dry soils; lack of speed, sensitivity and portability

Table 2.2 – Summary of Detection Technologies [MacDonald & R., 2003].

material.
In humanitarian demining applications, the GPR technology may provide useful information on the location and geometrical properties of buried metallic and non-metallic landmines [Brunzell, 1999], [Bruschini et al., 1998], [Scheers, 2001], [Savelyev et al., 2007], [van den Bosch, 2006]. Therefore, GPR may permit the detection of landmines which are not detectable by the widely used MD and could contribute to reduce the false alarm rate in mine clearing operations.
The most important requirements for a GPR system dedicated to landmine detection are substantial antenna elevation above the ground, large dynamic range, time stability, high accuracy of the measured data, efficient clutter reduction and high down-range and cross-range resolution [Groenenboom & Yarovoy, 2002]. Moreover, the need for immediate output and the significant risk to the life of the operator make it a severe technical challenge. Some of these topics will be further developed in the following sections.

2.2.1 GPR Performance and Operating Principles

Several references discuss and review the principles of GPR in general and present different case studies [Beres & Haeni, 1991], [Daniels, 1996], [Davis & Annan, 1976], [Davis & Annan, 1989].
The operational principle resembles that of a conventional radar system but applied to subsurface features. Basically, a transmitter is connected to a transmitting antenna through a waveguiding structure (usually a coaxial waveguide). The transmit antenna, which is directed towards the ground, radiates electromagnetic (EM) waves that follow different paths before being recorded by a receiver. If only one single antenna is employed, the radar is called monostatic. However, most GPR systems use separate transmit and receive antennas in what is termed bistatic mode. When the system consists of an array of more than two antennas the radar is called multistatic.
At frequencies below 1kHz, the EM behaviour is inductive in the nature and is typically described by the diffusion equation. This physical character is dominant for the EM fields used in metal detectors. At frequencies above 1MHz, the EM fields become "wave-like" and electromagnetic propagation is described by the wave equation. Then, GPR starts to be applicable [Annan, 2003]. At higher frequencies, above 1Ghz, depth penetration decreases drastically [Daniels, 1996], whereas resolution increases. When the frequencies approach 10 GHz, the relaxation of the dipolar water molecule causes very high attenuation making the use of GPR impractical in wet soils.
GPR systems typically operate in the VHF/UHF range (i.e. 30MHz-3GHz) of the radio spectrum. The wavelengths of the illuminating radiation are similar in dimension to the target, which makes its GPR image very different from its optical one: it is highly affected by the propagation characteristics of the ground and presents a lower definition. Moreover, the beam pattern of the antenna is widely spread in the soil degrading the spatial resolution of the image.
At GPR frequencies the following relationships are valid:
the phase velocity,

$$v_{ph} = \frac{1}{\sqrt{\epsilon\mu}} \approx \frac{c_0}{\sqrt{\epsilon_r}} \tag{2.1}$$

$$c_0 = \frac{1}{\sqrt{\mu_0\ \epsilon_0}} \tag{2.2}$$

the attenuation coefficient,

$$\alpha = \sqrt{\frac{\mu}{\epsilon}} \cdot \frac{\sigma}{2} \approx Z_0 \cdot \frac{\sigma}{2\sqrt{\epsilon_r}} \tag{2.3}$$

and the EM impedance,

$$Z = \sqrt{\frac{\mu}{\epsilon}} \approx \frac{Z_0}{\sqrt{\epsilon_r}}, \tag{2.4}$$

with the relative permittivity ϵ_r defined as

$$\epsilon_r = \frac{\epsilon}{\epsilon_0} \tag{2.5}$$

where ϵ is the dielectric permittivity of the material, ϵ_0 is the free space permittivity ($8.854\text{x}10^{-12}$ farad/metre), μ is the magnetic permeability of the material, μ_0 the permeability of the free space ($12.57\text{x}10^{-7}$ henrys/metre), σ is the electric conductivity and c_0 is the velocity of light in free space. The above approximations are accurate when the magnetic properties of the medium are close to the values in free space (which is true for most Earth materials), i.e., $\mu = \mu_0\mu_r \approx \mu_0$.
As we can see, the physical properties relevant for radio wave propagation are dielectric permittivity, electrical conductivity and magnetic permeability. More specifically, dielectric permittivity (or dielectric constant) controls the wave velocity and conductivity affects to the signal absorption by the medium, hence determining the signal attenuation.
In general, GPR performance is satisfactory through materials with a low conductivity such as granite, dry sand, snow, ice, and fresh water, but will not penetrate certain clays that are high in salt content or salt water because of the high absorption of electromagnetic energy of such materials [Daniels, 2004]. The radar reflections will occur when there is a change in the EM properties, especially in the aforementioned dielectric permittivity, since this parameter plays the main role on the variation of the characteristic impedance of the medium at the frequencies of interest. At low microwave frequencies, the relative permittivity of dry geologic materials ranges from 3 to 6 while the relative permittivity of water is about 80. Soils have properties between these two extremes depending mostly on the water content [Topp et al., 1980]. On the other hand, the relative permittivity for materials employed to fabricate AP mines is 3 or less, which often produces little dielectric contrast with the background, in particular for dry soils.
In most practical cases, part of the GPR signal will be scattered when it encounters a plastic landmine in soil, but the backscattered signal will be often difficult to isolate and identify from the whole response. This response contains not only the reflection from a potential target, but also undesirable effects from antenna coupling, system ringing and interface/soil contributions, which can mask the target response [Annan, 2003], [Daniels, 1996]. Different techniques are used to reduce such clutter contributions and retrieve the target reflection.
The principal parameters which influence the characteristics and magnitude of the signal reflected by the targets are: the contrast of the electromagnetic parameters between the host material and the target (in particular, the dielectric permittivity), the target size, the system operating frequency and resolution (i.e. the bandwidth), and the signal attenuation in the host material.
The impact of all these factors on the recorded target signatures and the GPR antenna performance will be explored later in this thesis.

2.2.2 GPR Design

The design of a GPR system can be classified into different categories according to its hardware implementation. There are two main classes: time domain radars and frequency domain radars and each type can be further subdivided depending on the modulation of the signal. Systems that transmit a short time pulse (or impulse) and receive and process the backscattered signal by means of a sampling receiver can be considered to operate in time domain. Systems that transmit individual frequencies in a sequential manner or as a swept frequency and receive the reflected signal using a frequency conversion receiver can be considered to operate in frequency domain. [Daniels, 2004].

Time Domain Radar

The time domain GPRs (also called impulse radars), constitute the majority of commercially available radar systems. They transmit a sequence of pulses (typically of Gaussian-like shape) of amplitudes lying between 20V to 200V and pulse widths within the range 200ps to 50ns at a pulse repetition interval between several hundred microseconds and one microsecond. The impulse generator is generally based on the technique of rapid discharge of the stored energy in a short transmission line. It is quite feasible to generate pulses of several hundred kV but at long repetition intervals. The output from the receiver antenna is applied to a flash A/D converter or a sequential sampling receiver.
The central frequency f_c of the pulse (which is the same as the carrier frequency) can vary from some MHz up to GHz, being its half-power (-3dB) bandwidth, almost equal to f_c. For example, a 1ns monocycle has a f_c and a 3dB bandwidth both equal to 1Ghz.
These GPRs are called Ultra-Wide Band (UWB), because of the very large relative bandwidth involved. The block diagram of a time domain UWB GPR is illustrated in Fig. 2.4. In general, the choice of the bandwidth for a UWB system depends on the desired spatial resolution and signal penetration. Unfortunately, attenuation increases with frequency in most environments. The resolution will be mainly dictated by the time duration of the pulse τ or, equivalently, its frequency bandwidth B:

$$\tau = \frac{1}{B}. \tag{2.6}$$

The equivalent spatial dimension Δx is obtained multiplying the time duration by the pulse travel velocity v in the medium

$$\Delta x = v \cdot T = \frac{v}{B} \tag{2.7}$$

For traditional radar systems it is accepted that two identical targets can be separated in range if they are at least the half of pulse width apart in time. Increasing the frequency bandwidth, results in shorter time duration signals, which has the ability to image or resolve closely spaced points in the ground. For instance, a receiver bandwidth of typically 1Ghz is required to provide a resolution between 5 and 20cm, depending on the relative permittivity of the material.

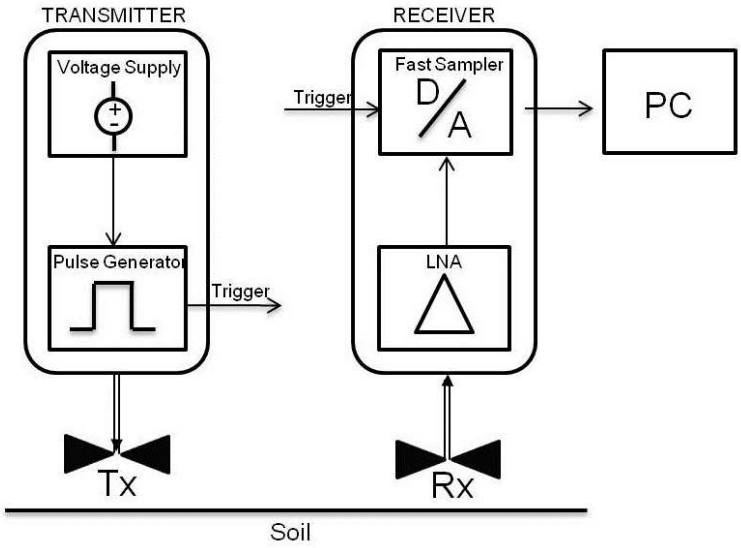

Figure 2.4 – Block diagram of a time domain UWB GPR.

Frequency Domain Radar

The main potential advantages of the frequency domain radar are the wider dynamic range, lower noise figure, and higher mean powers that can be radiated. There are two main types of frequency domain radar, Frequency Modulated Carrier Wave (FMCW) and Stepped Frequency Carrier Wave (SFCW). FMCW radar transmits a continuously changing frequency over a chosen frequency range on a repetitive basis. The received signal is mixed with a sample of the transmitted waveform and results in a difference in frequency, which, although fundamentally related to the phase of the received signal, is a measure of its time delay and hence the range of the target. The SFCW radar transmits a series of incremental frequencies and stores the received signal to afterwards carry out a Fourier transform reconstruction of the time-domain equivalent waveform. The SFCW has found many applications in GPR because the requirements on scan rate are relatively modest.
However, we are not going to give here any further detail about frequency domain radars since the commercial GPR system employed for this work is a pulsed radar.

2.2.3 Data Collection

Many GPR systems use separate, man-portable, transmit and receive antennas, which are placed and moved over the surface of the ground or material under investigation. By systematically surveying the area in a regular grid pattern, a radar image of the ground can be built up on a display in real time [Daniels, 2004].
The recorded data can be presented in the time or frequency domains, being possible to go from one domain to another via Fourier transform. Time domain data representation is useful for discriminating reflections from different objects and interfaces, which may help to interpret the

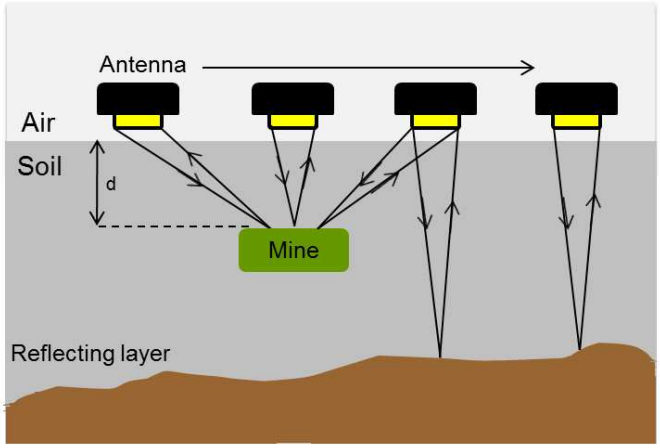

Figure 2.5 – Common Offset acquisition mode.

underground structure. Frequency domain representation provides information about the spectral dependence of the radar cross section (RCS) for a given target.

Acquisition Modes

The transmitter and receiver antennas can be used in different orientations: parallel (end-fire), perpendicular (broadside) and cross polarized orientation to the survey direction. A particular orientation of the antennas can significantly enhance responses from certain type of targets (for example, pipes or objects with symmetry in one direction) because the radiation pattern of GPR antennas is not omnidirectional, which means the antennas radiate or receive more efficiently in some directions than in others [Daniels, 2004].
There are four main modes of radar data acquisition: common offset, common source point, common receiver point and common midpoint. We describe below only the first of them, which is the one of interest for our case.
In common offset (CO) operation mode, the transmitter and receiver antennas are kept at a constant distance and moved along the survey track simultaneously. The measured travel times of the recorded signals are displayed on the vertical axis, while the antenna position is plotted along the horizontal axis. Most of GPR surveys use a common offset survey mode. Figure 2.5 shows a typical CO data acquisition configuration.

2.2.4 Data Visualization: A, B and C Scans

The GPR data visualization and display are crucial issues for the correct interpretation of subsurface structures. There are three standard ways of displaying the recorded data: a one-dimensional trace (A-scan), a two dimensional slice (B-scan or radargram), and a three dimensional cut (C-scan) [Daniels, 2007].

i. A-Scan

Time or frequency domain data acquired by a GPR antenna for one spatial localization is termed *A-scan*. When the velocity of propagation in the soil is known, the time vector can be transformed into distance/depth. Examples of time and frequency domain A-scans resulting from laboratory measurements in free space are shown at Fig. 2.6. The antenna crosstalk, which is the main contribution to the received voltage, is shown in black, while the echoes coming from both a metallic and a plastic sphere (after crosstalk subtraction), located approximately 8cm far from the antennas, are displayed in blue and red respectively. If the targets are buried in soil, the surface contribution (which is often mixed up with the crosstalk for small antenna heights) occurs earlier and is usually much stronger than the target reflection.

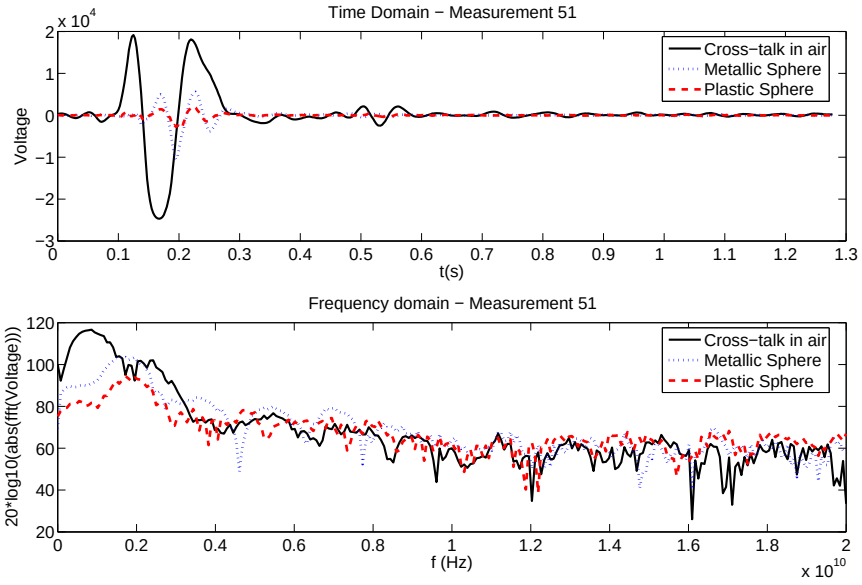

Figure 2.6 – Preprocessed A-scans in time (top) and frequency domain (bottom) for a metallic and a plastic sphere of radius r=5cm.

ii. B-scan

A *B-scan* is the denomination of a set of A-scans gathered alongside a line that forms a two dimensional data set. Fig. 2.7 schematically illustrates how GPR signal evolves with the position of the antennas with respect to the target. Reflections from targets appear as hyperbolic curves in the recorded data due to the difference in round-trip travel time between the target and the antenna system as the latter is moved along the measurement line. The apex of the hyperbola corresponds to the antenna system located just above the target. Its shape depends on the depth of the reflector as well as the wave propagation velocity (i.e. dielectric permittivity) in soil.

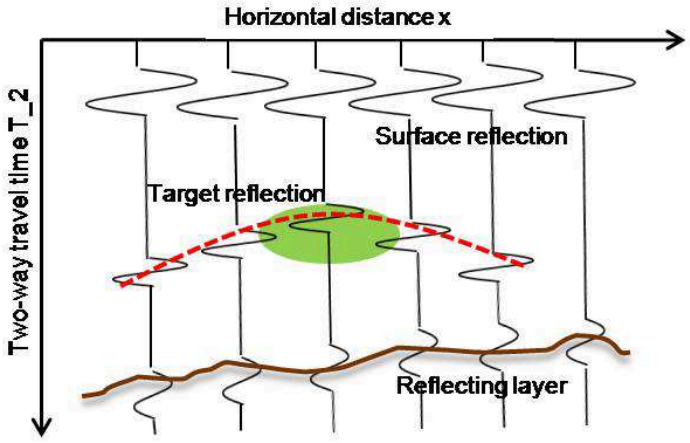

Figure 2.7 – B-scan and hyperbola formation.

Additionally, the response of the target decreases as the antennas are moved away from the target, due to the travel path lengthening and the reduction of the antenna gain in the direction of the target. Examples of measured time domain B-scans are given in Fig. 2.8.

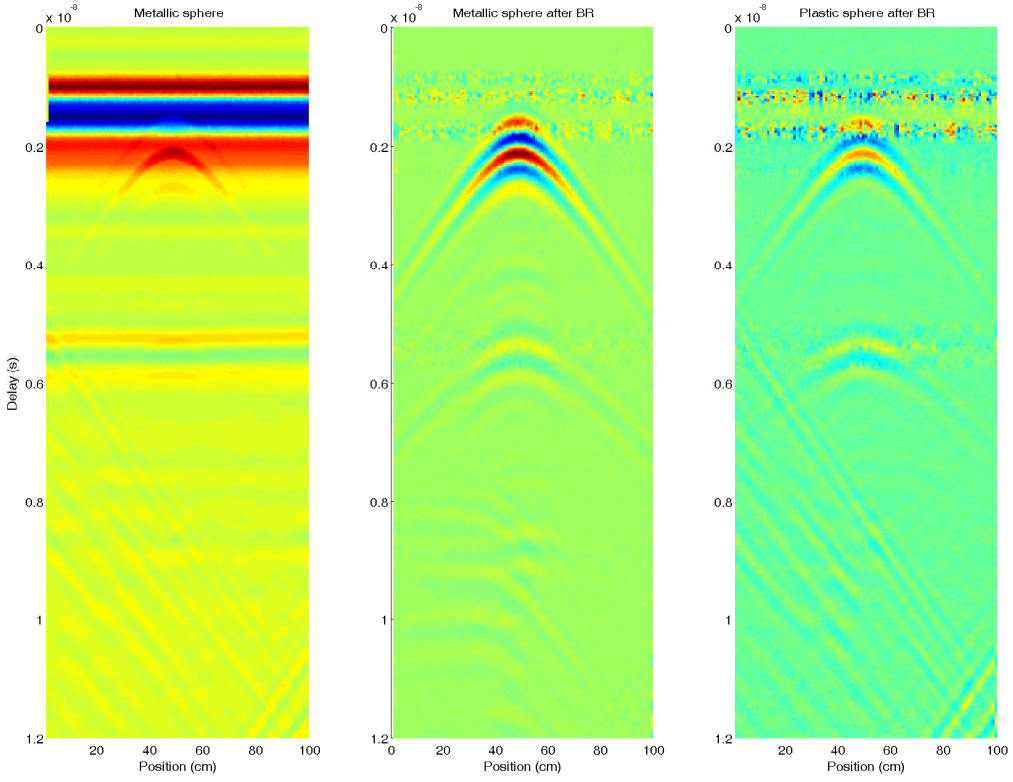

Figure 2.8 – Measured B-scans, received amplitude with a metallic sphere (left), with a metallic sphere after average background removal (middle) and with a plastic sphere after background removal (right).

In particular, the two-way wave travel time from the transmitter antenna Tx to the receiver antenna Rx is determined according to the following formula:

$$t_{Tx2Rx} = \frac{d_{Tx2P} + d_{P2Rx}}{v} \tag{2.8}$$

where v is the propagation velocity in the medium (soil) and d_{Tx2P} and d_{P2Rx} are respectively the distances between the transmitter antenna and a point target and vice versa. More specifically, if x is the scanning position along the measurement line respect to the scatterer, and d is the scatterer depth, the aforementioned travel paths can be calculated by:

$$d_{Tx2P} = \sqrt{(x - x_{Tx})^2 + d^2}), \tag{2.9}$$

$$d_{Rx2P} = \sqrt{(x + x_{Rx})^2 + d^2)} \tag{2.10}$$

with x_{Tx} and x_{Rx} the distances between the scanning point and the transmitter and receiver antenna respectively. These values will become zero if we have or we assume we have a monostatic GPR system without any offset between the transmit and receive antennas. Moreover, generally $d_{Tx2P} = d_{Rx2P}$ and the expressions above get simplified. In particular, assuming the latter simplifications and after some mathematical manipulation we get:

$$\frac{t^2_{Tx2Rx}}{(2d/v)^2} - \frac{x^2}{d^2}, \tag{2.11}$$

which represents a hyperbola with the vertex in the origin and an apex in $2d/v$.
On the other hand, when we assume a target of a certain radius r instead of an ideal punctual scatterer, the travel paths are now given by:

$$d_{Tx2P} = d_{Tx2Pc} - r, \tag{2.12}$$

$$d_{P2Rx} = d_{P2Rxc} - r \tag{2.13}$$

where d_{Tx2Pc} and d_{Rx2Pc} are the corresponding distances to the center of the targets.

iii. C-Scan

A *C-scan* is represented by a horizontal slice of a number of stacked B-scans, measured by repeated line scans along the measurement plane. Three dimensional displays are basically block views of GPR traces recorded at different positions on the surface. Obtaining good three-dimensional images is of great help for interpreting images and identifying targets, which are usually easier to isolate and identify on three dimensional datasets than on conventional two dimensional profiles. Figure 2.9 illustrates a sequence of C-scans for a metallic and a plastic sphere in air at a distance of 10cm to the antenna head. No signal processing has been applied and the targets show up as a "wave-like" structure.

2.2.5 The GPR System

The radar system chosen for our experiments is the SPRScan, a commercial impulse UWB GPR manufactured by ERA Technology (see Fig. 2.10 and 2.11). Its sampling head is able to acquire

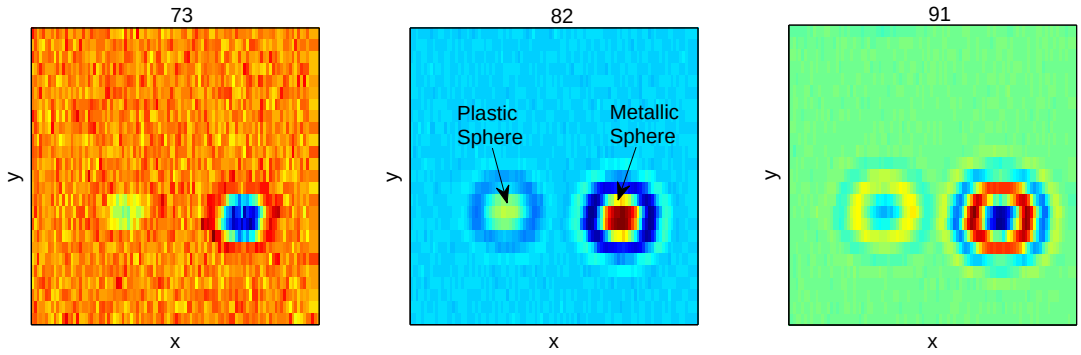

Figure 2.9 – Measured C-scans (raw data) at different time instants. Recorded amplitude with a plastic and a metallic sphere situated at the same distance from antenna head.

a maximum of 195 A-scans, of 512 points each, per second (or 390 A-scans of 256 points in coarse model). Before the A/D conversion, the signal is analogically averaged (10 or 20 samples) to improve the signal to noise ratio (S/N) and a time varying gain correction can be applied to partially compensate the soil attenuation and geometrical spreading, increasing the overall system dynamic range.

A pair of parallel bow-tie antennas enclosed in a sealed shielding box, are used as transmitter and receiver. The pulse generator (pulse width: 0.5ns, pulse repetition frequency: 1MHz) is integrated into the antenna case to minimize losses and transmission reflections. This antenna has a central operating frequency and bandwidth of 2GHz, which leads to an expected resolution of less than 5cm. No additional information is available regarding the SPRScan antennas.

Figure 2.10 – View of GPR Transmitter/Receiver Head.

Figure 2.11 – Test field and SPRScan Radar in the LIAG (Hannover).

3

Numerical Methods

I do not fear computers. I fear the lack of them
Isaac Asimov

3.1 State of the Art

The numerical modeling, and specifically the forward models, has been an active area of research since early 1990s, primarily due to a demand for a complete understanding of the fundamental GPR phenomena. In particular, accurate simulations may help to conceive a more effective sensor by testing different designs on the same scene without having to manufacture them; it can set an upper limit on the performance of a GPR system given the soil and target EM and geometrical properties; it can also be used for testing signal processing algorithms on GPR signals either free from or containing controlled measurement noise; finally, the predicted responses can be helpful to identify clutter and targets. In addition, the sophistication, size, and accuracy of GPR models have accelerated over the last years as computational resources have improved and become more accessible. All this, has made numerical modeling a useful and widely appealed approach to the GPR problem.

In computational electromagnetics, there are several methods for solving the Maxwell equations or equations related to Maxwell's theory. Many of these procedures can be classified as either boundary or domain techniques. Both classes involve a series expansion of a unknown function f, where f is typically a vector field. For a domain technique the computational domain Ω is discretized and the solution of the field equations in Ω has to be approximated numerically. Along a given boundary $\partial\Omega$, the series expansion have to fulfill analytically the corresponding boundary conditions. For a boundary technique, in the other hand, the boundary $\partial\Omega$ of the domain Ω must

be discretized and the boundary conditions are solved numerically, whereas the expansion of f has to fulfill analytically the given field equations in Ω. Some well-known examples of domain techniques are the Finite Element Method (FEM), the Method of Moments (MoMs), and the Finite Difference Method (FDM). An example of boundary technique is the Boundary Element Method (BEM).
All the computational techniques present compromises between computational efficiency, stability and the ability to model complex geometries. Our first task to carry out this work was to search and select a suitable method to simulate realistic GPR scenarios in the context of landmine detection.

3.2 Integral Equation Method, the Method of Moments

The integral equations methods, commonly referred as the Method of Moments (MoM), which was firstly introduced by Harrigton in 1968, are derived from solutions of the integral form of Maxwell equations and are between the most commonly used numerical techniques for solving electromagnetic problems [Balanis, 2005], [Harrigton, 1968], [Mittra, 1973], [Wang, 1990].
The key to solve any antenna or scattering problem is getting the physical or equivalent current density distributions on the volume or surface of the antenna or scatterer. Once these are known, the radiated or scattered fields can be found using the standard radiation integrals. The prediction of the current densities over the antenna or scatterer is accomplished by the Integral Equation Method (IEM), whose objective is to obtain the induced current density in the form of an integral equation where the unknown current is part of the integrand. The integral equation is then solved using numerical techniques such as the commonly applied MoM. For time-harmonic electromagnetics, two of the most popular integral equations are the Electric Field Integral Equation (EFIE) and the Magnetic Field Integral Equation (MFIE) [Balanis, 2005]. The EFIE enforces the boundary condition on the tangential components of the electric field while the MFIE enforces the boundary condition on the tangential magnetic field. These integral equations can be used for both radiation and scattering problems. And since MoM involves expanding the currents, which are restricted to a finite domain, instead of the fields, that may extend to infinite, it is convenient for open domains.
The MoM technique essentially transforms a general operator into a matrix equation which can be solved easily on a computer. The procedure is called matrix method because it reduces the original functions to matrix equations. A brief mathematical description of this method will be given in the following paragraphs.
The linear boundary-value problem is defined by a governing differential equation in the operational form

$$\hat{L}f = g \tag{3.1}$$

on the domain Ω, where $\hat{L}$ is a known linear operator (i.e., the EFIE), g is a known function (the excitation or the source), and f is the unknown field or response function to be determined. The objective here consists of determining f once L and g are specified. The MoM requires that the

unknown response function can be expanded as a linear combination and be written as

$$f = \sum_j c_j \phi_j, \tag{3.2}$$

where the c_j are the scalars to be determined, i.e., the complex current amplitudes, and ϕ_j are usually called basis or expansion functions. A certain number of terms in equation (3.2) leads to an approximation of the current distribution. The substitution of equation (3.2) into (3.1) and application of linearity gives

$$\sum_j c_j \hat{L}\phi_j = g. \tag{3.3}$$

The basis functions ϕ_j are chosen so that each $\hat{L}\phi_j$ in equation (3.3) can be evaluated conveniently. The only task remaining is to find the unknown constants c_j. Next, it is necessary to define a set of testing or weighting functions $(\omega_1, \omega_2, \omega_3, ...)$ in the L domain. These are essentially basis functions used to approximate the right hand side of equation (3.1). Thus they should be linearly independent and capable of approximating the excitation field. With every ω_i an inner product is taken, which results in:

$$\sum_j c_j \langle \omega_i, \hat{L}\phi_j \rangle = \langle \omega_i, g \rangle \qquad i = 1, 2, 3... \tag{3.4}$$

Equation (3.4) corresponds to a set of equations and can be written in a matrix form as

$$[l]\vec{c} = \vec{g}, \tag{3.5}$$

where $[l]$ is the matrix

$$[l] = [\langle \omega_i, \hat{L}\phi_j \rangle], \tag{3.6}$$

and $\vec{c} = [c_j]$ and $\vec{g} = [\langle \omega_i, g \rangle]$ are column vectors. Then, if $\hat{L}$ is non-singular, the unknowns $\vec{c}$ will then be given by

$$\vec{c} = [l]^{-1}\vec{g}. \tag{3.7}$$

The MoM has the advantages that it is conceptually simple, from an application viewpoint devoid of complicated mathematics and it is suitable for open domains. As a frequency domain technique, it can also solve problems very quickly if only one frequency is required.
Probably, one of the most important drawbacks of the use of MoM for the GPR problem is the difficulty of its setup for stratified media (since it involves the use of dyadic Green functions) and for complex inhomogeneous bodies, mainly due to the complexity of the associated surface integral equation [van den Bosch, 2006].

3.3 Finite Difference Time Domain Method

The FDM is one of the oldest and most popular numerical techniques. Richard W. Southwell [Southwell, 1946] used such method in his book published in the mid 1940's. Originally, the FD method was predominantly implemented in the frequency domain but is now widely applied in the time domain because of the increasing capacity of modern computers. The Finite Differences Time

Domain (FDTD) algorithm was presented in 1966 by Yee [Yee, 1966] and since then, continuously extended and improved [Bergman et al., 1998], , [Texeira et al., 1998], [Taflove & Hagness, 2005], [Giannopoulos, 2002]. By means of this technique, the differential operators in Maxwell equations or the derived differential equations are discretized in a staggered grid, where the electric and magnetic field components are offset both in time and space by half discretization intervals. The detailed formulation of the discretized fields can be easily found in the literature.
The building block of this discretized FDTD grid is the Yee cell, which is illustrated in Fig. 3.1.

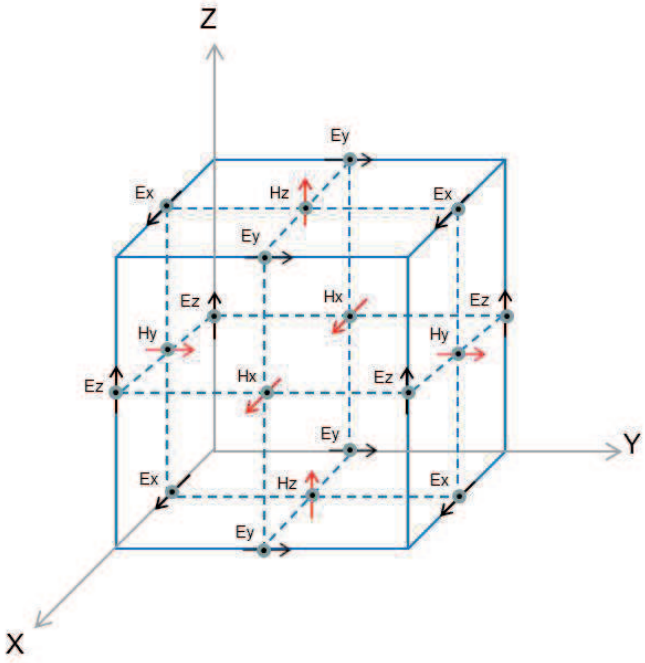

Figure 3.1 – Discretization scheme of the Yee cell. The six components of the EM field are discretized in a staggered grid and referenced by the spatial coordinates x, y and z directions, respectively. In addition to the spatial staggering the components of the magnetic field are also offset in time from those of the electric field by a half-time step.

Since the Maxwell equations, which are applied in each Yee cell, are discretized in both space and time, the solution is obtained in an iterative manner. In each iteration, the electromagnetic fields advance (propagate) in the FDTD grid and each iteration corresponds to an evolved simulated time of one Δt. Therefore, one can command the FDTD solver to simulate the fields for a given time window by setting the number of iterations. The values Δt, Δx, Δy, and Δz cannot be assigned independently. In order to ensure numerical stability, Δt must be bounded, and for the three dimensional case involving all six coupled electric and magnetic field vector components, it will be given by the Courant stability condition,

$$\Delta t \leq \frac{1}{c\sqrt{\frac{1}{(\Delta x)^2} + \frac{1}{(\Delta y)^2} + \frac{1}{(\Delta z)^2}}} \tag{3.8}$$

where c is the velocity of light.
Complex shaped objects can be also included in the models by assigning appropriate constitutive

parameters to the locations of the electromagnetic field components. However, objects with curved boundaries are usually represented using a staircase approximation.
The main variables when applying FDTD are the problem space size in cells required to model the scenario, and the number of steps needed. These determine the computer run time and computational cost. The cell size must be small enough to provide accurate results at the highest frequency of interest, and still be large enough to keep the resource requirements viable. Cell size is directly affected by the materials present. The greater the permittivity, the shorter the wavelength and the smaller the cell size needed. Due to the approximation inherent in FDTD, waves of different frequencies will propagate at slightly different speeds through the grid. This difference in speed depends on the direction of propagation relative to the grid. For accurate and stable results, this grid dispersion error must be minimized by reducing the cell size. The fundamental constraint is that the cell size must be much less than the smallest wavelength. In particular, it is generally accepted that the discretization step should be at least ten times smaller than the smallest wavelength of the propagating electromagnetic fields:

$$\Delta l = \frac{\lambda}{10}. \tag{3.9}$$

Another consideration, and one of the most relevant issues when modeling open boundary problems is the truncation of the computational space at a finite distance from sources and targets. An approximate condition known as absorbing boundary condition (ABC) needs to be defined in order to terminate the numerical domain without introducing additional reflections from the borders. The role of such an ABC is to absorb any waves impinging on it, in this way simulating an unbounded space. Therefore, the only reflected waves will be ideally the ones scattered by the target. A more detailed description of different ABC and a brief analysis of their influence on the simulation results is given in the Appendix A and the Section 5.3 respectively.

3.4 Finite Element Method

The Finite Element Method (FEM) is a numerical method used to approximate solutions of Ordinary and Partial Differential Equations (PDE). The procedure to reach a solution consists either of eliminating the differential equation completely (steady state problems), or translating the PDE into an approximate system of ordinary differential equations, which are then numerically integrated employing standard techniques. The FEM originated from the need of solving complex elasticity and structural analysis problems in civil, mechanical and aeronautical engineering. Its development can be traced back to the works by Alexander Hrennikoff (1941) and Richard Courant [Courant, 1943] in the early 40s. While the approaches proposed by these pioneers were totally different, they had one crucial characteristic in common: mesh discretization of a continuous domain into a set of discrete subdomains. The actual term 'finite element' appeared in a paper by R.W. Clough in 1960 [Clough, 1960] and since these early days, the technique has experimented a rapid growth in usage due to its versatility and underlying rich and robust mathematical basis. Nowadays, FEM is a well-developed numerical method [Huebner et al., 2001], [Jin, 2002] to solve boundary-value problems in a large variety of non-structural areas and new applications show up regularly in literature. Like other pure domain techniques, the FEM does

not explicitly account for open infinite domains and it is required the use of absorbing boundary conditions (ABC) at the model edges to terminate the computational domain.
It is interesting to compare this technique with the above presented FDM. Both methods discretize first the solution domain to approximate the solution of a given boundary-value problem, the former giving a point-wise approximation to the governing equations, and the latter a piecewise approximation. Specifically, the FEM creates a collection of arbitrarily shaped elements (normally triangular in 2D and tetrahedral in 3D) assigning a solution everywhere in the solution domain while FDM just on a set of orthogonal grid of points. This feature makes FEM much better suited for unstructured meshes and irregular geometries, such as arbitrary volumes or complicated curved faces, which are straightforward to deal with. Likewise, FEM is more flexible in handling complex boundary conditions when these are needed. All this makes FEM a suitable method to accurately model a near field GPR scenario, where the real antenna geometry/parameters along with surface roughness and soil heterogeneity should be accommodated. It is also a crucial issue to consider the amount of computational power needed to formulate and solve the problem, which usually supersedes FD method for problems in two or more dimensions. Then, special care needs to be taken in order to optimize the problem definition and select the most proper solver. In this context, the question of adaptivity involving either remeshing or increased interpolation order during the solution process (see Definitions), becomes very important. Within the FEM, the most widely used methods to approximate the governing differential equation (3.1) are the Rayleigh-Ritz and Galerkin methods. These techniques form the basis for the FEM and their fundamental principles will be introduced in the next section.

3.4.1 Rayleigh-Ritz Method

The underlying mathematical foundation of the FEM comes from the classical Rayleigh-Ritz method. The Rayleigh-Ritz procedure reformulates the original differential equation boundary-value problem, already given in (3.1), as a variational problem. So defined, the calculus of variations is applied to find the minimum or maximum of a given functional and this value corresponds to the solution of the differential equation. An approximate solution to this variational problem can be found by setting up a solution with respect to a number of variable parameters; hence, the minimization of the functional with respect to these variables gives the best approximation. This kind of approach provides the reasons why the finite element method worked well for the class of problems in which variational statements could be obtained.
The problem can be illustrated for the simplest case defining an inner product by

$$\langle u \mid v \rangle \equiv \int_{\Omega} u^* v d\Omega \tag{3.10}$$

and assuming the operator $\hat{L}$ to be self-adjoint and positive definite, and is referred to as the standard variational principle. The requirement of $\hat{L}$ to be self-adjoint, limits its application to lossless media. In such a case, the solution to Eq. (3.1) can be found by minimizing the functional given by

$$I(f) = \frac{1}{2}\langle \hat{L} f \mid f \rangle - \frac{1}{2}\langle f \mid g \rangle - \frac{1}{2}\langle g \mid f \rangle. \tag{3.11}$$

Proof of this statement follows in two steps: first, it must be shown that the differential equation (3.1) is a necessary consequence when $I(f)$ is stationary (either at a maximum or minimum) and second, that the stationary point is a minimum.
Once the functional given in Eq. (3.11) is determined, an approximate solution is developed using a finite basis trial expansion

$$f_t = \sum_{j=1}^{N} c_j \phi_j = \vec{c} \cdot \vec{\phi} = \vec{\phi} \cdot \vec{c}, \tag{3.12}$$

where ϕ_j are a finite set of expansion functions defined over Ω, and c_j are the coefficients to be determined. Then, Eq. (3.12) becomes

$$I(f_t) = \frac{1}{2}\vec{c} \cdot \langle \hat{L}\vec{\phi} \mid \vec{\phi} \rangle \cdot \vec{c} - \frac{1}{2}\vec{c} \cdot \langle \vec{\phi} \mid g \rangle - \frac{1}{2}\langle g \mid \vec{\phi} \rangle \cdot \vec{c}. \tag{3.13}$$

The next step is the minimization of $I(f_t)$ with respect to the coefficients c_j. When the problem is real, the partial derivatives are forced to be zero and the following set of linear equations are constructed

$$\begin{aligned} \frac{\partial}{\partial c_i} I(f_t) &= \frac{1}{2}\langle \hat{L}\phi_i \mid \vec{\phi} \rangle \cdot \vec{c} + \frac{1}{2}\vec{c} \cdot \langle \hat{L}\vec{\phi} \mid \phi_i \rangle - \langle \phi_i \mid g \rangle \\ &= \frac{1}{2}(\langle \hat{L}\phi_i \mid \vec{\phi} \rangle + \langle \hat{L}\vec{\phi} \mid \phi_i \rangle) \cdot \vec{c} - \langle \phi_i \mid g \rangle \\ &= \langle \phi_i \mid \hat{L}\vec{\phi} \rangle \cdot \vec{c} - \langle \phi_i \mid g \rangle = 0 \end{aligned}$$

for i= 1,2, ...,N, and where the last step follows because $\hat{L}$ is self-adjoint and the problem is real. In case the operator involved is complex (as it happens in lossy media), Eq. (3.11) is still valid but the inner product needs to be redefined.
The former result can be written as a matrix equation

$$A\mathbf{x} = \mathbf{b} \tag{3.14}$$

where

$$A_{ij} = \langle \phi_i \mid \hat{L}\phi_j \rangle, \qquad b_i = \langle \phi_i \mid g \rangle,$$

and where $\mathbf{x}$=$\mathbf{c}$ are the coefficients to be determined. By the self-adjoint property of $\hat{L}$ it is also seen that A is a symmetric matrix ($A_{ij} = A_{ji}$).
If the differential equation operator $\hat{L}$ is not capable of being formulated as self-adjoint, the Galerkin method is often used.

3.4.2 Galerkin Method

For the application of FEM to more sorts of problems, the classical theory cannot be applied (e.g. fluid related problems). And the extension of the mathematical basis to non-linear and non-structural problems is achieved through the method of weighted residuals (MWR), originally conceived by Galerkin. The MWR was found to provide the ideal theoretical basis for a much wider spectrum of problems as opposed to the Rayleigh-Ritz method. Basically, the method is based on weighting the residual of the differential equation and the resulting product integrated

over space. Technically, Galerkin's method is a special case of the general MWR procedure, since various types of weights can be employed.
If we have an approximate solution, f_t, the residual is defined as follows

$$r \equiv \hat{L} f_t - g, \tag{3.15}$$

which is not equal to zero for the approximate solution f_t. By forcing the weighted residuals, defined below, to be zero on Ω it gives the best approximation

$$R_i \equiv \int_\Omega w_i r d\Omega = 0, \tag{3.16}$$

where w_i are a given set of weighting functions. Galerkin's method employs as weighting functions the same as those used for the expansion of the trial solution in Eq. (3.12), i.e., $w_i = \phi_i$. The weighted residual integrals become

$$R_i = \int_\Omega (\phi_i \hat{L} \vec{\phi} \cdot \vec{c} - \phi_i g) d\Omega. \tag{3.17}$$

Similar to Eq. (3.14), this ends up in a matrix system for the coefficients $\vec{c}$. When the operator $\hat{L}$ is self-adjoint, the matrix system produced by Galerkin's method will reduce to the same matrix system produced by the Rayleigh-Ritz method. It should be added that a variety of other residual methods exist that employ different sets of weighting functions.
The Rayleigh-Ritz and Galerkin methods described above expand approximate solutions of Eq. (3.1) using a finite basis set of functions defined all over Ω (Eq.3.12). For problems in more than one dimension, it is usually a nontrivial matter defining these basis functions. The FEM approaches this problem by dividing the domain Ω into many subdomains; by making the subdomains small enough such that the solution does not vary in any complicated way, a trial function can be built from a linear combination of simple approximate solutions on each subdomain. Once these functions have been defined, either the Rayleigh-Ritz or Garlekin method may be used to solve the problem but most practitioners of the FEM now use Galerkin's method.
Hence, the FEM consists of dividing the domain into subdomains and constructing a trial solution composed of a linear combination of basis functions defined over each respective subdomain, which differs from the classical Rayleigh-Ritz and Galerkin methods since they construct the trial solution composed of a linear combination of basis functions defined over whole domain.

3.4.3 COMSOL Simulation Tool

The COMSOL Multiphysics is a powerful commercial tool for modeling and solving all kind of physical problems based on PDEs via the FEM. This simulation environment facilitates all steps in the modeling process defining your geometry, specifying your physics, meshing, solving and then post-processing the results.
Model set up is fast, thanks to a number of predefined modeling interfaces for applications ranging from fluid flow and heat transfer to structural mechanics and electromagnetic analyses. Material properties, source terms and boundary conditions can all be arbitrary functions of the dependent variables which is of special interest in our case, since we pretend to model the soil in a realistic

manner.
For a 2D geometry, COMSOL uses a meshing algorithm to generate an unstructured mesh consisting of triangular elements or a mapped mesh consisting of quadrilateral elements. A 3D mesh is either generated as an unstructured mesh containing tetrahedral elements or by extruding or revolving a 2D mesh. Figure 3.2 shows a pair of examples of typical domain discretization in both 2D and 3D.

Figure 3.2 – 2D and 3D FEM Meshes.

In fact, one major advantage of the FEM is that it allows the user to arbitrarily fine tune a mesh, such that there is more resolution in areas of the geometry where there may be abrupt variations in the solution, e.g., antenna elements. Specifying mesh size manually to minimize the error in the desired output, is often not easy and the mesh refinement and adaptive mesh generation (see Definitions) available in COMSOL identify the regions where high resolution is needed and produce an adequate mesh automatically. This factor was critical in the simulations presented in this thesis, since the resolution needed in such areas would have made a uniform mesh of the entire scenario computationally unviable.
In selecting the interpolation functions, COMSOL provides default cases optimized for each application mode. These include, first, second and higher-order polynomials in some 2-dimensional cases and linear vector elements for 2- and 3-dimensional cases. Linear vector elements are necessary in certain electromagnetic application modes in order to make the boundary conditions between subdomains self-consistent with Maxwell equations. The final steps of the FEM, formulating and solving the systems of equations, are both handled by numerous subalgorithms within COMSOL.

3.5 Absorbing Boundary Conditions (ABC) and Perfectly Matched Layers (PML)

One of the first issues to consider when dealing with radiation problems and one of the great challenges in finite element modeling is how to treat open boundaries. Due to the non-continuous nature of the discretized model space, some boundary reflections are always present. This reflected energy can, in general, be minimized by a suitable choice of the boundary conditions.
The Electromagnetics Module offers two closely related types of absorbing boundary conditions,

the scattering boundary condition and the matched boundary condition. The former is perfectly absorbing for a plane wave at normal incidence. The matched boundary condition is also perfectly absorbing for guided modes, provided that the correct value of the propagation constant is supplied. They are mainly intended to be used at boundaries that do not represent a physical boundary. However, in many scattering and antenna modeling problems, the incident radiation cannot be described as a plane wave with a well-known direction of propagation. In those situations, the use of *Perfectly Matched Layers* (PMLs) may be considered. A PML is strictly speaking not a boundary condition but an additional domain that absorbs the incident radiation without producing reflections. It provides good performance for a wide range of incidence angles and is not very sensitive to the shape of the wave fronts. The PML formulation can be deduced from Maxwell equations by introducing a complex-valued coordinate transformation under the additional requirement that the wave impedance should remain unaffected as explained in [Jin, 2002]. From the implementation viewpoint, it is more practical to describe the PML as an anisotropic material with losses. This formulation is used by COMSOL and also covered by [Jin, 2002]. In Appendix A we address how to implement planar, cylindrical and spherical PMLs in COMSOL along with the definition of the other absorbing boundary conditions utilized.

4

Physical and Geophysical Background

The eternal mystery of the world is its comprehensibility
A. Einstein

The basis for quantitatively describing GPR signals may be found by combining the physics of electromagnetic (EM) wave propagation with the material properties of the media.

4.1 Theory of Electromagnetic Wave Propagation

The EM analysis is basically a problem of solving a set of fundamental equations subject to given boundary conditions. In the next sections we review some basic concepts and equations of EM theory. Our emphasis will be on the presentation of the differential equations and boundary conditions that define the GPR problem.

4.1.1 Fundamental equations

In general, electric and magnetic fields are described as coupled, three-dimensional polarized vector quantities that have both magnitude and direction. The relations and variations of the electric and magnetic fields, charges and currents associated with electromagnetic waves are governed by the Maxwell equations. These equations can be written either in differential or in integral form. The differential form of Maxwell equations is the most widely employed representation to solve boundary-value electromagnetic problems. It is used to describe and relate the field vectors, current densities, and charge densities at any point in space and time. These expressions are valid if it is assumed that the field vectors are single-valued, bounded, continuous functions of

position and time and have continuous derivatives. Field vectors associated with electromagnetic waves possess these characteristics except where abrupt changes in charge and current densities are present. These discontinuities usually happen at interfaces between media where there are discrete changes in the electrical parameters across the interface. The variations of the field vectors across such boundaries (interfaces) are related to the discontinuous distributions of charges and currents by what are usually referred to as the *boundary conditions*. Hence, a complete description of the fields vectors at any point (including discontinuities) at any time requires not only the Maxwell equations but also the associated boundary conditions [Balanis, 2005].
In differential form, the Maxwell equations are:

$$\vec{\nabla} \times \vec{E}(\vec{r},t) = -\frac{\partial \vec{B}(\vec{r},t)}{\partial t}, \tag{4.1}$$

$$\vec{\nabla} \times \vec{H}(\vec{r},t) = \vec{J}(\vec{r},t) + \frac{\partial \vec{D}(\vec{r},t)}{\partial t}, \tag{4.2}$$

$$\vec{\nabla} \cdot \vec{D}(\vec{r},t) = \rho_e, \tag{4.3}$$

$$\vec{\nabla} \cdot \vec{B}(\vec{r},t) = 0, \tag{4.4}$$

where $\vec{E}$ in [V/m] is the vector representing the *electric field intensity*, $\vec{D}$ in [C/m^2] is the *electric flux density*, $\vec{H}$ in [A/m] is the *magnetic field intensity*, $\vec{B}$ in [T] is the *magnetic flux density*, $\vec{J}$ in [A/m^2] is the *electric current density*, ρ_e in [C/m^3] is the *electric charge density* and $\vec{\nabla}$ is the vector differential operator.
All the above electromagnetic field variables depend on the spatial position with respect to some coordinate system, $\vec{r}$ in [m], and the elapsed time, t in [s].
The first equation is known as Faraday's law of induction, the second is Ampere's law as amended by Maxwell to include the displacement current $\frac{\partial \vec{D}}{\partial t}$ and the third and fourth are Gauss' laws for the electric and magnetic fields.
The charge and current densities ρ_e, $\vec{J}$ may be thought as the sources of the electromagnetic fields. For wave propagation problems, these densities are localized in space; for example, they are restricted to flow on an antenna. The generated electric and magnetic fields are radiated away from these sources and can propagate to large distances to the receiving antennas. Far from the sources, that is, in source-free regions of space, these terms become zero.
In those four Maxwell equations only the vector $\vec{E}$ and $\vec{B}$ as well as $\vec{D}$ and $\vec{H}$ respectively are linked. Assuming isotropic media and field vectors with not too high intensities all four aforementioned vectors can be related. Therefore three constitutive relations are introduced.

$$\vec{D}(\vec{r},\omega) = \epsilon_0 \epsilon_r(\vec{r},\omega)\vec{E}(\vec{r},\omega), \tag{4.5}$$

$$\vec{B}(\vec{r},\omega) = \mu_0 \mu_r(\vec{r},\omega)\vec{H}(\vec{r},\omega), \tag{4.6}$$

where ϵ_0 and μ_0 are the electric and magnetic field constants and ϵ_r and μ_r are the relative dielectric permittivity and the relative magnetic permeability respectively. The parameter ω is the angular frequency which is related to the frequency f by,

$$f = \frac{\omega}{2\pi}. \tag{4.7}$$

The Ohm's law complete the previous constitutive equations:

$$\vec{J}(\vec{r},\omega) = \sigma(\vec{r},\omega)\vec{E}(\vec{r},\omega), \tag{4.8}$$

with σ the electrical conductivity. Although a relationship between $\vec{B}$ and $\vec{H}$ or $\vec{E}$ and $\vec{D}$ respectively is established, a direct transformation cannot be performed. If anisotropy is present, the three electrical properties ϵ_r, μ_r and σ become tensors. Generally, the four Maxwell equations (4.1) through (4.4) are valid in the time domain, whereas the constitutive equations (4.5), (4.6) and (4.8) are valid in the frequency domain. Only by assuming non-dispersive media, i.e. the relative permittivity, relative magnetic permeability and electric conductivity are not frequency dependent, the equations acquire the same form in time domain. Otherwise, the multiplication in frequency domain has to be substituted by a convolution in time domain. In many real cases, the assumption of non-dispersive media cannot be made. To allow the application of the three aforementioned constitutive equations, the four Maxwell equations have to be transformed into the frequency domain. This can be achieved by applying the Fourier transform to the Maxwell equations. Through the inverse Fourier transform, any time-varying field can be expressed as a linear combination of single-frequency solutions:

$$\vec{A}(\vec{r},t) = \frac{1}{2\pi}\int_{-\infty}^{\infty} \vec{A}(\vec{r},\omega)e^{i\omega t}d\omega, \tag{4.9}$$

where $\vec{A}(\vec{r},t)$ and $\vec{A}(\vec{r},w)$ is the vector field to be transformed from time to frequency domain. We assume that all fields are *time-harmonic*, i.e., harmonically oscillating functions with a single frequency that can be represented by $e^{i\omega t}$:

$$\vec{E}(\vec{r},t) = \vec{E}(\vec{r})e^{i\omega t}, \quad \vec{H}(\vec{r},t) = \vec{H}(\vec{r})e^{i\omega t},$$

where the phasor amplitudes $\vec{E}(\vec{r})$, $\vec{H}(\vec{r})$ are complex-valued.
Applying the transformation rule (4.9) to the Maxwell equations and substituting the constitutive relations (4.5), (4.6) and (4.8), we may rewrite equations (4.1) to (4.4) in the form:

$$\vec{\nabla} \times \vec{E}(\vec{r},\omega) = -i\omega\vec{B}(\vec{r},\omega), \tag{4.10}$$

$$\vec{\nabla} \times \vec{H}(\vec{r},\omega) = (\sigma(\vec{r},\omega) + i\omega\epsilon_0\epsilon_r(\vec{r},\omega))\vec{E}(\vec{r},\omega), \tag{4.11}$$

$$\vec{\nabla} \cdot \Big(\epsilon_0\epsilon_r(\vec{r},\omega)\vec{E}(\vec{r},\omega)\Big) = 0, \tag{4.12}$$

$$\vec{\nabla} \cdot \vec{B}(\vec{r},\omega) = 0, \tag{4.13}$$

where we have assumed a space absent of electrical charges (ρ), which is a correct assumption for most georadar applications since normally no free charges are present in the field.
To complement all fundamental equations to describe all phenomena in electromagnetism the Lorentz force has to be mentioned. The Lorentz force will not be considered here, since it describes effects of moving charges.

4.1.2 Dispersion Equations

For the following derivations an additional assumption is necessary. The investigated region is homogeneous, i.e. the relative permittivity, the relative magnetic permeability and the electrical conductivity do not show dependence on the position. With these assumptions equation (4.12) can be written as:

$$\vec{\nabla} \cdot \Big(\epsilon_0\epsilon_r(\omega)\vec{E}(\vec{r},\omega)\Big) = 0. \tag{4.14}$$

Using the relation $\vec{\nabla} \cdot (a\vec{A}) = a(\vec{\nabla} \cdot \vec{A}) + (\vec{\nabla}a) \cdot \vec{A}$, for a homogeneous medium (4.14) results in

$$\vec{\nabla} \cdot \vec{E}(\vec{r}, \omega) = 0. \tag{4.15}$$

Then, we apply the curl to (4.10) and employing the identity $\vec{\nabla} \times \vec{\nabla} \times \vec{A} = \vec{\nabla}(\vec{\nabla} \cdot \vec{A}) - \vec{\nabla} \cdot (\vec{\nabla}A)$ and introducing (4.15), this leads to

$$\vec{\nabla} \cdot \vec{\nabla}\vec{E}(\vec{r}, \omega) = i\omega\vec{\nabla} \times \vec{B}(\vec{r}, \omega). \tag{4.16}$$

$\vec{B}(\vec{r}, w)$ can be expressed by the constitutive equation (4.6). If we use the rule $\vec{\nabla} \times (a\vec{A}) = a(\vec{\nabla} \times \vec{A}) + (\vec{\nabla}a) \times \vec{A}$ and assuming μ_r to be constant inside the considered area, (4.16) results in

$$\Delta\vec{E}(\vec{r}, \omega) = i\omega\mu_0\mu_r(\omega)\vec{\nabla} \times \vec{H}(\vec{r}, \omega), \tag{4.17}$$

where $\Delta = \vec{\nabla} \cdot \vec{\nabla}$ is the Laplace operator. If we express $\vec{H}(\vec{r}, \omega)$ according to the Maxwell equation (4.11), the above equation finally yields

$$\Delta\vec{E}(\vec{r}, \omega) = -\omega^2\mu_0\mu_r(\omega)\epsilon_0 \left(\epsilon_r(\omega) - i\frac{\sigma(\omega)}{\epsilon_0\omega}\right) \vec{E}(\vec{r}, \omega), \tag{4.18}$$

which is known as *Helmholtz equation*. Generally all three parameters, i.e. relative magnetic permeability, relative permittivity and electrical conductivity, are complex and frequency dependent parameters:

$$\epsilon_r(\omega) = \epsilon_r'(\omega) - i\epsilon_r''(\omega), \tag{4.19}$$

$$\mu_r(\omega) = \mu_r'(\omega) - i\mu_r''(\omega), \tag{4.20}$$

$$\sigma(\omega) = \sigma'(\omega) - i\sigma''(\omega), \tag{4.21}$$

where $\epsilon_r'(\omega)$ is the dielectric polarization term, $\epsilon_r''(\omega)$ represents energy loss due to polarization lag, $\sigma'(\omega)$ refers to ohmic conduction and $\sigma''(\omega)$ is related to faradaic diffusion.
Considering typical GPR scenarios, a few constrictions can be assumed. In most soils the relative magnetic permeability is equal to one and will thereby be neglected. In the frequency range of common georadar applications from 10 MHz to few GHz, the imaginary part of the electrical conductivity can be ignored and the real part is assumed to be frequency independent and equal to the DC conductivity [Knight & Endres, 2005]. Hence, the expression inside the bracket in equation (4.18) is often merged into one parameter called the effective relative permittivity, ϵ_{eff}, or,

$$\epsilon_{\text{eff}} = \epsilon_{\text{eff}}'(\omega) - i\epsilon_{\text{eff}}''(\omega) = \epsilon_r'(\omega) - i\left(\epsilon_r''(\omega) + \frac{\sigma'(\omega)}{\epsilon_0\omega}\right), \tag{4.22}$$

with ϵ_{eff}' and ϵ_{eff}'' the real and imaginary part of the effective relative permittivity. The parameter ϵ_r' is associated with the electric permittivity, which may also be expressed in terms of relative permittivity. The parameter ϵ_r'' is related to losses due to both conductivity and frequency. In the frequency range of GPR, displacement currents are usually higher than conduction currents and for practical purposes, at frequencies up to 1GHz and conductivities below 0.1S/m, the effect of the ϵ_r'' term will be small and is usually disregarded.
Equation (4.18) can be easily solved substituting the $\vec{E}$ field by a plane wave 'ansatz':

$$\vec{E}(\vec{r}, \omega) = E_0 e^{i(\vec{k}\cdot\vec{r} - \omega t)}, \tag{4.23}$$

with $\vec{k}$ the wave vector. The solution is then the dispersion relation

$$k^2(\omega) = \omega^2\mu_0\epsilon_0\left(\epsilon_r'(\omega) - i\frac{\sigma'(\omega)}{\epsilon_0\omega}\right) = \omega^2\mu_0\epsilon_0\epsilon_{\text{eff}}. \tag{4.24}$$

The parameter k can be complex depending on the effective relative permittivity. It may be separated into real and imaginary parts:

$$k = \beta + i\alpha = \omega\sqrt{\mu_0\epsilon_0\epsilon_{\text{eff}}}, \tag{4.25}$$

where α corresponds to the attenuation factor and β is the phase constant.
From the solution (4.25) the following relationships can be derived:

$$\alpha = \omega\left[\frac{\mu_0\epsilon_0\epsilon_{\text{eff}}'}{2}\left(\sqrt{1+\tan^2(\delta)}-1\right)\right]^{\frac{1}{2}}, \tag{4.26}$$

$$\beta = \omega\left[\frac{\mu_0\epsilon_0\epsilon_{\text{eff}}'}{2}\left(\sqrt{1+\tan^2(\delta)}+1\right)\right]^{\frac{1}{2}}, \tag{4.27}$$

$$\tan(\delta) = \left(\frac{\epsilon_{\text{eff}}''}{\epsilon_{\text{eff}}'}\right). \tag{4.28}$$

The dimensionless parameter $tan(\delta)$ is more commonly called the material loss tangent [Daniels, 2004] and can be interpreted as the ratio between the conduction current density to the displacement current density. Then, the phase velocity v_{ph} can be determined by:

$$v_{ph}(\omega) = \frac{\omega}{\beta} = \frac{c_0}{\left[\frac{\epsilon_{\text{eff}}''}{2}\left(\sqrt{1+\tan^2(\delta)}+1\right)\right]^{\frac{1}{2}}} \approx \frac{c_0}{\sqrt{\mu_r(\omega)\epsilon_r'(\omega)}}, \tag{4.29}$$

with c_0 the speed of light in free space. In low-loss media where $\epsilon_{\text{eff}}'' << \epsilon_{\text{eff}}'$ and where wave propagation will occur, $\tan(\delta)$ approaches zero. In this case and assuming non-magnetic materials, the phase velocity of an EM wave can be simplified to the well-known relation:

$$v_{ph} = \frac{c_0}{\sqrt{\epsilon_{\text{eff}}'}}. \tag{4.30}$$

For most georadar applications (4.30) is sufficiently accurate since media with significant loss tangents will supply inferior data quality caused by the higher attenuation (4.26). For media with insignificant dispersion, i.e. $\epsilon_{\text{eff}}(\omega) \approx \epsilon_{\text{eff}}(\omega + \delta\omega)$, v_{ph} is equal to the EM propagation velocity v.

4.1.3 Reflection and Transmission of Electromagnetic Waves

In 4.1.2 the various phenomena of EM wave propagation through a homogeneous medium, i.e. attenuation and propagation velocity, were described. For typical georadar applications on the surface such condition is not given. In this section we will show what happens if a EM wave reaches an interface. Basically, a part of the incident energy will be reflected, while the remaining energy will be transmitted to the lower medium. For this analysis we choose a coordinate system as displayed in Fig. 4.1. In this system the position vector $\vec{r}$ is necessarily contained in the separation

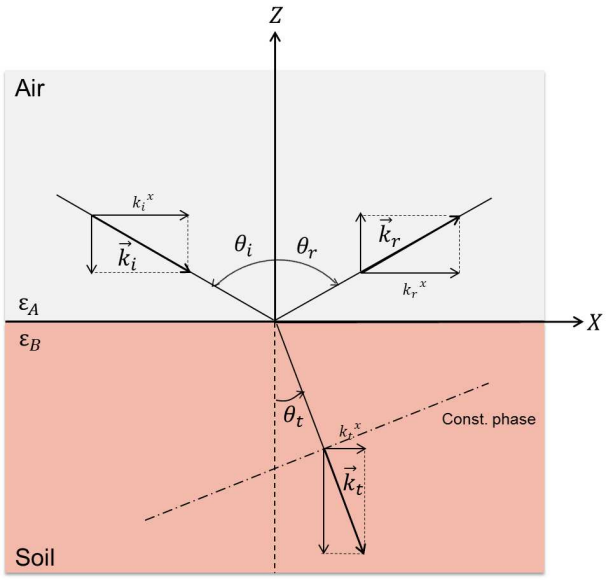

Figure 4.1 – Incidence, reflection and refraction angles of an electromagnetic plane wave at the interface between two dielectric media.

interface between the two media which corresponds to the XY-plane; the XZ-plane coincides with the incidence plane, which contains the incident $\vec{k}^i$ vector. Let's assume a plane wave (Eq. 4.23) approaching an interface from medium A with a relative permittivity $\epsilon^A_{\text{eff}} = \epsilon'^A_{\text{eff}}$ to a medium B with a relative permittivity $\epsilon^B_{\text{eff}} = \epsilon'^B_{\text{eff}} - i\epsilon''^B_{\text{eff}}$ and $tan(\delta) << 1$. The boundary conditions at a flat interface between two homogeneous media require that the tangential components of $\vec{E}$ and $\vec{H}$ and the normal components of $\vec{D}$ and $\vec{B}$ are temporally and spatially continuous [Jackson, 1999]. Consequently, the phase factors of the incident, reflected, and transmitted wave must be identical along the interface for all times: $\vec{k}^i \cdot \vec{r} - \omega_i t = \vec{k}^r \cdot \vec{r} - \omega_r t = \vec{k}^t \cdot \vec{r} - \omega_t t$.
To fulfill these conditions the frequencies of the three waves need to be equal: $\omega_i = \omega_r = \omega_t$. And similarly, the tangential components of the $\vec{k}$ vectors have to remain constant, implying that the $\vec{k}^r$ and $\vec{k}^t$ must lie in the plane defined by the incident wave vector $\vec{k}^i$ and perpendicular to the interface.
Since the incidence plane is chosen as the XZ-plane of the coordinate system ($k^i_y = 0$) and considering that the z component of $\vec{r}$ is also zero, they can be simplified as follows:

$$k^i_x = k^r_x = k^t_x, \tag{4.31}$$

$$0 = k^r_y = k^t_y. \tag{4.32}$$

Introducing now the angles of incidence φ^i, reflection φ^r and transmission φ^t we have

$$|\vec{k}^i| \sin\varphi^i = |\vec{k}^r| \sin\varphi^r = |\vec{k}^t| \sin\varphi^t. \tag{4.33}$$

Thus, as $|\vec{k}^i| = |\vec{k}^r|$, the following relationships can be deduced

$$|\vec{k}^i| \sin\varphi^i = |\vec{k}^r| \sin\varphi^r \Longrightarrow \varphi^i = \varphi^r, \tag{4.34}$$

$$|\vec{k}^i| \sin\varphi^i = |\vec{k}^t| \sin\varphi^t \Longrightarrow \frac{\sin\varphi^i}{\sin\varphi_t} = \frac{\sqrt{\epsilon^B_{\text{eff}}}}{\sqrt{\epsilon^A_{\text{eff}}}}. \tag{4.35}$$

Equation (4.34) is the so called *reflection law* and equation (4.35) is better known as *Snells law*. If the relative permittivity, which usually depends on the frequency, is of complex value the resulting angles and $\vec{k}$ vectors become also complex.

In the second part of this section we will obtain the amplitudes of the reflected and transmitted waves for a given incident wave taking into account the EM parameters of the media. From Eq. 4.1 and assuming again the fields $\vec{E}$ and $\vec{B}$ to be plane waves we get:

$$\vec{k} \times \vec{E}_0(\vec{r},\omega) = -\omega \vec{B}_0(\vec{r},\omega). \tag{4.36}$$

We define now a vector $\vec{e}_z$ normal to the interface. Then, using Eq. 4.36, the continuity conditions of the fields at the interface take the form:

$$\vec{e}_z \cdot (\epsilon^A \vec{E}_0^i(\vec{r},\omega) + \epsilon^A \vec{E}_0^r(\vec{r},\omega)) = \vec{e}_z \cdot \epsilon^B \vec{E}_0^t(\vec{r},\omega), \tag{4.37}$$

$$\vec{e}_z \cdot (\vec{k} \times \vec{E}_0^i(\vec{r},\omega) + \vec{k} \times \vec{E}_0^r(\vec{r},\omega)) = \vec{e}_z \cdot \vec{k} \times \vec{E}_0^t(\vec{r},\omega), \tag{4.38}$$

$$\vec{e}_z \times (\vec{E}_0^i(\vec{r},\omega) + \vec{E}_0^r(\vec{r},\omega)) = \vec{e}_z \times \vec{E}_0^t(\vec{r},\omega), \tag{4.39}$$

$$\vec{e}_z \times (\frac{1}{\mu^A}\vec{k} \times \vec{E}_0^i(\vec{r},\omega) + \frac{1}{\mu^A}\vec{k} \times \vec{E}_0^r(\vec{r},\omega)) = \vec{e}_z \times \frac{1}{\mu^B}\vec{k} \times \vec{E}_0^t(\vec{r},\omega). \tag{4.40}$$

To describe the whole behavior of the EM waves at an interface the vector $\vec{E}_0$ can be decomposed into a component parallel and one perpendicular to the plane of incidence (parallel and perpendicular polarizations). If the incident wave has another polarization, it can be expressed as a combination of both elementary polarizations. Moreover, due to the symmetry of the interface respect to the incidence plane, the polarization does not change when the wave is reflected or transmitted. Hence, both directions will be treated separately.
After applying some vectorial algebra to the continuity of the fields and using the Snell law, the coefficients of transmission τ and reflection ρ can be derived:

$$\begin{aligned}
\tau_\perp &= \frac{\vec{E}_{0\perp}^t}{\vec{E}_{0\perp}^i} = \frac{2\sqrt{\epsilon_{\text{eff}}^A}\cos(\varphi^i)}{\sqrt{\epsilon_{\text{eff}}^A}\cos(\varphi^i) + \sqrt{\epsilon_{\text{eff}}^B}\cos(\varphi^t)} = \frac{\sin(\varphi^t - \varphi^i)}{\sin(\varphi^t + \varphi^i)}, \\
\rho_\perp &= \frac{\vec{E}_{0\perp}^r}{\vec{E}_{0\perp}^i} = \frac{\sqrt{\epsilon_{\text{eff}}^A}\cos(\varphi^i) - \sqrt{\epsilon_{\text{eff}}^B}\cos(\varphi^t)}{\sqrt{\epsilon_{\text{eff}}^A}\cos(\varphi^i) + \sqrt{\epsilon_{\text{eff}}^B}\cos(\varphi^t)} = \frac{2\sin(\varphi^t)\cos(\varphi^i)}{\sin(\varphi^i + \varphi^t)},
\end{aligned} \tag{4.41}$$

$$\begin{aligned}
\tau_\parallel &= \frac{\vec{E}_{0\parallel}^t}{\vec{E}_{0\parallel}^i} = \frac{2\sqrt{\epsilon_{\text{eff}}^A}\cos(\varphi^i)}{\sqrt{\epsilon_{\text{eff}}^A}\cos(\varphi^t) + \sqrt{\epsilon_{\text{eff}}^B}\cos(\varphi^i)} = \frac{\tan(\varphi^i - \varphi^t)}{\tan(\varphi^i + \varphi^t)}, \\
\rho_\parallel &= \frac{\vec{E}_{0\parallel}^r}{\vec{E}_{0\parallel}^i} = \frac{\sqrt{\epsilon_{\text{eff}}^B}\cos(\varphi^i) - \sqrt{\epsilon_{\text{eff}}^A}\cos(\varphi^t)}{\sqrt{\epsilon_{\text{eff}}^A}\cos(\varphi^t) + \sqrt{\epsilon_{\text{eff}}^B}\cos(\varphi^i)} = \frac{2sin(\varphi^t)\cos(\varphi^i)}{\sin(\varphi^i + \varphi^t)\cos(\varphi^i - \varphi^t)}.
\end{aligned} \tag{4.42}$$

Equations (4.41) and (4.42) are also known as *Fresnel equations* and describe the behavior of a plane wave when reaching an interface. As we can see, the coefficients of reflection and transmission depend on the EM parameters of the media on both sides of the interface, the frequency, the angle of incidence, and the polarization of the incident wave. If we assume normal incidence ($\varphi^i = 0$), which is often the case for GPR applications, the polarization is of no significance anymore and (4.41) and (4.42) get simplified. We have to note that these relationships are valid for

incoming plane waves and this condition is only assured for sufficient distance between the EM source and the interface. Otherwise, the wave vector $\vec{k}$ will be a variable of the spatial position. Hence, to investigate shallow objects or interfaces in the close proximity of the illuminating antenna, the plane wave assumption and the Fresnel equations can only be used for a preliminary analysis.

4.1.4 GPR Resolution

The radar resolution is defined as the system capacity to discriminate between individual scatterers. When dealing with GPR technology, the resolution concept is essentially divided into two classes: vertical (downrange, depth or longitudinal) resolution R_V and horizontal (cross-range, angular, lateral, or plan) resolution R_H [Daniels, 1996].
In general, resolution will be the highest when the antenna is placed over the surface of the medium, and it decreases as the antenna is elevated above the surface [van der Kruk, 2004]. It is also demonstrated that spatial resolution improves when the attenuation rises [Daniels, 1996].

Vertical Resolution

Vertical resolution provides knowledge about the equipment's ability to differentiate in time two adjacent reflections as different events. For the type of system considered in this thesis (pulsed radar) the vertical resolution mainly depends on the duration of the radar pulse, which is related to the center frequency of the antenna. The shorter the pulse duration, the better its resolution will be. It is popularly accepted that two close events can be distinguished if the targets are separated in time by a difference of half the effective The shorter the pulse duration, the better its resolution will be. It is popularly accepted that two close events can be distinguished if the targets are separated in time by a difference of half the effective pulse duration τ_P, which is obtained from the width of the signal envelope at its -3 dB level. Therefore the expected spatial vertical resolution can be calculated from τ_P and the wave propagation velocity v in the medium as follows [Annan, 2003]:

$$R_V = \frac{\tau_P v}{2} = \frac{\tau_P c}{2\sqrt{\epsilon_r}}. \tag{4.43}$$

Fig. 4.2 displays graphically the resulting vertical resolution for different pulse lengths and media. This theoretical approach does not take into account that the characteristics of the transmitted radar signal will change in the media it is traveling through. In most natural materials, the attenuation of the electromagnetic waves increases with frequency, widely known as the dispersion effect. This low-pass filtering effect produced by the media causes an increase in the length of the pulse (the effective bandwidth is reduced) and, therefore, worsens the resolution. The above formula will be also affected by the spreading losses of the signal, which means that targets that are far away from the source have different vertical resolution than those closer. Another important issue to consider when trying to estimate the vertical resolution is the composition of the targets to resolve. Materials with a high dielectric contrast are more likely to mask the objects that are close to them since they produce strong reflections.

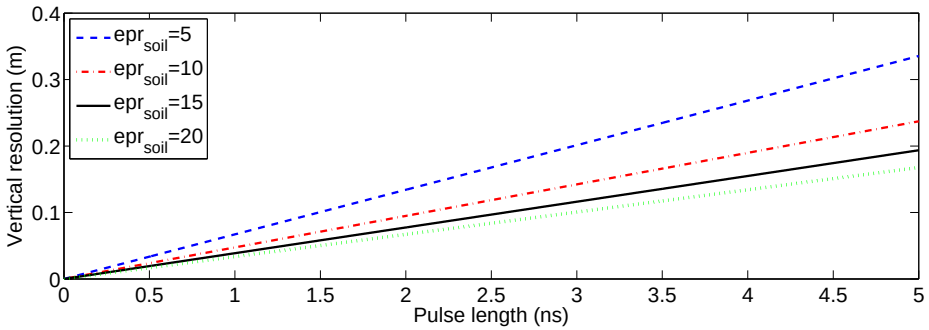

Figure 4.2 – Vertical resolution against pulse length for different media.

Horizontal Resolution and First Fresnel Zone

Horizontal resolution indicates the minimum distance that should exist between two reflectors located next to the other at the same depth (parallel to the analyzed medium surface) so that the radar detects them as separate events [Daniels, 1996]. To simplify the problem, we consider that the wave is emitted and recorded at the same point (zero offset).

The horizontal resolution of any antenna depends on the trace interval, the beam width, the radar cross section of the reflector and the depth of the target. The beam geometry depends on the propagation medium, the antenna characteristics and its height above surface. In general, a narrower beam results in a better horizontal resolution, which also means that closer to the source (shallow targets) the resolution will be in general higher since the beam is narrower. The beam can be approximately considered as the cone of energy that intersects with the reflector surface, illuminating an area that is called antenna footprint. An estimation of the footprint size can be obtained by various formulas proposed in specialized bibliography. In fact, there is much controversy with respect to the horizontal resolution since there are many factors influencing it and different criteria to set a definition. A common approximation identifies the antenna footprint with the diameter d_1 of the first Fresnel Zone [Igel, 2007], [Rial et al., 2009], which determines the maximal horizontal resolution of the radar system: $R_H = d_1$, i.e, objects which are less than d_1 apart cannot be resolved. The zone construction was first proposed by Fresnel in 1818 in an attempt to explain diffraction phenomena using Huygens principle [Born & Wolf, 1975].

To illustrate the importance of the notion of a Fresnel zone we consider a spherical wave incident on a reflecting circular target. Each element of the target's surface originates a reflected spherical wave; the net disturbance at the location of a detector consists of the coherent sum of all these reflected waves. If the two-way path difference ΔL is less than $\lambda/2$, then all the reflected waves constructively interfere. On the other hand, waves originating from the annular region for which $\lambda/2 < \Delta < \lambda$ contribute to the detected signal with opposite sign, resulting in partial destructive interference. Successively larger annular regions contribute with alternating signs, resulting in a well-defined progression of reflecting zones. The first Fresnel zone is traditionally defined as the largest reflecting disk for which all reflected waves reach the detector with phase shifts $\Delta\phi \leq \pi$. The diameter of the first Fresnel zone is given by the following expression,

$$d_1 = \sqrt{h\lambda + \frac{\lambda^2}{4}} \tag{4.44}$$

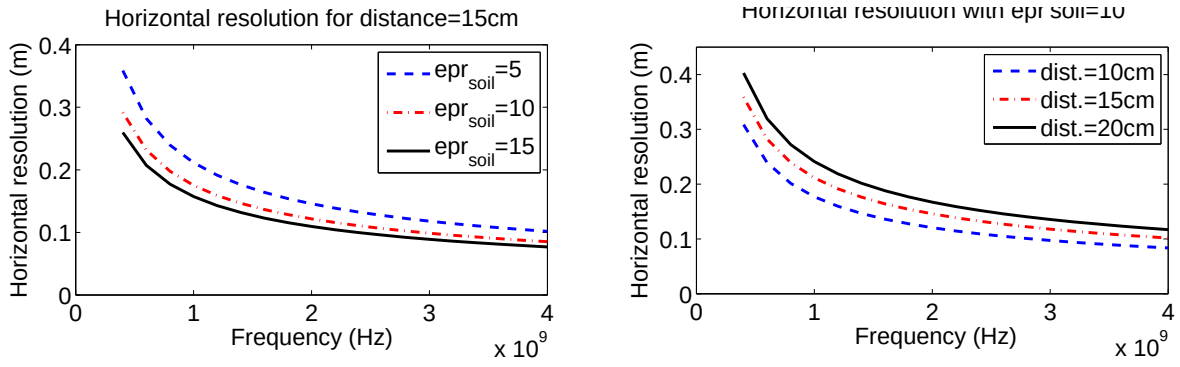

Figure 4.3 – Horizontal resolution versus pulse length for different media.

where h is the distance between the antenna and the reflector surface and λ is the center wavelength of the emitted radar pulse. According to this relationship and as it is shown in Fig. 4.3, the horizontal resolution worsens with decreasing soil permittivity and with object depth (i.e. larger distances to the antenna) and improves for higher frequencies. Another formula for the radius r_1 of the antenna footprint that has been found to fit the results well in real conditions, is given by the following expression [Conyers & Goodman, 1997]:

$$r_1 = \frac{\lambda}{4} + \frac{h}{\sqrt{(\epsilon_r + 1)}} \qquad d_1 = 2r_1 \tag{4.45}$$

4.2 Analytical Methods of determining Electromagnetic Scattering

The physical models which are used to predict the propagation and scattering of electromagnetic waves in dielectric materials have two main sources: the already described electromagnetic wave theory and the geometrical optics (GO). The latter method is only relevant when the wavelength of the electromagnetic radiation employed is considerably shorter than the dimensions of the object or medium being illuminated and when the materials involved can be considered to be electrical insulators. Optical theory is therefore most relevant for dry materials. Materials containing significant amounts of moisture will behave as conducting dielectrics, especially if the water contains ions.

4.2.1 Rayleigh Scattering (RS)

Rayleigh scattering (named after Lord Rayleigh) takes place when the particle is much smaller than the wavelength (scattering from particles up to about tenth of the wavelength of light), i.e., the particle is electrically small [Bohren & Huffman, 1983]. It happens when light travels in transparent solids and liquids, but is most prominently seen in gases. RS can be considered to be elastic scattering since the energy of the scattered photos does not change. The amount of RS that occurs to a beam of light is dependent upon the size of the particles and the wavelength of the

light; in particular, the scattering coefficient, and thus the intensity of the scattered light, varies as the sixth power of the particle size and inversely with the fourth power of the wavelength, a relation known as the Rayleigh law. The angular intensity polarization relationships for this type of scattering are conveniently simple. For particles not larger than the Rayleigh limit, there is complete symmetry of scattering about a plane normal to the incident direction of the radiation, so that the forward scatter equals backward scatter. This is due to the symmetry of the angular distribution of Rayleigh scattering, governed by the $(1 + \cos^2\theta)$ term as shown in Eq. 4.46.
In general, if the incident field is a beam of unpolarized light of wavelength λ and intensity I_i, the intensity I_s of the scattered light is [Bohren & Huffman, 1983]:

$$I_s = \frac{I_i 8\pi^4 N r^6}{\lambda^4 d^2} \frac{|n^2 - 1|^2}{|n^2 + 2|^2} \, (1 + \cos^2\theta), \tag{4.46}$$

where r is the radius of the scattering sphere, d is the distance from scatterer, n is the refractive index, and N is the number of scatterers. Integrating over the sphere surrounding the particle gives the Rayleigh scattering cross section for a single particle,

$$\sigma_s = \frac{2\pi^5}{3} \frac{d^6}{\lambda^4} \frac{|n^2 - 1|^2}{|n^2 + 2|^2}. \tag{4.47}$$

Rayleigh scattering of sunlight from particles in the atmosphere is the reason why the light from the sky is blue. This means that blue light (shorter wavelength) is scattered much more than red light.

4.2.2 Mie Scattering (MS)

Perhaps the most important exactly soluble problem in the theory of absorption and scattering by small particles is that for a sphere of arbitrary radius and refractive index. Although the formal solution to this problem has been available for many years, only since the advent of large digital computers, it has been a practical means for detailed computation. In 1908 Gustave Mie [Born & Wolf, 1975] developed the theory based on the Maxwell equations for a plane monochromatic wave incident upon a homogeneous sphere in a nonconducting medium in an effort to understand the varied colors in absorption and scattering exhibited by small colloidal particles of gold suspended in water.
The Mie theory allows the calculation of the electric and magnetic fields inside and outside a spherical object and the formalism is applicable to spheres of all sizes, refractive indexes and for radiation at all wavelengths. MS is then more general than RS.
Briefly, Maxwell equations are solved in spherical coordinates through separation of variables. The incident plane wave is expanded in Legendre polynomials so that the solution inside and outside the sphere can be matched at the boundary. The solution sought is at a distance much larger than the wavelength, $d \gg \lambda$, in the so called far field zone. Some remarkable features of these results are the Mie resonances, sizes that scatter particularly strongly or weakly.
When the particle size becomes larger than around 10% of the wavelength of the incident radiation, the RS starts to break down and MS model can be used to determine the intensity of the scattered radiation. This scattered light pattern is then like an antenna radiation lobe, with

sharper and more intense forward lobe for larger particles. This effect can be observed in Fig. 4.4 where an incoming plane wave of 50cm wavelength is scattered by a circular target of different diameters. The transition between RS and MS is clear, as the scattering goes from more symmetric scattering by the smallest infinite cylinder to increasing forward scattering as its size becomes of the order of the wavelength.
MS is roughly independent of wavelength and produces almost white glare around the sun when the density of particles in air is high. It is also responsible of the white light from mist and fog.
The available analytical solutions for the scattering by an infinite circular cylinder in 2D and a sphere in 3D can be found in the Appendix B.

4.2.3 Geometrical Optics (GO)

Since the wavelength of visible light is only of order a micron, it is very easy to find situations in which the wavelength of light is much smaller than the dimensions of the radiating or scattering objects. In this case, high-frequency asymptotic techniques are applied. Three of such techniques widely used are the Geometrical Optics (GO), Geometrical Theory of Diffraction (GTD) [Keller, 1962], [Borovikov & Kinber, 1994] and the Physical Theory of Diffraction (PTD) [Ufimtsev, 2007].
GO is the oldest and most popular theory of light propagation, and it is an approximate high-frequency method where the scattered light is obtained as a superposition of reflected, refracted and diffracted rays. Because it uses ray concepts, it is often referred to as ray optics. In GO light is treated as a set of rays emanating from a source, which propagate through homogeneous media according to a set of three simple laws. The first law is the law of rectilinear propagation, which states that light rays propagating through a homogeneous transparent medium propagate in straight lines. The second law is the law of reflection, which dictates the interaction of light rays with conducting surfaces. The third law is the law of refraction, which dictates the behaviour of light rays as they traverse a sharp boundary between two different transparent media (e.g. air and glass). Originally, GO was developed to analyze the propagation of light at sufficiently high frequencies where it was not necessary to consider the wave nature of light. Instead, the transport of energy from one point to another in an isotropic lossless medium is accomplished by Snell's law of reflection: the angle of reflection is equal to the angle of incidence. The scattering intensity in the geometrical optics theory is given by [van de Hulst, 1957] as

$$I_s^{(j)}(p, m, \theta_i) = \frac{\epsilon_j^2 I_0 a^2 \sin\theta_i \cos\theta_i d\theta_i \phi}{r^2 \sin\theta d\theta d\phi}, \tag{4.48}$$

where θ_i is the incidence angle, θ is the scattering angle, a corresponds to the radius of the spherical particle and m refers to the relative refractive index. The subscript j=1 is for the perpendicular and j=2 for the parallel polarization component of light with respect to the scattering plane. The fraction ϵ_j of the scattering intensity due to the reflection and/or the refraction for the emergent ray is given in terms of the Fresnel coefficients already defined in Section 4.1.3.
For sufficiently high frequencies GO fields may dominate the scattering phenomena and may not require any corrections. This is more evident for backscattering from smooth curved surfaces whose curvature is large compared to the wavelength.

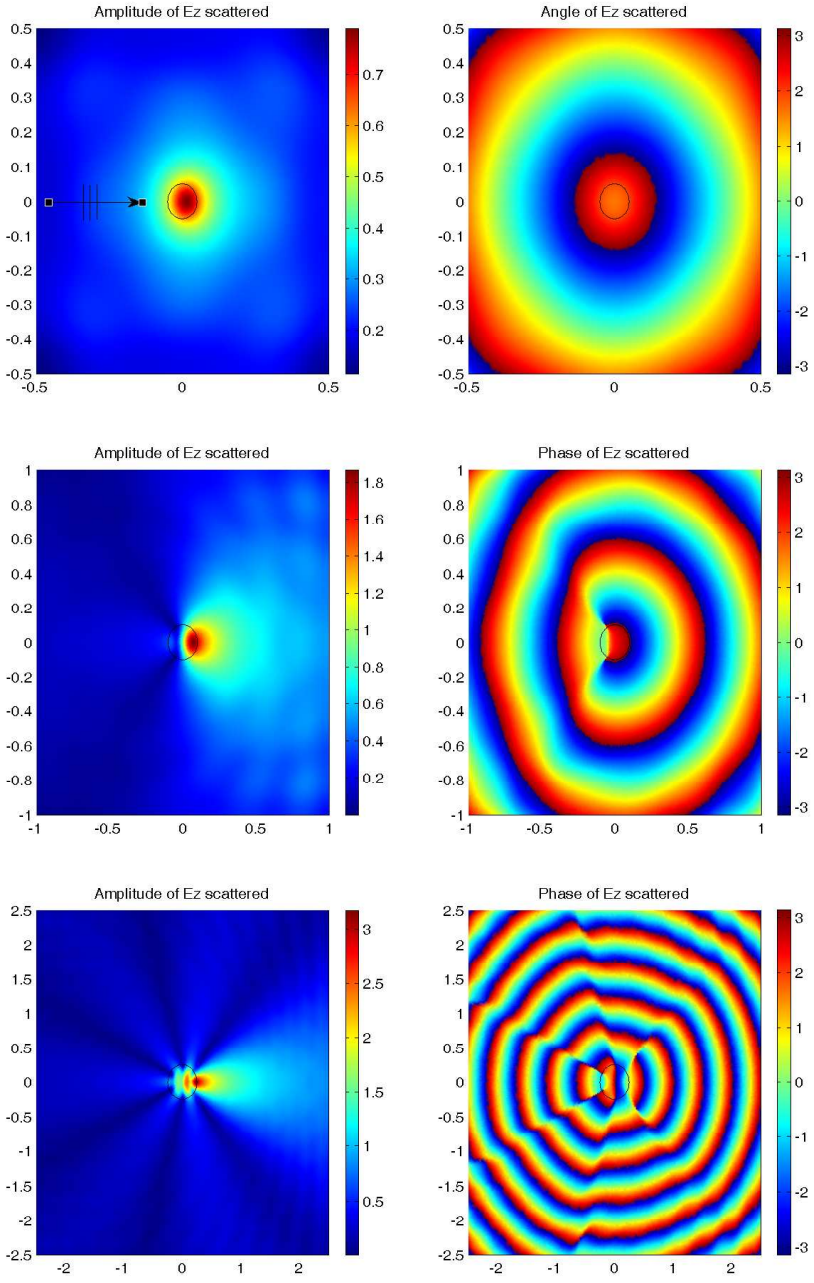

Figure 4.4 – Modeled amplitude and phase of the scattered electric field by a dielectric circular cylinder of 5 cm (top), 10cm (middle) and 25cm (bottom) radius applying ABC at the borders, f=0.6Ghz ($\lambda = 50cm$).

GTD is a generalization of GO which accounts for diffractions, introducing diffracted rays in addition to the usual rays of GO. These rays are produced by incident rays which hit edges, corners or vertices of boundary surfaces, or which graze these surfaces. Various laws of diffraction, analogous to the laws of reflection and refraction, are employed to characterize diffracted rays.
PTD is another high-frequency asymptotic technique which consists of using the ray optics to estimate the field induced on the objects and then integrating that field over the scattering surface to calculate the radiated field. This theory is the natural extension of the physical optics approximation for nonuniform sources, i.e, sources that concentrate near edges, being a satisfactory approach specially for objects of complicate shape.

4.3 Antenna Structures

Antennas are probably the main components on a radar system. Most commercially available GPR antennas are either dipole type (or element) or horn (or aperture) type antennas and the majority of GPR equipments employ resistively loaded dipoles for ground-coupled applications, and unloaded horns for air-launched applications. These antennas are designed to achieve a large bandwidth, stable transient response and efficient impedance matching to the ground.
Typically, for ground-coupled applications, independent and identical transmitter and receiver antennas are used in close proximity. They are housed in the same enclosure and they operate in direct contact or a few centimeters above the ground. Most of them are shielded to minimize the aboveground clutter and radio-frequency interference as well as to focus the radiation downwards.
An inherent problem to ground-coupled antennas is that their radiation characteristic changes greatly with varying soil conditions due to the modification of the surface current distribution along the radiating element. As we will see in Chapter 6 and Chapter 7, numerical modeling can provide valuable information to quantify and determine this change on the antenna performance under different conditions.
Dipole antennas can be further subdivided into linear dipoles or bow-tie dipoles. In the next sections we briefly describe and compare the infinitesimal Hertzian dipole and the half-wave dipole with the commonly used bow-tie dipole.

4.3.1 Infinitesimal Dipole (Hertzian Dipole)

A type of antenna regularly considered when studying the basic characteristics of an electromagnetic radiator is a short dipole, also called Hertzian dipole. Both the length dl and radius a of this antenna are very small relative to the wavelength λ, i.e., $dl \ll \lambda$ ($dl \ll \lambda/50$), so that the electric current used to excite the antenna is spatially constant along its length. This type of idealized short dipole cannot be physically constructed but can be utilized as building block to simulate real antennas.
The corresponding radiation pattern shape, which is not a function of the radial distance r, is a circular section toroid shaped and symmetrical about the axis of the dipole. Then, emission is maximal in the plane perpendicular to the dipole and zero in the direction of the wire, that is, the

current direction. The maximum theoretical antenna gain for this type of dipole (a parameter closely connected with its maximum directivity) has a typical value of 1.5, which corresponds to 1.76 dBi, where dBi means decibels gain relative to an isotropic antenna (definitions of some basic antenna concepts are found in the Definitions section at the end of this thesis).
Within the scope of this work the Hertzian dipole is used to simulate a punctual current source of intensity I=1A.

4.3.2 Half-wave Dipole

Antennas whose lengths are much less than that of the emitted radiation tend to be extremely inefficient. In fact, it is necessary to have $l \sim \lambda$ in order to obtain an efficient antenna where l is the total length of the dipole. Probably the most common practical antennas are the half-wave antenna and the full-wave antenna.
A half-wave dipole is typically formed by two quarter wavelength conductors or elements placed back to back for a total length of $\lambda/2$. The two conducting wires are fed at the center of the dipole. A standing wave on an element of a length $\lambda/4$ produces the maximum voltage differential, since one end of the element is at a node while the other is at an antinode of the wave. The larger the differential voltage, the greater the current flow between the elements. The half-wave antenna radiation pattern is very similar to the characteristic pattern of a Hertzian dipole but the former provides a more efficient radiator. The radiation resistance of a half-wave antenna is $R_r \approx 73\Omega$, a value substantially larger than that for a Hertzian dipole. On the other hand, the full-wave antenna radiation pattern is considerably sharper (i.e., it is more concentrated in the transverse directions $\theta = \pm\pi/2$). The emission diagram results accordingly in a slightly flattened torus. In other words, a half-wave antenna is a significantly more efficient electromagnetic radiator than a Hertzian dipole; more specifically its maximum theoretical gain is 2.15dBi.
According to standard transmission line theory, if a transmission line is terminated by a resistor whose resistance matches the characteristic impedance of the line, then all of the power transmitted down the line is dissipated in the resistor. On the contrary, if the resistance does not match the impedance of the line then some of the power is reflected and returned to the generator. We can think of a half-wave antenna, center-fed by a transmission line, as a resistor terminating the line. The only difference is that the power absorbed from the line is radiated rather than dissipated as heat. The resistance, however, is not enough to characterize the dipole impedance, as there is also an imaginary part.
The gain of a linear half-wave dipole antenna is ~ 2.15. To simulate the $\lambda/2$-dipole, we assume a dipole radius r=1.6μm and length l= 7.5cm which corresponds to 2Ghz resonance frequency. A voltage of 1V is applied.

4.3.3 Bow-Tie Dipole

The most interesting case to model a realistic scenario is the use of the actual antenna in the GPR system, namely, a triangular (bow-tie) dipole.
Bow-tie antennas are very popular within the GPR community because they are easy and cheap

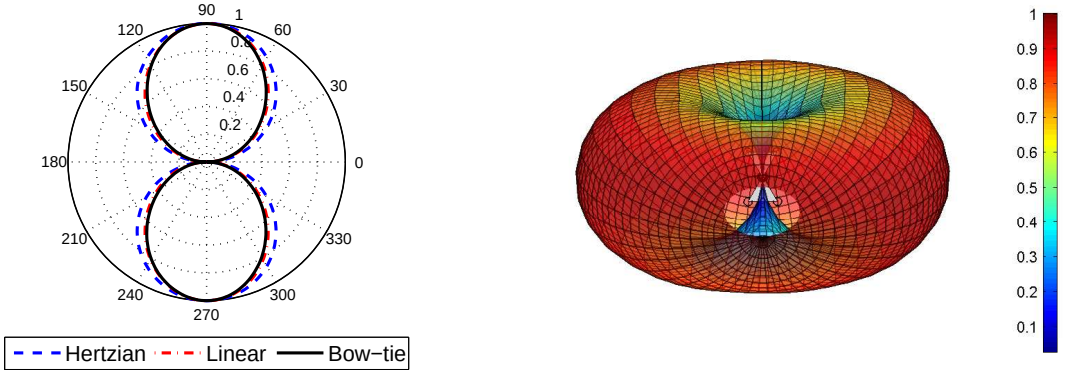

Figure 4.5 – Radiation pattern of the three dipoles in the far field (left) and 3D radiation pattern of the bow-tie dipole (right).

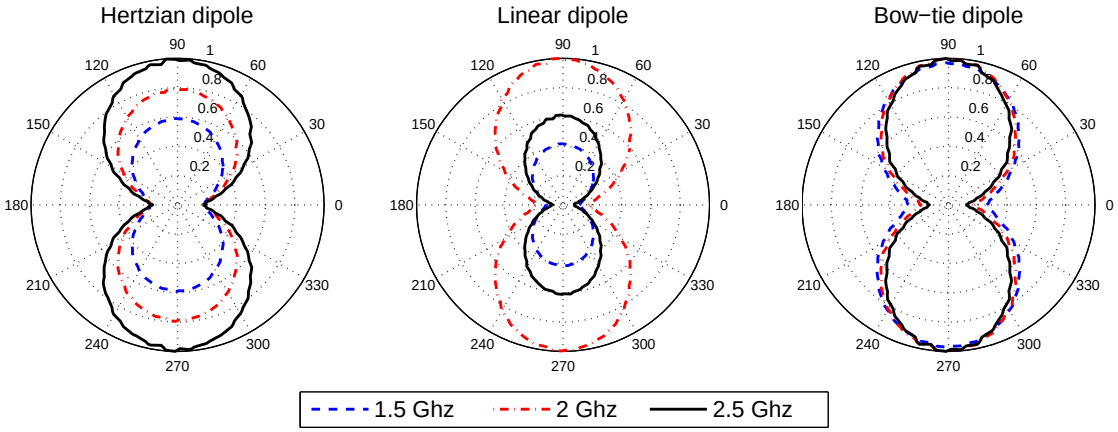

Figure 4.6 – Radiation patterns of the dipole antennas at different frequencies: 1.5, 2 and 2.5GHz.

to design and manufacture and reasonably ultra-wideband [Daniels, 1996].
The antenna structure consists of two triangular metal sheets and provides a 3dB gain over a simple dipole. They are usually connected to a symmetric line (twin line), which is matched to the feed point impedance. This input impedance will depend on the antenna length and flare angle. Figure 4.5 (left) shows the far field (FF) E-plane pattern in air of the a Hertzian, a linear half-wave and a bow-tie dipole (with same length and port excitation as the $\lambda/2$-dipole and 53^o flare angle). It can be clearly appreciated that the patterns of the half-wave and bow-tie dipole antennas are narrower (i.e. they show more directivity) than that of an ideal infinitesimal dipole. Figure 4.6 displays the corresponding near field (NF) (at a distance d=25cm) radiation patterns of the three dipoles we have introduced so far assuming 3 different operating frequencies. As expected, the radiated power by the bow-tie stays almost constant for the considered frequency range while for both dipoles it decays drastically. This happens due to the broadband performance of this sort of antenna, what makes it a very popular one in GPR commercial systems.
Several models with bow-tie illumination are presented in Chapter 6, where we analyze in detail the radiation characteristic of a GPR antenna under different configurations and scenarios.

MATERIAL	$\epsilon_\mathbf{r}$	σ (mS/m)	**v** (m/ns)	α (dB/m)
Air	1	0	0.3	0
Distilled Water	80	0.01	0.033	2e-3
Fresh Water	80	0.5	0.033	0.1
Sea Water	80	3e3	0.01	103
Dry Sand	3-5	0.01	0.15	0.01
Saturated Sand	20-30	0.1-1	0.06	0.03-0.3
Limestone	4-8	0.5-2	0.12	0.4-1
Shales	5-15	1-100	0.09	1-100
Silts	5-30	1-100	0.07	1-100
Clays	5-40	2-1000	0.06	1-300
Granite	4-6	0.01-1	0.13	0.01-1
Dry Salt	5-6	0.01-1	0.13	0.01-1
Ice	3-4	0.01	0.16	0.01

Table 4.1 – Relative permittivity (ϵ_r), conductivity (σ), velocity (v) and attenuation (α) from [Davis & Annan, 1989].

4.4 Electrical Properties of Soils

The ability of the GPR system to locate buried objects depends strongly on the EM properties of the soil, namely, relative dielectric permittivity, ϵ, conductivity, σ and magnetic permeability, μ. As mentioned above, magnetic permeability will not be considered here, since for nonmagnetic materials μ_r equals 1 in the GPR frequency range and it can be assumed that the only factor influencing the speed and attenuation of the radar wave is the complex dielectric constant of the media.

In Table 4.1 we display typical values of these parameters for different materials and soils. As explained in section 4.1, the real part of the dielectric permittivity ϵ' (the relative permittivity) of a material is related to its capability to store energy when an alternating electrical field is applied whereas the imaginary (loss) part ϵ'' is mainly associated with the energy dissipation. The electrical conductivity, which is included within the loss part, controls the detection range of the system: the radar signals travel with least attenuation through insulating materials (materials having low electrical conductivity) and, on the contrary, they cannot penetrate through conductive materials. Thus, materials like air, sand and gravel soils and fresh water present low attenuation for GPR signals while clay and silt soils and salt water are conductive and cause high attenuation. The determination of the dielectric properties of earth materials remains largely experimental. Rocks, soils, and concrete are complex materials composed of many different minerals in widely varying proportions, and their dielectric parameters may differ notably even within materials that are nominally similar. A big number of researchers have investigated the relationships between the physical, chemical, and mechanical properties of materials and their electrical and, in particular, microwave properties. In general, they have tried to develop suitable models to link the properties of the material to its electromagnetic parameters. Such models provide a basis for

understanding the behavior of electromagnetic waves within the media and some of them will be shortly described in the next sections.

Frequency Dependence of the Electrical Parameters

An important process contributing to the frequency dependence of permittivity is the polarization arising from the orientation with the imposed electric field of molecules that have permanent dipole moments. The mathematical formulation of Debye [Debye, 1929] describes this process for pure polar materials:

$$\epsilon'(f) = \epsilon_\infty + \frac{\epsilon_s - \epsilon_\infty}{1 + (2\pi f\tau)^2}, \tag{4.49}$$

$$\epsilon''(f) = \frac{\epsilon_s - \epsilon_\infty}{1 + (2\pi f\tau)^2} 2\pi f\tau + \frac{\sigma_{dc}}{2\pi f\epsilon_0}, \tag{4.50}$$

where ϵ_∞ represents the permittivity at so high frequencies that molecular orientation does not have time to contribute to the polarization, ϵ_s represents the static permittivity (i.e., the value at zero frequency), σ_{dc} is the DC conductivity (Sm^{-1}) and τ is the relaxation time.
Water in its liquid state is a prime example of polar dielectric. The Debye parameters of water are: $\epsilon_s = 80.1$, $\epsilon_\infty = 4.2$, and $\tau = 9.3x10^{-12}$s at 25°C [Hasted, 1973]. In sandy soils, most water is in its free liquid state while in high clay content soils, pore water is not necessarily in its free liquid state. Sometimes it is physically absorbed in capillarities, limited in motion by electrostatic interaction with clay particles. Dielectric relaxation of absorbed water takes place at lower frequencies than the relaxation of free water.
In the case of GPR measurements, which commonly have a frequency band from 10 MHz to 3GHz, $\epsilon''(f)$ is often small compared with $\epsilon'(f)$. Furthermore, many soils do not exhibit relaxation of permittivity in this frequency range.

Water Content-Permittivity Relationships

The dielectric properties of a soil depend on a number of factors, the volumetric water content, the frequencies of interest, the texture of the soil particles (sand, silt, or clay), the bulk density, and the temperature [Hoekstra & Delaney, 1974].
The water content is the component that plays the main role in the electrical permittivity of the soil (due to its high permittivity value compared with that of the background soil); hence, many empirical and semi-empirical relationships between volumetric moisture content Θ and the apparent permittivity of a soil have been proposed in literature [Topp et al., 1980], [Dobson et al., 1985], [Peplinski et al., 1995], [Mironov et al., 2004], [Wang & Schmugge, 1980], [Wobschall, 1977]. One of the simplest and most popular empirical models is probably Topp's equation [Topp et al., 1980], which fits a third order polynomial function to the empirically determined permittivity response of mineral soils:

$$\epsilon'_{\text{eff}} = 3.03 + 9.3\Theta + 146\Theta^2 - 76.7\Theta^3, \tag{4.51}$$

with ϵ'_{eff} the real part of the bulk effective permittivity. This model is appropriate for frequencies in the 10MHz-1GHz range and it agrees quite well with the experimental data for a wide range of

water contents (5-50%). However, for getting accurate results, this formula needs to be adjusted for each type of soil.

In contrast to empirical relationships, dielectric mixing models seek to determine the resulting relative permittivity of a mixture on the basis of the relative permittivity and volume fractions of its constituents. These semi-empirical models basically assume that the material is a matrix with a multi-phase mixture of geometrically simple inclusions. From them, the most general is the Complex Refracted Index Method (CRIM) [Mavko et al., 1998], which is a volumetric model that requires only knowledge about the permittivity of the materials and their fractional volume percentages. It can be used on both the real and imaginary components of the complex permittivity and its general form is written as follows:

$$\epsilon_{\text{eff}}^{\text{mix}} = \left(\sum_{i=N}^{l-1} f_i \sqrt{\epsilon_i} \right)^2, \tag{4.52}$$

where $\epsilon_{\text{eff}}^{\text{mix}}$ is the complex bulk effective permittivity of the mixture, f_i is the volume fraction of the ith component and ϵ_i is the complex permittivity of the ith component. Although any number of phases can be incorporated, in most cases, it is assumed a three-phase soil consisting of mineral solids, air and water. It is easy to apply and it produces accurate results for various soils in the range 1-10GHz. For such a mixture, the CRIM formula becomes:

$$\sqrt{\epsilon} = (1 - \Phi)\sqrt{\epsilon_P} + \Theta\sqrt{\epsilon_w} + (\Phi - \Theta)\sqrt{\epsilon_a}, \tag{4.53}$$

with ϵ_w, ϵ_P and ϵ_a, the relative dielectric permittivities of the water, the soil matrix and the air respectively, Θ the volumetric water content and Φ the porosity.

Another example of a mixing model is the semi-empirical power-law presented by [Peplinski et al., 1995]. This model includes the textural composition of the soil and provides frequency dependent expressions for the complex relative dielectric constant in terms of the sand and clay fractions, the volumetric water content and the bulk density of the soil. The deduced model is valid for a frequency range between 0.3 and 1.3GHz and it is based on an earlier model for dielectric constants in the 1.4-18GHz frequency band developed by [Dobson et al., 1985]. The real part of the complex relative dielectric permittivity for the bulk soil is approximated as

$$\epsilon'_{\text{eff}} = 1.15 \left[1 + \frac{\sigma_s}{\sigma_P} \left(\epsilon_P^{\varphi} - 1 \right) + \Theta^{\beta'} \epsilon_{fw}'^{\varphi} - \Theta \right]^{\frac{1}{\varphi}} - 0.68. \tag{4.54}$$

The imaginary part is derived as

$$\epsilon''_{\text{eff}} = \left[\Theta^{\beta''} \epsilon_{fw}''^{\varphi} \right]^{\varphi}, \tag{4.55}$$

where: σ_s is the bulk density of the soil and typically varies between 1.1 gr/cm for clay and 1.6 gr/cm for sandy soil, $\sigma_P = 2.66\,\text{gr/cm}^3$ is a typical value for the specific density of the solid soil particles for sand textural class, $\epsilon_P = (1.01 + 0.44\sigma_P)^2$ is the empirical model for the dielectric permittivity of the soil particles, $\varphi = 0.65$ is empirically obtained in [Dobson et al., 1985] and [Peplinski et al., 1995], and finally, $\beta' = 1.2748 - 0.519S - 0.152C$ and $\beta'' = 1.33797 - 0.603S - 0.166C$ are two frequency independent constants which join the soil type into the model, being S the mass fraction of the sand constituent and C the mass fraction of the clay constituent.

Furthermore, the frequency dependent variables ϵ'_{fw} and ϵ''_{fw} are the real and imaginary parts,

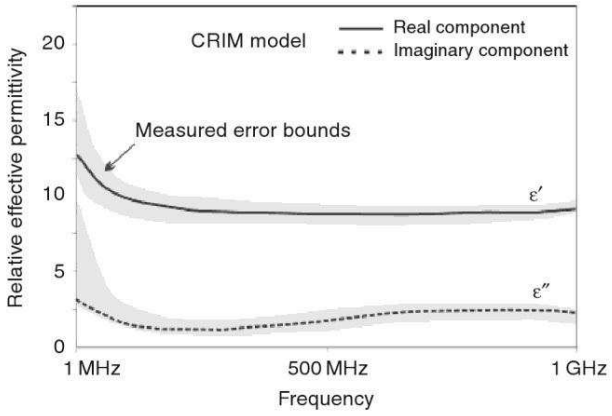

Figure 4.7 – Comparison between measured and CRIM modelled complex, frequency-dependent permittivity of sandy soil with 20% water content and < 2% clay content [Cassidy, 2009].

respectively, of the dielectric constant for free water given by a modified Debye model. The latter depends on the effective conductivity σ'_{eff}, which is derived in [Peplinski et al., 1995] as:

$$\sigma'_{\text{eff}} = 0.0467 + 0.2204\sigma_S - 0.4111S + 0.6614C. \tag{4.56}$$

In the next illustrations we show the practical use of CRIM and Peplinski models. In Fig. 4.7 [Cassidy, 2009], the CRIM-model based effective permittivity spectrum of a damp sandy soil with approximately 20% water content and < 2% clay content is compared to its measured values. In general, the mixing model performs well over the GPR frequency range.
In Fig. 4.8 (left) different values of the real and imaginary parts of ϵ_{eff} are shown for frequencies below 1.4 GHz and 15% moisture assuming the Peplinski formula and sandy soil with 60% sand content. We have selected such a soil to match the values obtained from the CRIM model. If the sand and water contents are increased, ϵ'_{eff} grows up to 20 for pure sand and 20% moisture. Then, it seems that Peplinski model is overestimating ϵ'_{eff} for a given moisture, the more for higher water contents. A similar conclusion is achieved in [Sabouroux & Ba, 2011], where the performance of the above presented empirical and semi-empirical models are compared with measured data for sandy soils. The above results, according to the results reported also by other authors, indicate that the real part of the dielectric permittivity stays almost constant over the frequency band 300MHz-1.3GHz (and even higher) whereas the imaginary part slightly decreases when the frequency increases. The former observation is of particular relevance when working with an ultra-wideband system, since we wish to assume a constant soil permittivity value when carrying out the GPR simulations.
Nevertheless, more investigation is required about soil hydrological processes to investigate the role played by the different parameters. In principle, the values obtained employing both models may be a satisfactory approximation to estimate the soil effective permittivity. For certain soils, it may be important to take into account soil porosity and the CRIM model performs better than a model purely based on soil texture as in the Peplinski approach, but for other soil types, this model may work very well. On the other hand, if we apply the Topp's formula for $\Theta = 20\%$,

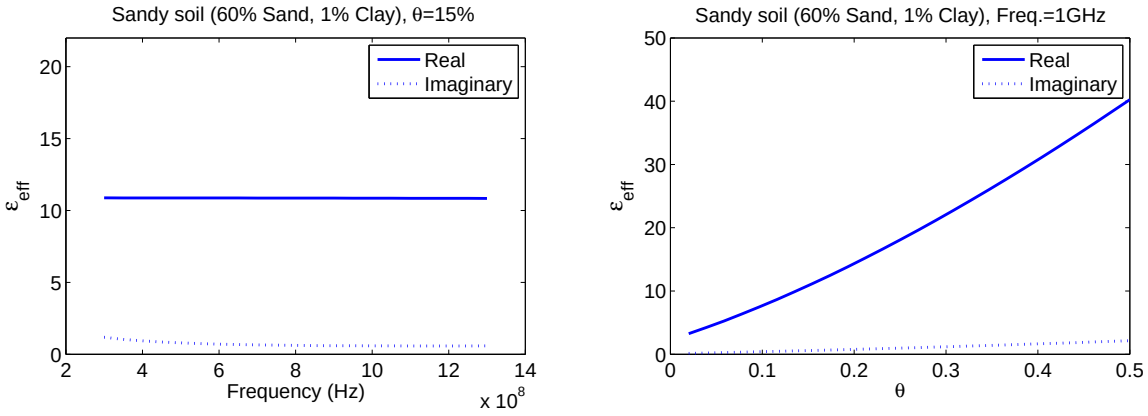

Figure 4.8 – Real and imaginary parts of the relative effective permittivity for sandy soil against frequency (left) and water content fraction (right).

a value of $\epsilon'_{\text{eff}} = 10.11$ is obtained, which is not a bad estimate. However, the Topp's formula, which does not take into account the soil texture and composition, appears to underestimate the soil real permittivity, specially for those soils with porosities below 40%.
In practice, the choice of one or other model depends ultimately on the available information about subsurface materials and the particular circumstances, but in general, it is fair to expect that any of these approaches will provide acceptable results for typical soils in the GPR bandwidth of interest for the present application.

4.5 Spatial Variability of Soils: Fluctuations in Electromagnetic Parameters

Soils are characterized by a high degree of spatial variability due to the combined effect of physical, chemical or biological processes that operate with different intensities and at different scales.
The parametrization of these models can be expressed as follows

$$s(\mathbf{r}) = \bar{s} + \Delta s(\mathbf{r}), \tag{4.57}$$

where s is a model parameter (either elevation h, relative permittivity ϵ_r, or conductivity σ), $\mathbf{r}$ denotes the location on the computational domain, and $\bar{s}$ and Δs (either Δh, $\Delta\epsilon$, or $\Delta\sigma$) are the deterministic mean value of the background and the stochastic component of the model parameter respectively (often mapped to a mathematical function such as the exponential or gaussian distribution). The two statistical parameters that are important to characterize this variability are the standard deviation of the considered parameter, also called root mean square (RMS) and abbreviated as σ, and the correlation length l. For the data vector of an arbitrary parameter $s = s_i$, with i=1,2, ..., N and N the number of elements in the sample, the RMS is defined by this equation:

$$\sigma = \sqrt{\frac{1}{N-1}\left(\sum_{i=1}^{N}(s_i - \bar{s})^2\right)} \tag{4.58}$$

where

$$\bar{s} = \frac{1}{N}\sum_{i=1}^{N} s_i \tag{4.59}$$

is the mean or average of the sample.
The simulated random data can be fitted into several models. In this thesis we will only study normal distributed random distributions for all the variables considered, i.e., surface elevation, electrical permittivity and conductivity.

4.5.1 Correlation Length and Statistical Considerations

The correlation length is a measure of the range over which fluctuations in one region of space are correlated with those in another region. Values for a given property at distances beyond the correlation length can be considered purely random, i.e., there is no further statistical relationship between them. To statistically describe the variation of a given property with separation it is necessary to determine either its variogram or its autocorrelation and from these functions the correlation length can be easily determined. Both values behave contrarily and are directly related.
The theoretical variogram $2\gamma(\mathbf{d})$ is a function describing the degree of spatial dependence of a spatial random variable $s(\mathbf{r})$. It is defined as the expected squared increment of the values between locations separated a distance d [Wackernagel, 2003], i.e, it describes the difference of data with increasing distance.

$$2\gamma(\mathbf{d}) = \frac{1}{N(\mathbf{r})}\sum_{i=1}^{N(\mathbf{r})}(s(\mathbf{r}_i) - s(\mathbf{r}_i + \mathbf{d}))^2 \tag{4.60}$$

where i is the sample index, N the number of pairs which are separated by the distance vector $\mathbf{d}$ and $\gamma(\mathbf{r})$ itself is called the semivariance or semivariogram (when represented against d). If the semivariance only depends on the absolute lag distance d but not on the direction, the semivariogram is considered to be isotropic and an only one omnidirectional semivariogram can be used.
The correlation or covariance describes the degree of similarity between random variations, and the autocorrelation for a random variable is the similarity between its values as a function of their separation. The variation in the value of the autocorrelation coefficient as the distance between the two points increases is referred to as the autocorrelation function. The normalized autocorrelation function ρ, takes this form in the discrete form:

$$\rho(\mathbf{d}) = \frac{1}{N(\mathbf{r})}\sum_{i=1}^{N(\mathbf{r})}\frac{s(\mathbf{r}_i)s(\mathbf{r}_i + \mathbf{d})}{\sigma^2} \tag{4.61}$$

The above definitions require the random variable to be intrinsically stationary which implies that the mean is constant. The property of $\rho(\mathbf{d})$ is then independent of $\mathbf{r}$ and depends only on d. When d=0, the numerator coincides with the sample variance σ^2.
The correlation length is usually defined as the displacement d when $\rho(\mathbf{d})$ is equal to 1/e. In the following we will express the correlation length of the soil inhomogeneities and surface roughness according to this definition.

4.5.2 Rough Air-Ground Interface

The contribution of the roughness element depends on surface characteristics. It has been demonstrated that changes in surface roughness influence substantially the magnitude of the backscatter energy.

The roughness of a surface can be represented by a number of parameters, but we need to characterize the roughness at the scale of the interactions that are occurring. It is well known that scattering effects are a response to interactions with surface features that are of the order of the wavelength of the signal (Rayleigh criterion). Likewise for the soil electrical parameters, we will model surface roughness assuming normal distributed random height oscillation with a characteristic RMS and horizontal correlation length. The standard deviation of the height of the surface indicates to what degree discrete values of surface elevation above a reference plane vary, i.e., describes the topography. Correlation length shows the horizontal scale at which these height changes are produced, which is a direct indication of terrain roughness degree.

In Fig. 4.9 two of the soil/surface scenarios generated for our simulations are depicted and below them, in Fig. 4.10, we display the autocorrelation functions of their dielectric spatial fluctuations. The influence of the soil variability and surface roughness over the target scattering response and the GPR antenna performance are analyzed in the next chapters.

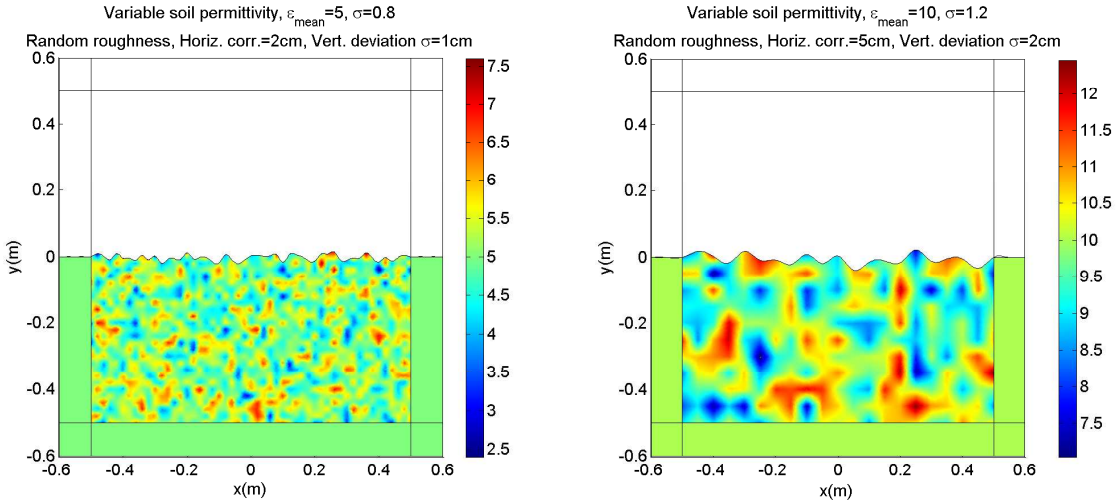

Figure 4.9 – Two generated scenarios with rough surface and inhomogeneous soil.

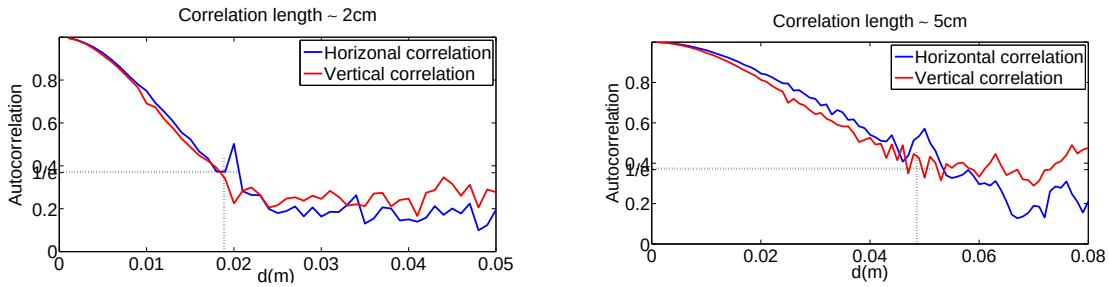

Figure 4.10 – Autocorrelation function of the permittivity distribution for both inhomogeneous scenarios.

5

A 2D Parametric Study of the Scattering by Small Objects

Great things are done by a series of small things brought together
Vincent van Gogh

This chapter contains several two-dimensional (2D) modeling results in frequency and time domain. The gathered information may be of great help to better visualize and understand the different target responses both in free space, and when they are shallow buried in soil.
The electromagnetic scattering by a target is usually represented by its 'echo area' or *Radar Cross Section* (RCS) (σ). The echo area or RCS is defined as "the area intercepting the amount of power that, when scattered isotropically, produces at the receiver a density that is equal to the density scattered by the actual target" [Balanis, 1989]. For a 2D object the scattering parameter is referred to as the Scattering Width (SW) or alternatively as the *the radar cross section per unit length*. In equation form the scattering width of a target take the form of

$$\sigma_{2D} = \lim_{\rho \to \infty} \left[\frac{| \mathbf{E}_s |^2}{| \mathbf{E}_i |^2} \right], \tag{5.1}$$

where ρ is the distance from the target to observation point and $\mathbf{E}_i$, $\mathbf{E}_s$ are the incident and scattered electric fields respectively.
The RCS of a target is most easily viewed as the product of three factors: projected cross section, reflectivity and directivity. Thus, apart from the mentioned electromagnetic contrast between the target and the background material, target's shape plays a decisive role to understand its scattering behaviour.
The SW or RCS of targets are defined under homogeneous plane wave illumination, which represents the mathematical simplest form of EM excitation. A plane wave front can be assumed when the target is placed in the far field of the source. The corresponding models are easy to implement

and fast to compute, making plane wave illumination a convenient approach to the GPR modeling problem. In particular, the study of the radar cross section of basic shapes may be an interesting starting point to analyze the GPR scattering because such study gives insight into the scattering from more complex objects and because many basic shapes are good approximations to some real landmines. Moreover, the display of the EM field distribution over the domain surrounding the target, in particular when the target is buried in soil, will provide a general understanding of the whole scattering process.
In this chapter only representative data sufficient to illustrate the important parameter dependencies of EM propagation and radar cross section, are presented.

5.1 COMSOL Electromagnetic Module

The Electromagnetic Module is an optional add-on package for COMSOL Multiphysics adapted to a broad range of electromagnetic problems [COMSOL, 2005] that we have used in most of the simulations presented along this thesis.
The Electromagnetic Module contains a set of application modes that handles static, time-dependent, time-harmonic, and eigenfrequency/eigenmode problems which fall into three main categories: statics, quasi-statics and high-frequency analysis, which are available for harmonic and transient analysis in 2D and 3D.
One major difference between the quasi-static and high-frequency modes is that the design of the modes depends on the 'electrical size' of the structure. This dimensionless measure is the ratio between the largest distance between two points in the structure divided by the wavelength of the electromagnetic fields. The quasi-static modes are suitable for simulations of structures with an electrical size in the range up to 1/10. The physical assumption of these situations is that the currents and charges generating the fields vary so slowly in time that the electromagnetic fields are practically the same at every instant as if they had been generated by stationary sources.
In the case of GPR simulations, the variations in time of the sources are more rapid and it becomes necessary to use the full Maxwell application modes for high-frequency electromagnetic waves. They are appropriate for structures of electrical size 1/100 and larger. Thus, an overlapping range exists where you can use both the quasi-static and the full Maxwell application modes.
Independently of the structure size, the Electromagnetics Module accommodates any case of nonlinear, inhomogeneous, or anisotropic media, which is a very useful characteristic for modeling wave propagation in realistic media. It also handles materials with properties that vary as a function of time as well as frequency-dispersive materials. The functions or data tables to describe the media parameters can be interpolated and imported into COMSOL via Matlab or COMSOL script. The boundary setting dialog box adapts to the current application in the module and you can select application specific boundary conditions, which might require some parameters to be specified.
Finally, and for further postprocessing calculations and visualization, the solution can be directly exported to script.

5.2 PDE Formulation

For this first 2D approach to the GPR problem, we consider a situation where there is no variation in the z direction, and the electromagnetic field propagates in the modeling x-y plane. To carry out the simulations we use the *In-plane waves* application mode for the case of Transverse Electric (TE) waves. A TE wave has only one electric component in the z direction, and the magnetic field lies in the modeling plane. Thus, for this case the time-harmonic fields can be written:

$$\begin{aligned}\mathbf{E}(x,y,t) &= E_z(x,y,t) = E_z(x,y)\mathbf{e_z}e^{j\omega t}\\ \mathbf{H}(x,y,t) &= H_x(x,y,t)\mathbf{e_x} + H_y(x,y,t)\mathbf{e_y} = [H_x(x,y)\mathbf{e_x} + H_y(x,y)\mathbf{e_y}]e^{j\omega t}.\end{aligned} \tag{5.2}$$

From the assumption of time-harmonic fields, the time-dependent wave equation

$$\nabla^2\mathbf{E} - \mu_r\mu_0\epsilon_c\frac{\partial^2\mathbf{E}}{\partial t^2} = 0$$

becomes a Helmholtz type equation

$$\nabla^2\mathbf{E} + \mu_r\mu_0\epsilon_c\omega^2\mathbf{E} = 0, \tag{5.3}$$

where we have introduced the complex permittivity $\epsilon_c = \epsilon_0\epsilon_r - i\frac{\sigma}{\omega}$ and $\mathbf{E}$ is the total vector electric field. For TE waves, Eq.5.3 can be simplified to a scalar equation for E_z,

$$\mu_r^{-1}\nabla^2 E_z - \left(\epsilon_r - j\frac{\sigma}{\omega\epsilon_0}\right)k_0 E_z, \tag{5.4}$$

where $k_0^2 = \omega^2\epsilon_0\mu_0$ is the wave number of the free space.
Equation 5.4 is the PDE equation that will be solved along this chapter assuming plane wave illumination and for frequencies within the bandwidth of interest.

5.3 The Boundary Conditions

The first question to address when dealing with an scattering problem is the proper selection of the boundary conditions to truncate the numerical domain. This topic was briefly introduced in section 3.5; for a detailed description of the mathematical definition and implementation of PML and the ABC available in COMSOL see Appendix A.
In the first simulations we analyze the performance of the absorbing boundary conditions for scattering problems in free and a medium half-space. To investigate their ability to prevent unwanted reflections we solve a simple scattering problem in free space applying either an ABC or adding PML. In this model, we consider the incident electrical field E_0 to be a linearly polarized plane wave which travels in the direction parallel to y-axis: $E_0 = (0, 0, e^{ik_0 y})$. The wave propagates from top to bottom through air and is scattered by a dielectric target in different directions. Figure 5.1 show the scattered electric field with and without PMLs for 3 different frequencies. To define the PMLs we introduce new subdomains around the air domain as described in [Berenger, 1994] representing absorbing layers. In the corners the PMLs absorb the waves in both the x and y directions, on the sides only the waves propagating in x direction are absorbed and on the top

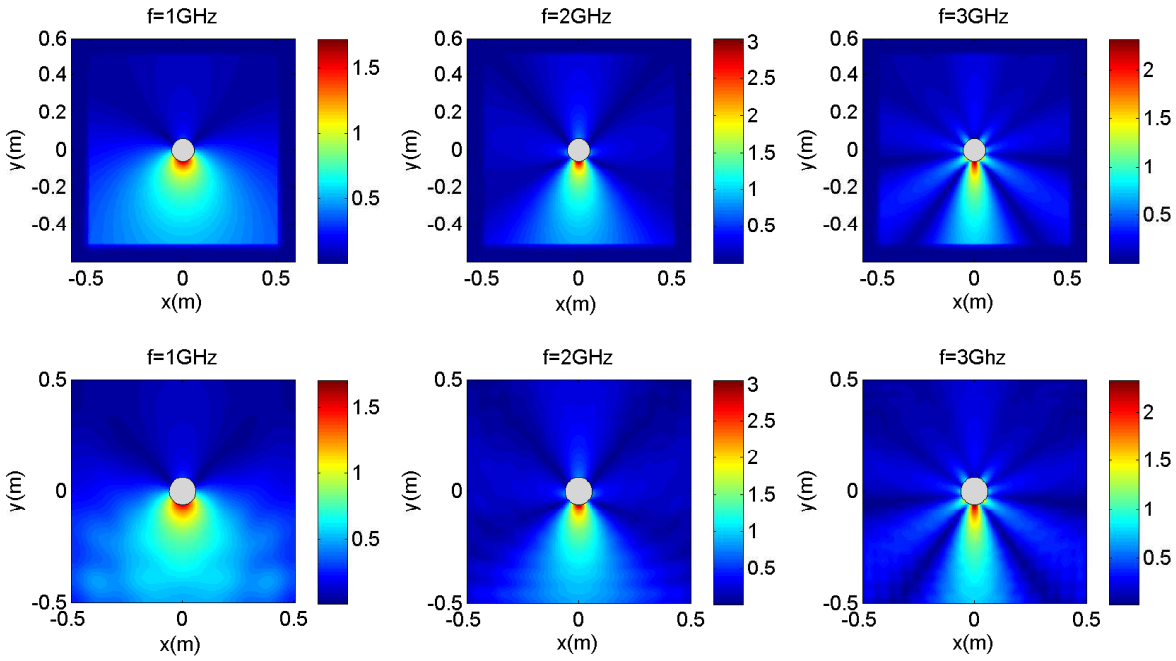

Figure 5.1 – Amplitude of the scattered field by a dielectric circular cylinder (r=6cm) with PML (top) and ABC (bottom) for f=1,2,3 GHz.

and bottom the waves propagating in y direction are absorbed. Then, on the top boundary of the layers we use a low-reflecting condition with $E_z = 1V/m$ to generate a plane wave propagating downwards. On the bottom border we apply a low-reflecting boundary condition with a source field of zero. Finally, on the left and right boundaries we need to assume a perfectly magnetic conductor (PMC) boundary condition, because the wave is propagating parallel to these boundaries and therefore the magnetic field is normal to them. The achieved results are quite similar (see Fig. 5.2) but the PMLs absorb the scattered energy with a minimum of reflections while without them some clear reflections arise for all the three cases. If there was no dielectric object inside the domain, the low-reflecting and PMC boundary conditions would be enough because the waves would only propagate in y direction and the low-reflecting boundary would absorb the plane wave perfectly. Otherwise, with a scatterer present, the PMLs are needed to absorb the scattered wave.

In Fig. 5.2, we quantify the error introduced by the application of low-reflecting boundary conditions and PMLs to truncate the numerical domain. The relative error measure for each frequency value (calculated after applying the mean of the relative error per pixel over the whole 1x1m spatial domain) is obtained by comparison of the simulated scattered field by a 5cm radius metallic sphere in free space (placed in the middle of the domain) with the corresponding analytical solution. The already expected good performance of the PMLs is confirmed by these results. In particular, we can see that the value of the error associated with the PMLs is clearly smaller than that generated by the presence of low-reflecting boundaries. It remains below 0.1% for all the frequencies evaluated and it grows slightly with the frequency. On the other hand the error due to the low-reflecting boundary condition is always above 0.15% and follows an opposite trend: it

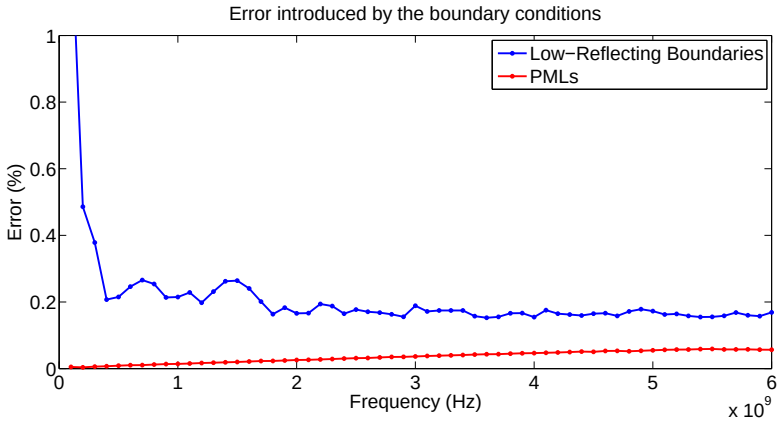

Figure 5.2 – Relative error introduced by the boundary conditions.

decreases with increasing frequency.
The example presented before corresponds to a homogeneous unbounded medium but many real life applications involve stratified media where the interfaces among the layers are unbounded. As far as we know, there does not exist any theoretical result that guarantees the accuracy in problems where the interface between two different media continues through the PML domain. Even without theoretical support, in the literature there exist a wide range of works dealing with stratified media which claim good numerical accuracy from the PML technique. The mentioned numerical accuracy is demonstrated here by comparing the performance of ABC and PML in the half-space simulation illustrated in Fig. 5.3, where we see that the PMLs are still working well. In the present thesis, we apply PML to all the simulations in frequency domain.

5.4 Scattering by Circular and Rectangular Cylinders in Frequency Domain

The RCS of a target for the most general case of a bistatic configuration, is function of the polarization of the incident wave, the polarization of the received wave, the angle of incidence, the angle of observation, the geometry of the target (target shape and size), the electrical properties of the target and the frequency of operation [Balanis, 2005].
In the next sections we study the scattered field behaviour for several objects (infinite in z-direction) under different conditions and assuming plane wave illumination (traveling downwards in y-direction as described in the previous section). The targets will be initially considered in free space, and afterwards buried at shallow depth in two representative soils.

5.4.1 Free Space

First, we analyze the scattered electric field in free space by targets of distinct geometry and composition and for frequencies in the range of interest: 1, 2 and 3 GHz.
The computed scattered field by different objects is displayed in Fig. 5.4, 5.5 and 5.6. The field

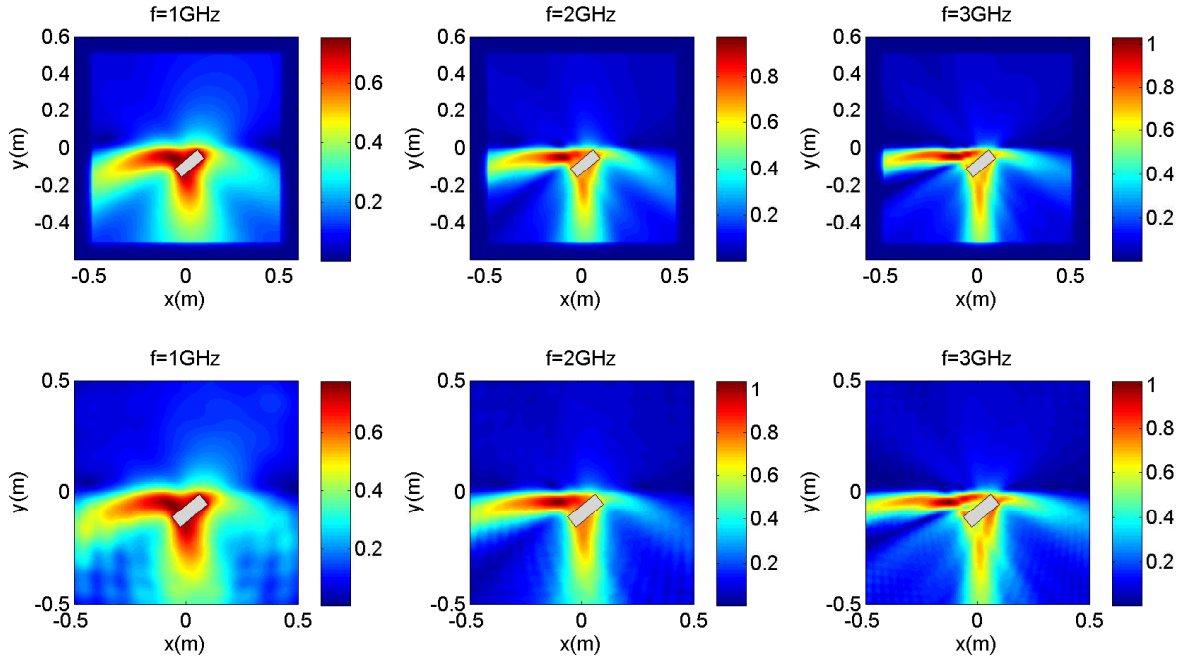

Figure 5.3 – Amplitude of the scattered field by a tilted metallic rectangular cylinder with PML (top) and ABC (bottom) for f=1,2,3 GHz.

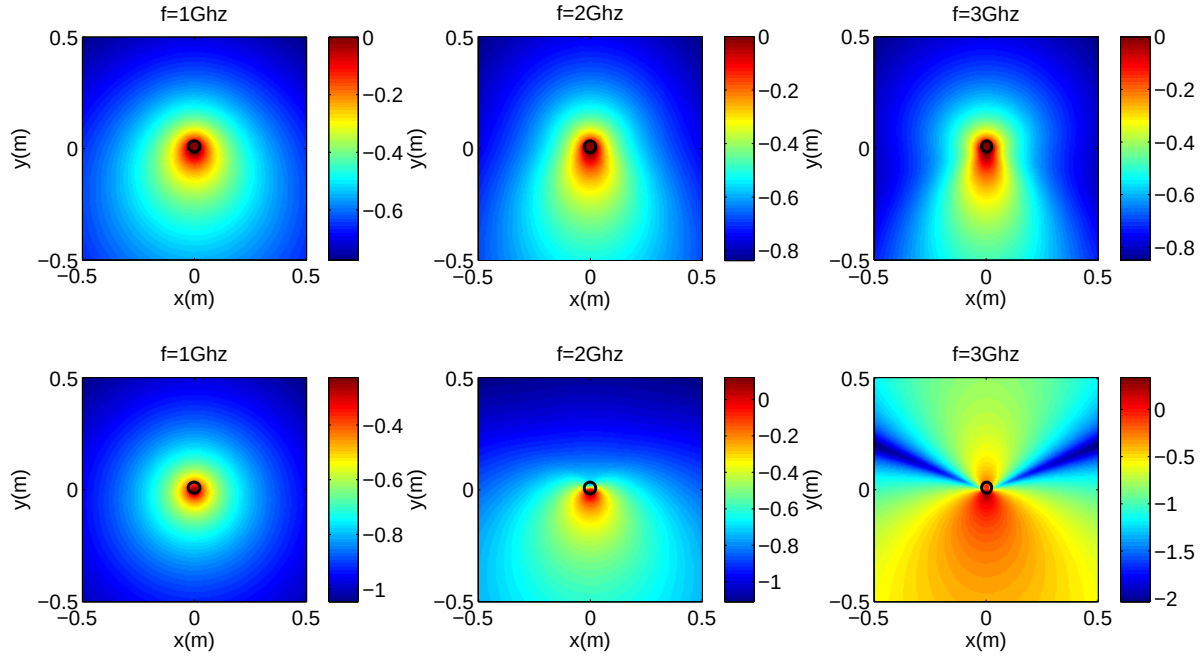

Figure 5.4 – Amplitude of the scattered field by a metallic (top) and a dielectric (bottom) circular cylinder (r=2.5cm) in free space.

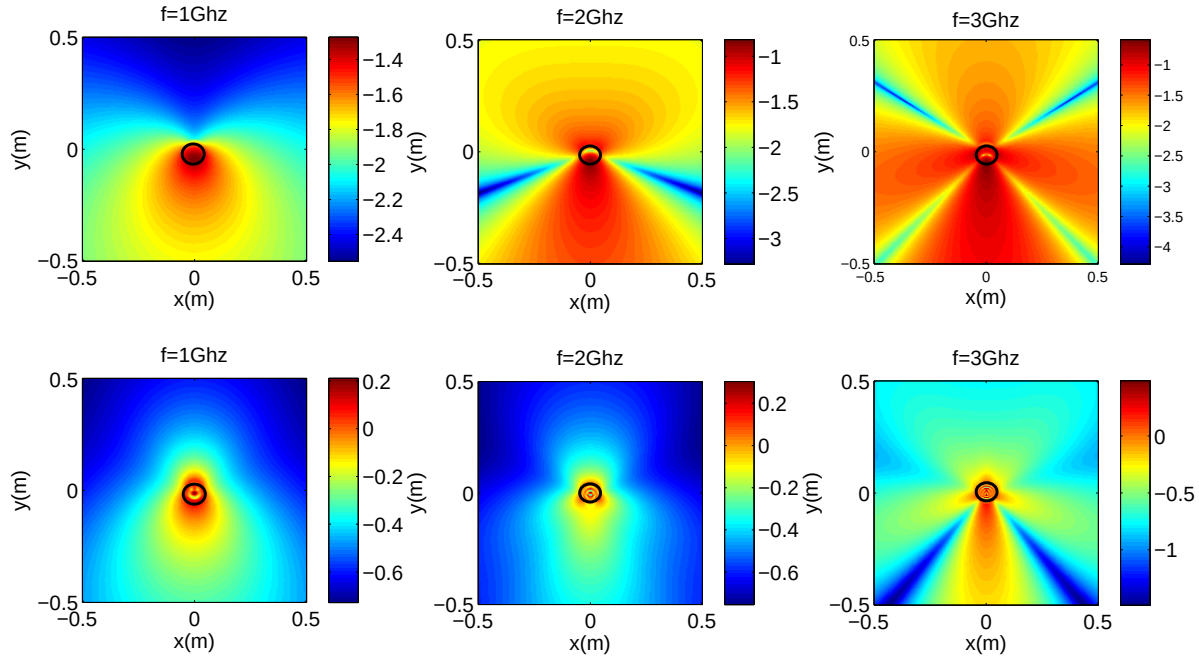

Figure 5.5 – Amplitude of the scattered field by an empty (top) and a water filled plastic pipe (r=5cm) (bottom) in free space.

amplitude values are given in dB (in order to enhance the visualization) and they are calculated by subtraction of the incoming field from the total field.

According to the scattering theory already introduced in Section 4.2, when the particle size is small in comparison with the wavelength (as it is the case for the 1GHz wave impinging on 2.5cm radius circular cylinder in Fig. 5.4 or a thin rectangular cylinder in Fig. 5.6), we get close to the the Rayleigh region and the scattering is almost symmetric about the plane normal to the incident direction. When the size of the object becomes of the order of the wavelength, i.e, for higher frequencies, it appears a forward radiation lobe, which is clearly visible at the mentioned figures for the 2GHz and 3GHz illumination. For bigger and more complex objects at the same frequencies, like the pipes in Fig. 5.5, the scattering behaviour gets more complicated giving rise to secondary radiation lobes. It can be noticed that in the case of the metallic circular cylinder, the radiation characteristic and the amount of energy scattered upwards is the same or at least very similar for all the frequencies. This does not happen when the scatterer is a dielectric object.

In Fig. 5.7 we compare the amount of energy that is scattered back when the above referred plane wave is impinging on objects of diverse shapes and dimensions. The presented results were taken at a distance of 10cm above the top surface of the target and circular and rectangular objects of different sizes are investigated. Hence, this can be considered a kind of target cross section calculation in the near field, which is the actual region of interest for our particular application.

As stated for the field distribution figures, the metallic circular cylinder presents an almost constant behaviour for frequencies above the Rayleigh limit. All the other objects present resonances whose amplitude and frequency depend on the object dimensions and the dielectric material. The analytical solution to the canonical case of the scattering by circular cylinders is given in Appendix B together with an illustration for three of the cases represented in Fig. 5.7. By com-

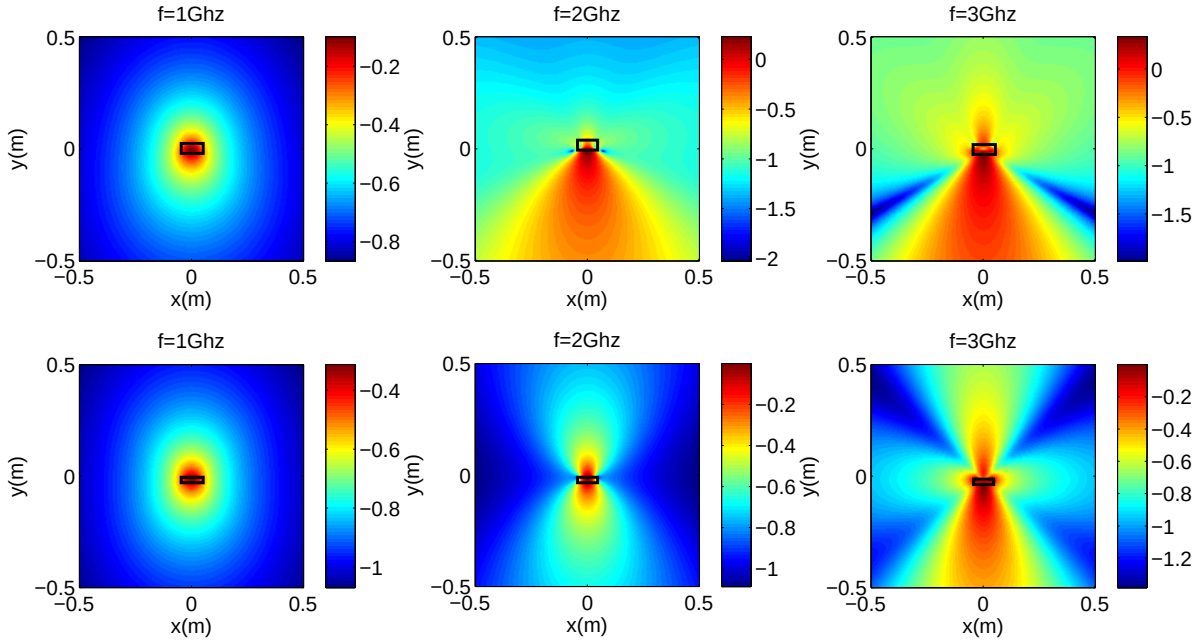

Figure 5.6 – Amplitude of the scattered field by a plastic (top) and half-plastic (bottom) rectangular cylinder (length w=10cm, height h=4cm) in free space.

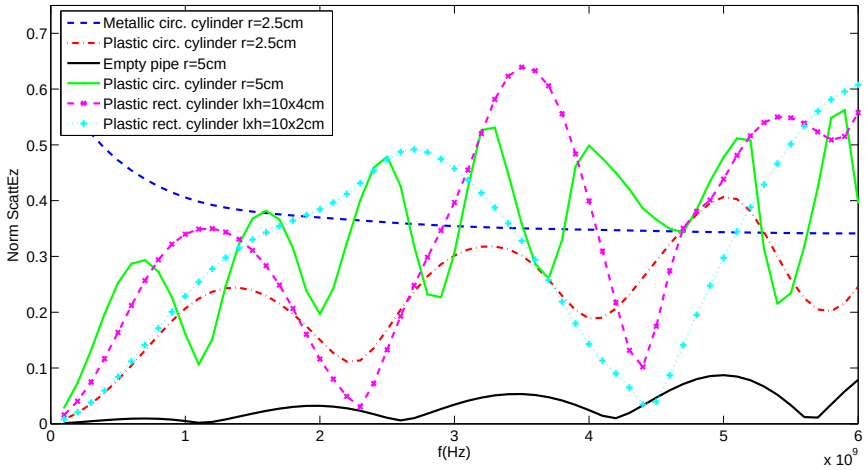

Figure 5.7 – Backscattered electric field by different objects in free space and plane wave excitation; receiving point at a distance of 10cm.

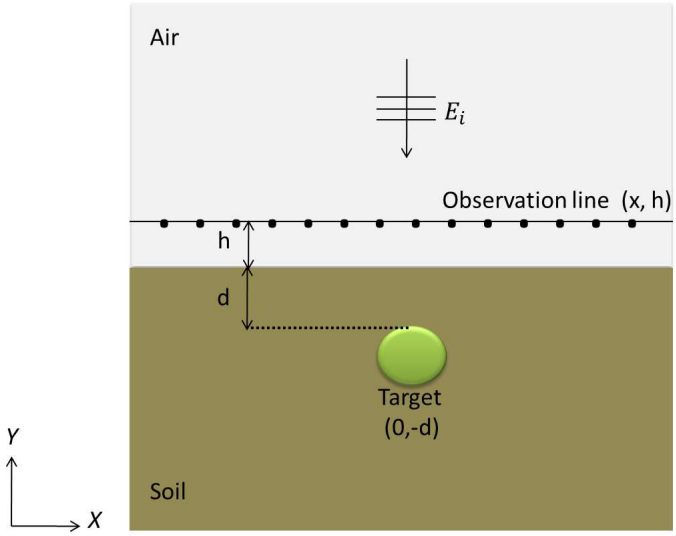

Figure 5.8 – Scattering by a buried target illuminated by a downward propagating plane wave.

paring the figures from both analytical and simulated field calculations, we see that the resulting values are in very good agreement.

5.4.2 Wet and Dry Soils

The following step is to investigate 2D dielectric targets when they are shallow buried in the ground. The computational domain is now composed of air ($y > 0$), ground ($y < 0$) and the air-ground interface ($y = 0$) and we consider once more the incoming field to be a linearly polarized plane wave traveling from top to bottom in y-direction (see Fig. 5.8).
In the presence of a half-space, the backscattered signal is the sum of the scattered field at the air-ground interface and the scattering by the buried object. In order to eliminate this interface contribution the model output is processed with a background subtraction. The PML have been also adapted to the ground electrical parameters, but there are still a few reflections coming back from the boundaries, in particular produced at the air-soil discontinuity. Nevertheless, their effect over the scattered field is negligible and it will not be further considered here.
Two soil types which are representative of real wet and dry soils have been chosen for our simulations. For the wet soil which is a lossy medium, we assume $\epsilon_r = 10$ and $\sigma = 50\text{mS/m}$. The dry soil, on the other hand, has $\epsilon_r = 5$ and $\sigma = 1\text{mS/m}$, i.e., the attenuation losses will be negligible due to its low conductivity. The targets are buried 10cm deep (respect to their top boundary, Fig. 5.8) and we consider again 1GHz, 2GHz and 3GHz operating frequencies. The scattered field distribution for both soil types is presented in Fig. 5.9. Here we observe again that unlike for the other targets, the backwards scattering pattern and amplitude by the buried metallic cylinder is almost constant for all the frequencies. In the case of wet soil and particularly for the frequency of 3GHz, there are some artifacts only present for this target that seem to be connected with a high frequency resonance effect but they cannot be well explained. For the rest of the dielectric objects (see Figures 5.10-5.14), it is clear that there are oscillations, and neither higher frequen-

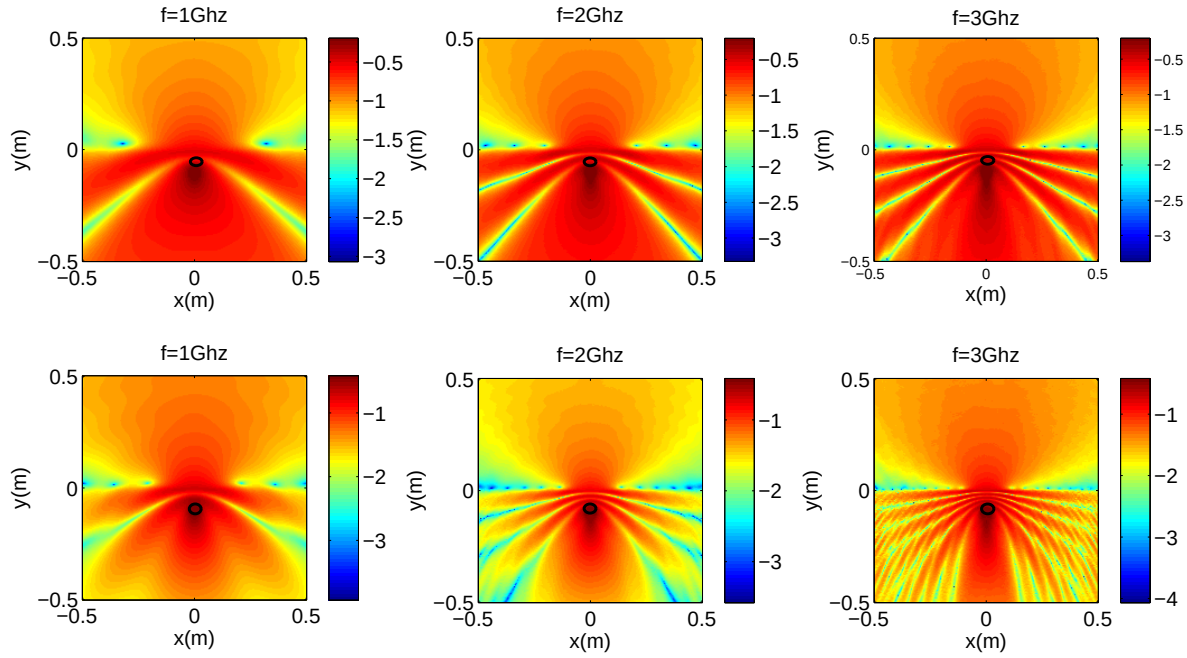

Figure 5.9 – Amplitude of the scattered field by a buried metallic circular cylinder (r=2.5cm) in dry(top) and wet (bottom) soil.

cies nor bigger permittivity contrasts are always associated with more energy radiated back to the surface. Regarding the downward radiation, secondary radiation lobes appear in all the cases, which increase both with frequency and with permittivity, i.e., in wetter soils. The width and intensity of these lobes respect to the main lobe depend on the geometry and composition of the object and the background soil parameters. We can also observe from the amplitude of the lobes in dry and wet soils, that as expected, due to the higher conductivity, the energy in wet soil is dissipated much faster than in dry one, which decreases the penetration depth of the waves significantly.

For buried dielectric targets, the scattering in wet soil is in general more intense than in dry soil because of the higher dielectric contrast with the background soil, but as we see, this signal is rapidly attenuated in its way to the target and back to the receiver. Therefore, for targets that are buried a few centimeters deep in moist soils, there is a trade-off between the higher dielectric permittivity of the wet soil, which increases the magnitude of the scattered signal by a plastic target, and the higher conductivity, which produces a faster attenuation.

When we represent the scattered amplitude against frequency (see Fig. 5.16), the resonant behaviour of the buried targets becomes slightly more complicated than in free space. The behaviour of the scattered field by the metallic cylinder is again almost constant, but when buried in soil there are multiple little oscillations present which might be due to a numerical error or reflections at the domain boundaries. However, when we look at the overall shape of the signatures for each particular target, we observe that the number of main resonances and their positions are the same for both types of soils. Moreover, all the objects present also the same number of resonances as in free space except for the thinner rectangular cylinder, which now shows several resonances, while in free space contains just one.

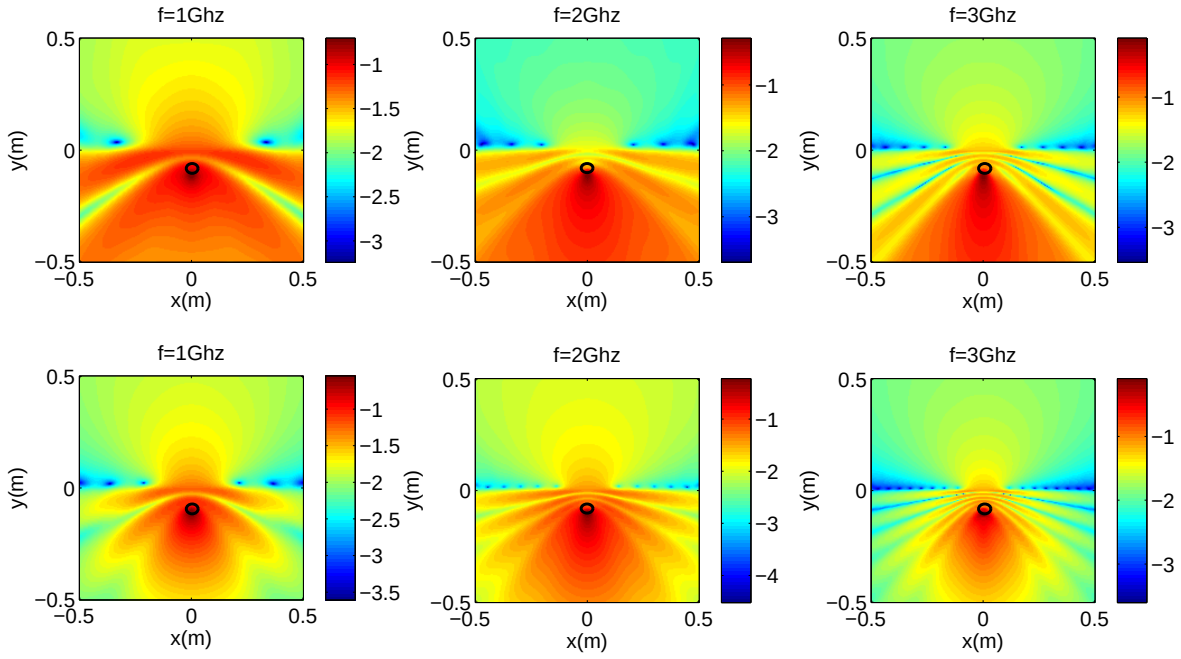

Figure 5.10 – Amplitude of the scattered field by a buried dielectric cylinder (r=2.5cm) in dry (top) and wet (bottom) soil.

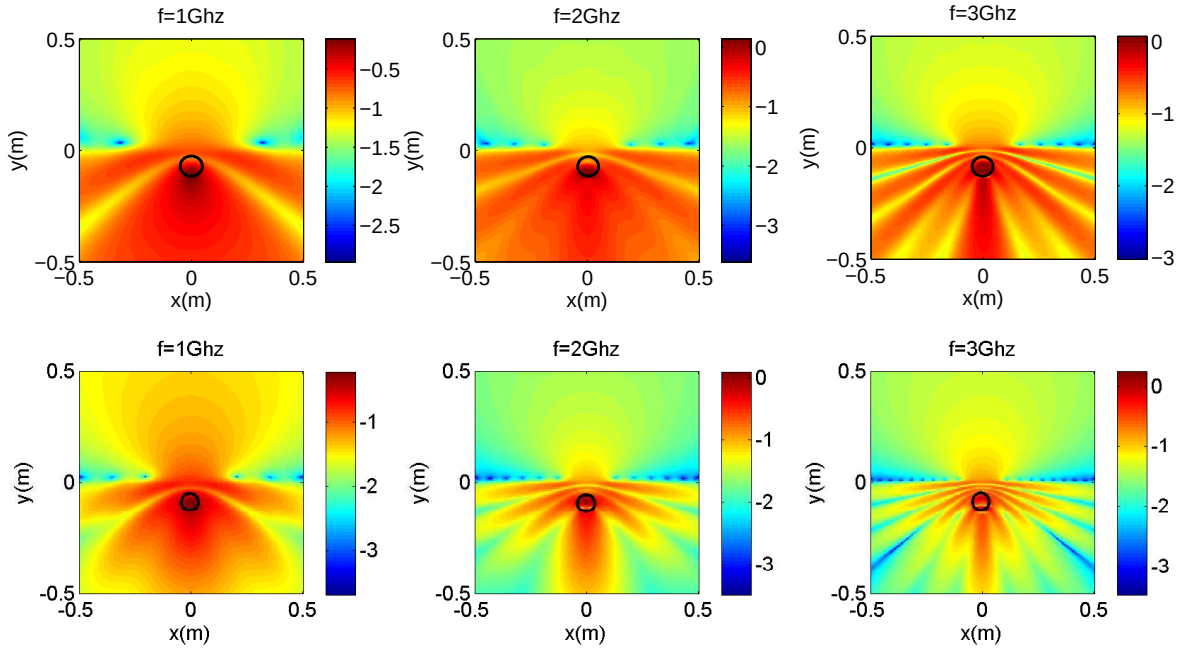

Figure 5.11 – Amplitude of the scattered field by a buried empty pipe (r=5cm) in dry (top) and wet (bottom) soil.

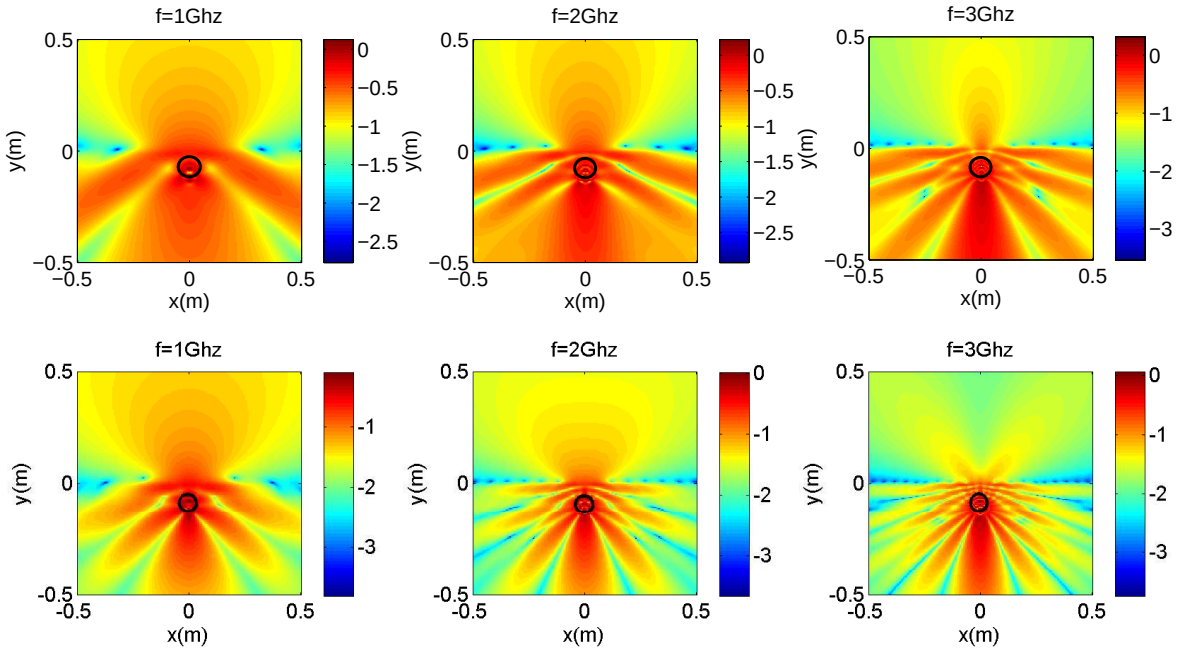

Figure 5.12 – Amplitude of the scattered field by a buried plastic pipe full of water (r=5cm) in dry (top) and wet (bottom) soil.

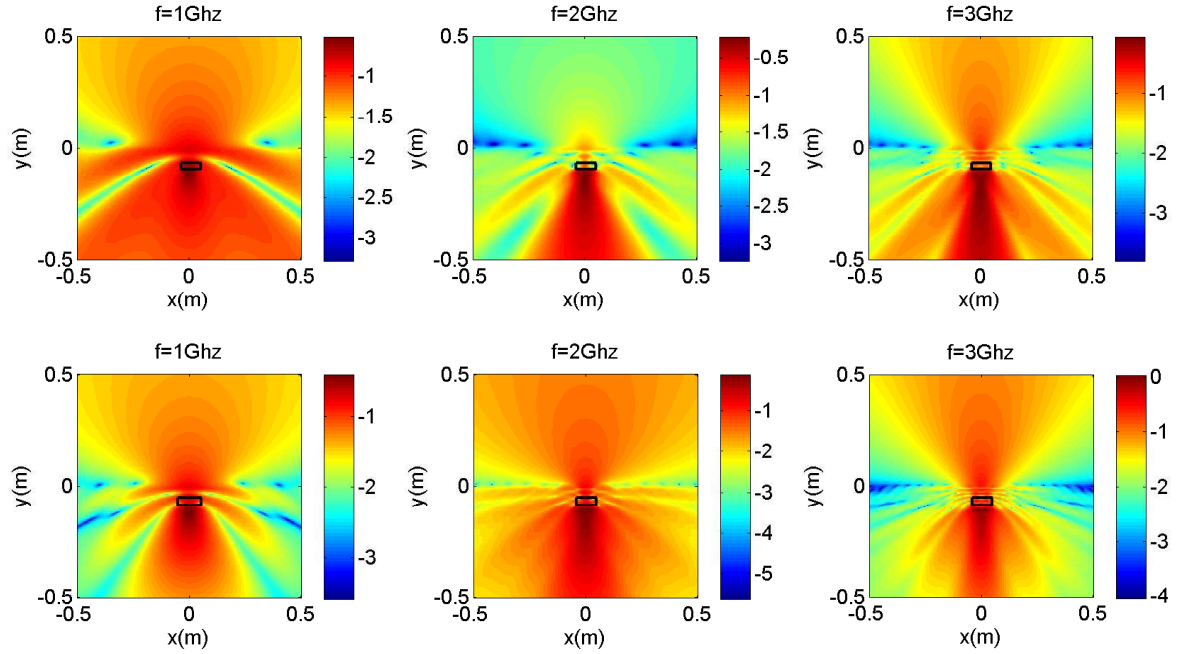

Figure 5.13 – Amplitude of the scattered field by a buried plastic rectangular cylinder (w=10cm, h=4cm) in dry (top) and wet (bottom) soil.

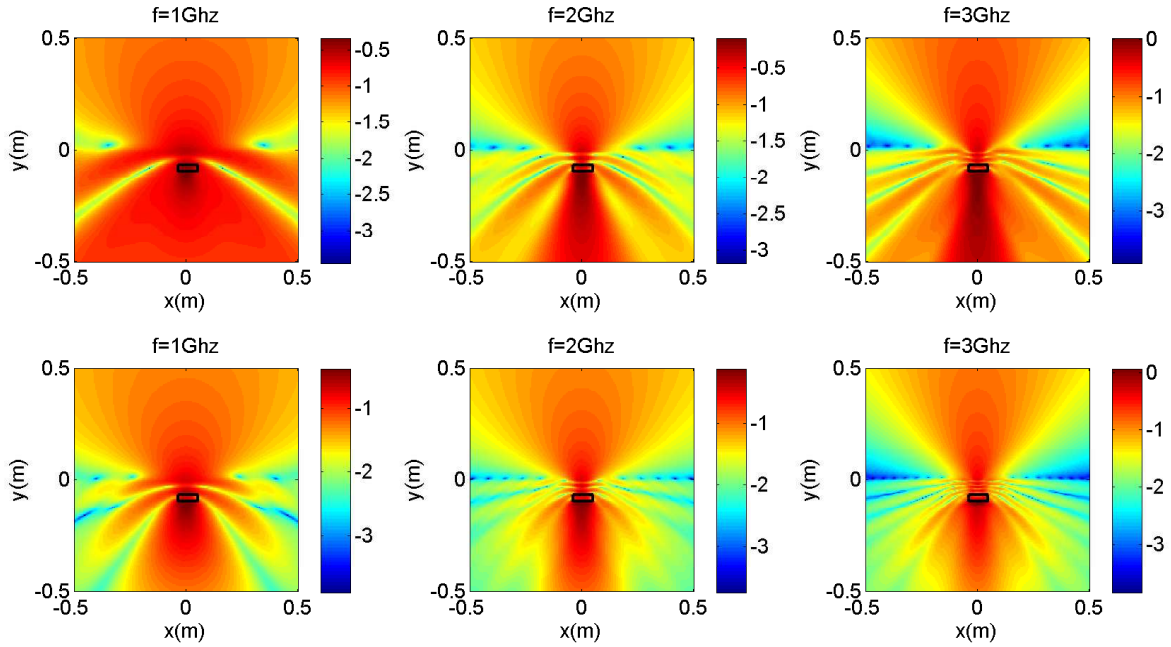

Figure 5.14 – Amplitude of the scattered field by a buried half-plastic rectangular plate (w=10cm, h=4cm) in dry (top) and wet (bottom) soil.

Inhomogeneous soils and rough surface

The following simulations depict the scattered signal from targets buried in dry and wet non-dispersive inhomogeneous soils. For this analysis we will show the real part of the scattered field instead of the absolute value since the effect of the inhomogeneities deforms totally the radiation lobes that were visible in the amplitude representations for homogeneous soils and displaying the real part, the propagation of the waves and their distortion can be better distinguished.
In the considered models, the relative permittivity takes values according to both configurations described in section 4.5.2. Generally, the inhomogeneities closer to the ground surface have higher conductivities due to the presence of organic material. Therefore, conductivities in the range 0.01-0.05S/m have been selected in both cases. The results are processed applying average background removal.
As we can notice in Figures 5.17 to 5.20, the effect of the surface roughness is in both cases more remarkable than the effect of the soil inhomogeneity. For the second configuration, where the topographic variability is stronger than for the first one, we see that the field distribution seems the same for both targets while for the first configuration the difference due to the object scattering is more evident. This is because in the second case the contribution to the scattered field coming from the target is negligible in comparison with the scattering produced at the rough surface. On the contrary, when the surface is flat, the contribution of the targets in comparison with that coming from the inhomogeneity is more important in wet soils, due to a higher permittivity contrast of the objects with the background soil.

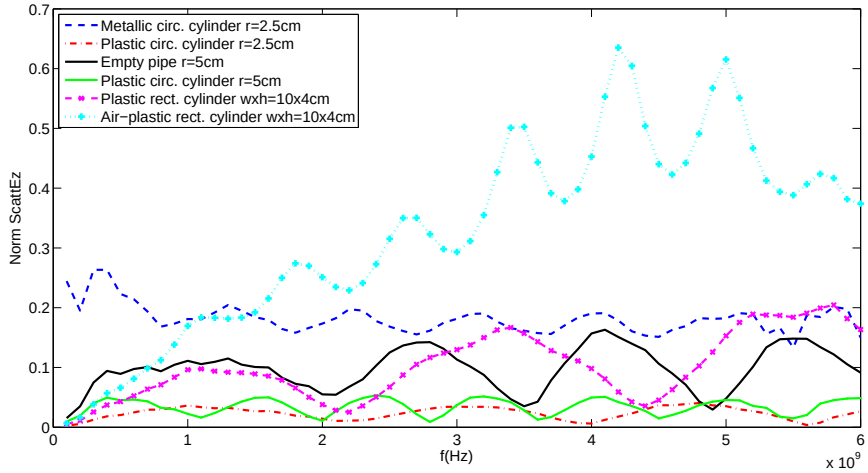

Figure 5.15 – Backscattered electric field by different objects buried in dry soil and plane wave excitation; receiving point at a 10cm height above the surface.

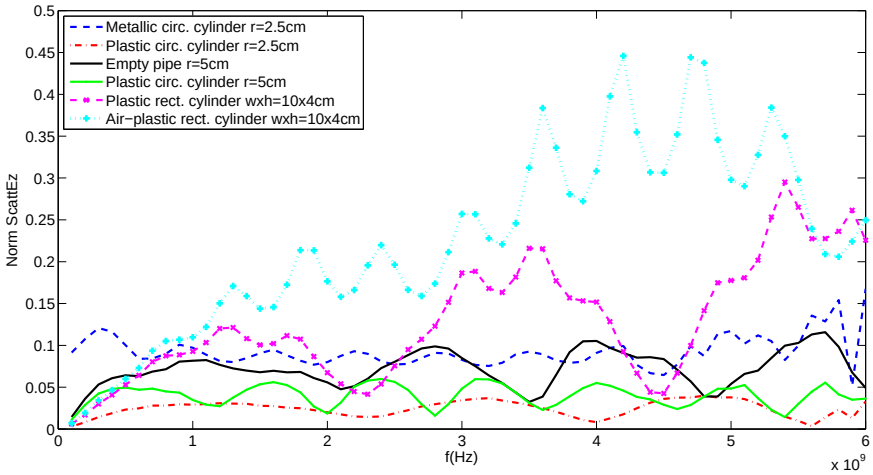

Figure 5.16 – Backscattered electric field by different objects buried in wet soil and plane wave excitation; receiving point at a 10cm height above the surface.

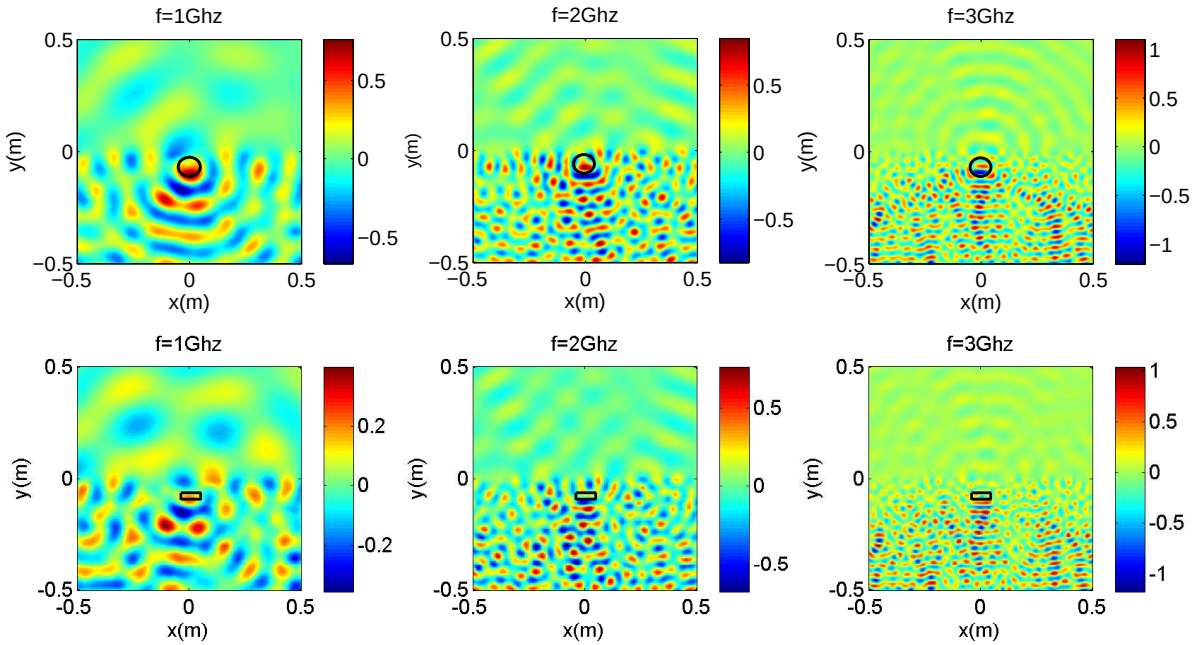

Figure 5.17 – Real part of the scattered field by a buried empty pipe (r=5cm) (top) and an air-plastic rectangular cylinder (w=10cm, h=4cm) (bottom) in inhomogeneous dry soil with flat surface.

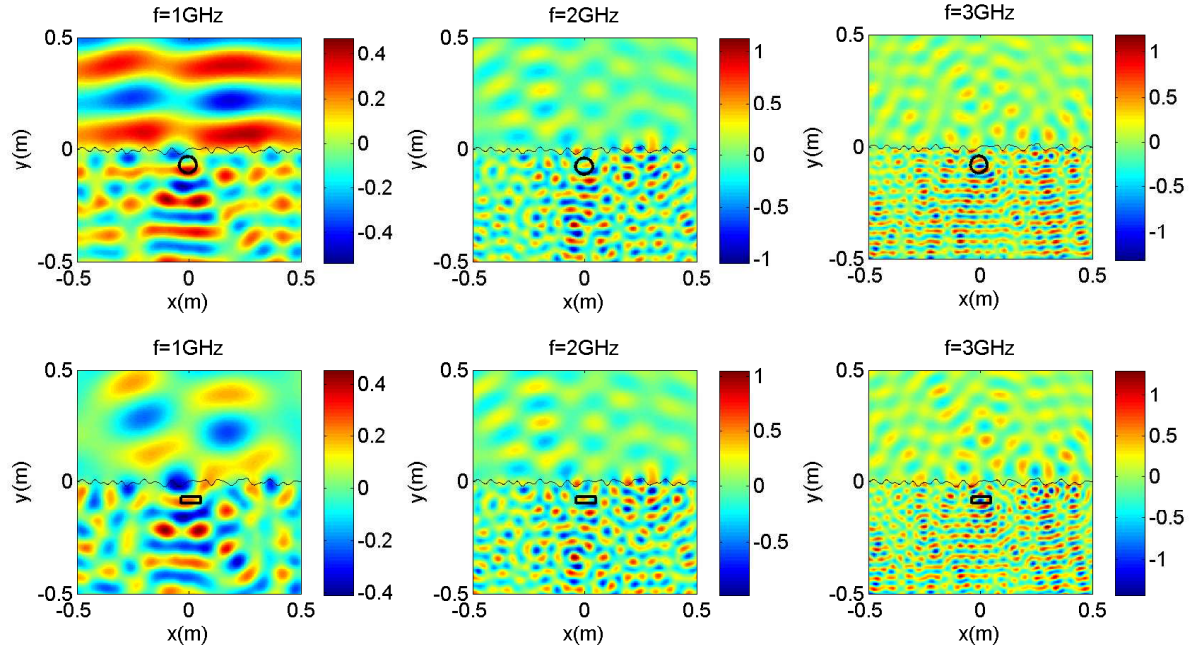

Figure 5.18 – Real part of the scattered field by a buried empty pipe (r=5cm) (top) and an air-plastic rectangular cylinder (w=10cm, h=4cm) (bottom) in inhomogeneous dry soil with rough surface.

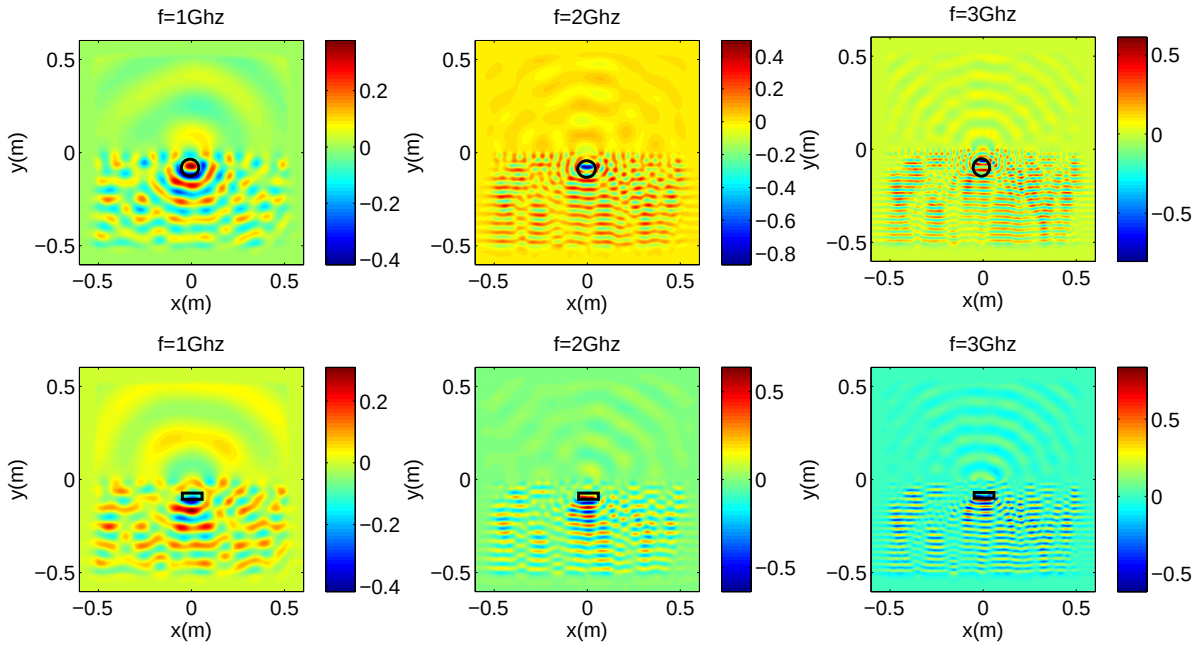

Figure 5.19 – Real part of the scattered field by a buried empty pipeline (r=5cm) (top) and an air-plastic rectangular cylinder (w=10cm, h=4cm) (bottom) in inhomogeneous wet soil with flat surface.

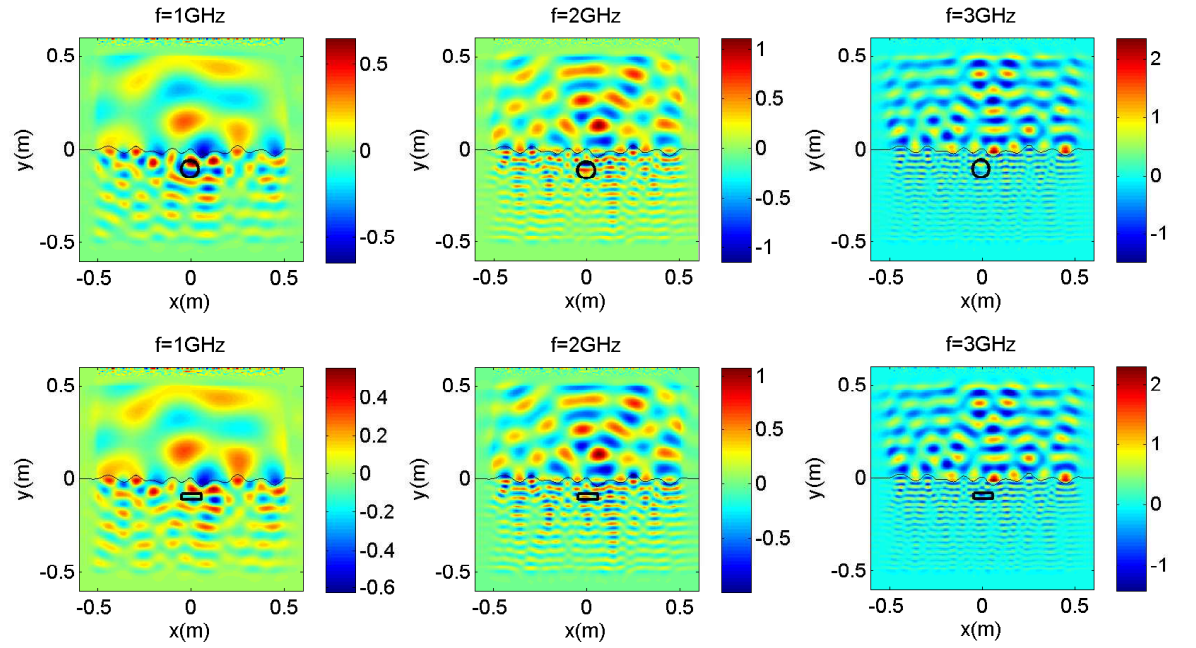

Figure 5.20 – Real part of the scattered field by a buried empty pipeline (r=5cm) (top) and an air-plastic rectangular cylinder (w=10cm, h=4cm) (bottom) in inhomogeneous wet soil with rough surface.

5.5 Signatures of Circular and Rectangular Cylinders in Time Domain

Once we have calculated and studied the behaviour of the scattered wave for an input signal with single frequency values, we can extend our modeling to the case of broadband illumination according to the real external source we have. In order to obtain the broadband response of the system, we decompose the broadband applied signal $I(w)$ into a sum of narrowband contributions I_i which are defined by the electrical parameters at the central frequency of each of them. Thereby, the excitation can be approximated by the following sum,

$$I(\omega) = \sum_{i=0}^{n} I_i(\omega). \tag{5.5}$$

When the bandwidth of these components is narrow enough, this approximation is accurate.
To extend the problem to the whole bandwidth, we just need to apply the model for one frequency to each of the narrowband components with their respective central frequency and input signal. Then, we obtain a system of Helmholtz equations:

$$-\nabla^2 E_i - k_i^2(x,y)E_i = f_i, \quad \text{in} \quad \Omega \tag{5.6}$$

where $k_i^2(x,y) = w_c^2\mu\epsilon(x,y) + iw_c\mu\sigma(x,y)$ and the source $f_i = (k_i^2 - k_{0i}^2)E_{0i}$.
This problem can be directly solved with COMSOL applying the parametric solver over the desired frequency band. Thus, the target scattering for every spectral component can be easily calculated.
In this thesis we assume the material electrical parameters σ and ϵ to be constant with frequency (non-dispersive), which seems to be a good approximation for high frequencies.
For our numerical experiments, we consider a frequency band of 0.1-6GHz and 60 contributions, so we obtained a spectral resolution of 0.1GHz. Then, we modify these contributions applying a linear frequency-domain filter to each input plane wave signal to describe the frequency-dependent excitation:

$$I(\omega) = B_i(\omega)I_i(\omega), \tag{5.7}$$

where B_i is the transfer function.
The Gaussian bandpass filter represents properly the solution for an impulse input for most of the systems; we apply thus a gaussian window centered at 2GHz with 2GHz bandwidth.

5.5.1 Synthetic Radargrams

When we have the frequency domain response for a normalized gaussian broad-band input signal, we can compute the system response in time domain. This is done by applying the discrete Fourier transform to the scattered field spectral distribution at the receiver positions.
In the following section we will display some radargrams obtained with this method.

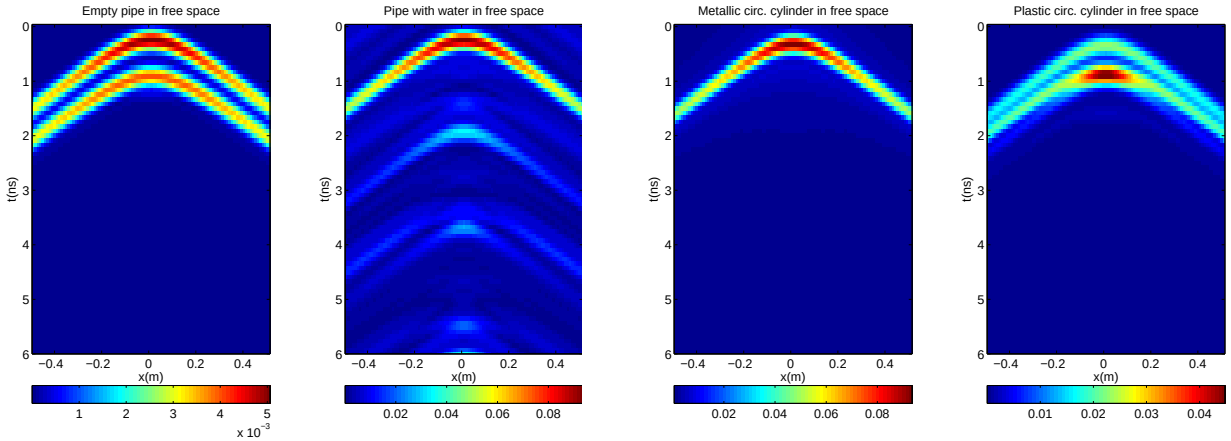

Figure 5.21 – Backscattered amplitude by an empty plastic pipe, a water filled pipe (r=5cm), a metallic circ. cylinder and a plastic circ. cylinder (from left to right).

Free Space

For the case of objects in free space, we calculate the scattered field every 1cm over an aperture synthesized along the x-axis a few centimeters above the target. In this way, we obtain a simulated radargram or B-scan. The scattering scenarios and the investigated objects are the same as in the previous section. Fig. 5.21 depicts the corresponding radargrams for the scattered signal in free space. As expected, the wave reflected by the different targets has an hyperbolic shape [Daniels, 1996]. The shape of the hyperbola is in general a function of the distance to the object and the propagation velocity in the medium above the object. Hyperbola fitting techniques can help to get an estimation of the background soil permittivity if the object depth is known.
In these radargrams, the top and bottom reflections for the three non-metallic objects considered are clearly resolved due to the broad bandwidth of the signal. As it can be noticed, the highest reflectivity is related to the metallic circular cylinder while the lowest corresponds to the empty pipe that is just produced by its thin plastic cover. The pipe filled with water has the highest permittivity ($\epsilon_{water} = 81$), which makes the wavelength of the signal nine times smaller than in free space. It is then required very small grid to get enough accuracy inside the pipe, and this numerical error is probably producing the artifacts present in the associated radargram. These artifacts are also present when we consider this pipe buried in soil in the next calculations.
Another interesting phenomenon that can be observed in the right image of Fig. 5.21 is that the bottom reflection (sometimes referred in literature as the glory wave) is stronger than the top reflection (or specular wave). This is an effect than can happen for certain dielectric objects in free space as demonstrated in [Cloude et al., 1996], where the authors study the different scattering mechanisms by dielectric cylinders.

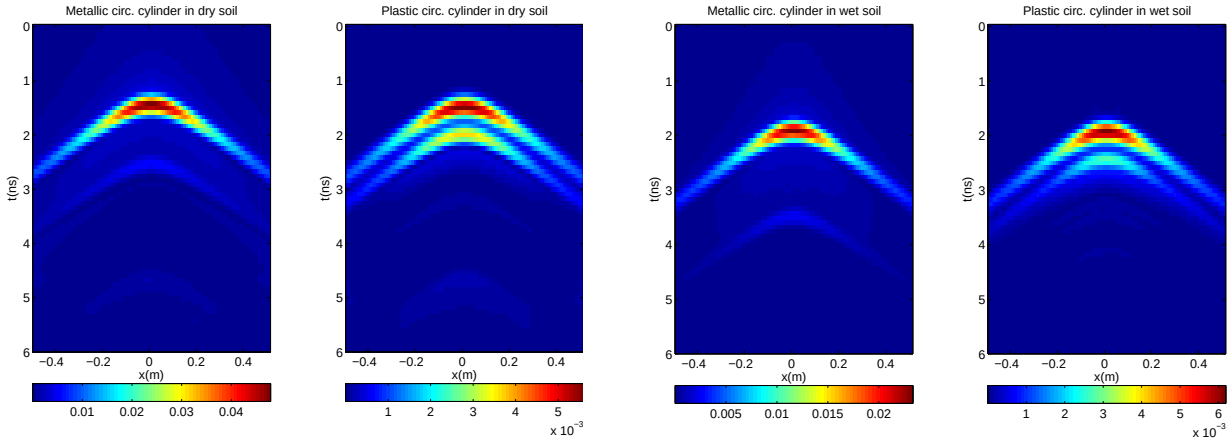

Figure 5.22 – Backscattered amplitude by a metallic and a plastic circular cylinder (r=2.5cm) buried in dry and wet soil.

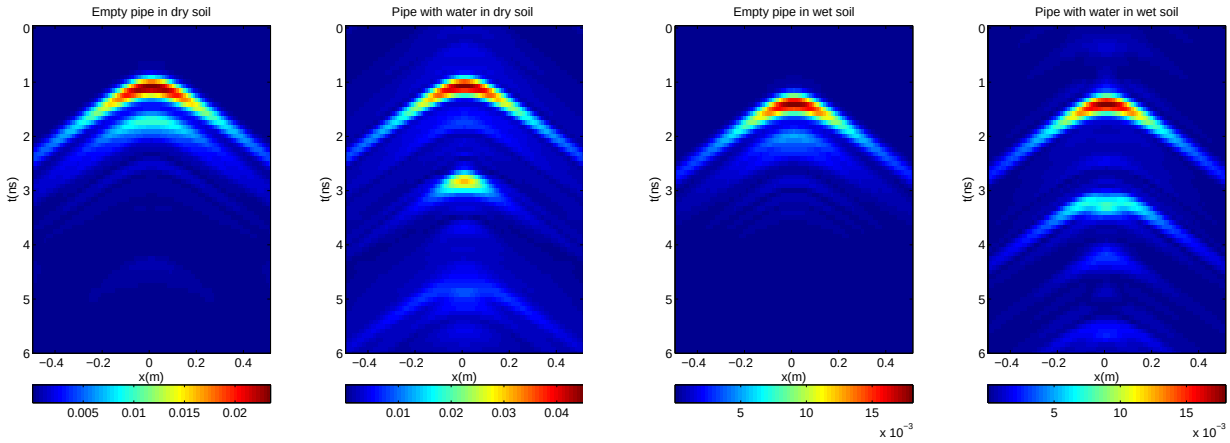

Figure 5.23 – Backscattered amplitude by a plastic empty pipe and a pipe full with water buried in dry and wet soil.

Wet and Dry Soils

Figures 5.22 to 5.24 correspond to the backscattered signals by several targets buried in wet and dry soil respectively. The receiver positions are located 10cm above the interface and the excitation is again a normalized gaussian modulated incoming plane wave.

For most of the targets we are again able to distinguish top and bottom reflections, except for two of the objects: the circular metallic cylinder, since the energy is totally reflected at its top boundary; and the half air-plastic cylinder, whose vertical dimension lies in the limit of the signal range resolution. As the waves travel faster through air than in plastic, the top and bottom reflections are superimposed in the latter case, while for a cylinder of the same dimension but just made of plastic, we can still distinguish both reflections. We observe that in all the cases the bottom reflection intensity decreases respect to the top reflection intensity when the targets are buried in wet soil and, as expected, the hyperbolas are slightly delayed in time and narrowed.

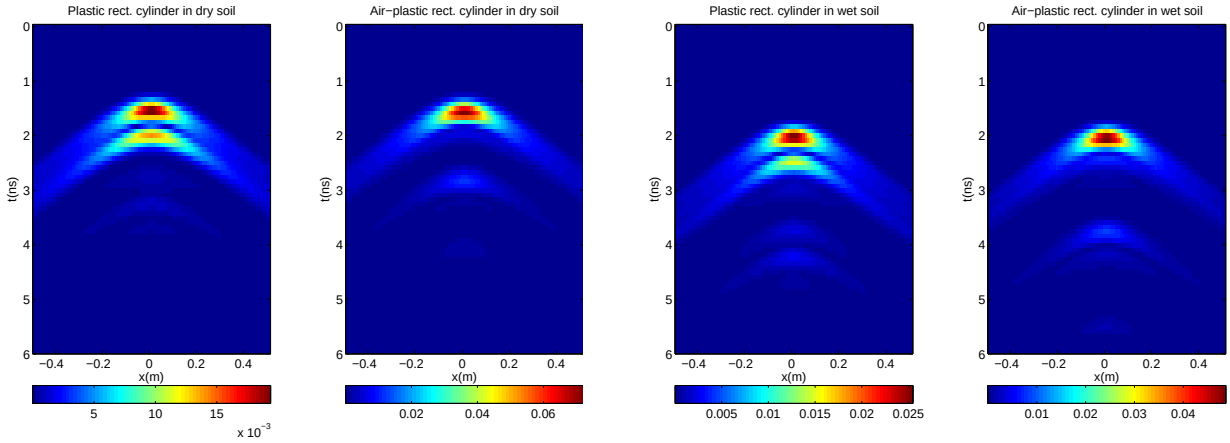

Figure 5.24 – Backscattered amplitude by a plastic rectangular cylinder and air-plastic rectangular cylinder buried in dry and wet soil.

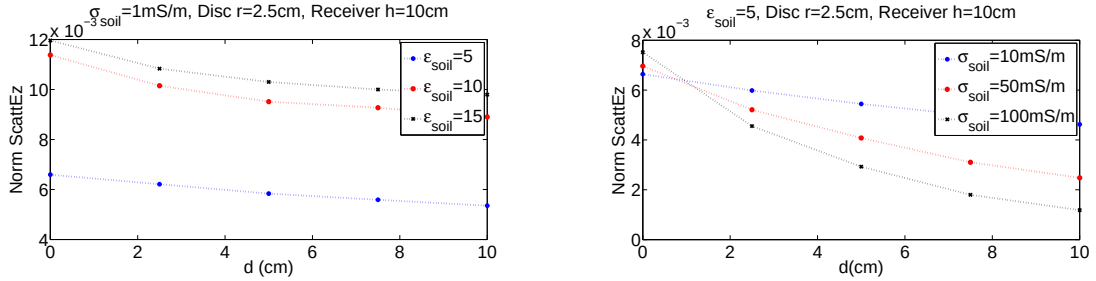

Figure 5.25 – Maximum scattered amplitude by a dielectric cylinder (r=2.5cm) in different soils.

There is also an evident difference between the scattering patterns of rectangular cylinders and the rest of the targets which are circular. The scattering patterns are in the latter case clearly flattened, and these are the type of echoes that we will mostly observe for typical buried mines. Regarding the amplitude we see that a higher contrast between the object and the background does not always mean an stronger backscattering, due to the higher attenuation connected with a wetter soil. Which of both effects dominates will depend on the depth of the scatterer.

In the plots displayed in Fig. 5.25 and 5.26, we show the amplitude behaviour depending on the target depth, the soil parameters and the object dimensions and composing material. As we can see, the attenuation of the signal with depth increases rapidly when the conductivity increases, and for depths below ∼4cm the attenuation gets dominant over the contrast. On the other hand, an increase in the permittivity does not accelerate the attenuation with depth, which in this case decays soft and constantly for the three permittivities considered.

The next illustrations (Fig. 5.27 to 5.29) correspond to the simulated radargrams for the scattering by targets buried in inhomogeneous dry and wet soil for both cases, with rough and flat interface. The soil models are the ones previously presented in Fig. 4.9. For the dry soil scenario we have an average permittivity of 5 and conductivity of 5mS/m with a standard deviation of 0.8 and a correlation length of 2cm, and the wet soil scenario presents an average permittivity of 10 and conductivity of 50mS/m with a standard deviation of 1.2 and a correlation length of 5cm. Apart from the inhomogeneity we make these models more realistic adding surface roughness:

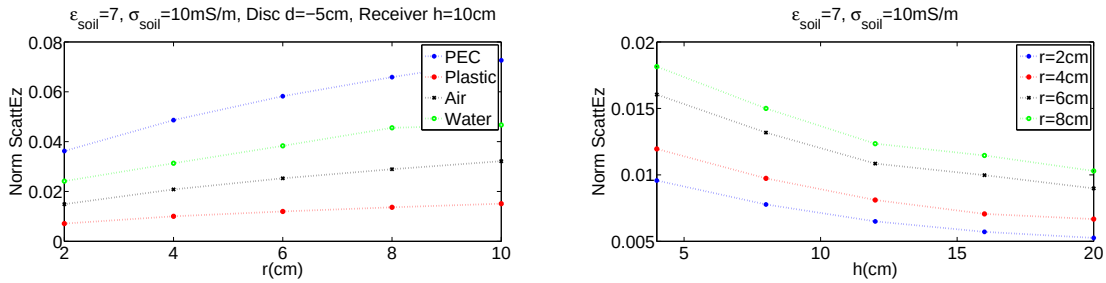

Figure 5.26 – Maximum scattered amplitude for different cylinder radius and different receiver heights.

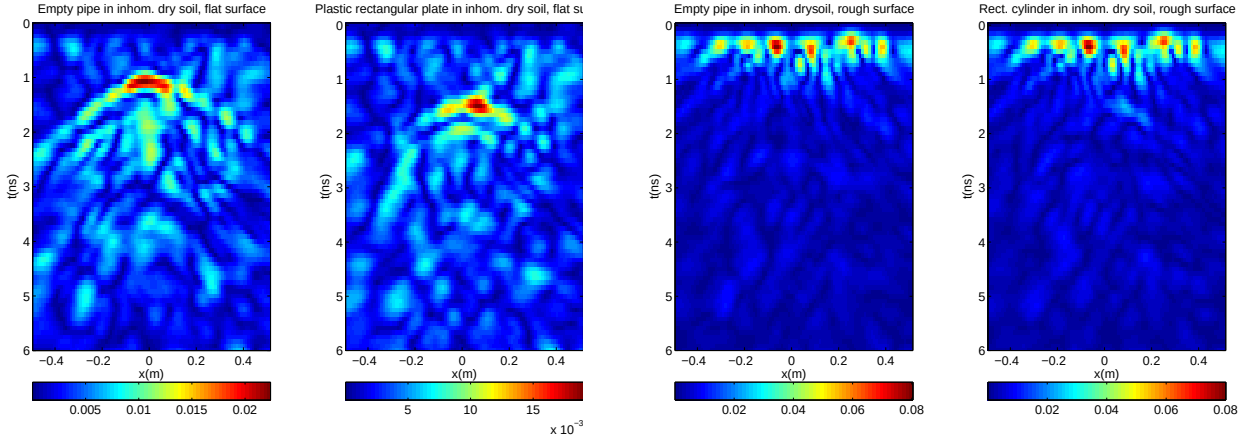

Figure 5.27 – Backscattered amplitude by a buried empty pipeline (r=5cm) and an air-plastic rect. cylinder (w=10cm, h=4cm) in inhomogeneous dry soil with flat and rough surface.

related to the dry soil, we consider a randomly varying surface with a mean height variation of ±1cm with 2cm correlation length and for the wet soil the variation in height is ±2cm with 5cm correlation length. We don't present here the results for conductivity variations because we have observed that the effects caused by permittivity fluctuations of the models are much stronger than the effects caused even by considerable conductivity variations with exception of very conductive soils ($\sigma > 0.05$S/m).

The analysis of the simulations reveal that if the soil permittivity is heterogeneous, the form and the absolute traveltime of the hyperbolas change notably due to the velocity variations. Another consequence of the heterogeneity are numberless reflections which interfere with the signals from the targets. These effects worsen when the surface is not flat.

If the contrast of the objects to the soil is high enough, as is the case for moist soil, and we don't introduce roughness, the target signal is still visible. As the contrast gets smaller, the objects become more difficult to detect or cannot be detected any more. In the simulations with both soils (Figures 5.27 and 5.28), we can clearly see the diffraction hyperbolas, but particularly for the dry soil case, they appear rather distorted. When we add surface roughness, the hyperbolas are hardly to distinguish even after applying time gating (subtracting early arrival times to eliminate partially the surface contribution to the radargram). In both cases, but in particular for the wet soil environment, the surface roughness contribution is much more important than the soil

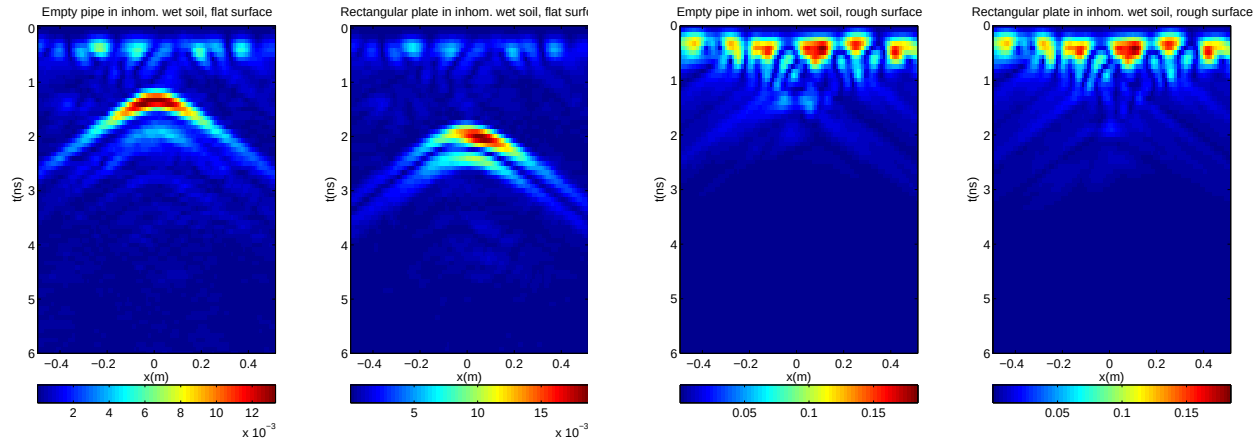

Figure 5.28 – Backscattered amplitude by a buried empty pipeline (r=5cm) and an air-plastic rect. cylinder (w=10cm, h=4cm) in inhomogeneous wet soil with flat and rough surface.

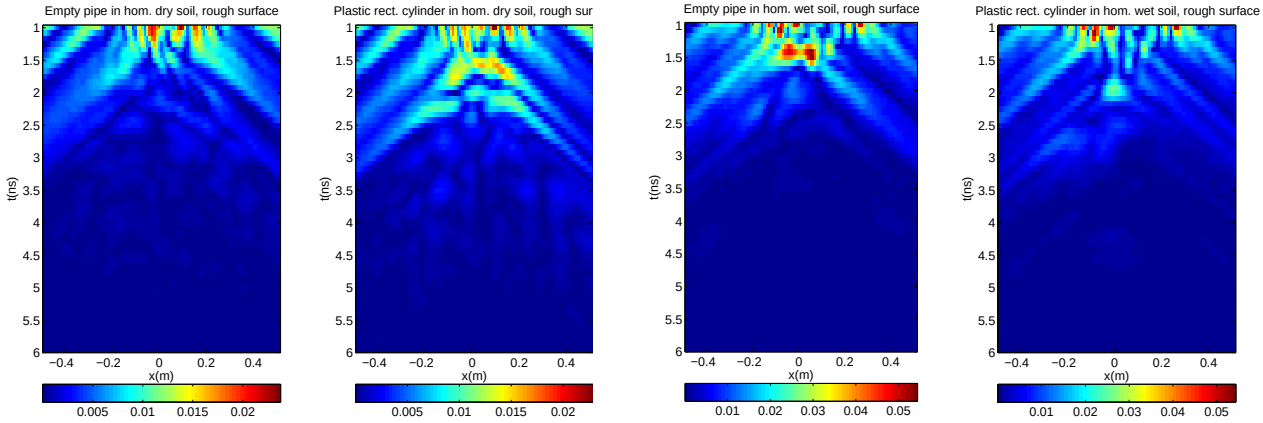

Figure 5.29 – Backscattered amplitude by a buried empty pipeline (r=5cm) and an air-plastic rect. cylinder (w=10cm, h=4cm) in homogeneous dry and wet soil with rough surface applying time gating.

heterogeneity contribution due to the larger fluctuation in height of this configuration.
Summarizing, the simulation results reveal that in general the contribution of the surface roughness is clearly stronger than the contribution of the heterogeneity even for slight height variations. Only when the contrast is large enough and the target is not very shallowly buried (in this case its diffraction hyperbola usually gets totally masked by the rough surface scattering), it may be possible to distinguish the target.

6

GPR Antenna Modeling in Frequency Domain

Essentially, all models are wrong, but some are useful
George Box

GPR systems often operate in direct contact with the ground and very close to the target. When the target is so close to the radar, it interacts with the reactive fields of the antenna (i.e., it is in the near field region of the antenna), and only accurate models would reflect this mode of operation and produce reliable results. The antenna is probably the most important component of the modeling scheme as it has a significant influence on the nature of the propagating waves and therefore, the final recorded signal; it also determines the detection capacity of the system. Hence, accurate GPR simulations are fundamental to understand and characterize real antenna performance.

The early GPR 2D simulations ignored the antenna concept, using excitations modeled as simple plane waves, line sources or infinitesimal sources (Hertzian dipoles) [Liu & Chen, 1991], [Moghaddam et al., 1991], [Wang & Tripp, 1996]. Later, fully 3D simulations of typical GPR antennas were published by some authors. In [Bourgeois & Smith, 1996] a GPR antenna system consisting of shielded and resistively loaded bow-tie antennas fed by 1D transmission lines was modeled. Other models with unshielded finite length dipoles situated directly above surface were introduced in the following years by [Gürel & Oğuz, 2000], [Texeira & Chew, 2000], [Holliger & Bergman, 1998] and although reasonably successful, they did not simulate the antenna directivity and ground coupling with enough accuracy for near-surface high resolution applications. Recently, there have been some contributions which have modeled more realistic shielded bow-ties or dipole antennas obtaining satisfactory results in modeling the coupling, propagation and reflection response of the GPR wave [Uduwawala & Norgren, 2004], [Lampe & Holliger, 2005], [Warren & Giannopoulos, 2009]. Nevertheless, most of these studies

were either focused only on the antenna modeling itself or they assumed some ideal conditions to describe soil parameters, surface roughness or target's internal structure. In many cases these simplifications are a good compromise, but when high resolution and accuracy are required, some of these assumptions may not be acceptable any more.
When dealing with GPR antenna modeling, although it is possible to conduct very realistic simulations using FEM and in particular COMSOL simulation tool, it is not required to model in detail all the hardware components of the antenna system to achieve accurate results. This information is in any case not available for most commercial systems and such a complex model would increase unnecessarily the computational demand.
In this chapter, we intend not only to find a satisfactory model to represent the antenna system but to get a better knowledge about the influence of the most important parameters on the performance of an UWB antenna in near field, and to state some guidelines for the GPR antenna modeling problem in near-surface applications. This analysis is accomplished in frequency domain, as it is desirable to select a design which shows a good behaviour in terms of radiation pattern, power density and impedance along the frequency band of our commercial system.

6.1 Bow-Tie Antenna

As mentioned in Chapter 3, the GPR equipment employed in our investigation is a time domain UWB system manufactured by ERA Technology with a nominal central frequency of 2Ghz and 2Ghz bandwidth. The antenna system consists of two bow-ties placed side by side (Fig. 6.1) and enclosed in a shielding box designed to isolate the antenna from external interference and to enhance the radiation downwards. The antenna casing is presumably filled with an absorbing material in order to eliminate internal reflections. As already stated, the spatial dependence of the radiation pattern from a shielded bow-tie antenna will be different from that of a bow-tie in free space and it is necessary to understand how the effective field pattern, beamwidth and impedance change for a real configuration. However, the exact shape and size of the bow-ties inside the antenna unit is unknown and we will create an approximate model which fulfills our system specifications and matches the measurements.

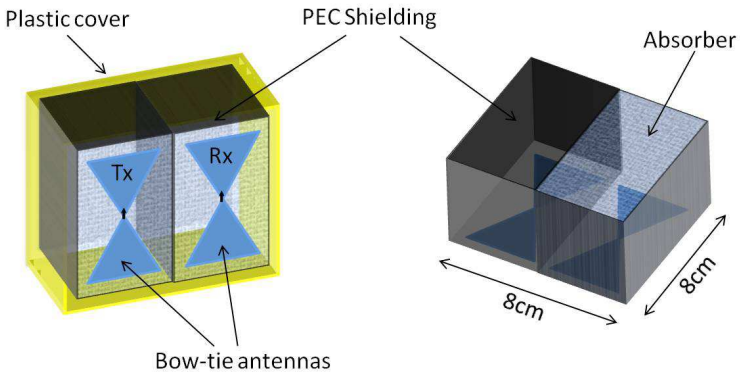

Figure 6.1 – Model of the GPR antennas (with a transmitter and a receiver bow-tie, EM absorbing material and metallic shielding.)

In order to reach a satisfactory design and gain knowledge about GPR antenna radiation characteristics, in the following sections we analyze the whole modeling process step by step, investigating the effect of various antenna parameters and every element introduced in the model.
First, the antenna is modeled in free space from the simplest case of the bow-ties alone to the most realistic one where the antennas are surrounded by a metallic reflector filled with absorbing material. Secondly, we analyze the antenna-medium energy coupling when the antenna is operating in contact or at a certain height above the ground. In this way, we will gather enough understanding to develop a satisfactory model to simulate the actual GPR antenna illumination. However, this model still has to be optimized via time domain analysis and comparison with measurements.

6.2 Antenna Feed

Ports are a unique type of boundary condition, which are defined on a 2D planar surface and allow energy to flow into and out of a structure. The lumped port (port excitation) boundary condition is recommended only for surfaces internal to the geometric model. It allows excitation in terms of voltage potential and is considered the interface between voltages/currents and electric/magnetic fields. The port is based upon transmission line theory and the feed point must be defined in a way similar to a transmission line feed, thus the gap must be much less than the wavelength.
The relationship between the electric field and the input voltage is defined as

$$V = \int_l Edl = \int_l (E \cdot u_l) dl, \tag{6.1}$$

where l corresponds to the line length between the terminals in which the port is placed. The input voltage at the port is set to 1V and the impedance should be set to fit the estimated antenna impedance (as shown in the following section). A good matching reduces the reflections back to the cable and maximizes the radiated energy. The ringing is thereby also reduced.

6.3 Antenna Radiation Pattern and Impedance

To describe the electromagnetic behaviour and performance of an antenna, it is necessary to consider a series of parameters which will determine the antenna characteristic; in particular, along this chapter we focus on the analysis of the radiation pattern, the power density and the antenna impedance for different antenna models (for detailed parameter descriptions see Definitions).
When we display the radiation patterns, we are representing the radiated power density (or the electric or magnetic field) at a constant distance in 2D cuts of the principal E-plane and H-plane (defined in Chapter 4). The pattern observations are usually made on a sphere of constant radius extending into the far field. Then, the radiated power density corresponds to the radial component of the time-averaged Poynting vector which is proportional to $|E|^2$, since in far field electric and magnetic fields are perpendicular. More specifically, the radiation power density can

be expressed in terms of the far-zone electric field by [Balanis, 2005]

$$W_{rad} = \frac{1}{2\eta}|\mathbf{E}|^2, \tag{6.2}$$

with η the intrinsic impedance of the medium. This magnitude is also directly related to the directivity and gain of the antenna, which are sometimes preferred parameters to measure the antenna performance. Since in practice the difference between maximum and minimum power values is very large, it is quite common to express the power density or electric field in decibels (dB) and refer to relative power/amplitude patterns according to:

$$\text{Relative power density (dB)} = 10\log_{10}\frac{W}{W_{max}} = 20\log_{10}\frac{|\mathbf{E}|}{|\mathbf{E}|_{max}}. \tag{6.3}$$

In the formula above, the power expression is normalized respect to its maximum angular value for a given radius. In Fig. 4.5 a 2D-cut together with a three dimensional normalized plot of the average power density of a bow-tie dipole was already illustrated. However, in the present chapter we show all the simulated radiation patterns without applying any normalization in order to keep the information about the amplitude. It must be mentioned that the distances at which we evaluate the radiation patterns, are convenient for investigation purposes in landmine detection, where we are interested in objects located within a region up to 20-25cm far from the antennas. More precisely, we have analyzed the power patterns at a radial distance d of 25cm from the antennas in free space and 20cm in dielectric medium. Such distances can be assumed in the far field region of the antenna, although for the higher frequencies of the bandwidth they are very close to the boundary with the Fresnel region or even inside (see Definitions). However, we have observed from these simulations that the reactive component of the power density is insignificant and overall behaviour of the EM fields corresponds to that characteristic of the far field, being the power density associated with the fields predominantly real. Thus, the equality between the power density and the electric field defined by Eq. 6.2 still holds and we use this relationship to derive the power patterns in the following sections.

6.4 Antenna Contribution

6.4.1 The Antenna Flare Angle

Firstly, we analyze the impact of modifying the antenna flare (or aperture) angle between typical values. Figures 6.2 and 6.3 show some results from the corresponding simulations. These illustrations demonstrate that the input impedance as well as the power patterns are not very sensitive to small changes in flare angle. The impedance decreases slowly when increasing the angle but the difference is not significant. From the plot of the radiated power density, we observe that for all the frequencies within the bandwidth, the behaviour of the three considered antennas looks almost the same and hence, the three radiation patterns are very similar. It is only appreciated that the radiated power plateau is achieved at a slightly lower frequency when the flare angle increases; this is an expected result since the antenna bandwidth increases with flare angle.
We have seen that realistic variations of the flare angle produce slight effects on the frequency

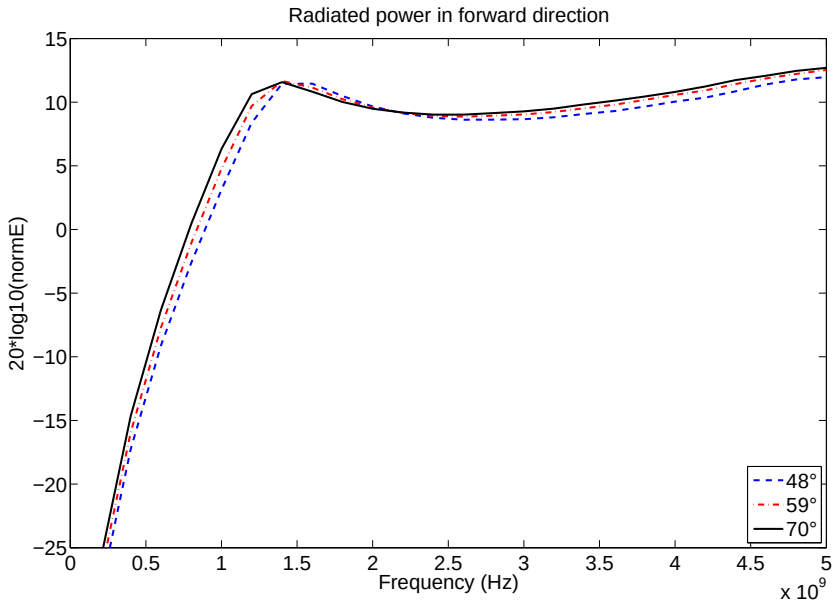

Figure 6.2 – Radiated power in forward direction (d=25cm) for different flare angles.

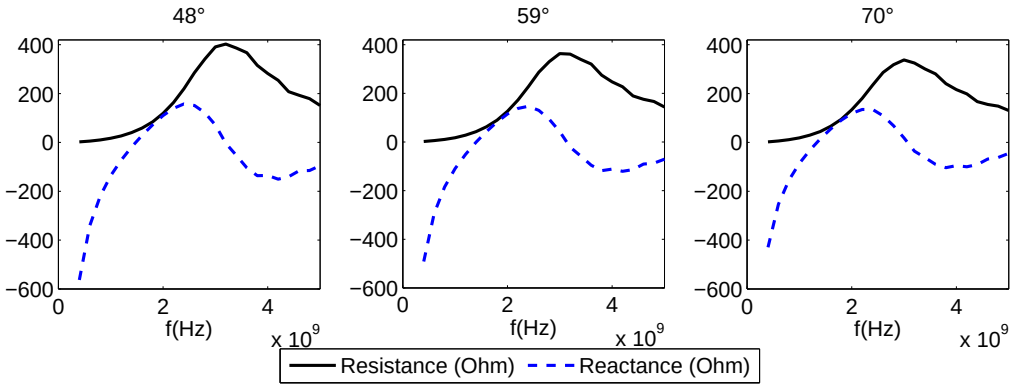

Figure 6.3 – Impedances for 3 different flare angles.

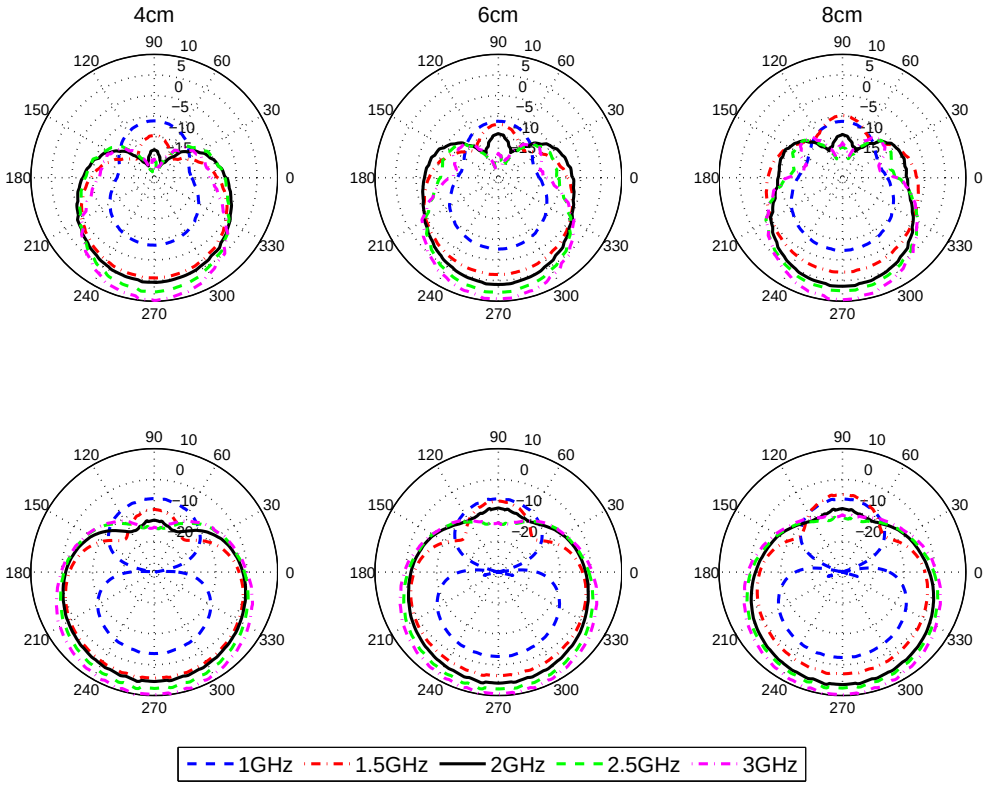

Figure 6.4 – Radiation pattern (d=25cm) for different box heights and frequencies=1, 1.5, 2, 2.5 and 3Ghz, E-plane (top), H-plane (bottom).

domain characteristic of the antennas that are irrelevant for our analysis. Therefore, from now on this parameter is fixed at the intermediate value of 60° and will not be further investigated in the next simulations.

6.4.2 The Antenna Shielding

In this section we add a rectangular shielding enclosure to our 2 bow-tie antenna model. The dimensions of this metallic casing are 8cm long and 4cm wide and for the height we have tested different values varying from 2cm to 10cm. We have also considered five frequencies within the bandwidth of interest. As it can be appreciated in Fig. 6.4, the presence of the shielding has a noticeable effect on the radiation characteristics in both E- and H-plane. The corresponding radiation patterns are no more symmetric and the energy is efficiently directed downwards for all the antenna heights and frequencies considered except for the 1GHz case. This is because the associated wavelength is much bigger than the shielding height. Then, when increasing the distance to the shielding, the amount of energy radiated backwards starts to decrease and the forward directivity gets better. Besides, the radiation patterns are narrower than for the unshielded case and therefore, in the standard acquisition mode, a shielded antenna illuminates a significantly smaller volume of the subsurface (higher directivity and gain) than the corresponding unshielded antenna, which also improves the horizontal resolution. When we look at the radiated

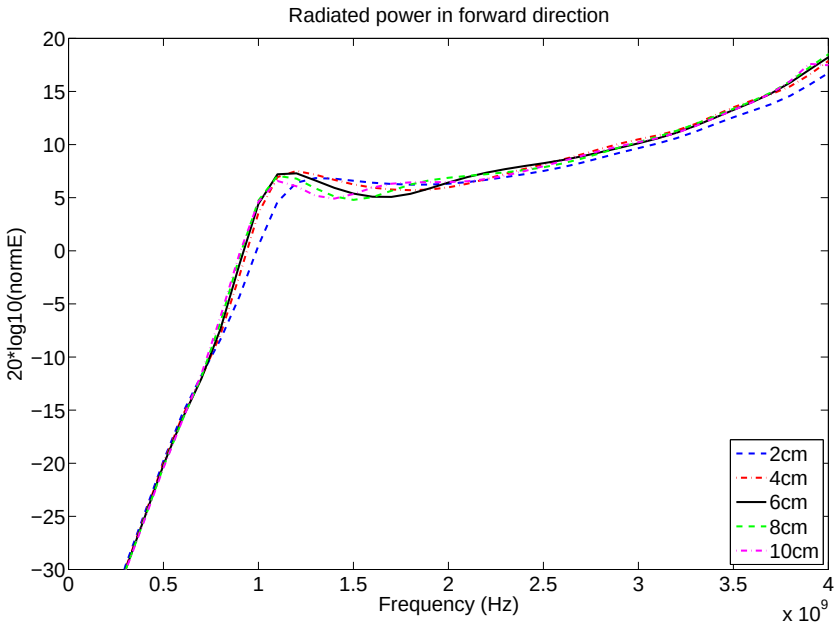

Figure 6.5 – Radiated power in forward direction (d=25cm) for different box heights.

power density diagrams displayed in Fig. 6.5, we observe that there is not a big change for the diverse heights. In general, shorter antenna casing heights tend to enhance the high frequency gain while greater ones enhance the low-frequency contribution. More precisely, we noted that for the shortest height (2cm), the bandwidth was slightly reduced but the rest of the simulated curves from 4cm to 10cm were very similar. Hence, a box height of 4cm is chosen for the following simulations.

6.4.3 The Absorbing Material

The presence of a shielding reflector produces signal reverberation (ringing) inside the box. A common solution to overcome the problem of antenna ringing is to fill the shielding box with absorbing material. Adding a dielectric absorbing material increases the antenna electrical size and gives rise to remarkable effects on the radiation patterns that need to be investigated and accounted for. In Fig. 6.6 and 6.7 we display the radiation patterns when we consider absorbing materials of relative permittivities 6, 8, 10 and 12 and conductivities taking the values of 0.2, 0.3 and 0.4S/m for each of them. In all the cases, the E-plane radiation patters are broadened substantially. By increasing the permittivity of the absorbing material, the ratio of lower to upper half-space maximum amplitude decreases, i.e., the antenna becomes less directive.
To better show the effect of the absorber ϵ_r and σ over the whole bandwidth, Fig. 6.8 illustrates the radiated power in forward direction for diverse absorber parameters. As expected from the analysis of the radiation patterns, the radiated power (and consequently, the gain) in forward direction decreases as the absorber permittivity rises. This trend holds true over the full frequency band. Moreover, the oscillations in the forward radiated power along the frequency band are softened for increasing conductivity, which favours the impedance matching. Due to this

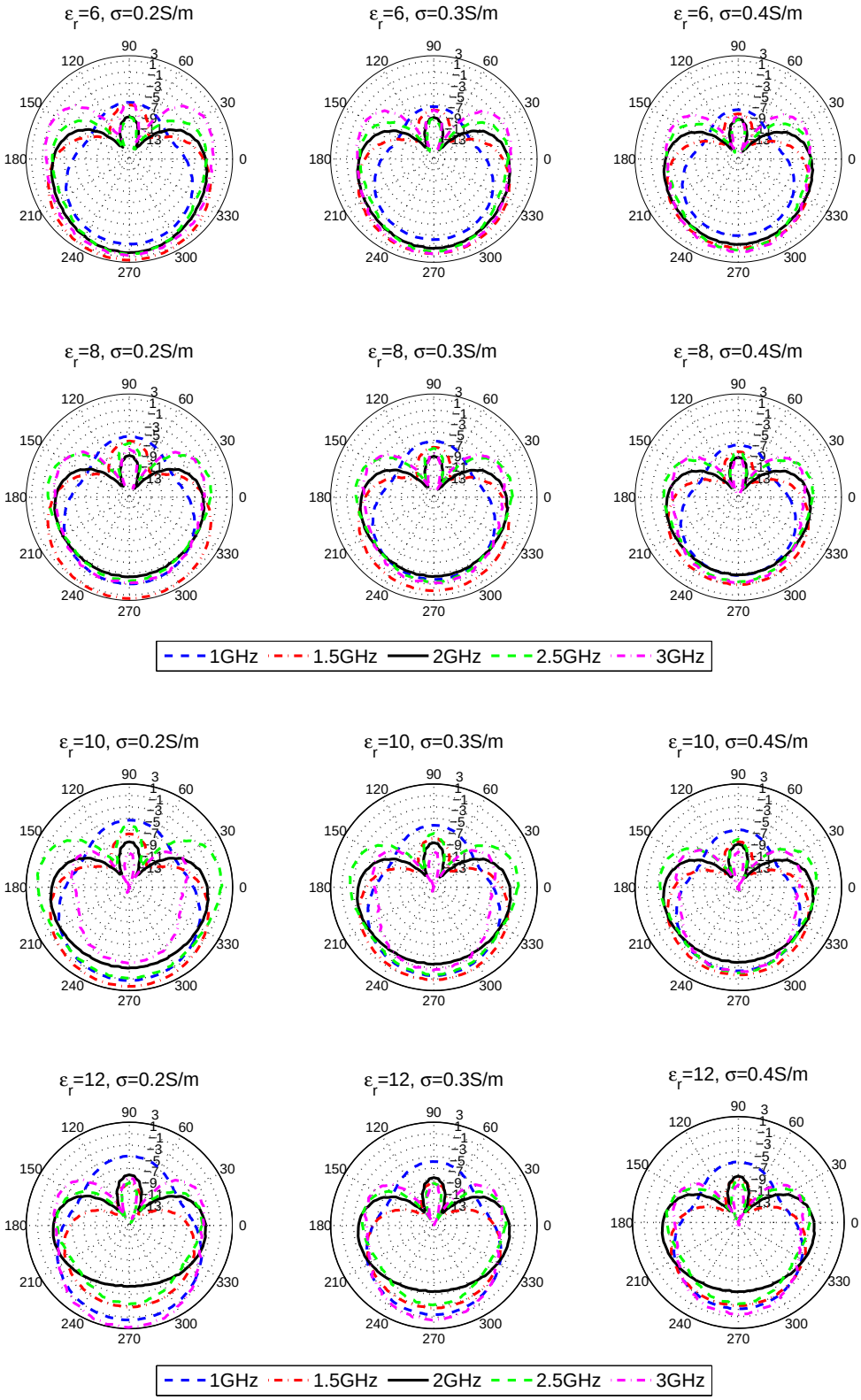

Figure 6.6 – Radiation pattern (d=25cm) in free space for variable ϵ_{box} and σ_{box}, E-plane.

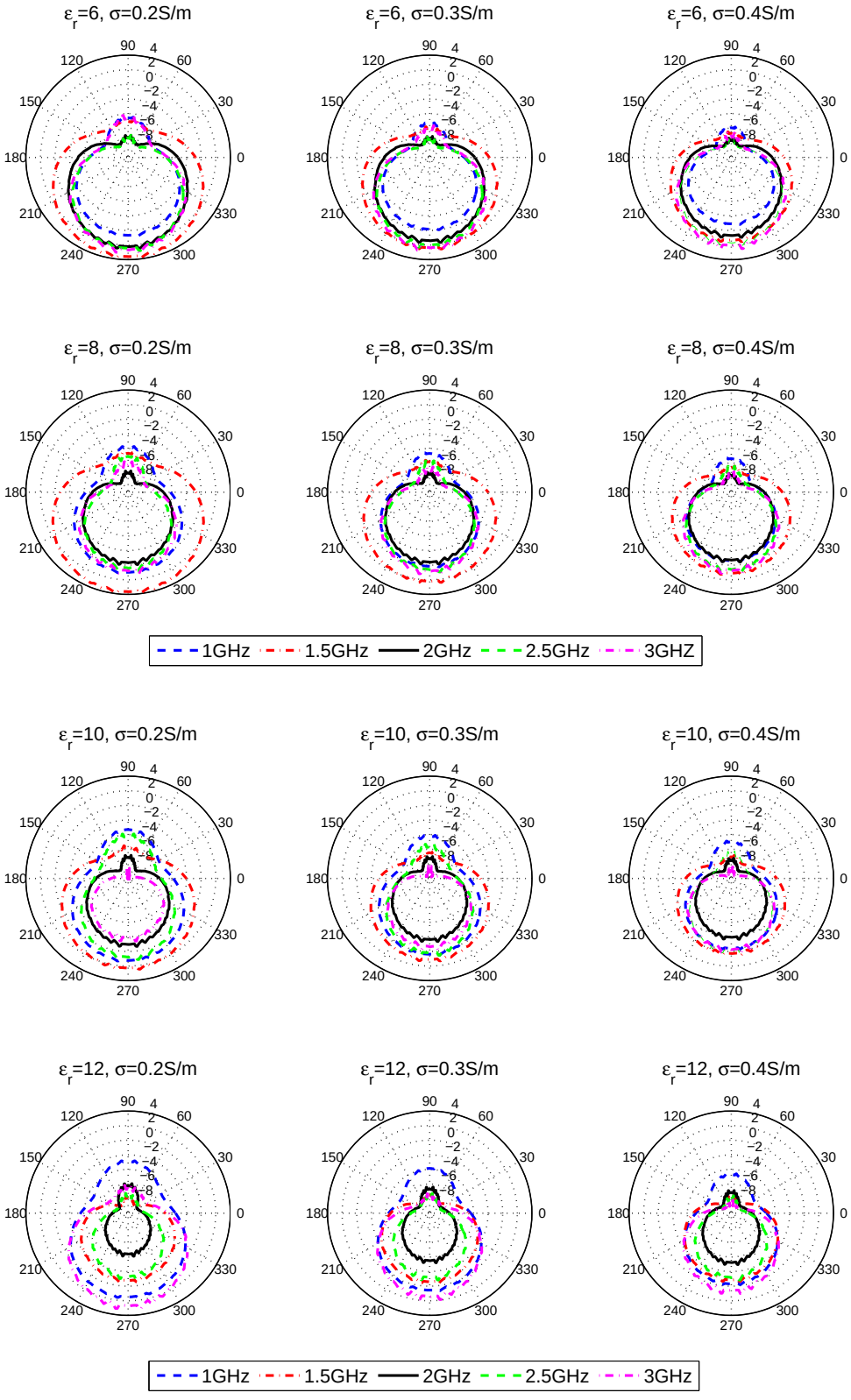

Figure 6.7 – Radiation pattern (d=25cm) in free space for variable ϵ_{box} and σ_{box}, H-plane.

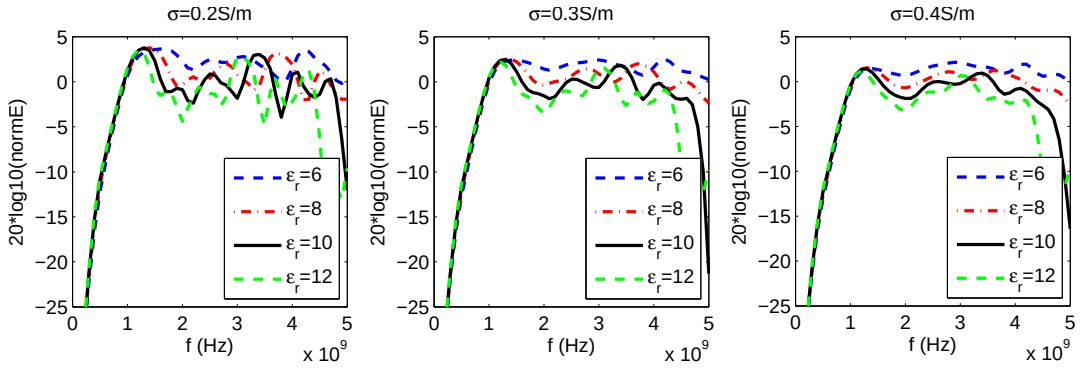

Figure 6.8 – Radiated power in forward direction (d=25cm) for variable absorber ϵ_{box} and σ_{box}.

reason, a high conductivity material would be in principle preferred to model the absorber of our commercial antenna. Figures 6.9 and 6.10 display the computed impedances for the different absorber parameters considered. From these results, we see that after a first peak, the real part of the impedance reaches a constant value which decreases with rising permittivity values. This behaviour can be roughly explained applying transmission line (TL) theory to estimate the input impedance at the open end of the shielding box.

A bulk absorbing material (no variation in the transverse plane, which means that the field depends on transverse components only through a transient factor) of permittivity ϵ_r and conductivity σ can be modeled with a transmission line as displayed in Fig. 6.11. One end of the transmission line is terminated in a load impedance Z_L, and the input impedance at the other end is for a lossy material [Pozar, 2005]:

$$Z_{in} = Z_0 \frac{Z_L + Z_0 \tanh(kd)}{Z_0 + Z_L \tanh(kd)}, \tag{6.4}$$

where k is the complex propagation constant defined in Eq. 4.25, Z_0 is the characteristic impedance of the absorber defined in Eq. 2.4 and d its thickness. If we assume a PEC shielding (short circuit, $Z_L = 0$), Eq. 6.4 is transformed into

$$Z_{in} = Z_0 \tanh(kd). \tag{6.5}$$

We have applied Eq. 6.5 (which is based on the model represented in 6.11) to estimate the input impedance for different absorber permittivity ϵ_r and thickness. The results are depicted in Fig. 6.12 and 6.13.

As we can see in these figures, the impedance values obtained applying TL theory are very close to the simulated ones showed in Fig. 6.9 and 6.10, which demonstrates that this can be an effective method for a first evaluation of the impedance behaviour of different absorber configurations (for example, the more complex case of a layered absorber) avoiding the performance of time consuming 3D simulations for every single setup. Nevertheless, in the measurement there is a peak at lower frequencies which is more pronounced for low conductivities and that cannot be explained by our simple model. This peak is most probably due to the influence of the lateral walls of the shielding box, which becomes more important for low frequencies and for the lower conductivities, i.e., lower attenuation values. Then, this behaviour is not present in Fig. 6.12

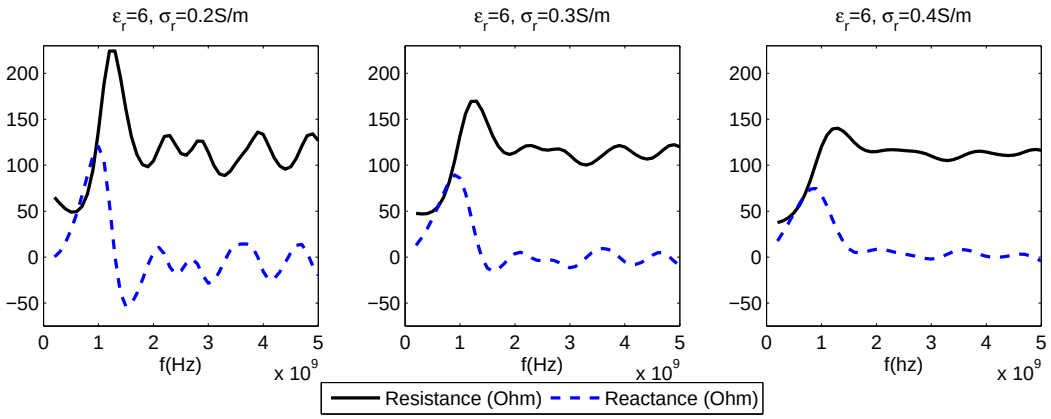

Figure 6.9 – Impedances for $\epsilon_{box} = 6$ and variable σ_{box}.

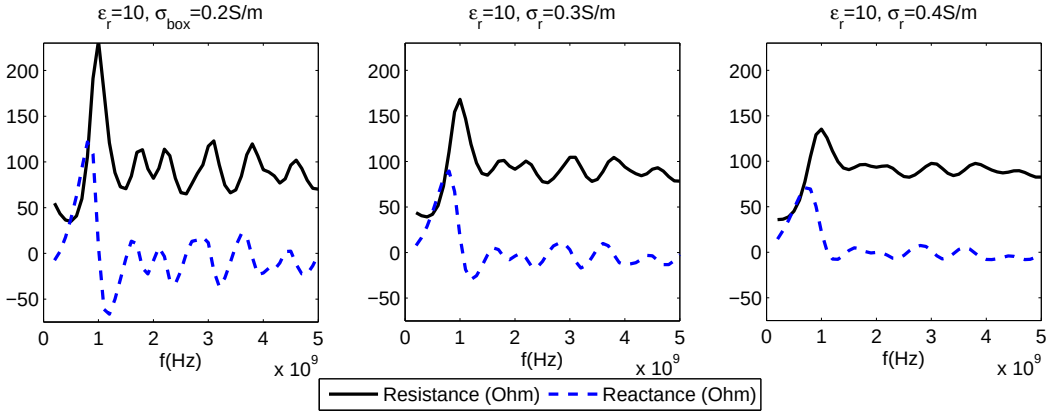

Figure 6.10 – Impedances for absorber $\epsilon_r = 10$ and variable σ_r.

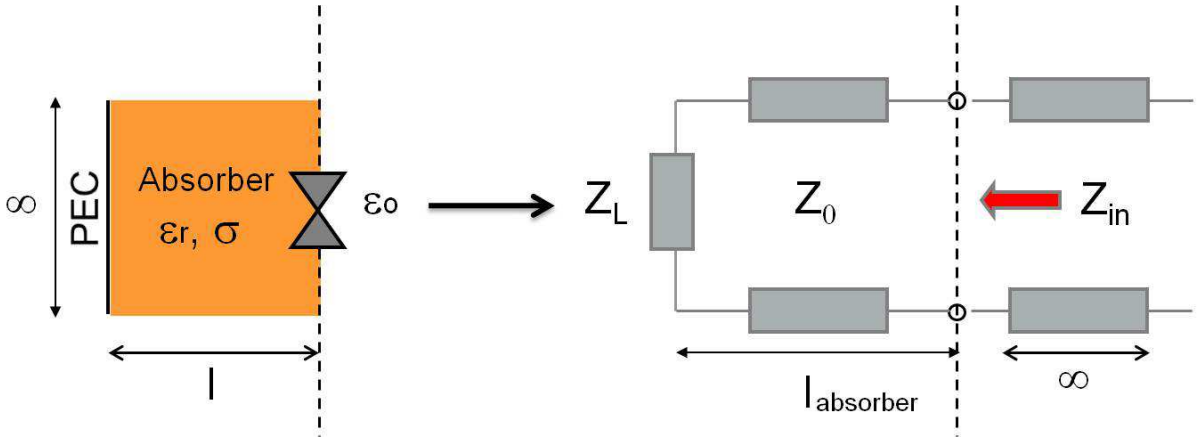

Figure 6.11 – Transmission line model of the antenna box.

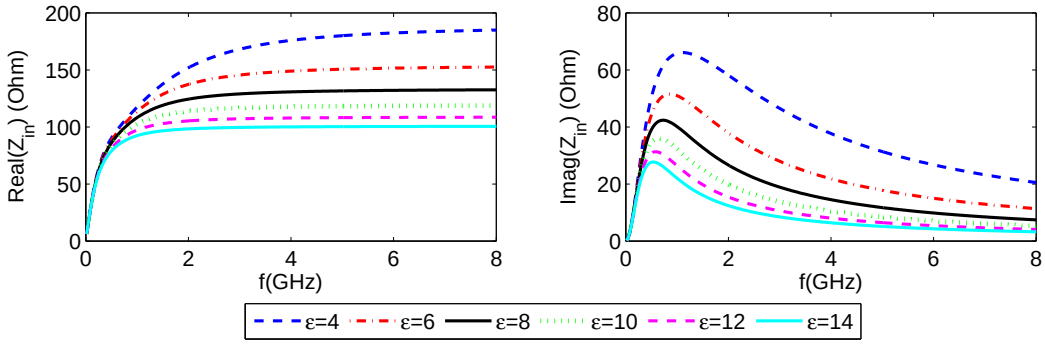

Figure 6.12 – Input impedance for different permittivities, $\sigma = 0.4S/m$.

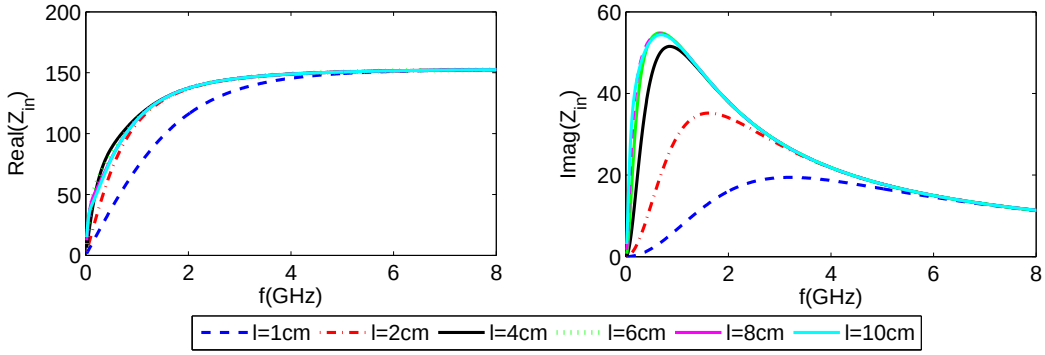

Figure 6.13 – Input impedance for different absorber thicknesses, $\epsilon = 6$, $\sigma = 0.4S/m$.

because in our model the transversal dimension has been considered infinite and this assumption is not true in the real case.

6.4.4 The Receiver

To investigate the effects of the nearby receiving antenna on the transmitted radiation pattern, we computed the responses of a model comprising a shielded transmitter bow-tie antenna with 60° flare angle and the corresponding receiver antenna juxtaposed in the perpendicular-broadside mode. The receiver antennas were placed 4cm apart from the transmitter antennas and we considered the three different cases already analyzed for the transmitter antenna alone in the previous sections: the bow-ties without any casing, and the bow-ties with empty and absorber filled metallic casing. The radiation patterns (Fig. 6.14) reveal that the receiver antennas have only minor impact on the energy transmitted into the subsurface for all the three cases. Nevertheless, the effect of the receiver is evident in the H-plane where the radiation pattern appears clearly biased to the right side. This happens due to the asymmetry of the arrangement and the presence of the shielded receiver on the left side of the transmitter.

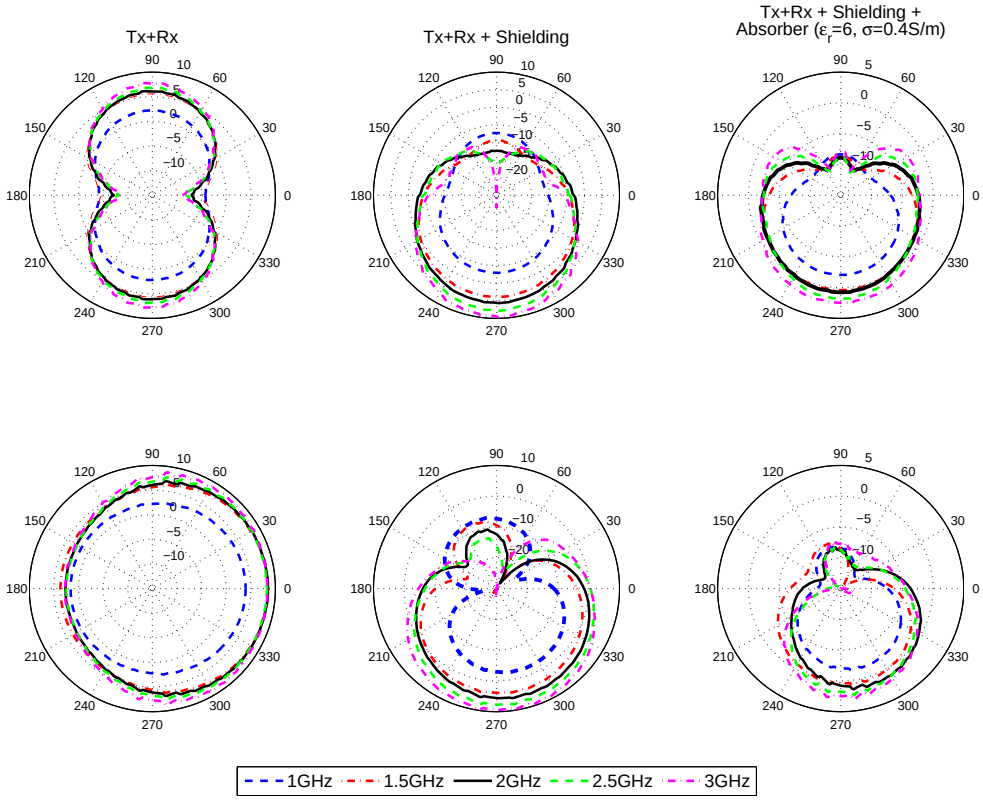

Figure 6.14 – Radiation pattern in free space (d=25cm) of two bow-ties alone, with shielding box and with absorbed filled shielding box, E-plane (top) and H-plane (bottom).

6.5 Soil Influence

When the antennas are located near the surface, the antenna current distribution and consequently the radiation pattern are significantly affected. It is known, that the medium generally acts as a low pass filter modifying the spectrum of the transmitted signal as a function of its electromagnetic properties. Additionally, if the medium is dissipative, an exponential damping reduces rapidly the field intensity limiting drastically the wave penetrating depth. Hence, it is very important that ground-coupled antennas maximize the power radiated into the material medium, and in particular, that they concentrate the electromagnetic field in the forward direction (in our case defined at polar angles near $\theta = 270°$). The investigation of the radiation behaviour for different soil types and antenna elevations becomes thereby of great interest to understand the antenna performance in a realistic situation.

6.5.1 Soil Parameters

In this section we explore the radiation characteristics of the antennas coupled directly into a dielectric nonconductive medium surface (antenna height h=0cm). The GPR scene is modeled assuming no ground surface roughness and three different media with permittivity $\epsilon_r = 4, 7, 10$ and conductivity $\sigma = 0.001, 0.01, 0.05 S/m$ respectively. These parameters are representative of dry, slightly wet (medium) and wet soil. First, and for comparison purposes, we display the E-plane and H-plane radiation patterns and the forward radiated power density corresponding to the dipoles alone and with shielding box. Figure 6.16 shows that with increasing soil permittivity, the resonance frequency is displaced to lower values. The important reduction of power amplitude related to wet soil is due to its higher conductivity (higher attenuation).
In Figures 6.17 and 6.18, we consider two antenna models with two different absorbers, displaying again the E-plane and H-plane radiation patterns for both cases. From these figures, we observe that for wetter soil, the radiation coupled into the ground is rapidly attenuated, in particular when the conductivity reaches 0.05S/m this effect becomes more prominent.
In general, the amount of energy transmitted to the soil will depend on the EM contrast between the antenna and the soil: when the permittivity of the soil is equal or very close to the permittivity of the absorber more energy will be coupled. This is an important issue to take into account when selecting an absorber material to design a GPR antenna. For instance, the dry sand present on the shallow subsurface has typically a permittivity equal to 4-5 and wetter sand can reach values between 8-10. If we consider this fact and the rest of the results derived from the simulations, a permittivity of 6-7 for the absorber material seems to achieve a good performance and it could be a good compromise. However, it still needs to be validated through time domain simulations.
Respect to the radiation distribution, we see that when the antennas are in contact with soil, there is a significant difference in comparison to the patterns of the same dipoles in free space. In E-plane, several lobes appear, and their intensity strongly depends on the frequency and soil/absorber contrast. As we can see for some cases there is a principal lobe in forward direction, for others the radiation is split into two intense lobes, and some other times there may be three

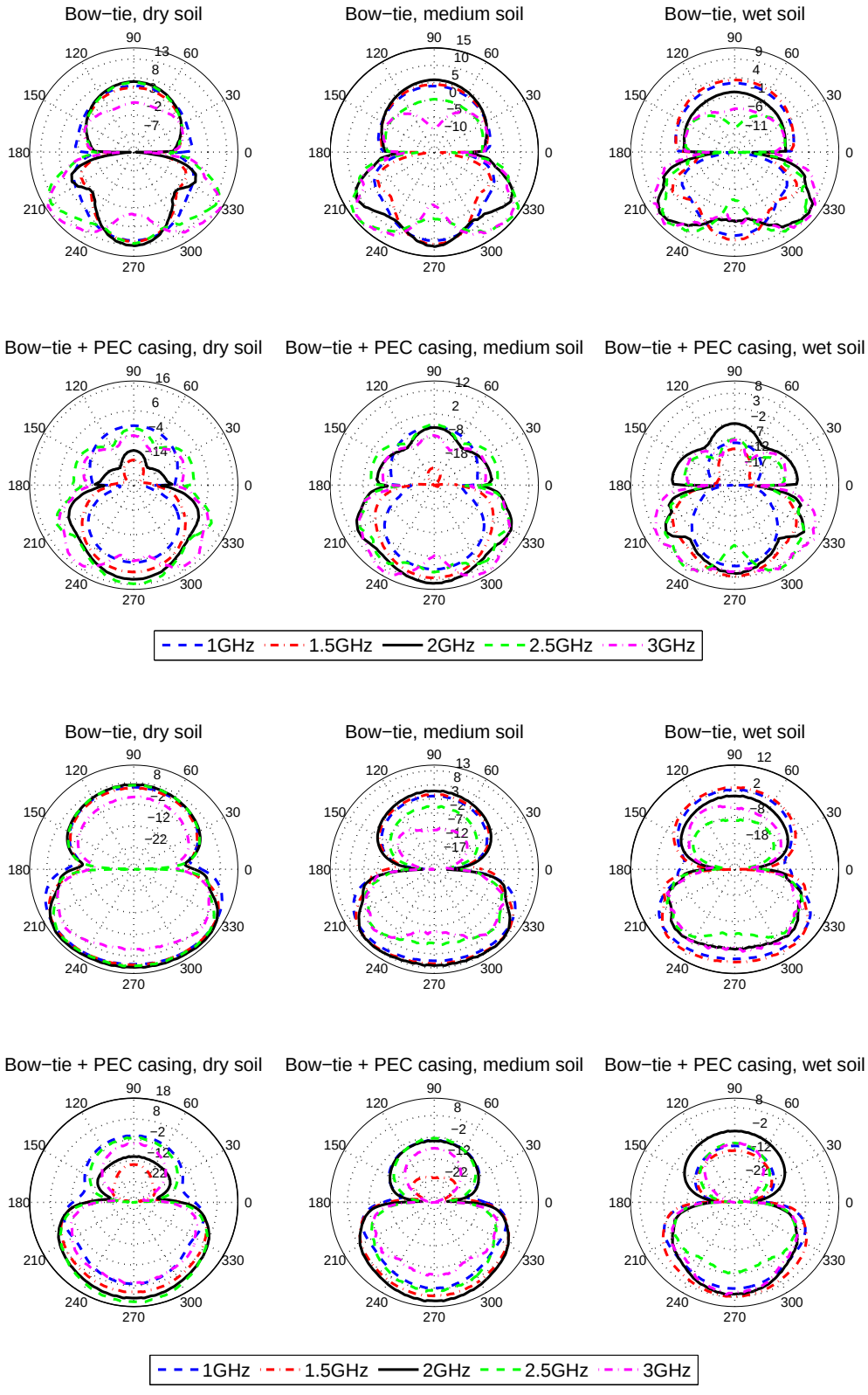

Figure 6.15 – Radiation patterns (d=20cm) in medium half-space of the bow-ties alone and enclosed in a PEC casing. Dry (left), medium (center) and wet soil (right), E-plane (half-top) and H-plane (half-bottom).

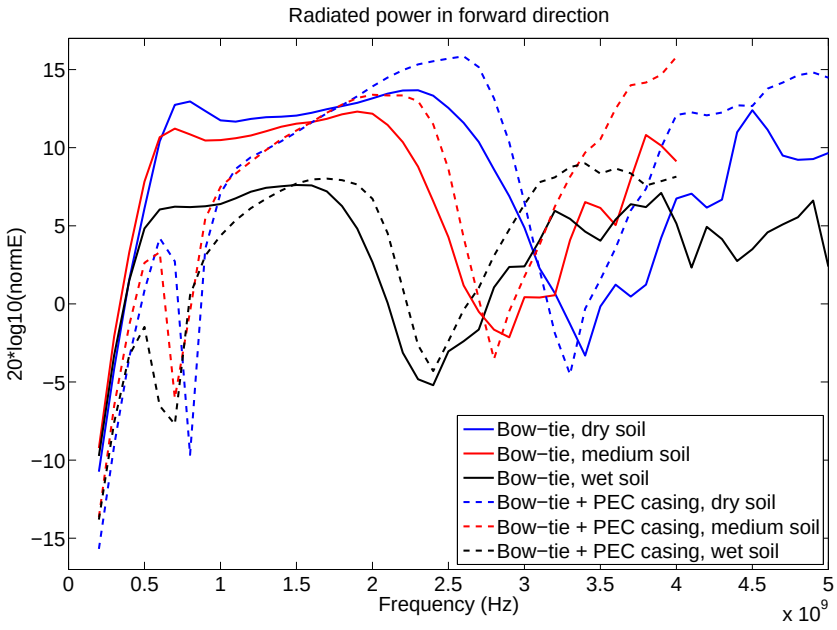

Figure 6.16 – Radiated power in forward direction (d=20cm) for of the bow-ties alone and enclosed in a PEC casing above different soils.

lobes, whose relative intensity change with frequency and soil, being not always the central lobe the main one. The H-plane patterns present differences as well but in general, they are more homogeneous and directive.
For convenience, in the next section the antenna impedance curves corresponding to the previous models will be also displayed and briefly commented too.

6.5.2 Antenna Height

The height of the antenna above the ground has little influence on the antenna input impedance. This is demonstrated in Fig. 6.19, where the input resistance and input reactance are plotted as functions of frequency for antenna heights of 1cm, 3cm and 6cm above 3 different soils together with the impedance when the antenna lies directly on the ground. Although the overall shapes of the curves are similar, the main peaks and troughs are shifted to lower frequencies when the antennas are placed on the surface, and the reason for this effect is that the antennas become electrically longer as they "sense" the higher permittivity and effective smaller wavelengths in the underlying half-space. Moreover, the maximum values of the input impedance curves are reduced due to the lower wave impedance of the soil in comparison to that of the free space. When they are elevated 1cm, 3cm or 6cm the curves are very similar to each other and also almost identical to their free-space analogs. The impact on the radiation pattern is on the other hand very important. As we can see in Fig. 6.20 and 6.21, when we increase the antenna height the amount of the energy that penetrates the soil decays drastically in all the cases, i.e., the coupling with the soil worsens, and the backward lobes become bigger. Nevertheless, when the antenna is slightly elevated (1-2cm for the frequency band used: 1-3GHz), the antenna directivity towards

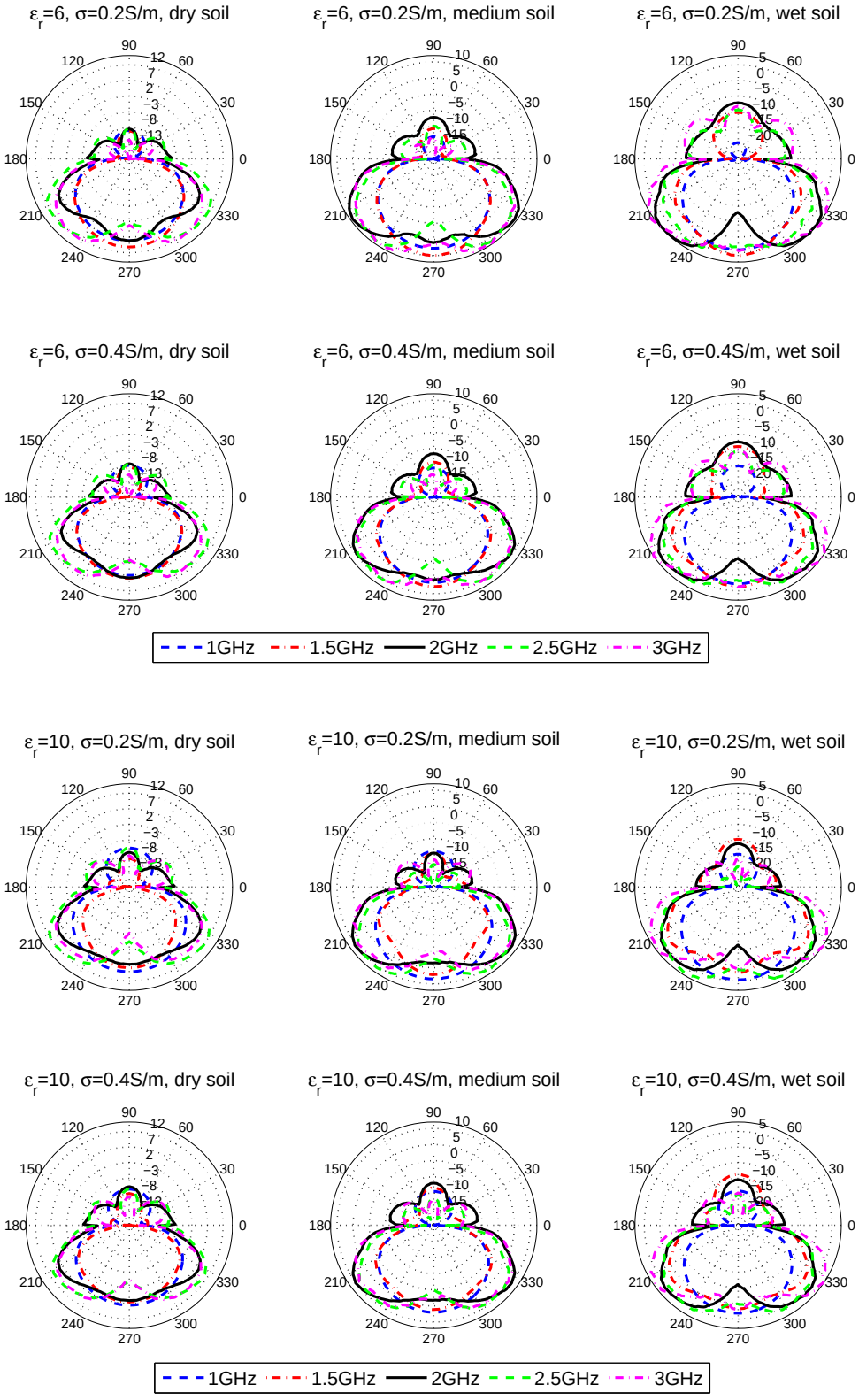

Figure 6.17 – Radiation pattern (d=20cm) in medium half-space for $\epsilon_{box} = 6, 10$, $\sigma_{box} = 0.2, 0.4 S/m$. Dry (left), medium (center) and wet soil (right), E-plane.

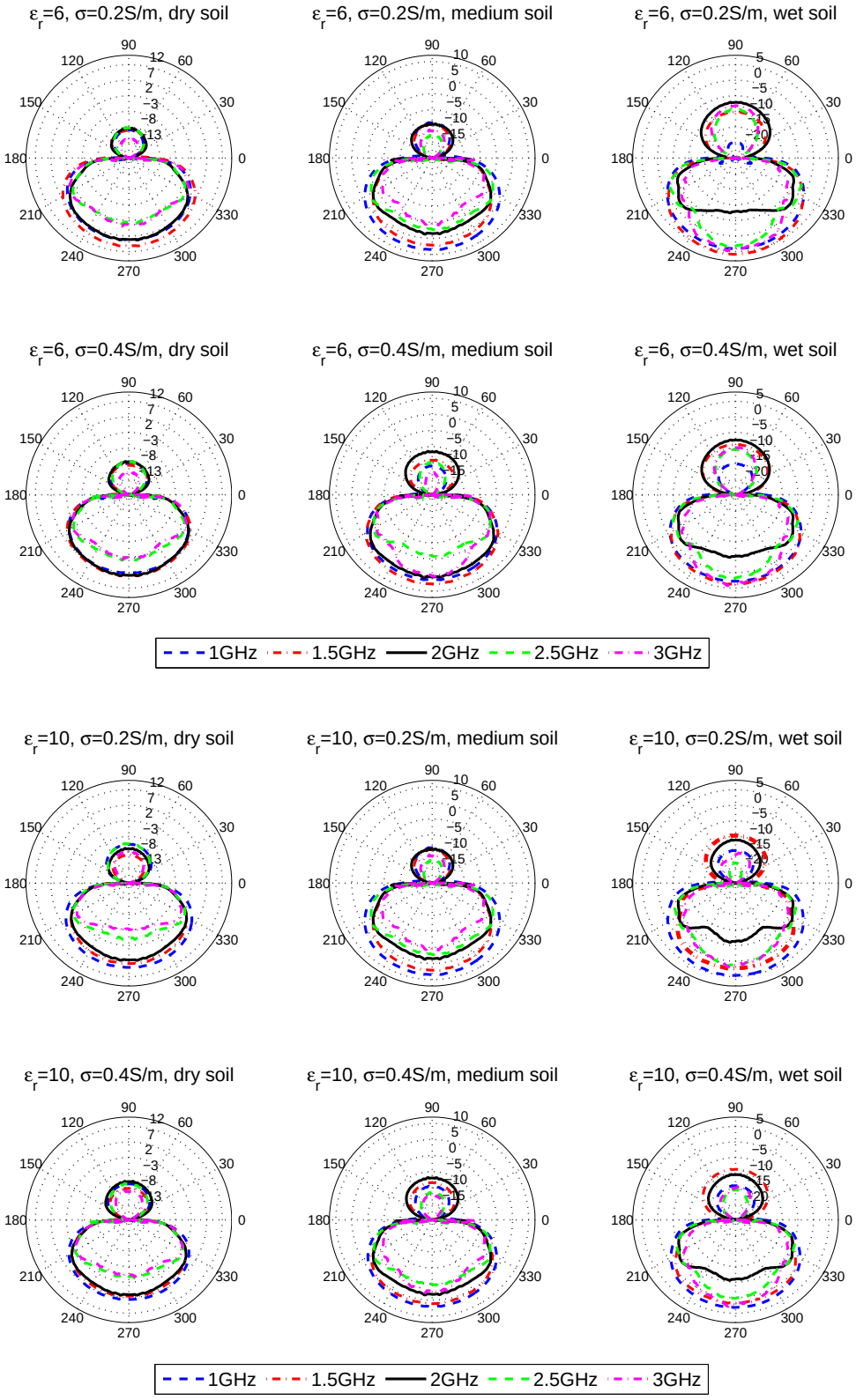

Figure 6.18 – Radiation pattern (d=20cm) in medium half-space for $\epsilon_{box} = 6, 10$, $\sigma_{box} = 0.2, 0.4 S/m$. Dry (left), medium (center) and wet soil (right), H-plane.

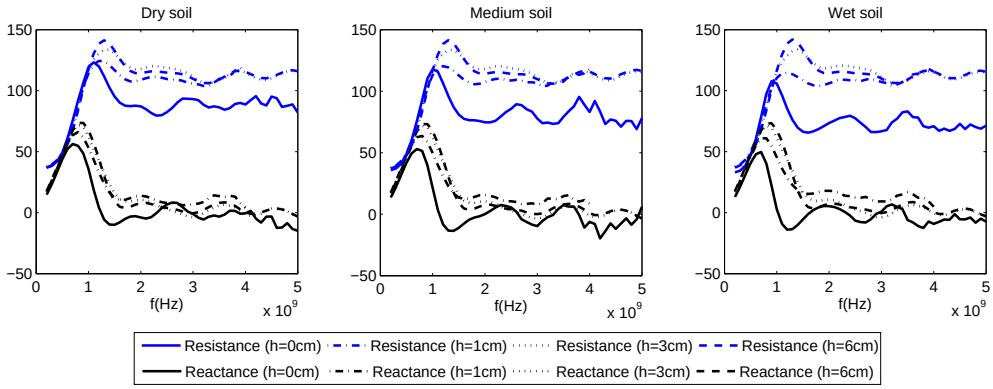

Figure 6.19 – Input impedance for different antenna heights and soil types.

the soil increases since the referred coupling is enhanced. This behaviour can be recognized when we compare the radiation patterns for elevated antennas (heights equal to 1, 3 and 6cm from left to right) displayed in figures 6.20 and 6.21 with the patterns corresponding to the antennas placed just above the soil (previously shown in figures 6.17 and 6.18).
When we look at the forward radiated power energy for different elevations (illustrated in Fig. 6.22) this effect becomes even more clear being the height of 1cm the most suitable one to get a high energy coupling and best matching (flat along the whole frequency band of interest) for all the investigated antenna setups. For elevations of 3cm or above less energy penetrates the soil and the bandwidth tends to reduce. Similar results were reported by [Smith, 1984] in the 80's, where after investigating the performance of a half-wave dipole located at different heights above a dielectric medium half-space, the elevation for the best coupling was estimated to be at $\lambda/10cm$, being λ the operating frequency of the dipole. These results confirm such conclusion, since for an antenna with a central frequency of 2GHz, the corresponding wavelength is equal to 15cm; hence, according to [Smith, 1984], an elevation of 1.5cm would be optimum for our impulse GPR system.

6.5.3 Interface Roughness

In the next and last simulations, the flat air-ground interface of the homogeneous half-space model is replaced by random topographic fluctuations described by a zero-mean normal distribution with a standard deviation of 0.5cm for the first scenario and 1cm for the second scenario and a correlation length equal to 3cm. We have considered dry and wet soil for both configurations. The resulting radiation patterns reveal distortions in both planes with respect to the reference patterns for the flat half-space. However, the overall shape is still approximately the same. The same effects due to the antenna elevation are visible here. Again the backward radiation lobe grows for wetter soil and the energy transmitted to the soil is notably reduced.
These scenarios represent just a couple of examples of more complex and realistic cases. The soil inhomogeneity could also be included in these models but, as we have seen in 2D case, the impact over the field distribution is in general less remarkable; then, we will not show more examples adding inhomogeneities in this thesis.

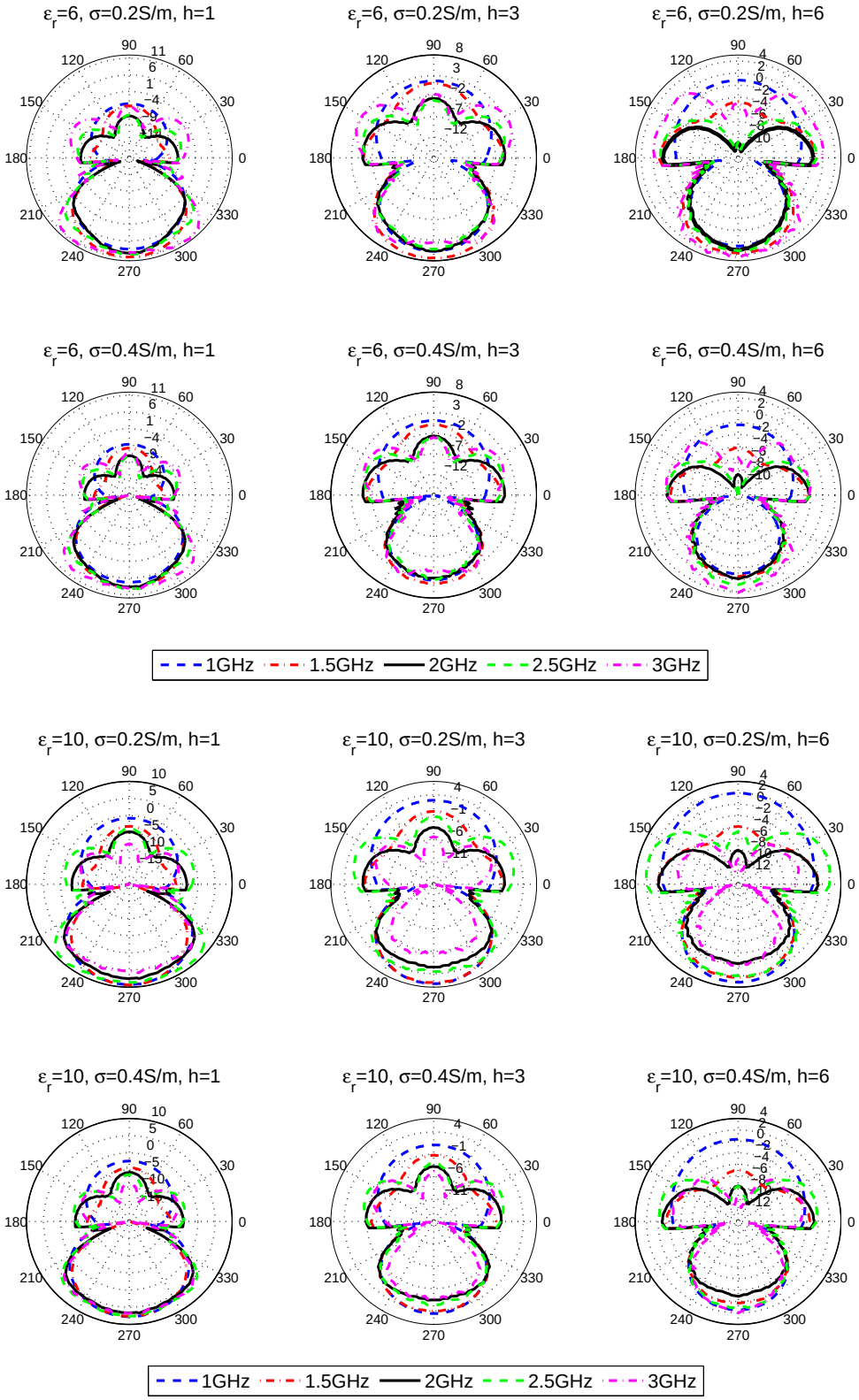

Figure 6.20 – Radiation pattern (d=20cm) in medium half-space for $\epsilon_{box} = 6, 10$, $\sigma_{box} = 0.2, 0.4 S/m$ and antenna heights h=1cm (left), h=3cm (center) and h=6cm (right), E-plane.

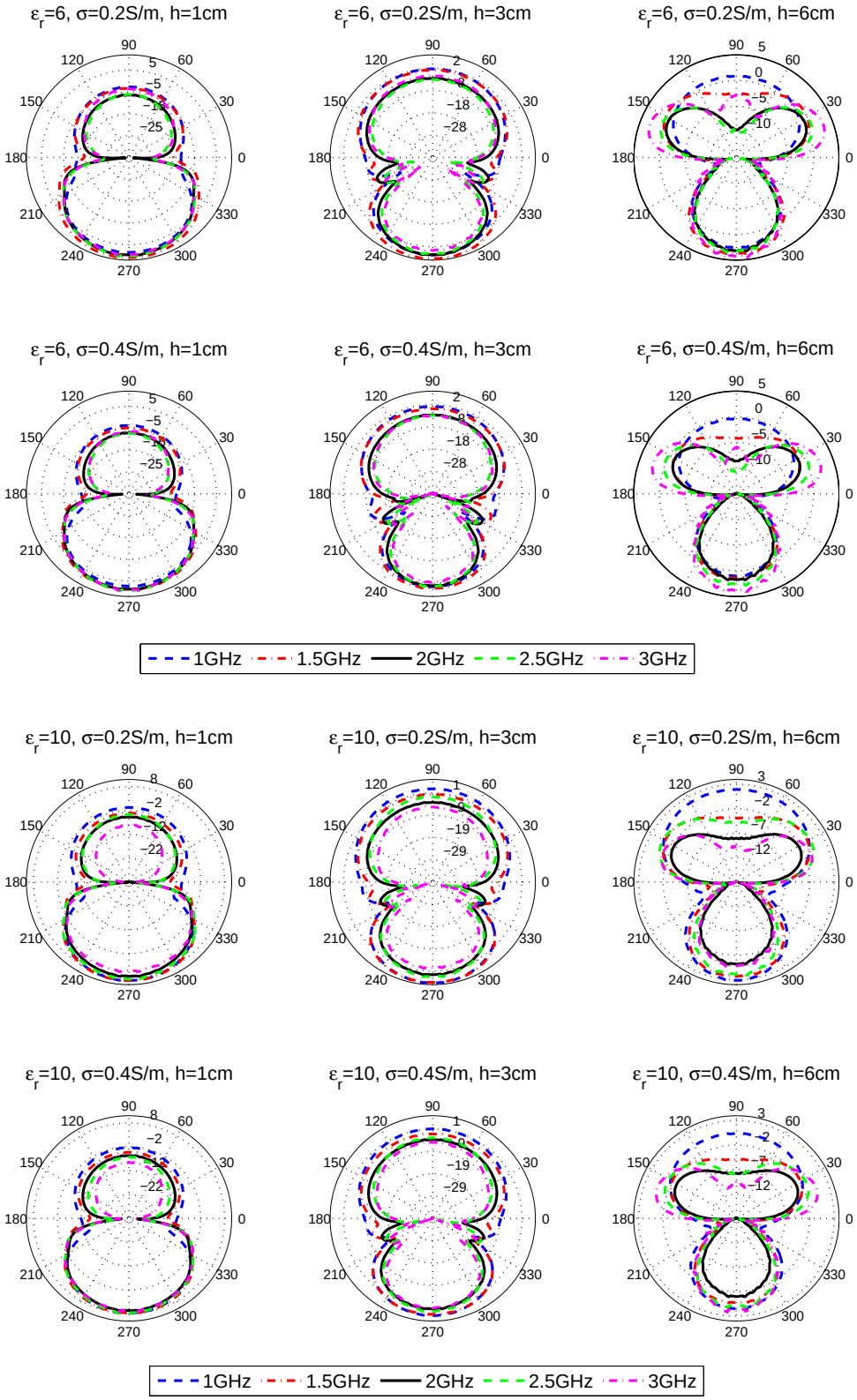

Figure 6.21 – Radiation pattern (d=20cm) in medium half-space for $\epsilon_{box} = 6, 10$, $\sigma_{box} = 0.2, 0.4 S/m$ and antenna heights h=1cm (left), h=3cm (center) and h=6cm (right), H-plane.

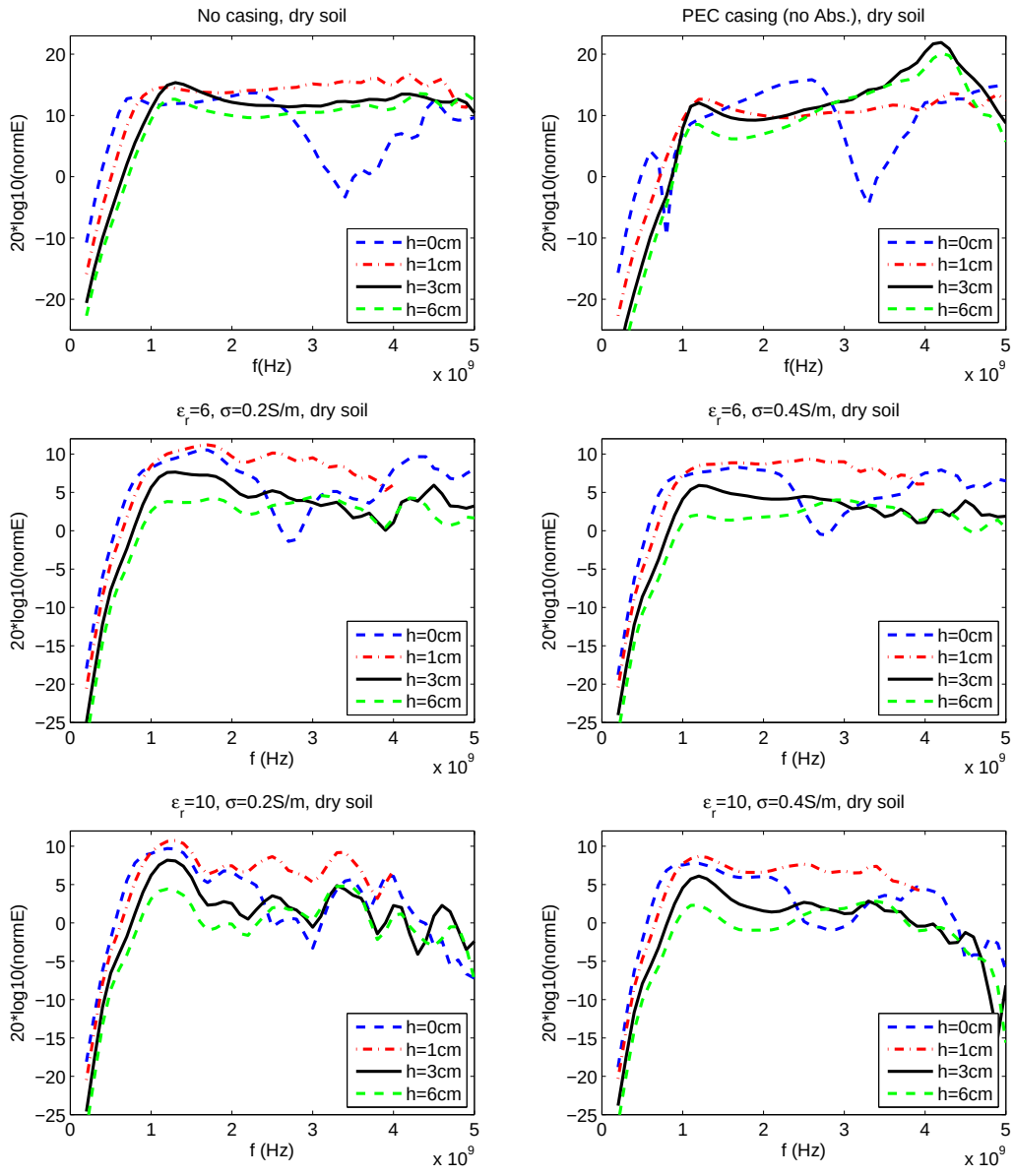

Figure 6.22 – Radiated power in forward direction (d=20cm) for different antenna elevations without PEC casing, with empty PEC casing and with PEC casing + absorber of $\epsilon_{box} = 6, 10$ and $\sigma_{box} = 0.2, 0.4 S/m$.

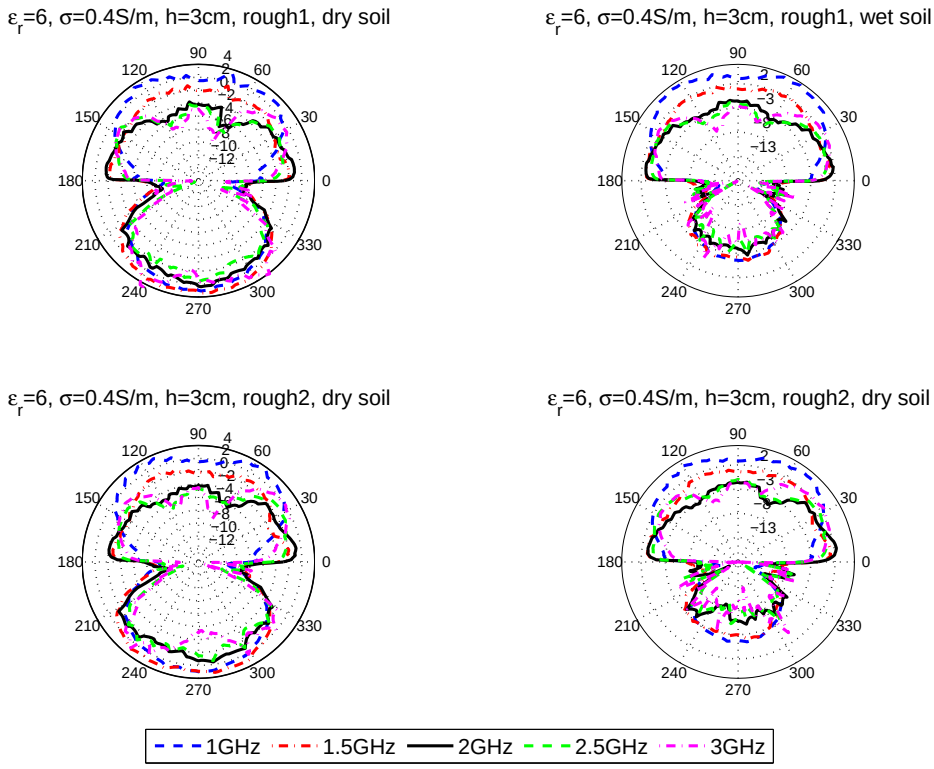

Figure 6.23 – Radiation pattern (d=20cm) in medium half-space with rough interface, E-plane.

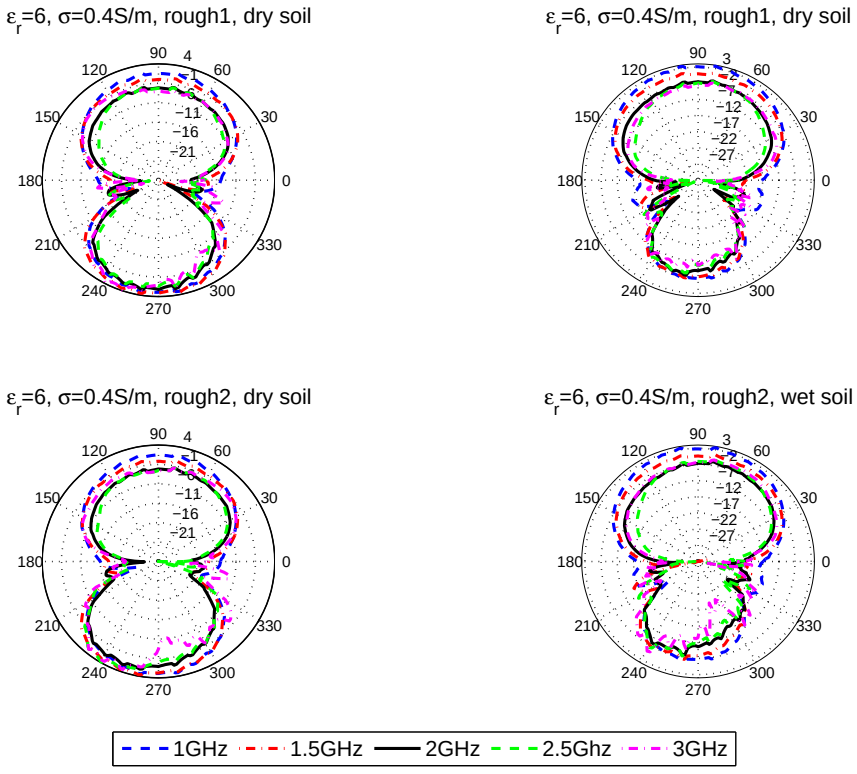

Figure 6.24 – Radiation pattern (d=20cm) in medium half-space with rough interface, H-plane.

7

GPR Antenna and Target Responses in Time Domain

There is nothing like looking, if you want to find something. You certainly usually find something, if you look, but it is not always quite the something you were after
J.R.R Tolkien

7.1 Time domain Characteristics of GPR antennas

In Chapter 6 we have investigated the frequency domain characteristic of several antenna configurations in order to obtain a better understanding of the radiation behaviour of a GPR antenna and the influence of different parameters on its performance. The gained knowledge may be useful to build an appropriate model to represent the antenna. However, when UWB systems directly radiate fast transient pulses rather than employing a continuous wave carrier, the effect of the antenna on the transmitted waveform becomes a critical issue and typical frequency dependent parameters such as radiation pattern and gain get less meaning. Moreover, these parameters need to be described over the whole frequency band, thus becoming less convenient to characterize UWB time domain systems. On the other hand, parameters like ringing, received signal amplitude, impulse response duration, etc. get more important. A good time domain performance for the specific application, which means producing good quality raw data before processing, is a primary requirement of an UWB antenna.
In general every time-invariant linear system is completely described in the time domain by its Impulse Response $h(t)$, which mathematically relates the input signal $x(t)$ to the output $y(t)$ of the system by a convolutional integral that can be expressed by the convolution operator $\otimes$:

$$y(t) = h(t) \otimes x(t). \tag{7.1}$$

In frequency domain this relationship is given by the Fourier transform; the convolution becomes then a multiplication and the impulse response the so called transfer function.
The impulse response of a given system will result of the combined contribution of the radar electronics (pulse generator, receiver, digitizer, etc.), the antennas and the shallow soil. The need to use separate transmit and receive antennas causes a convolution of both radiation patterns and the effective waveform recorded is dependent of the characteristics of both dipoles, not only the transmitter. The soil has to be included in the response because, as we have seen for ground-coupled antennas, the antenna response changes as a function of the properties of the soil in the antennas's reactive near-field region. The referred combined system response can be either approximated analytically [Scheers, 2001] or estimated via numerical simulation, being the latter the selected procedure for this investigation.
Since the purpose of this study is to obtain highly precise target signatures, we need to introduce a realistic target illumination in the simulations as well as an accurate model of the entire GPR scenario. This is accomplished in the first part of the chapter through the design and optimization of a GPR antenna model which must exhibit analogous time domain response to the measured one. Once an adequate model for the antenna is defined, the second part is devoted to the analysis of the target response for different system and environmental parameters.

7.1.1 Definition of source pulses

The gaussian and the monocycle (which is given by the first derivative of the Gaussian function) are naturally wide bandwidth signals, with the center frequency and the bandwidth completely dependent of the pulse's width. In practice, the center frequency of the pulse f_c is approximately the reciprocal of the pulse's length and the bandwidth is approximately equal to the center frequency. Thus, for a 0.5ns pulse width, the center frequency and the half power bandwidth (shown with red dashed lines in Fig. 7.1) are approximately 2GHz. In time domain, these pulses are mathematically described as follows:

$$V(t, fc, A) = Ae^{-2[\pi f_c(t-\tau)]^2} \tag{7.2}$$

$$V(t, fc, A) = 2\sqrt{e}\pi f_c A(t-\tau)e^{-2[\pi f_c(t-\tau)]^2} \tag{7.3}$$

where A determines the peak amplitude and $\tau = 1/f_c$.
Then, to simulate the real system the transmitter port is excited using 0.5ns gaussian and monocycle pulses. Figure 7.1 shows both pulses in time and frequency domain after normalization. These pulses are the most common waveforms considered in literature to simulate the feed of impulse GPR antennas. Here the power spectral density (PSD) describes how the power of the signal is distributed with frequency.

7.1.2 Optimization of the GPR Model

In order to choose a particular model to accurately represent the real antenna, we carry out a parametric study of diverse antenna features that play a role on its time domain response. In

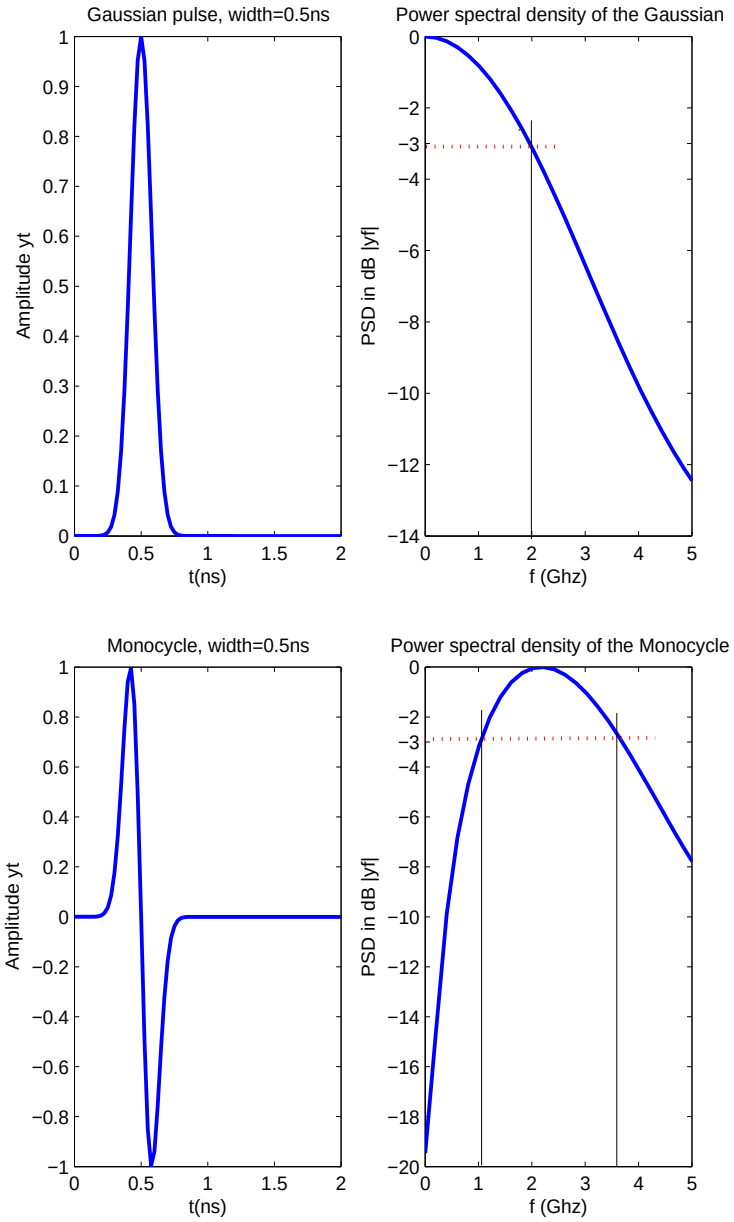

Figure 7.1 – Applied source pulses in time and frequency domain.

particular, we analyze the impact of those parameters on the simulated crosstalk (direct signal between antennas recorded at the receiver) which is an indication of the system impulse response for every configuration. The simulations in this section are carried out in free space, since we pretend to optimize the model by direct comparison with laboratory measurements. The resulting crosstalks are all normalized to the maximum signal amplitude for each figure.

Received Signal Waveform Before any other consideration we display below the actual crosstalk between transmitter and receiver recorded by our commercial GPR system without applying any preprocessing (see Fig. 7.2).

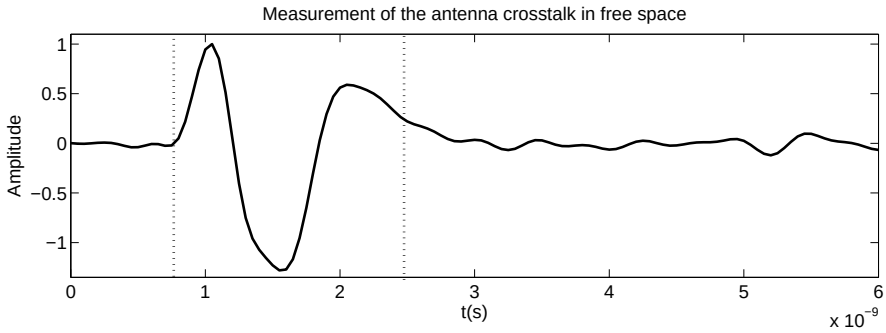

Figure 7.2 – Measurement of the antenna crosstalk in laboratory.

In the next sections, we attempt to find a two bow-tie model which produces a crosstalk response as close as possible to the measured one (in width and shape) and which fits the system's physical dimensions. At the same time this model should meet the antenna specifications (antenna type and overall geometry, bandwidth, source pulse length) and demonstrate a good performance according to the previous analysis in frequency domain. We accomplish this investigation in a parametric way.

Antenna Flare Angle

First, we explore the influence of the antenna flare angle over the crosstalk. To do it, we initially consider both bow-ties alone, transmitter and receiver, without any shielding box in order to avoid adding other effects to the synthetic results. We perform the computation for 3 different flare angles which were already considered in the frequency domain analysis of Chapter 6. The bow-tie length is maintained constant and temporarily equal to 3.3cm from the antenna open end to the center. We feed the transmitter with a gaussian and a monocycle pulse as described in the section above. From the curves in Fig. 7.3 we can clearly infer that increasing the angle has a positive effect on the impulse response. More precisely, the ringing amplitude decreases respect to the crosstalk amplitude for increasing flare angles. The width of the crosstalk also grows for bigger angles (since the lower frequencies are more efficiently radiated), getting closer to the measured crosstalk (Fig. 7.2), in particular when applying a gaussian pulse. However, it is still clearly narrower.

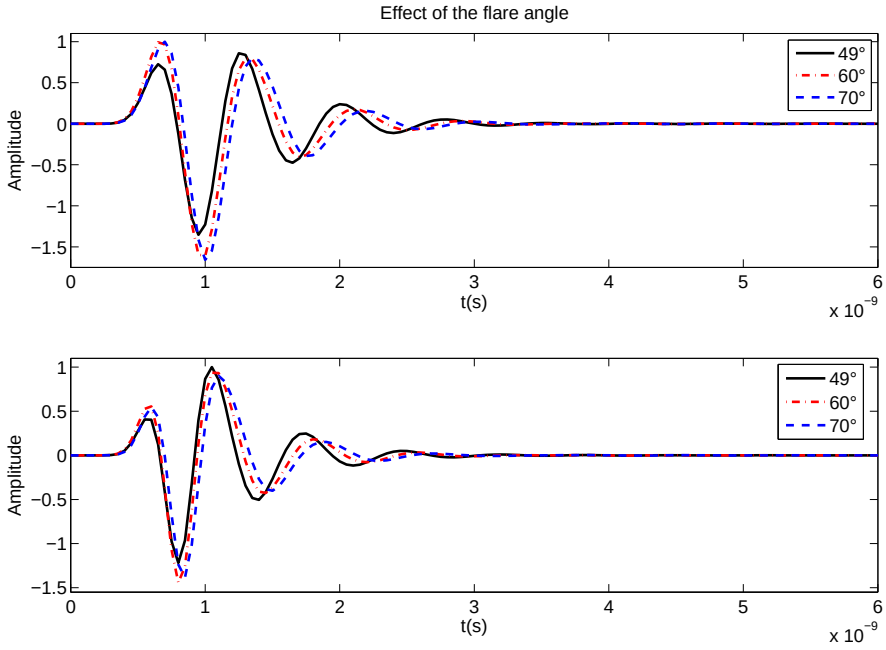

Figure 7.3 – Simulated crosstalks for different flare angles for a gaussian pulse (top) and a monocycle (bottom) pulse.

Antenna length

To conduct this calculation we maintain a constant flare angle equal to 60°. We have selected this value because we don't want to exceed the actual antenna physical dimensions when increasing the length; however, for the final model we may choose another angle. We observe that as the antenna becomes longer, the crosstalk amplitude grows and broadens (Fig. 7.4). This effect happens because a bigger antenna size is associated with lower frequencies, which is translated into a wider pulse. The shape of the pulse is also slightly modified but the ringing is not significantly affected with the size change.

Cable Impedance

We see that an increase of the impedance reduces the ringing. It also affects the crosstalk slightly, being the influence a bit more significant when the excitation at the feed port is a gaussian pulse (Fig. 7.5). This is probably because the impedance mismatch between the radiating element and the cable affects more to the frequencies below the antenna central frequency ($\sim$ 2GHz), and the gaussian contains stronger lower spectral components than the monocycle (Fig. 7.1).

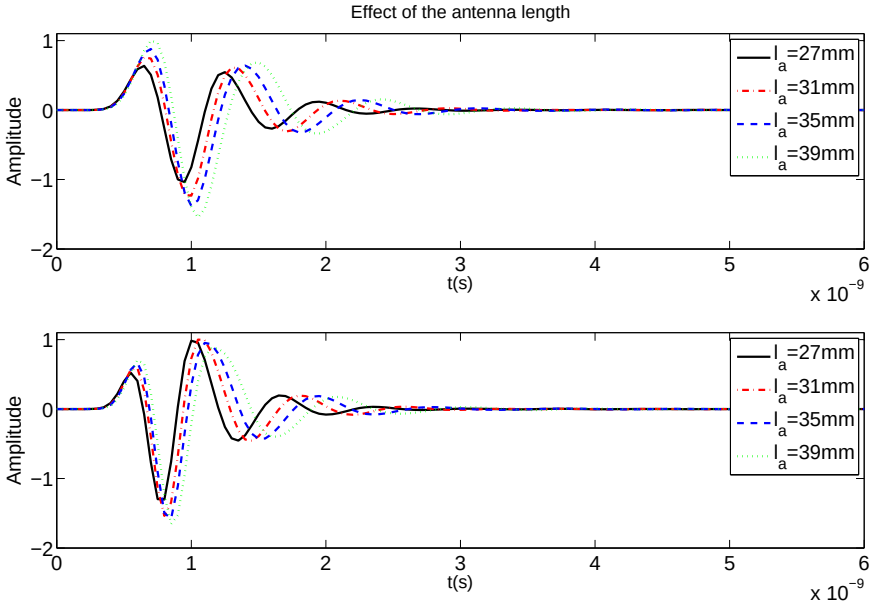

Figure 7.4 – Simulated crosstalks for different antenna lengths and constant flare angle for a gaussian pulse (top) and a monocycle (bottom) pulse.

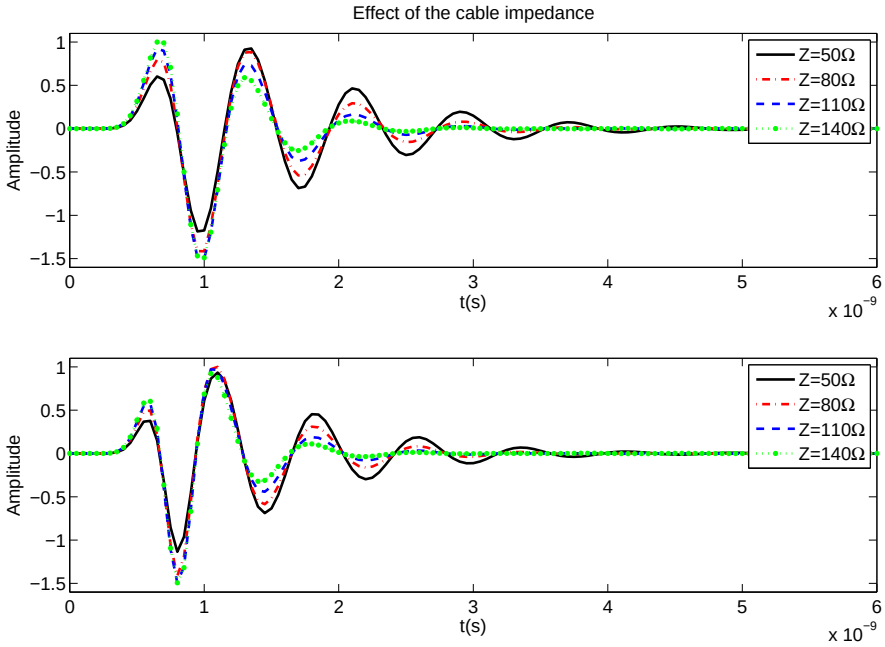

Figure 7.5 – Simulated crosstalks for different cable input impedances for a gaussian pulse (top) and a monocycle (bottom) pulse.

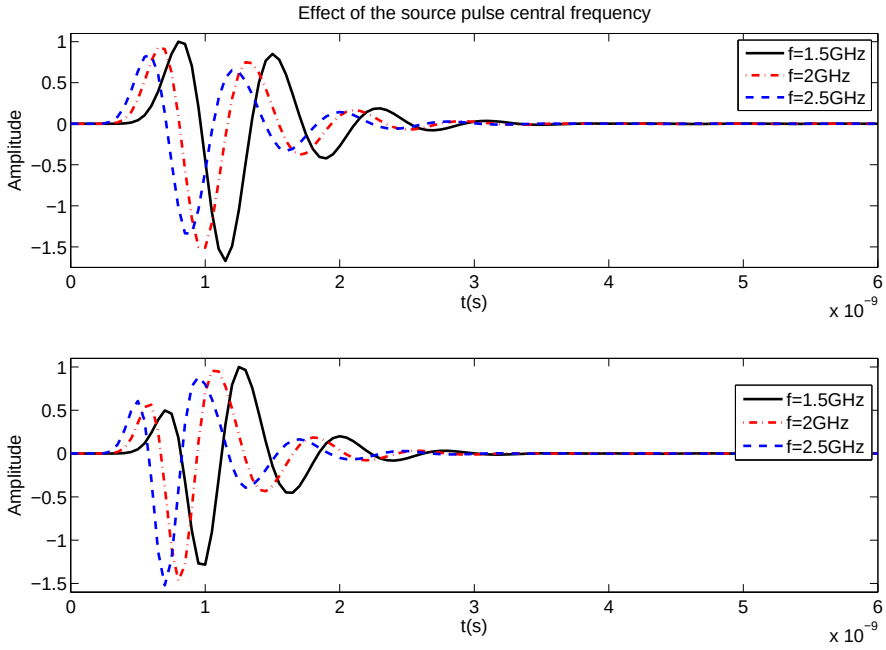

Figure 7.6 – Simulated crosstalks for a gaussian pulse (top) and a monocycle pulse (bottom) with different central frequencies.

Source Pulse Frequency

The effect of decreasing the source pulse central frequency is as expected to broaden the pulse width. The overall shape of the crosstalk does not change very much but the amplitude of the peaks changes with varying frequency, becoming larger for lower frequencies. On the other hand, late-time ringing remains at the same level respect to the peak amplitude for all the cases (Fig. 7.6).

Shielding Box

The addition of a a shielding box to the model has a positive effect since it isolates the antennas from other external radiation sources, reduces the direct coupling, and directs the radiated energy downwards. Hence, the presence of the shielding has a strong impact on the radiation pattern, which was already reported in Chapter 6.
In this section we illustrate the effect on the crosstalk when the shielding box size (height h, length l and width w) is varied. A sketch of the antenna model with the corresponding dimensions is shown in Fig. 7.7.

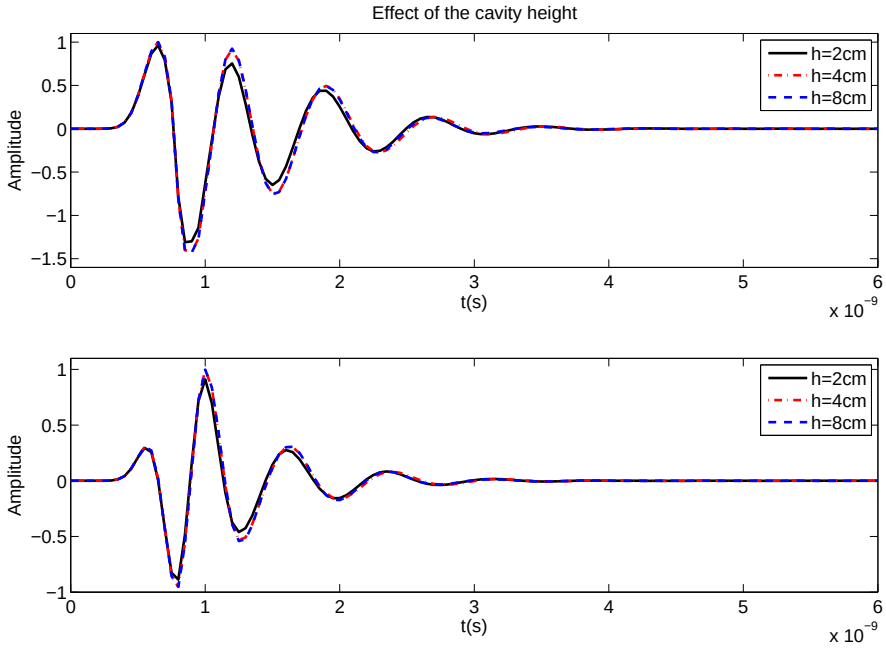

Figure 7.8 – Simulated crosstalks for different cavity heights for a gaussian pulse (top) and a monocycle (bottom) pulse.

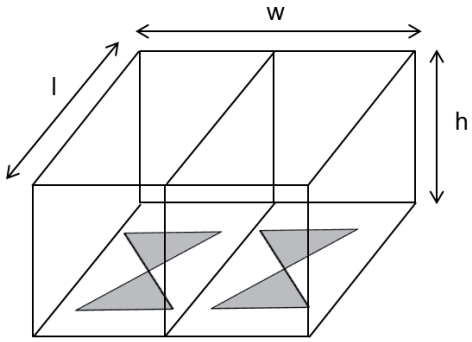

Figure 7.7 – Sketch of the antenna head with shielding box.

As expected we observe that in general the ringing with shielding box is clearly stronger than without box due to the reflections at the cavity walls (Fig. 7.8, Fig. 7.9 and Fig. 7.10). In Fig. 7.8, we can also see that the height variation does not influence significantly the pulse shape. Only in the case of 2cm box height we see a small difference, but for the other three values the crosstalk does not reveal any noticeable change. Therefore, we will assume a 4cm high box for the next simulations and the final model.

On the other hand, when we modify the cavity size in width (Fig. 7.9) and length (Fig. 7.10), we observe some changes in the pulse shape and amplitude. The variations are more significant for width than for length changes and follow an opposite trend: for increasing width the amplitude grows while for increasing length, the amplitude decreases. This behaviour is probably due to the omnidirectional pattern of the bow-tie, which predominantly radiates in the direction

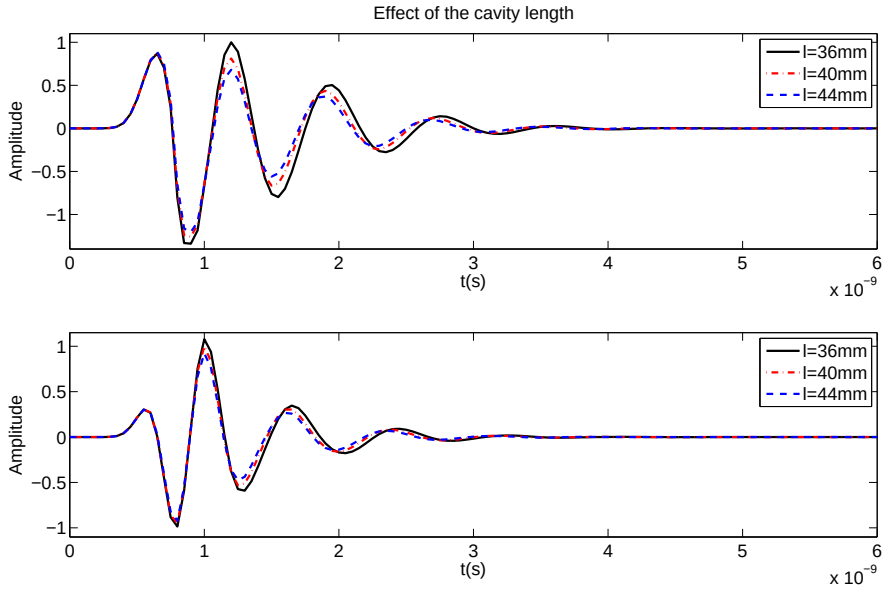

Figure 7.9 – Simulated crosstalks for different cavity lengths for a gaussian pulse (top) and a monocycle (bottom) pulse.

perpendicular to the polarization axis of the antenna. Moreover, it seems that the effect of the dimension change for both directions is stronger when the feeding pulse is gaussian. As expected we also observe from the figures that the ringing is clearly stronger than without shielding due to the reflections at the cavity walls.

Absorber

In order to reduce the ringing introduced by the metallic walls, we consider the effect of filling the shielding box with absorbing material. The high conductivity of this material will attenuate the waves reflected by the walls inside the box and hence, reduce the associated ringing. However, as we have seen in Chapter 6, the drawback of having such a high conductivity is a remarkable reduction of the antenna gain. In general, the value of the absorber conductivity will affect to the shape of the crosstalk, in particular changing significantly the ratio between the first and second peaks. Another effect of the absorber is to increase the electrical size of the antenna due to its permittivity different from that of free space; the consequence is a broadening of the crosstalk as the permittivity grows (Fig. 7.11 and Fig. 7.12).
We know that when the absorber parameters change, the antenna impedance will vary but in a real situation the impedance of the cable has a fix value. Therefore, for simplicity, we will assume a typical cable impedance of 50Ω in the next simulations.

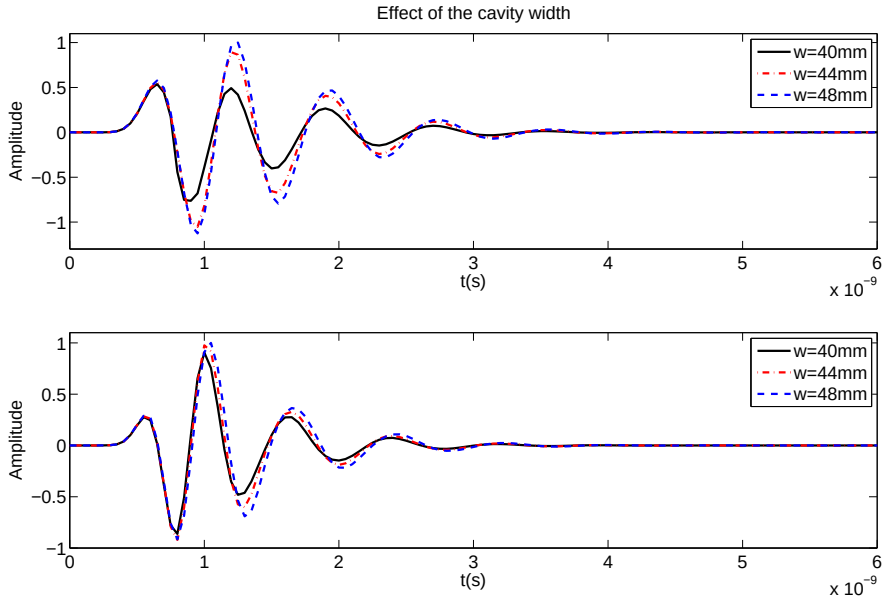

Figure 7.10 – Simulated crosstalks for different cavity widths for a gaussian pulse (top) and a monocycle (bottom) pulse.

The Optimized Model

After performing a comprehensive analysis to investigate the impact of various parameters on the crosstalk signal we are in the right position to choose the best antenna model to obtain realistic signatures of the different targets to be used for further processing.
Before presenting the final model, let's summarize the results obtained from the parametric study:

1. for increasing flare angle the crosstalk is lengthened and the clutter reduced,
2. for increasing size the amplitude grows slightly, the pulse is also widened and the clutter level stays almost constant,
3. an increase of the cable impedance reduces the ringing,
4. a decrease in the central frequency of the pulse broadens the crosstalk and increases the amplitude,
5. adding a shielding introduces more ringing,
6. changing the height of the metallic enclosure does neither affect significantly the pulse shape nor its amplitude,
7. modifying the length and particularly the width of the metallic enclosure has a slight effect in both, the amplitude and shape of the pulse,
8. and finally filling the metallic cavity with absorbing material eliminates the late-time ringing without introducing other artifacts and broadens the pulse the more with growing absorber permittivity.

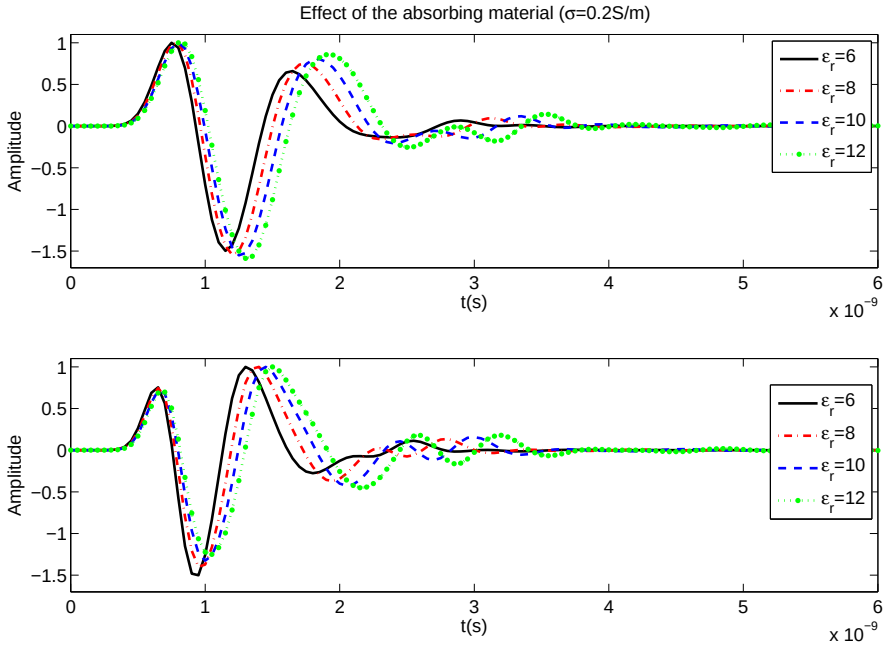

Figure 7.11 – Simulated crosstalks for different absorbing materials (ϵ_r variable and $\sigma = 0.2S/m$) for a gaussian pulse (top) and a monocycle (bottom) pulse.

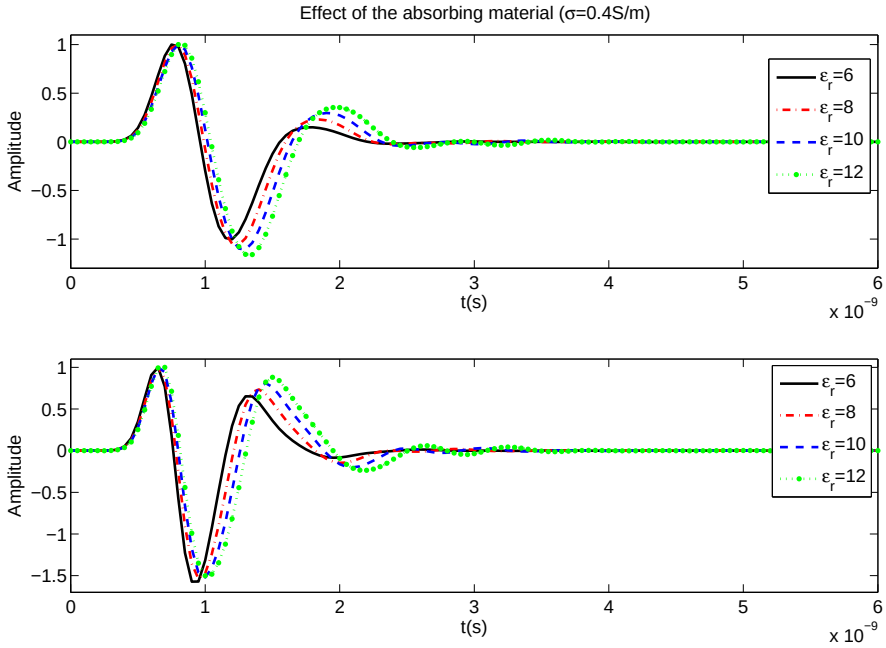

Figure 7.12 – Simulated crosstalks for different absorbing materials (ϵ_r variable and $\sigma = 0.4S/m$) for a gaussian pulse (top) and a monocycle (bottom) pulse.

Source Pulse	$\epsilon_{\mathbf{r}}^{\mathbf{abs}}$	$\sigma^{\mathbf{abs}}$ (S/m)	f_c (GHz)	bow-tie lxw (mm)	Box lxw (mm)
Gaussian	7.2	0.14	2	72.9x42.83	80.5x94.2
Monocycle	7.2	0.39	1.65	86.6x41.1	94.7x95.9

Table 7.1 – The parameters of the optimized models.

The optimized parameters for each of the models are summarized in the Table 7.12. It must be noted that these are not the only models possible, since other combinations of bow-tie dimensions/flare angle and absorber parameters may also produce a similar crosstalk. However, and based of the observed performance in frequency domain, we have selected a configuration with an absorber material of 'low' permittivity to have a better energy coupling into the soil, instead of for instance decreasing the antenna dimensions and increasing the absorber permittivity. The simulated crosstalks after optimization of the antenna model are compared with the measured crosstalk in Fig. 7.13.

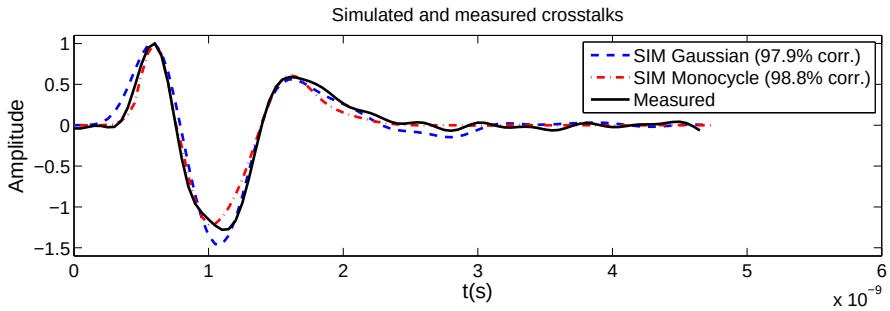

Figure 7.13 – Simulated crosstalks after optimization for Gaussian and Monocycle pulses compared with the measured crosstalk.

7.1.3 Field Distributions for Different Antenna Configurations

In this section we display some time snapshots of the electric field norm for several GPR antenna models (analyzed in the previous sections) above dry soil. More precisely, the soil beneath the dipoles has a permittivity of $\epsilon_r = 5$ and a conductivity of $\sigma = 0.001$S/m. The illustrations are in logarithmic scale (dB) and the field is represented along both planes, parallel (E-plane) and perpendicular (H-plane) to the bow-tie polarization direction.
Figures 7.14 and 7.15 show the temporal evolution in the case of transmitter and receiver side by side without any shielding in two situations: placed on the surface and at 6cm elevation respectively. The limits of the color scale are the same for all the snapshots to better recognize the temporal evolution of the energy distribution. Due to this, the space where the energy is out of the range of the scale is empty. The snapshots display spherical waves in the upper and lower half-space, being the wavelength in soil shorter and the propagation velocity slower than in air due to the higher permittivity. When comparing both situations we observe a clearly better energy coupling into the soil when the antennas are placed directly on the interface, i.e., more energy

penetrates the soil for surface laid antennas. Figures 7.16 and 7.17 represent the snapshots of the field when the antennas are shielded by a metallic enclosure without any absorber inside and again placed above the interface and 6cm high respectively. In these cases the radiation is efficiently focused in downward direction, being the fraction of energy radiated upwards notably lower and the directivity into the soil better than for the unshielded case. In particular, the energy coupling into the soil is larger when the antennas are located on the surface.
If we add an absorber ($\epsilon_r = 7.2, \sigma = 0.39 S/m$) less energy is radiated outside the enclosure due to the wave attenuation produced by the filling material. This attenuation avoids the signal reflected at the walls of the metallic shielding to be reradiated producing undesired ringing.
In Figures 7.18, 7.19 and 7.20 we compare different elevations (0cm, 2cm and 6cm) for this antenna model. As we can see, at 2cm the energy coupling into the soil is slightly worse than at 0cm, which is demonstrated not only by the amount of energy that penetrates the soil, but by the higher intensity of the reflected energy traveling in the upward direction. On the other hand, the directivity improves when the antennas are elevated 2cm or 6cm, confirming the expected results from the frequency domain simulations in Chapter 6.
Finally, and for comparison purposes, Fig. 7.21 exhibits the wave propagation for the same antenna model but this time with an absorber material of ϵ_r=10 (and the same σ as before). For this permittivity value, more energy is trapped within the casing and the radiation intensity towards the soil is less strong than for an absorber with an smaller permittivity. This is an already expected behaviour from the radiation patterns analysed in Chapter 6.
In all the cases with a shielding enclosure, we can also observe that while the field distribution in E-plane is totally symmetric, in H-plane it is clearly affected by the presence of the receiver antenna.

7.2 Target Scattering Analysis

The rest of this chapter is devoted to the investigation of the sensitivity of the target scattering signatures to the different parameters that configure a GPR environment. For this analysis we will consider the backscattered signal by a collection of objects: a plastic sphere, a metallic sphere (both of r=2.5cm), an empty cylinder, a water filled cylinder (r=4cm, l=30cm), two mine-like targets representative of the PMA2 and Type72 AP mines and two small plastic cylinders with the same dimensions as the two mine-like respectively but with no internal structure. One of the mine-like targets has an air-gap on the top and dielectric filling on the bottom and the other one is just full of dielectric material and has an small piece of metal in the middle (Fig. 7.22). These targets are located either in free space or buried a few centimeters in wet or dry soil and the antenna system is placed at few centimeters above the ground. In our simulations we vary the target dimensions, position and orientation as well as the antenna height. The cases with inhomogeneous soil and rough interface are also considered. This setup covers a broad and significant set of scenarios and we are able to analyze the influence of different antenna-target-soil parameters over the corresponding signatures.
The signatures illustrated in the following sections are normalized with respect to the maximum amplitude obtained for each configuration.

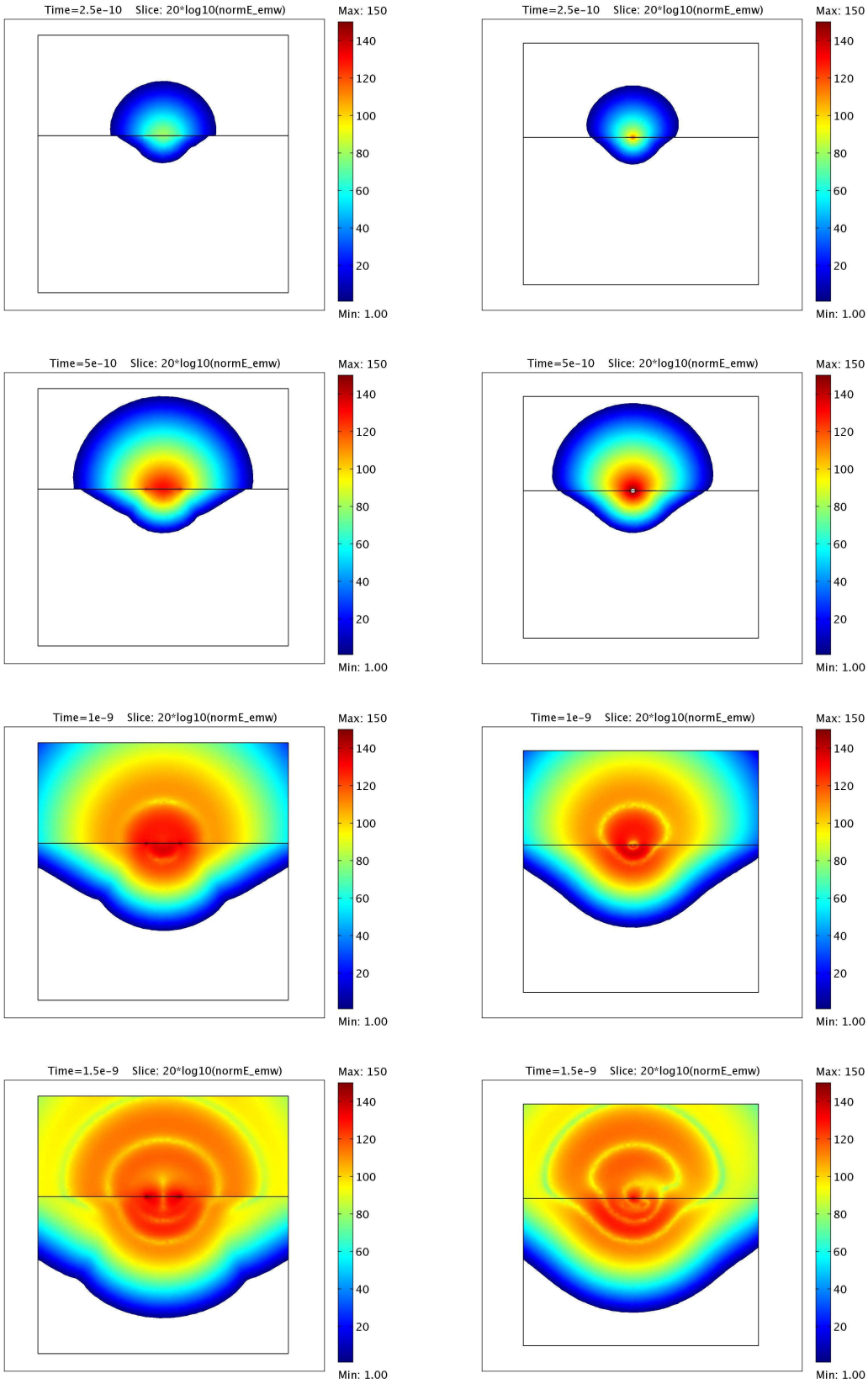

Figure 7.14 – Snapshots for Tx and Rx alone (without shielding and absorber) on the surface (dry soil), E-plane (left) and H-plane (right).

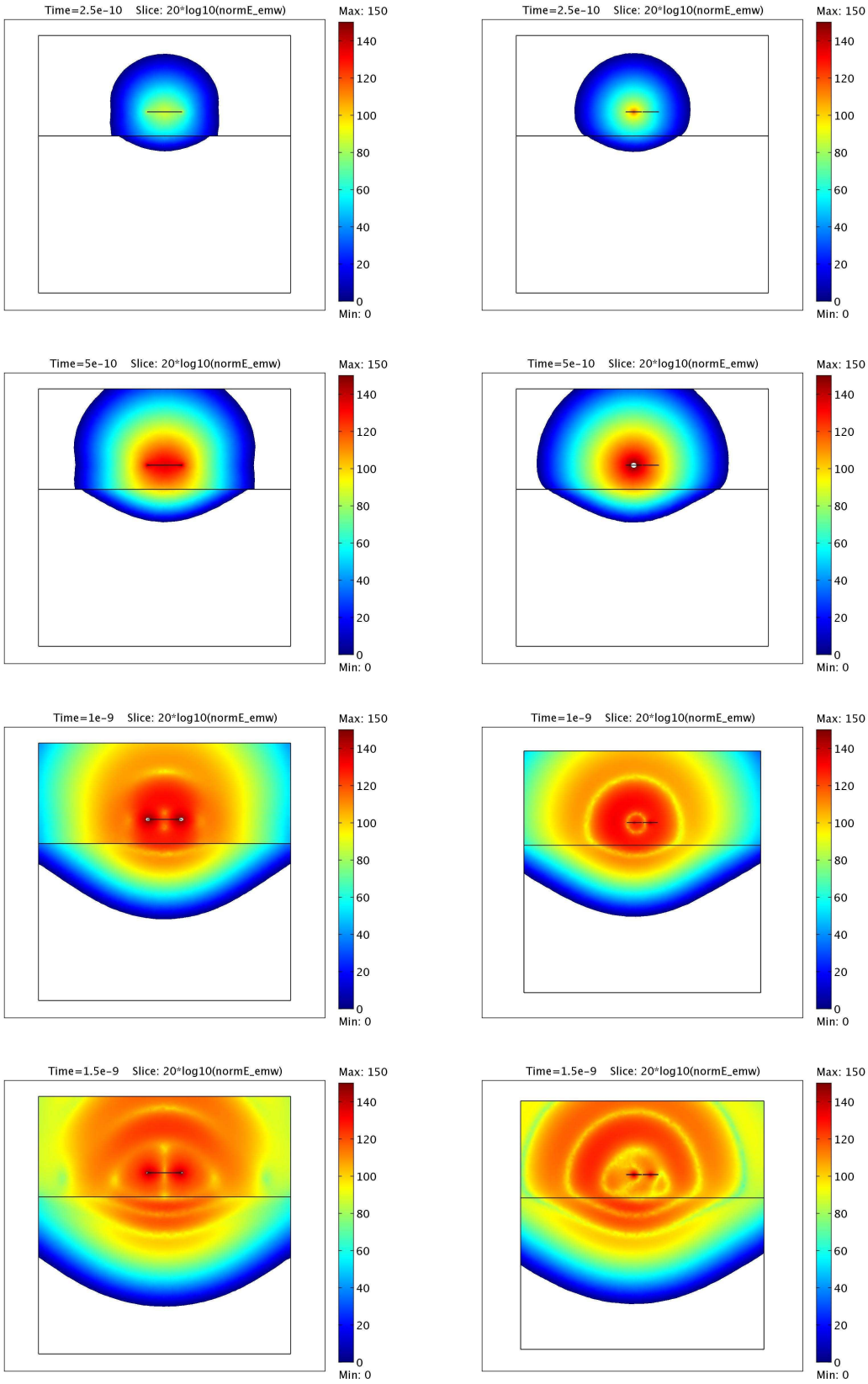

Figure 7.15 – Snapshots for Tx and Rx (without shielding and absorber), at height=6cm above dry soil, E-plane (left) and H-plane (right).

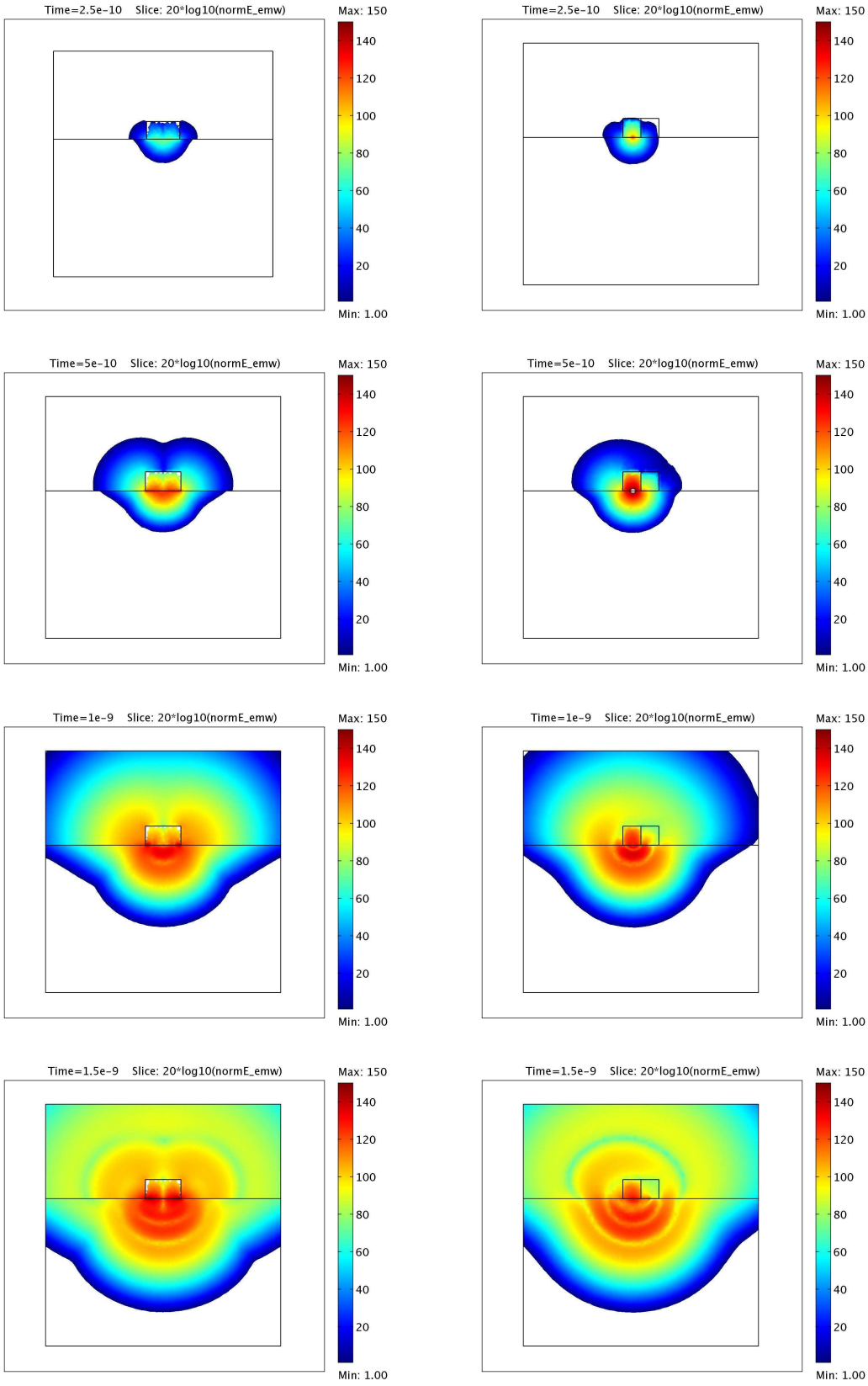

Figure 7.16 – Snapshots for Tx and Rx with metallic shielding on the surface (dry soil), no absorber, E-plane (left) and H-plane (right).

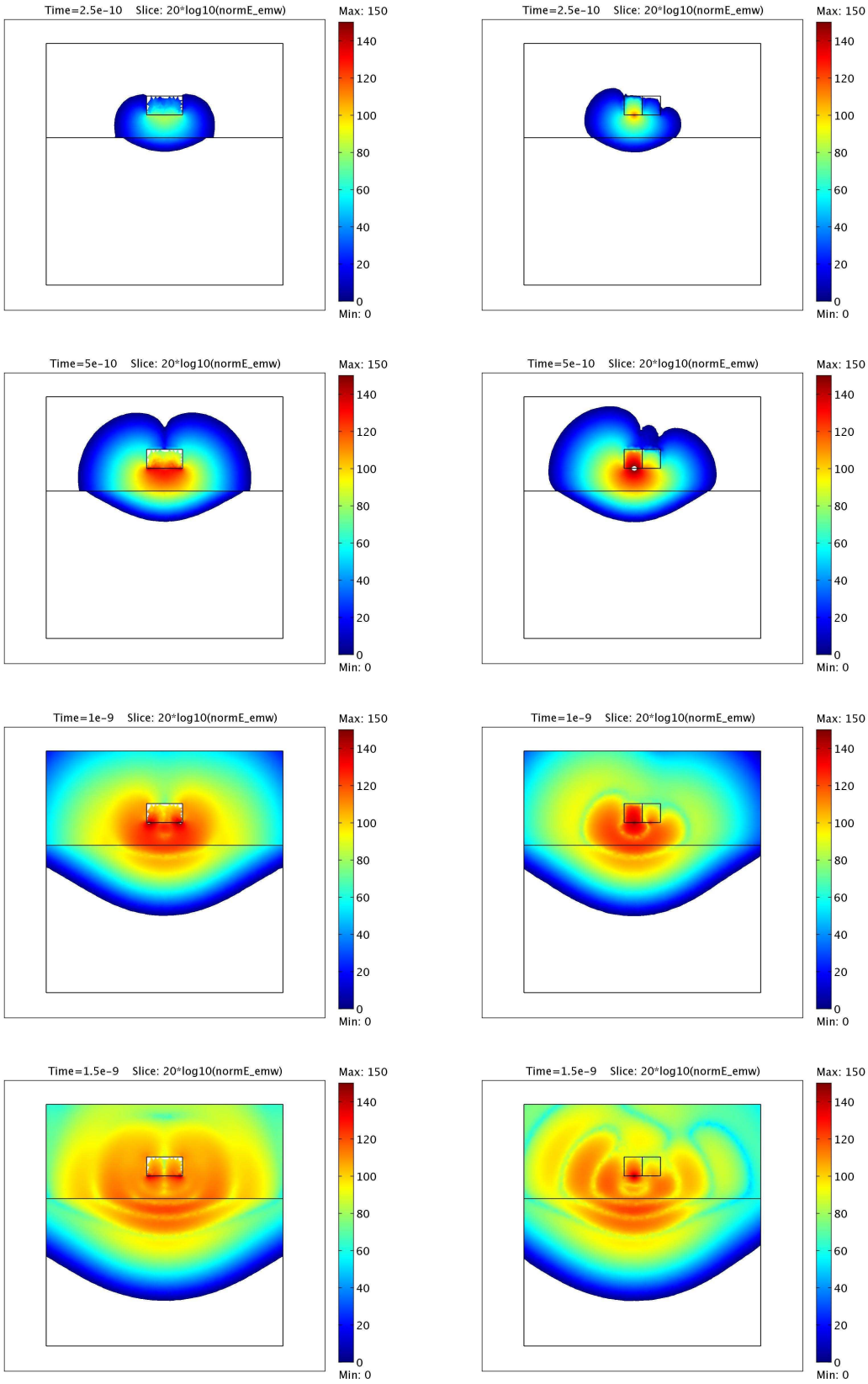

Figure 7.17 – Snapshots for Tx and Rx with metallic shielding, no absorber, at height=6cm above dry soil, E-plane(left) and H-plane (right).

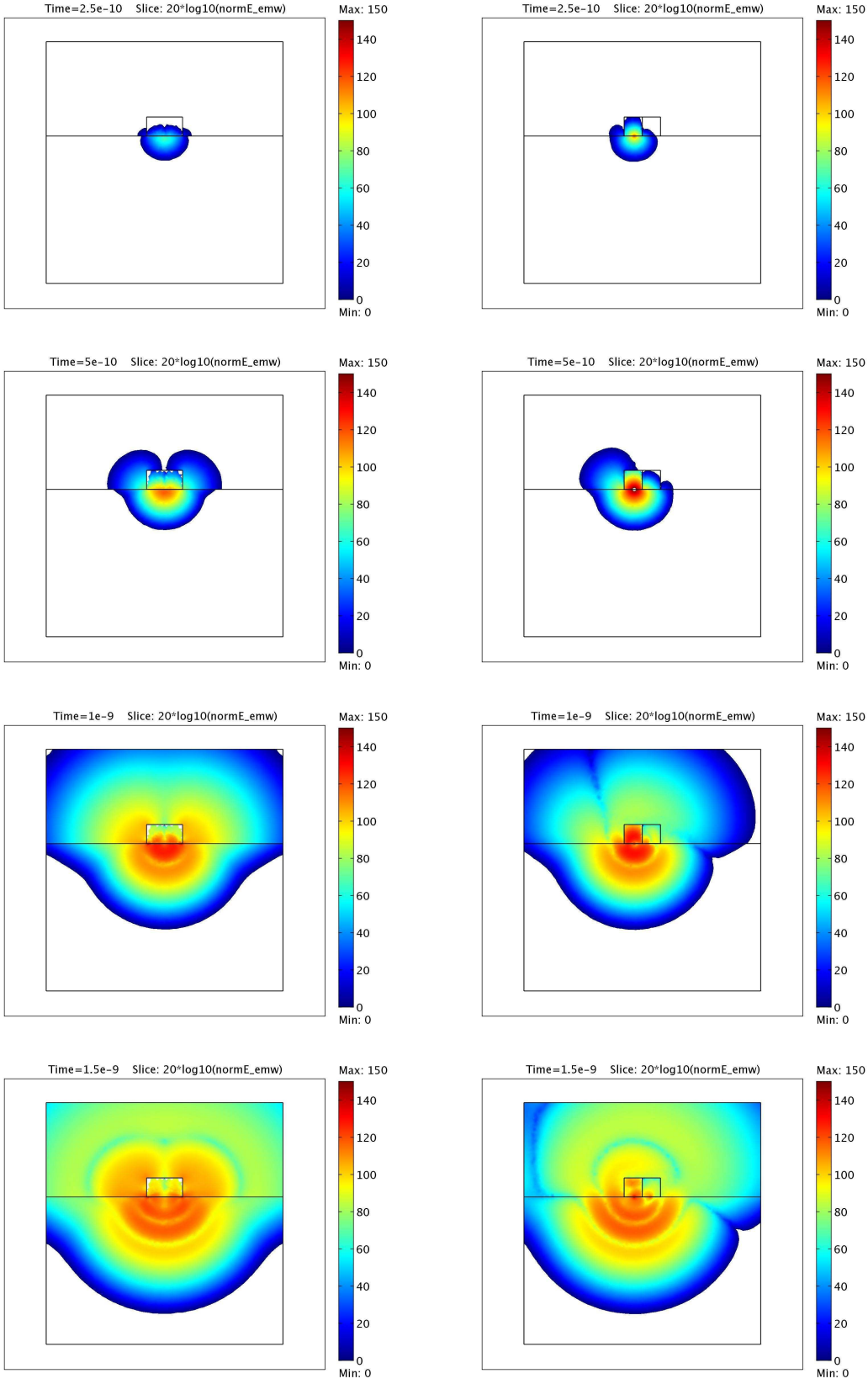

Figure 7.18 – Snapshots for Tx and Rx with shielding and absorber of $\epsilon_r = 7.2$, $\sigma = 0.39$S/m on surface, E-plane (left) and H-plane (right).

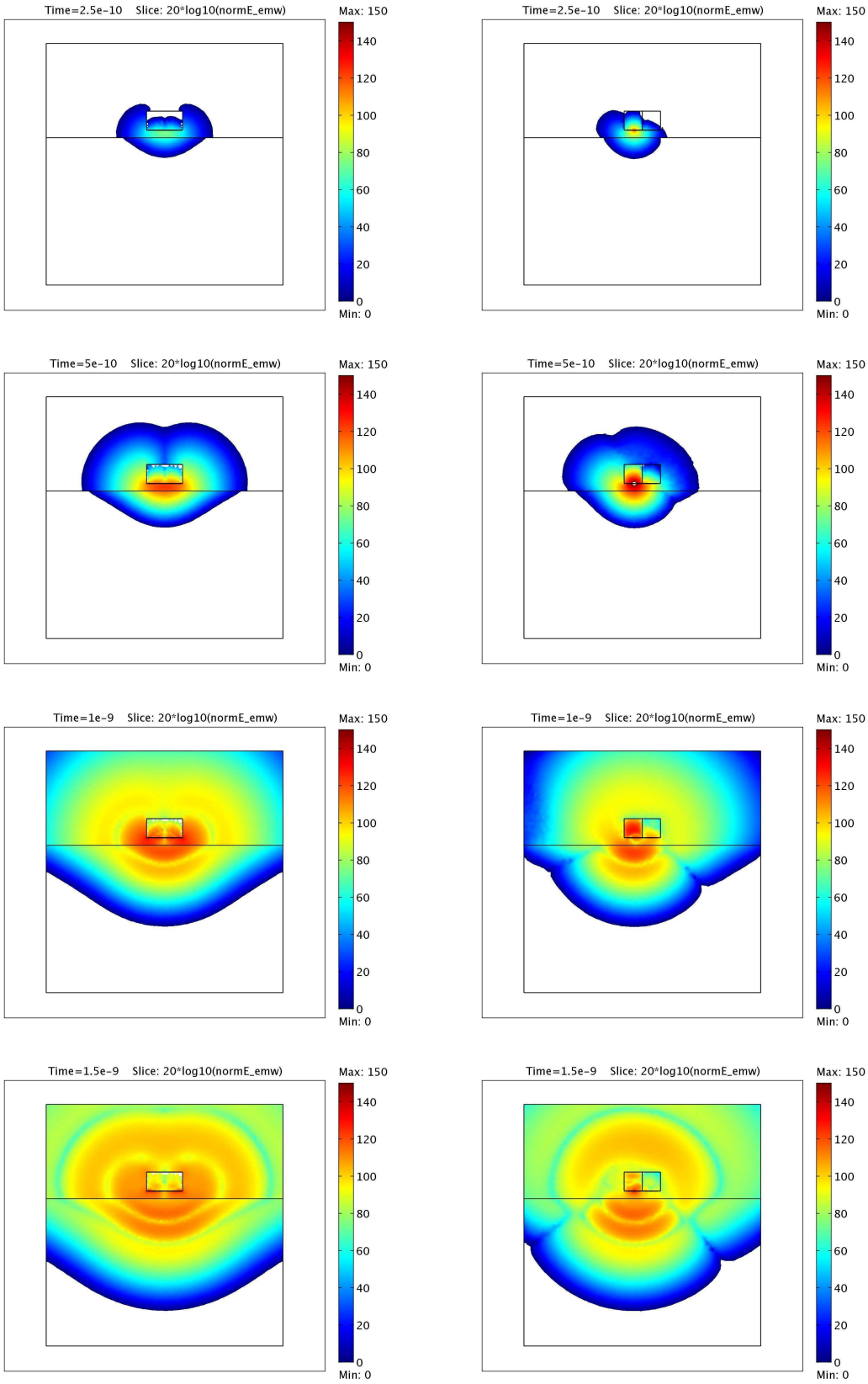

Figure 7.19 – Snapshots for Tx and Rx with shielding and absorber of $\epsilon_r = 7.2$, $\sigma = 0.39$S/m, at height=2cm above dry soil, E-plane (left) and H-plane (right).

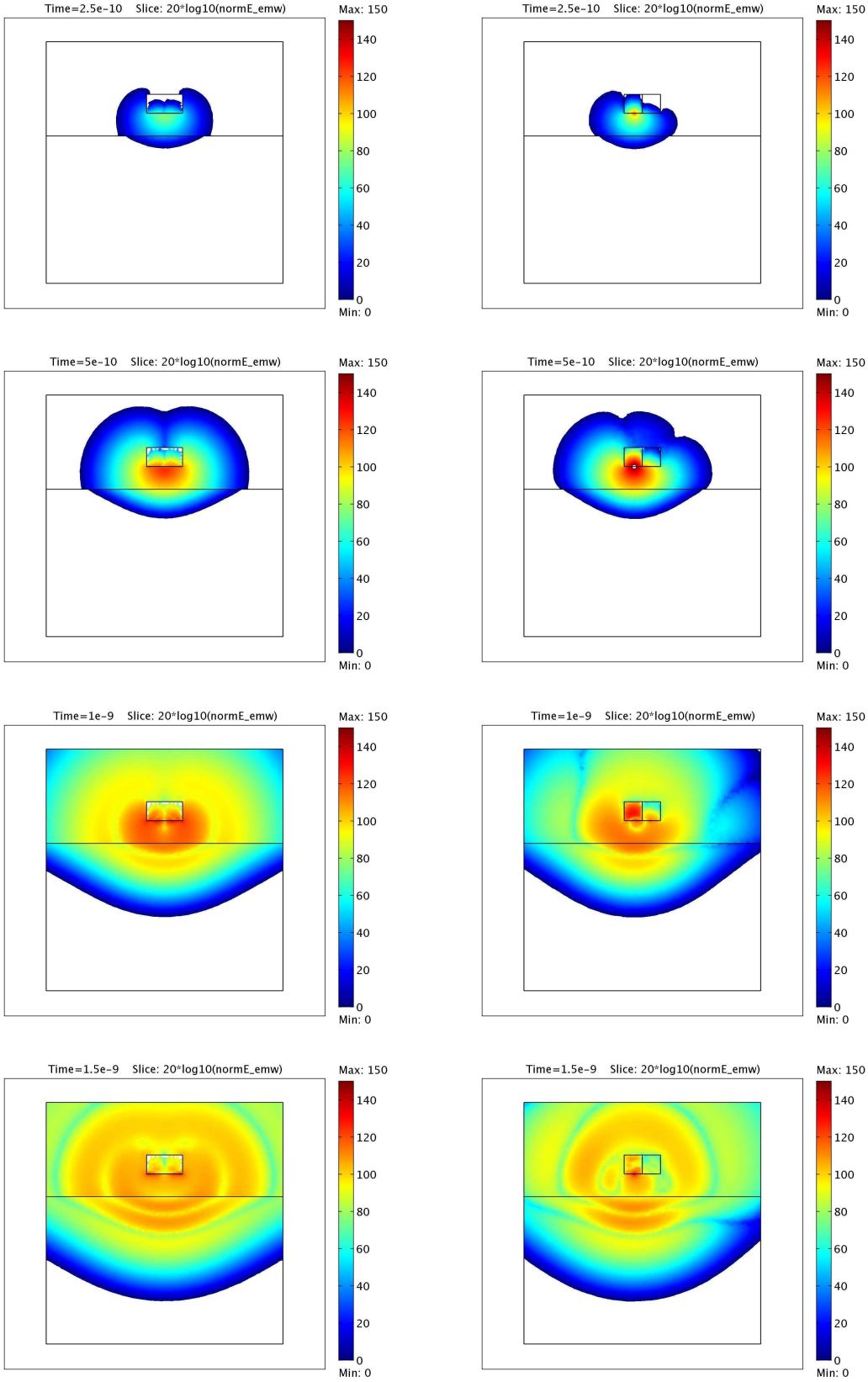

Figure 7.20 – Snapshots for Tx and Rx with shielding and absorber of $\epsilon_r = 7.2$, $\sigma = 0.39$S/m, at height=6cm above dry soil, E-plane (left) and H-plane (right).

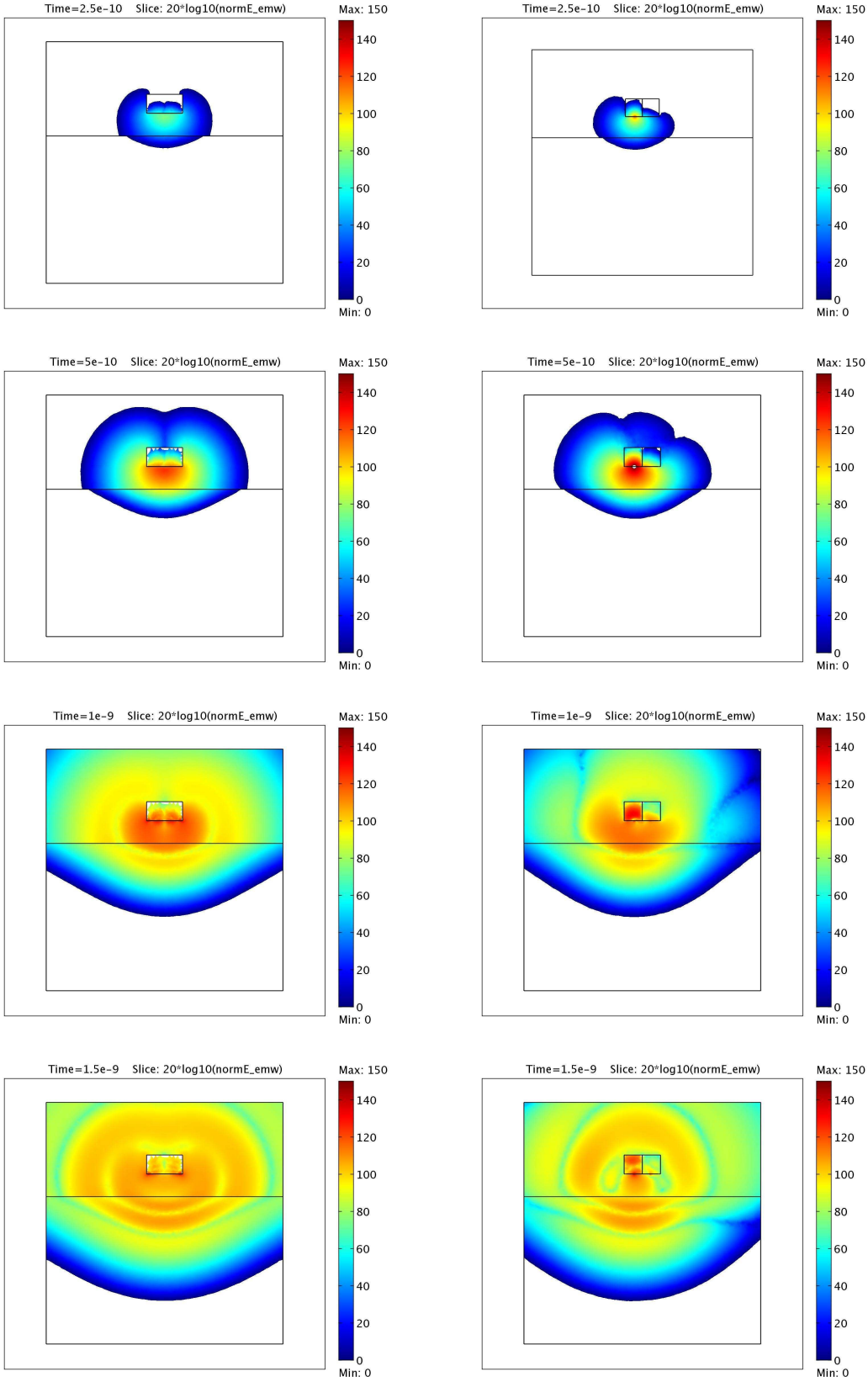

Figure 7.21 – Snapshots for Tx and Rx with shielding and absorber of $\epsilon_r = 10$, $\sigma = 0.39$S/m, at height=6cm above dry soil, E-plane (left) and H-plane (right).

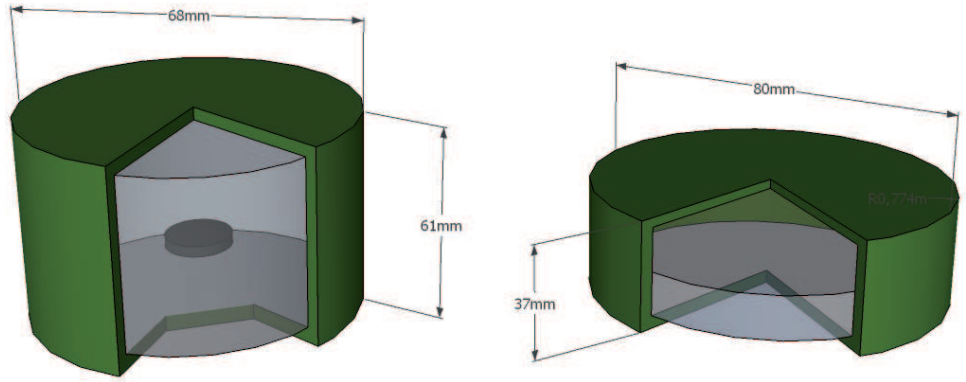

Figure 7.22 – Models of a mine Type 1 (left) and Type 2 (right).

7.2.1 Source Pulse Influence

Before any further analysis, we firstly compare the effects on both mine-like targets' signatures when we consider the previously introduced gaussian and monocycle pulses to feed the transmitter antenna. The picture in Fig. 7.23 depicts the corresponding signatures. The shape of the echoes is rather similar but not equal, and the waveforms are slightly longer for the gaussian source. This difference comes from the different spectral content of both excitation pulses (see Fig. 7.1). The higher spectral components associated to the monocycle generate shorter responses and increase the vertical resolution (as it can be more clearly recognized from the scattering signature of the target Type 1).

7.2.2 Frequency Influence

As it can be seen in Fig. 7.24, the effect of changing the pulse central frequency (and consequently the pulse width) is the change of the vertical resolution of the antenna. In particular, for the higher frequency and the biggest target considered (Type 1), the top and bottom reflections start to separate from each other and there is a clear difference between the signatures. On the other hand, in the case of the target Type 2, its height is still too short and all three signatures look very similar even for the highest frequency. Finally, for both targets, there is a slight reduction of the echo length for increasing frequencies, which was already expected.

7.2.3 Target Influence

i. Target size

We analyze here the effects of changing the size of the two mine-like targets in horizontal and vertical dimension, i.e., its diameter and height. In Fig. 7.25 and Fig. 7.26 we display the signatures of the two targets when their horizontal and vertical dimension are modified 0.75, 1.5

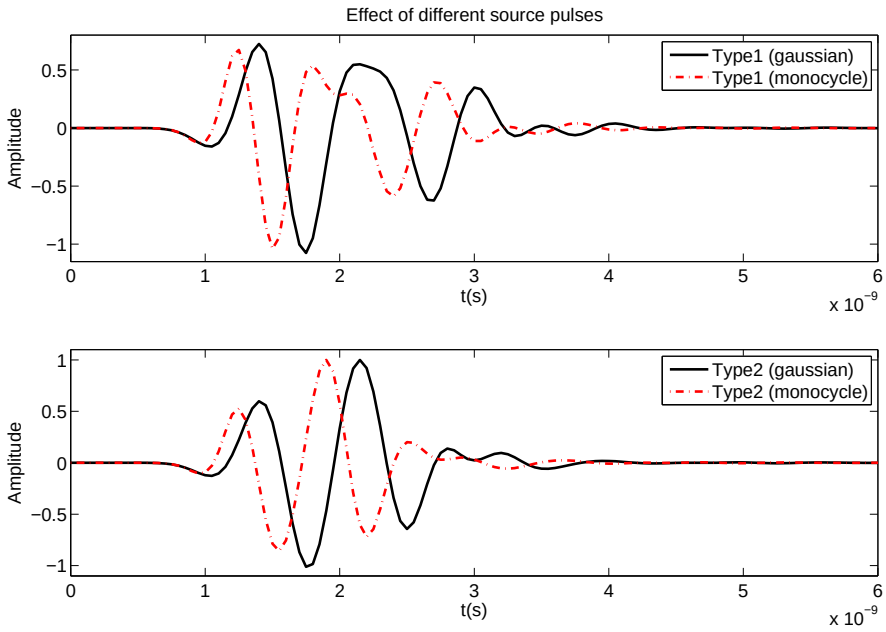

Figure 7.23 – Amplitude of the scattered signal by mine Type 1 (top) and mine Type 2 (bottom) for gaussian and monocycle source pulses.

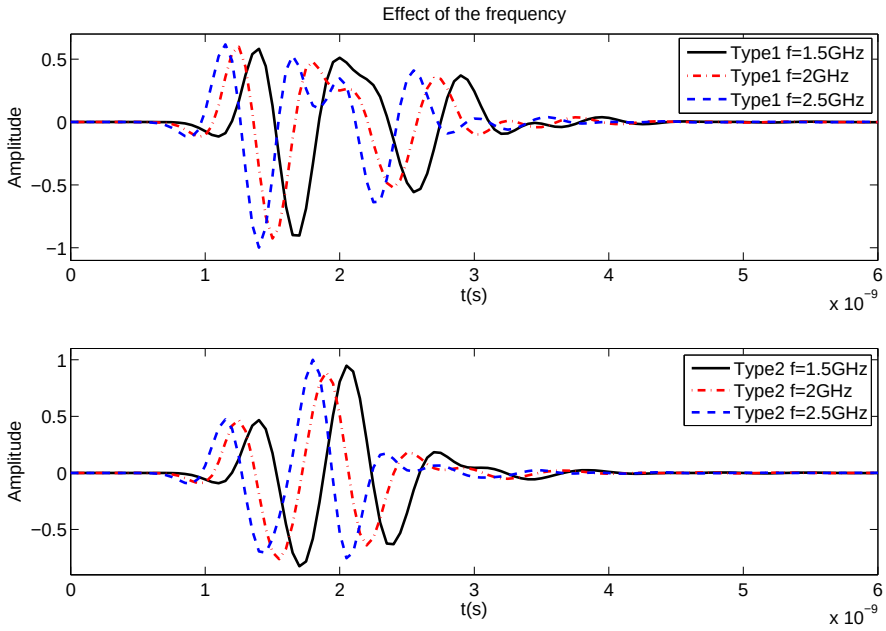

Figure 7.24 – Amplitude of the scattered signal by mine Type 1 (top) and mine Type 2(bottom) when the transmitter is excited with monocycle pulses of different central frequencies.

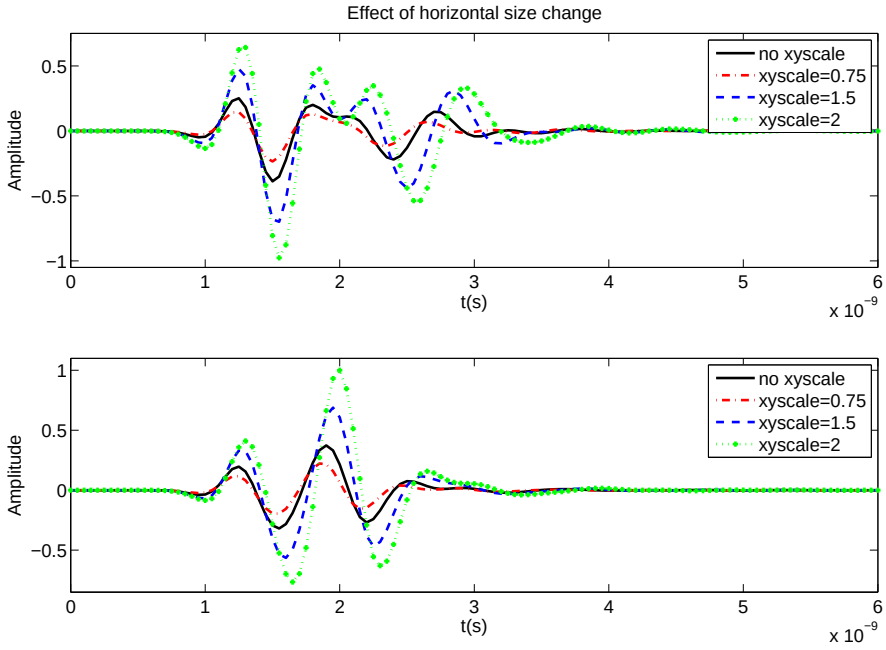

Figure 7.25 – Amplitude of the scattered signal by mine Type 1 (top) and mine Type 2 (bottom) when their horizontal dimensions are modified.

and 2 times its original size. The figures show that the diameter of the target has a remarkable effect on the signature magnitude, increasing considerably its value as the diameter increases. In contrast, the shape of the signature seems to be independent of the diameter and remains almost the same in both cases. On the contrary, targets' height alters the shape of the echoes displacing the position of the maxima and minima: the higher is the target, the longer will be the corresponding signature. And when the height of the target considered is big enough, the top and bottom reflections will be differentiated, as it is clearly recognized in the example where Type 2 target's height is taken the double of original one.

ii. Target Tilt and Orientation

In this section the sensitivity of the scattering response to the orientation and position of the targets with respect to the GPR antennas is investigated. In the simulations presented until now, the targets were always located just below and parallel to the antenna unit. The next figures illustrate the influence of target horizontal displacements as well as target rotations on the scattering signatures. Fig. 7.27 depicts the amplitude of the scattered signal by mine-like targets of Type 1 and Type 2 when they are displaced 4 centimeters along both directions x and y. Figure 7.28 shows the scattered amplitudes when the targets are tilted 20°, 40° and 60° respect to the x-axis. We observe that little lateral displacements affect just very slightly to the echo shape. When the target is just below the antenna unit (i.e., in the middle between transmitter and receiver), the magnitude of the signature is a bit stronger, and when the target is displaced 4cm in both x and y directions the signatures are very similar because of the size of the antenna

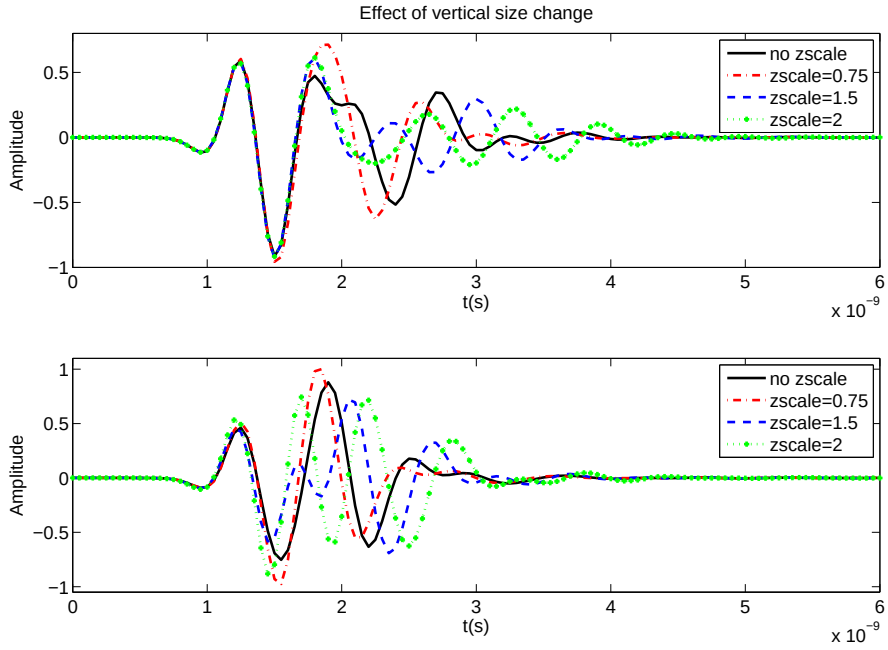

Figure 7.26 – Amplitude of the scattered signal by mine Type 1 (top) and mine Type 2 (bottom) when their vertical dimension is modified.

beamwidth and the equal length of the wave travel paths.
On the other hand and as it could be expected, Fig. 7.28 evidences that the target orientation with respect to the incident fields has a stronger impact on its signature. This impact is bigger for the smaller target, because the relative change when it is tilted, is bigger. Its apparent cross-section to the illuminating waves becomes smaller and then the amplitude decreases with tilt. For the Type 1 this effect is not so evident because its vertical dimension is longer than the horizontal one, and then the change of the echo is not very relevant.

iii. Target Shape and Contrast

This section shows the signatures for a collection of targets to study the effects of the different geometries and the influence of their internal structure on the signatures. In addition to the mine-like targets we consider here the targets that were previously described at the beginning of this analysis (see Section 7.2) are: two cylinders with the same dimensions as the two mine-like targets respectively, but made only of plastic (with the same electromagnetic parameters as the plastic cover of the mines); two cylindrical pipes filled with water parallel to the antenna polarization direction (x) and perpendicular to it (y); and one metallic and one plastic sphere.
As we can see from Fig. 7.29, slight modifications in target internal structure don't produce an appreciable impact on the object signature. This is the case of target Type 1 and the corresponding homogeneous cylinder, where we recognize that the small metallic piece and the little contrast between the plastic cover and the TNT, don't make any big difference between both signatures. On the other hand, in the case of the target Type 2 and the corresponding homoge-

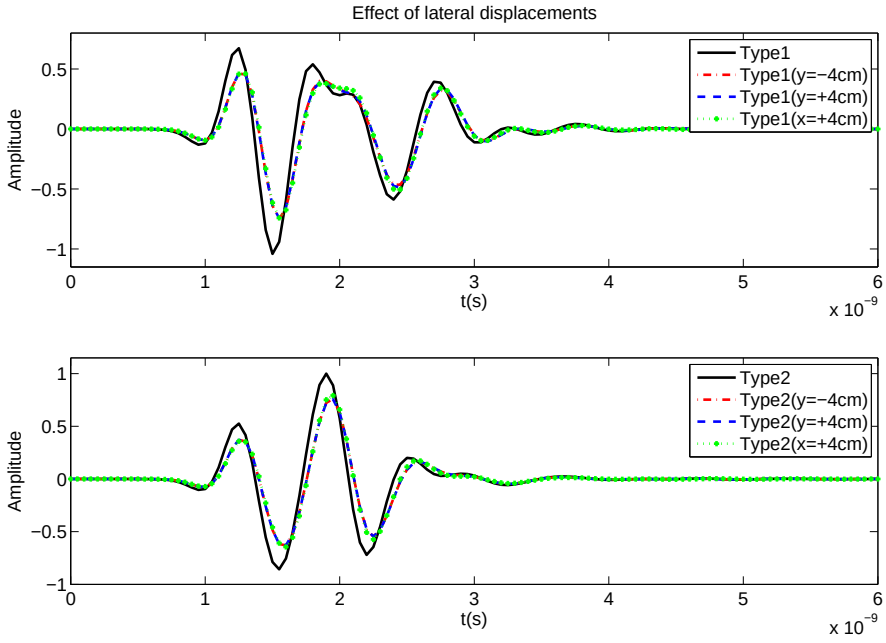

Figure 7.27 – Amplitude of the scattered signal by mine Type 1 (top) and mine Type 2 (bottom) for horizontal displacements. The displacement x=-4cm is not displayed because due to the configuration symmetry the signature is the same.

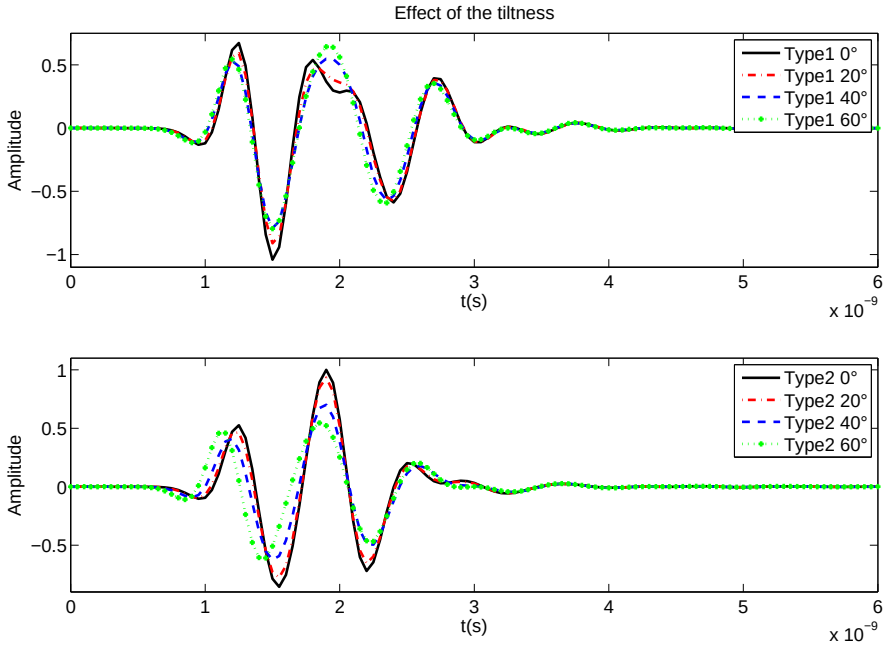

Figure 7.28 – Amplitude of the scattered signal by mine Type 1 (top) and mine Type 2 (bottom) for different tilt angles respect to the horizontal.

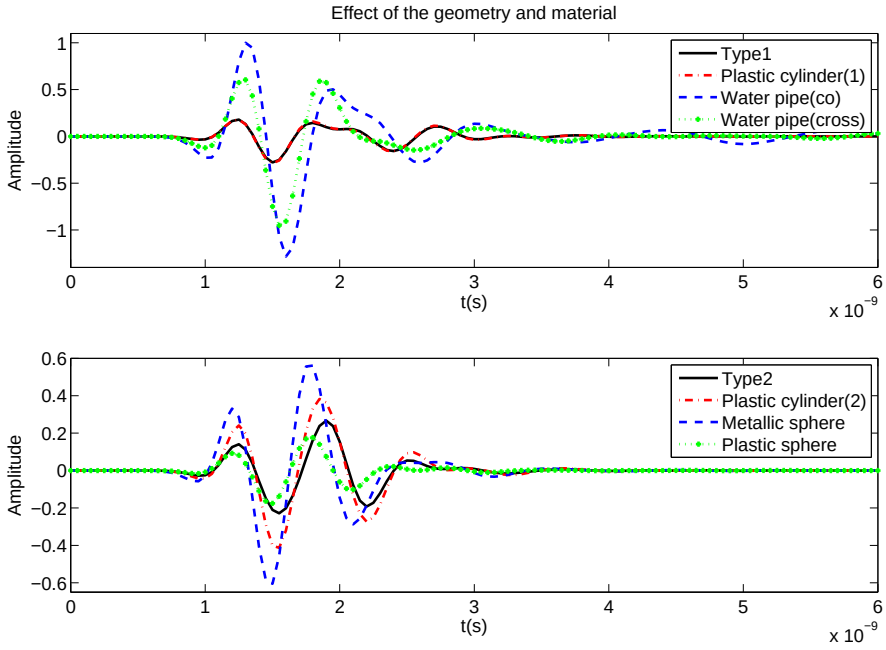

Figure 7.29 – Amplitude of the scattered signal by different objects in comparison with the signature by mine Type 1 (top) and mine Type 2 (bottom).

neous plastic cylinder, we observe that the void present of the mine-like target has a remarkable effect on the signature, increasing the amplitude and changing slightly its shape. Regarding the other objects, we recognize a big difference between the pipe echoes and all the others due to the very high permittivity contrast of the water with the (background) free-space. This fact, apart from lengthening the signature (due to the slower propagation velocity of the waves in water), generates a very intense top reflection (because the most of the energy is reflected at the top of the pipe); the second reflection is in comparison much weaker. With respect to the spheres, we observe that their signatures are similar in length to the one scattered by the target Type 2, since their vertical size is also rather similar. However, their shape (equal for both spheres, and just stronger for the metallic one than for the plastic one) is slightly different to the shape of the signatures produced by the cylindrical objects, being the first minimum much more intense than the second one, while for the cylindrical objects this contrast between minima is not so strong.

7.2.4 Soil Contribution

This section focuses on the influence over the signatures of diverse model parameters when the target is buried in soil.

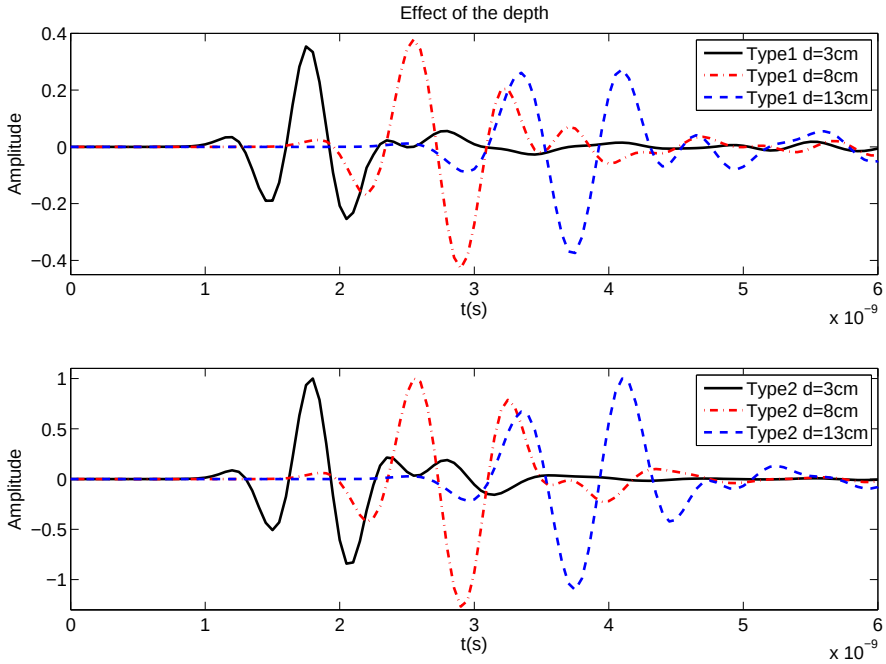

Figure 7.30 – Amplitude of the scattered signal by mine Type 1 (top) and mine Type 2 (bottom) buried in dry soil at 3, 8 and 13cm. The value of the amplitude is normalized for both objects at every depth.

i. Target depth

Here the responses of both mine-like targets buried in dry and wet soil at different depths (3, 8 and 13cm) were simulated. As we can note from the Fig. 7.30 and Fig. 7.31, the width of the signatures rises with the depth for both targets and soils due to the low-pass filter effect of the soil (and lower frequencies are associated to longer widths). On the other hand, the changes in overall shape when comparing the signatures of each target in dry and wet soil are not relevant and just the arrival times of the echoes for the different depths change due to the different propagation velocity in dry and wet soil. Another effect that can be noticed in both soils and for both types of targets is that there is a polarity reversal for the case of 13cm target depth in comparison with the other two smaller depths investigated. This effect needs further investigation.

ii. Dielectric Contrast

An increase in soil permittivity (usually related to a higher moisture content) results in general in an increase of the response magnitude due to the bigger contrast. However, for highly lossy soils, an increase in the permittivity can produce a decrease in the echo amplitude due to the higher associated attenuation.
In Fig. 7.32 and Fig. 7.33 we can see a change in the polarity of the reflected signal in the case of the water pipe with respect to the other targets, i.e, the polarity of the scattered wavelet is the opposite, which is an effect that can happen when the emitted pulse encounters an interface

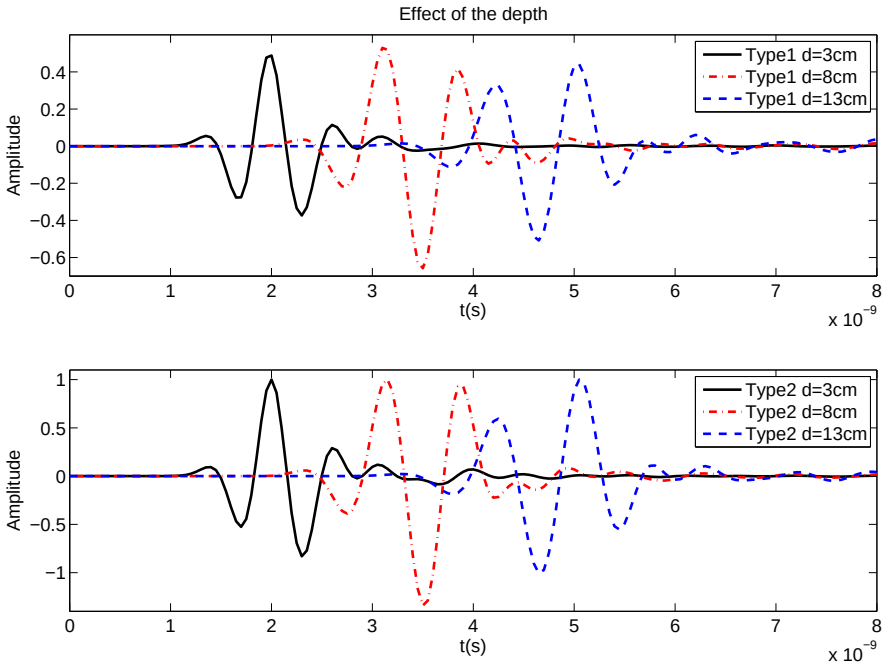

Figure 7.31 – Amplitude of the scattered signal by mine Type 1 (top) and mine Type 2 (bottom) buried in wet soil at 3, 8 and 13cm. The value of the amplitude is normalized for both objects at every depth.

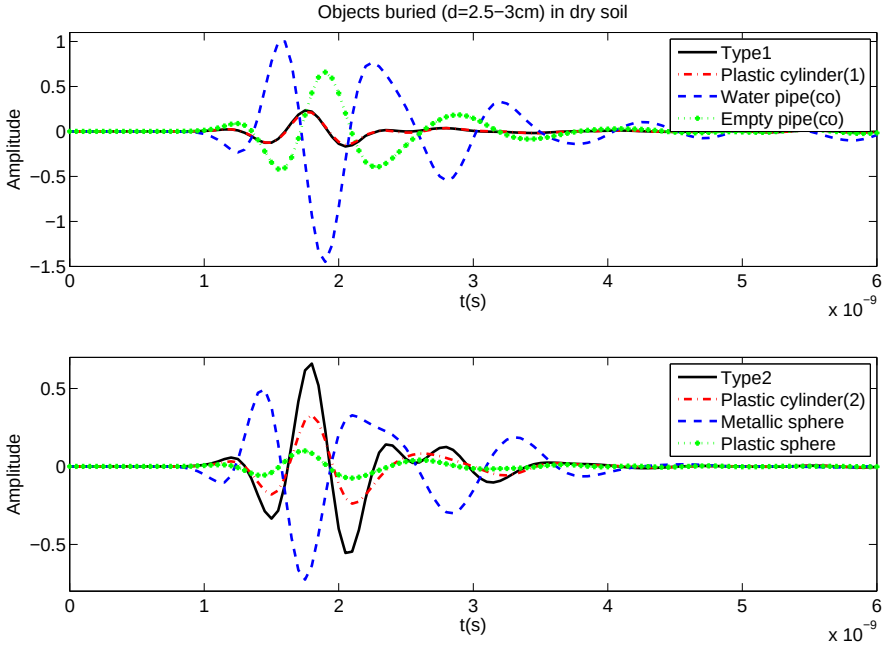

Figure 7.32 – Amplitude of the scattered signal by different shallow buried objects in dry soil.

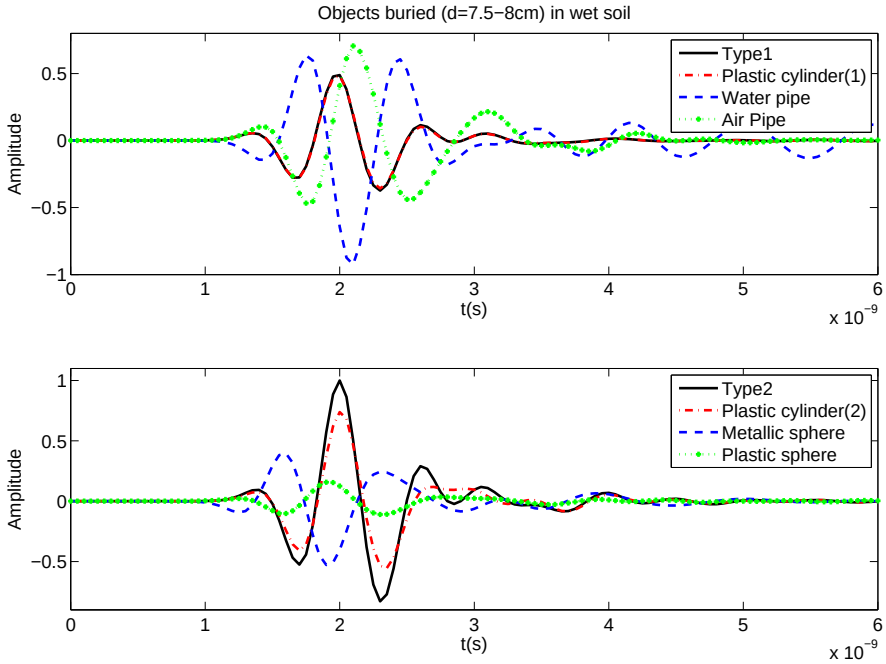

Figure 7.33 – Amplitude of the scattered signal by different shallow buried objects in wet soil.

between two different materials.
The polarity flip of the reflected pulse occurs only when the impedance of the second medium (or object) is higher (i.e., lower permittivity) than the first medium, being then an indication of the transition from low velocity to higher velocity across a boundary. This phenomenon, which can be easily deduced from the Fresnel equations when calculating the corresponding reflection coefficient, is the reason why the polarity of the reflected signals by the water pipe and the metallic sphere (whose permittivites are not lower than that of the background) are not reversed and are opposite to the polarity of the rest of the considered targets.
The changes in the signal polarity can be used for detecting certain underground structures or cavities.

iii. Soil Type and Water Content

Here we will analyze the effect of changing the soil permittivity and conductivity on the amplitude and shape of the scattered signatures. As it was expected the reflected pulse amplitude increases with permittivity due to the highest contrast between the target and the background soil (Fig. 7.34). At the same time it broadens slightly because the bandwidth of the incoming pulse is reduced due to the low-pass filter effect of the soil. There is also a delay of the scattered signal associated to the lower propagation velocity for increasing permittivity values. The overall shape of the signal does not change very much, but the last tail associated with the ringing grows notably when the permittivity increase.
When changing the conductivity (Fig. 7.35), we observe that the received signal strength slightly

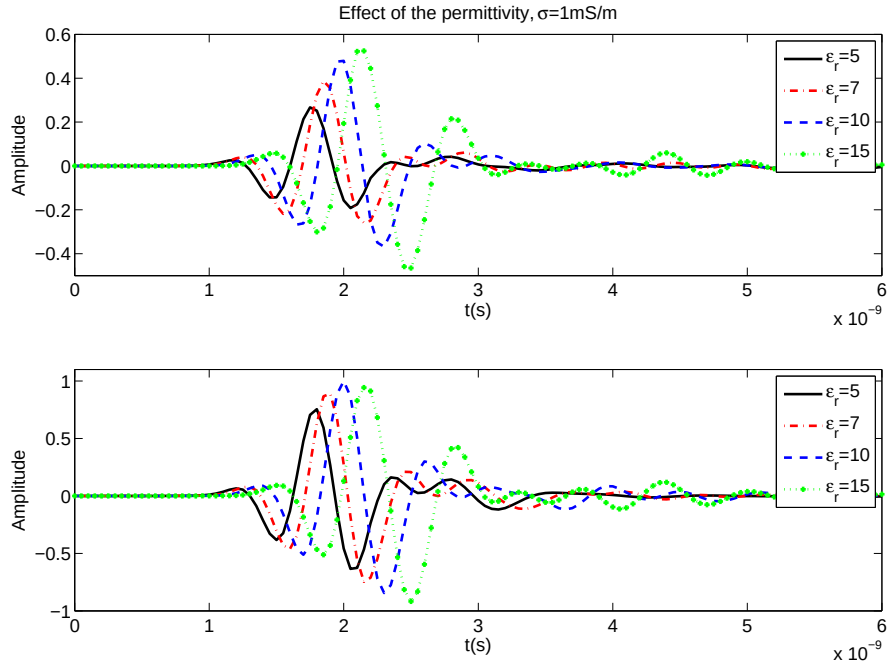

Figure 7.34 – Amplitude of the scattered signal by mine Type 1 (top) and mine Type 2 (bottom) buried in dry soil with different permittivities and constant conductivity $\sigma = 1mS/m$.

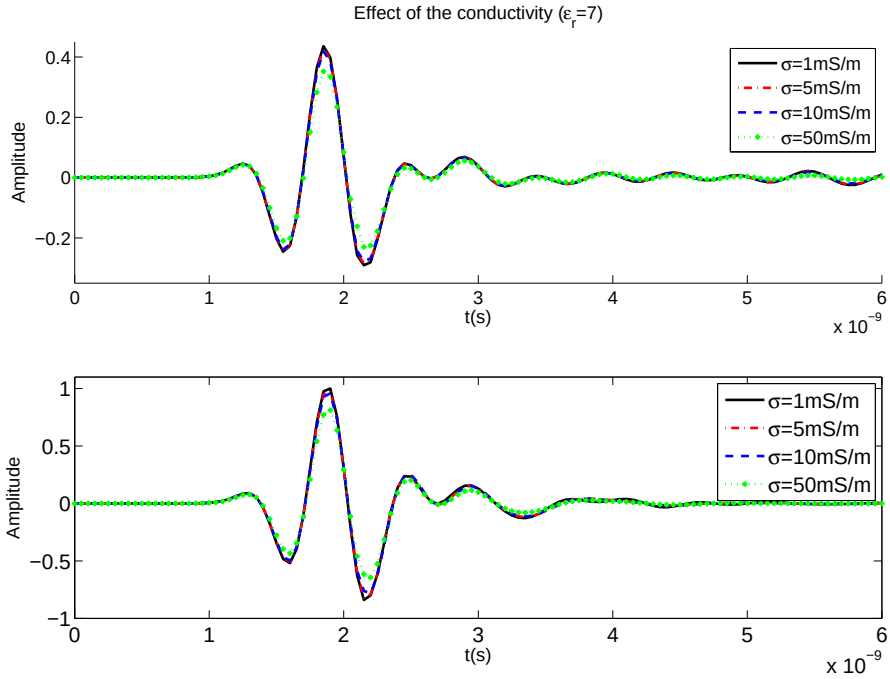

Figure 7.35 – Amplitude of the scattered signal by mine Type 1 (top) and mine Type 2 (bottom) buried in dry soil of different conductivities and constant permittivity $\epsilon_r = 7$.

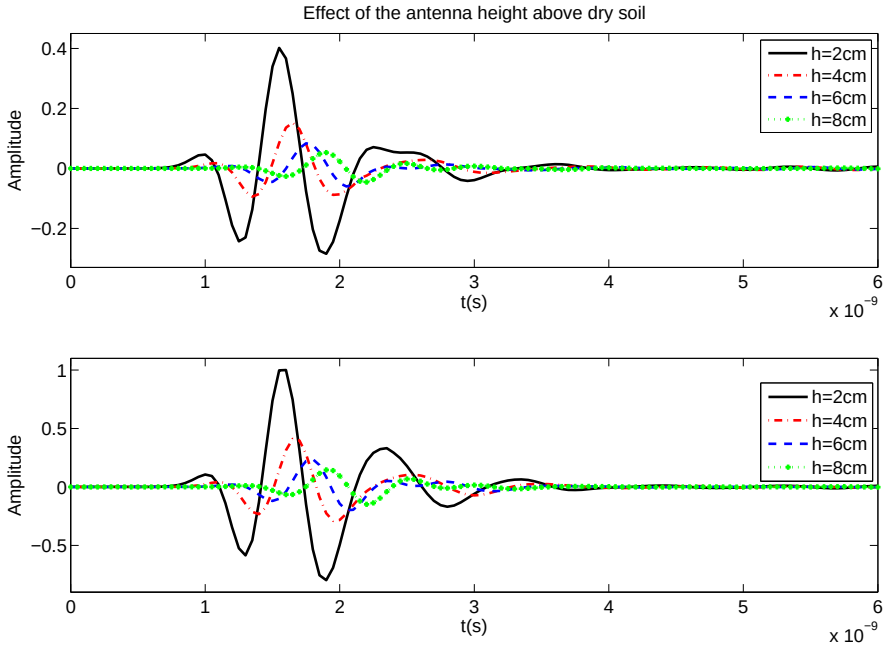

Figure 7.36 – Amplitude of the scattered signal by mine Type 1 (top) and mine Type 2 (bottom) for different antenna heights above dry soil.

decreases with the growing conductivity (more attenuation), which usually is related to a higher moisture content. Nevertheless, this difference is really small due to the shallow depth of the targets. For depths up to 10cm the influence will be still small for such conductivity values but above 50mS/m, the attenuation starts to be more important. The good news are that even wet soils usually don't reach higher values. Regarding the shape of the scattered signals, we don't see any significant change either.

iv. Antenna Height

As expected, the increase of the antenna-soil distance yields a decrease in the magnitude of the scattered signal, i.e., the energy coupling into the soil worsens with antenna elevation (Fig. 7.36). The amplitude reduction is faster for the first 4cm.

v. Soil Heterogeneity

We have modeled two inhomogeneous soils, one representative of dry soil and the other one representative of wet soil. In the configuration with dry soil, we have assumed relative permittivities with a mean value of 5 and standard deviation 0.8 (i.e., in the range $\epsilon_r \sim 2-8$), and for the wet soil with a mean value of 10 and standard deviation 1.2 (in the range $\epsilon_r \sim 7-13$), both of them according to a normal gaussian distribution as described in section 4.5. Generally, inhomogeneities closer to the ground surface have higher conductivities due to the presence of organic

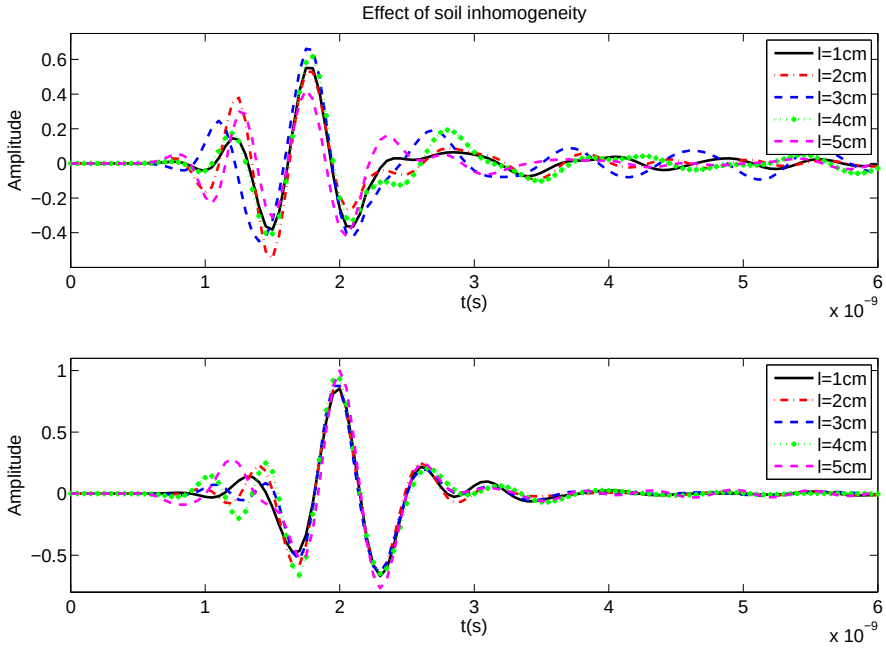

Figure 7.37 – Amplitude of the scattered signal by mine Type 1 buried in inhomogeneous dry (top) and wet soil (bottom) for different correlations lengths.

material, and conductivities in the range $\sigma = 0.01 - 0.04$S/m can be expected. However, since we have seen that conductivity variations up to 50mS/m do not have a relevant impact on the signatures (at least for shallow buried objects), we consider here a constant conductivity of 1mS/m for the dry soil and 50mS/m for the soil with a higher moisture content.

In Fig. 7.37 we illustrate the signatures of the Type 1 target when it is buried 3 centimeters in the above mentioned soils. We have changed the correlation length from 1 to 5cm for both cases to study the influence of this parameter on the corresponding signatures. In the pictures above, we observe that for dry soil the influence of the inhomogeneity on the signature is much more important than in wet soil. This happens because the target permittivity ($\sim$3) lies within the range of the background soil permittivity variability being the contrast rather small, while in the case of wet soil the target permittivity stays always considerably below the background permittivity. In addition to this, we also see that the deviation from the target response in homogeneous soil grows slowly as the correlation length increases from 1 to 5cm, and the reason is that the soil inhomogeneity becomes the same order in size as the target, producing reflections of similar intensity. If we consider higher correlation lengths this tendency will continue but above a certain value, the effect will decrease again since then, the soil will become apparently homogeneous in comparison with the target dimensions.

More specifically, the correlation between the signature of the Type 1 target in homogeneous dry soil and in inhomogeneous dry soil varies from 97.1% for 1cm to 80.5 % for 5cm correlation length. In wet soil, on the other hand, the change is very slight, going from 99.7% for 1cm to 95.7 % for 5cm correlation length.

7.2.5 Summary and Some Guidelines to Create a Representative Signature Database

With the acquired knowledge about the different parameters influence, we have the required information to create a representative database. This must be large enough to represent a majority of scenarios but at the same time not contain redundancy or unnecessary information, which would increase the processing time and slow down the recognition process.
Next, we summarize the obtained results and present some guidelines for building a convenient database:

1. When considering different source pulses (typically a gaussian or a monocycle), we obtain slightly different echoes in shape and width even for pulses of the same length. The difference in the signatures might be more important if the vertical dimension of the object is similar to the pulse vertical resolution, since in this case top and bottom reflections can be distinguished and the different spectral content of the source pulses may produce rather distinct signatures. Then, it is important to choose the source pulse correctly.

2. The same happens when we apply sources with different central frequencies. If we consider a deviation above 20%, the difference on the echo shape may be significant depending on the target vertical dimension due to the effect stated before. In addition, the signature will logically elongate for a smaller central frequency and compress for a higher central frequency. Nevertheless, for small changes (up to 15-20% the central frequency) most probably there will be no impact in shape and just a irrelevant increase or decrease of the signature width. And we will assume that the actual pulse length of our commercial system corresponds to the length given in the specification with an accuracy not below a 20%.

3. The object size is a important point when building the database, in particular the vertical dimension. As we have seen a change in the vertical dimension of the objects alters completely the shape of the signature: the amplitude and position of the maxima and minima are modified. The change in diameter affects mostly to the signature amplitude, but it can also produce a slight change in shape. Thus, it is crucial to include signatures for objects of different sizes. From the simulations we can affirm that changes above 15-20% in vertical dimension should be at least represented in the database. For horizontal dimension 25% would be sufficient.

4. Regarding the lateral displacements of the target respect to the antennas, we have seen that the signature shape does not change significantly in shape for displacements of the order of the size of the object, and just slightly in amplitude for the shorter travel path (object in the middle between transmitter and receiver). Then, this point does not need to be considered and including the simulated signature for only one position would be enough to achieve a good correlation. If the object is rounded (for example an sphere) it would be better to make an average of the simulated signatures for various positions.

5. The target tilt might introduce a significant difference of its echo, which will be more or less remarkable depending on the object geometry. In general, for objects with a horizontal

dimension larger than the vertical dimension, the impact of tilt will be more important. Hence, according to the simulation, it would be recommended to introduce at least two signatures per object, one for no tilt, and a second one for 45° tilt angle.

6. The target material need to be considered specially for those objects whose vertical dimension is enough large (or their permittivity is high enough) to make their top and bottom reflection visible for the considered illumination. Then, the appearance of the complete signature will be rather different depending on the composition. For very small objects respect to the pulse length, a bigger or smaller contrast will just affect to the amplitude and not the shape, and it is not necessary to consider different materials in this case. For the case of internal structure, it does need to be taken into account when the dimension of the internal structures are of the order of the vertical resolution, and when the contrast between the materials in contact is at least of 25% or above.

7. Another relevant issue to take into account is the target depth. The signatures differ significantly when we consider the same object at different depths. The signatures are clearly elongated with depth due to the low-pass filter effect of the soil and it seems to occur a polarity change when the target is deep enough. This effect happens in both soils considered. Then, to account for this, we need to include the signatures of the targets at different depths, at least every 3cm until the depth of interest for landmine detection (maximum 20cm).

8. The soil permittivity affects mainly to the signature amplitude due to the change in the contrast. Apart from the amplitude change, the signature widens with increasing permittivity and the late-time ringing grows, in particular for soil permittivities above 10. Then, it is a good idea to include the signatures for different soils, at least one signature for soils with permittivity below 10, typically 5 for dry sand, and 2 or 3 signatures more for permittivity 10 and bigger. Nevertheless, the permittivity of most common soils does not get over 20, then it is not necessary to consider values above 20.
   With respect to the conductivity, we have seen that this factor does not modify the shape of the signature, at least not for typical values of the conductivity, and it is only responsible of a decrease of the amplitude when it grows due to the increasing attenuation with conductivity. Then, it seems not necessary to pay too much attention to the conductivity when creating the database; we have just to take into account that if the target is 5cm or deeper, conductivities of $\sim$ 100mS/m can produce an important decrease of the target amplitude making it very difficult to detect.

9. The antenna height produces a decrease in the signature amplitude since the coupling to the soil worsens. The overall shape and the length of the signatures don't change significantly but the last tail of the signatures is modified when changing the height. Then this issue should be also taken into account. However, since this parameter is known, one can directly reduce the signatures to consider in the database when doing the automatic recognition if they are separated into groups associated to each simulated antenna height.

10. The soil inhomogeneity affects to the signatures, and the magnitude of the impact depends on the correlation length of the inhomogeneity and its standard deviation. If the variable

values of the permittivity are far from the object permittivity (for example permittivities varying between 10-15 and object permittivity of 3), the object signature will not be strongly affected by the inhomogeneity. If the object permittivity lies on the interval of variation, the signature will be clearly distorted unless the correlation length is very small. As we have observed, only for correlation lengths similar to the dimension of the object, the impact may become significant. Correlation lengths of less than the half of the size of the considered object don't need to be taken into account (unless the standard deviation is very high, which is not realistic).

However, considering that the soil inhomogeneity distribution is not exactly known, we cannot model the exact response of the target in such scenarios. Hence, when we are dealing with objects buried in inhomogeneous soil, it is more feasible to assume than the soil is homogeneous, and reduce the threshold for the similarity constraint with the synthetic signatures depending on the estimated soil variability degree.

8

Experimental Analysis and Validation

The true method of knowledge is experiment.
William Blake

In this last chapter we study the potential application of synthetic GPR target responses in buried landmine detection/recognition and clutter suppression. The proposed methodology is a combined approach that comprises an energy based detection algorithm and a cross-correlation based identification algorithm. Basically, the latter consists in a shape comparison between measured and simulated reference signals and it can be implemented before conducting the detection as an additional filtering step in the form of a similarity constraint. As described in previous chapters, to obtain accurate one-dimensional temporal signatures for such a comparison, we need to incorporate an optimized antenna model as well as realistic CAD representations of the targets into our simulations.
To evaluate the performance of this approach, we carried out a measurement campaign in the test field of the Leibniz Institute for Applied Geophysics (LIAG) Hannover where different test mines were buried in inhomogeneous sandy soil. In the next sections the test targets, the experimental setup and the test site are described. Then, GPR data preprocessing is briefly discussed and the applied postprocessing algorithms are introduced. In particular, we describe in detail the proposed cross-correlation based identification technique together with the energy-based detection algorithm, as well as the combined strategy. Next, we show the achieved similarity degree (correlation coefficient) comparing some simulated and measured signatures in free space. Finally, the results obtained from the application of the individual algorithms and the combined methodology to a collection of surveys acquired in Hannover using a little dataset of simulated waveforms, are presented and analyzed.

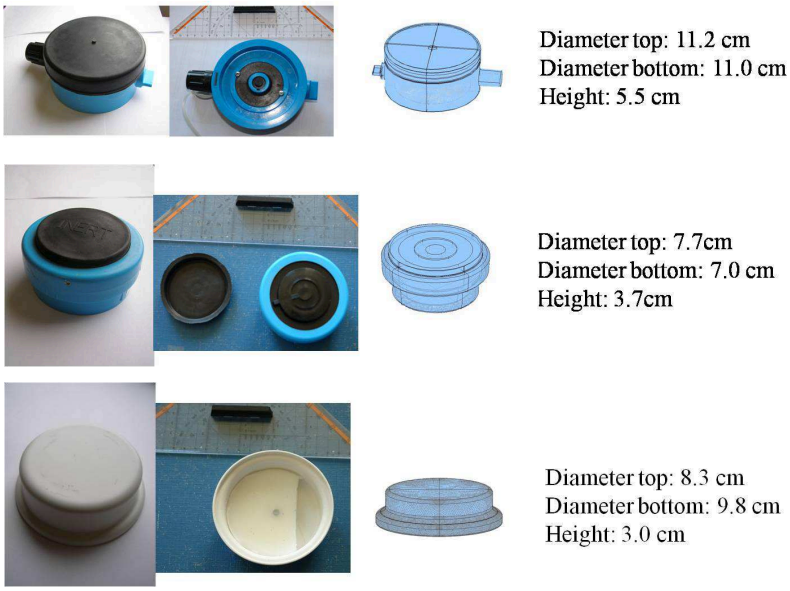

Figure 8.1 – PMN mine simulant (top), Type-72 mine simulant (middle) and ERA test mine (bottom) employed in the measurements and the corresponding CAD models.

8.1 Test objects

As explained in Chapter 1, there are a wide variety of non-metallic AP mines that come in several sorts of sizes and shapes. Some of the mines have small cavities, metal springs or trigger mechanisms of a few centimeters which, in some cases, will increase the amplitude of the reflected signal. The contribution of small metal components inside the landmines is not significant at frequencies around or below 1 GHz. For investigation purposes a collection of test objects can be employed. The biggest difference is the size and shape of the mines, the metal trigger mechanisms and clamping rings.

A Standard Test Target (STT) is a simulant or surrogate landmine used in the test of landmine detection equipments. They are intended to interact with countermine systems in a way representative of, or identical to, that of a real landmine or landmine category. A simulant landmine (SIM) is an STT that has features or characteristics representative of a 'category' of landmine types, but does not replicate any specific landmine type or model. A STT that lacks some (one or more) features or characteristics of an actual landmine class is called a Surrogate Landmine (SUM) [ITOP, 1999]. In this study we are going to present some results for two landmine simulants (PMN, Type-72) and a Standard Test Target (ERA) (see Fig. 8.1).

Typical values for the electrical properties of the materials used in STT are provided in Table 8.1. They are given on the basis of the mine descriptions available. These electrical properties are used along with the physical model to generate the numerical simulations of the GPR response.

MATERIAL	ϵ_r	σ (S/m)	Source
3110 RTV Silicone rubber	2.20 @ 100 kHz	1.4 x 10^{-12}	Dow Corning
Bakelite	3.5-4.5 @3GHz	0.01-0.07 @3GHz	von Hippel (1966)

Plastic (mine body)	2-4 @3GHz	0.001-0.1 @3GHz	von Hippel (1966)
Rubber	2-3 @3GHz	0.001-0.1 @3GHz	von Hippel (1966)
Metal	NA	1-5 x 10^7	
Wood	1-2 @ 3GHz	0.003-0.03	von Hippel (1966)
TNT	2.9 @1GHz	0.0029 @1GHz	
Beeswax	2.4 @3GHz	0.003 @3GHz	von Hippel (1966)

Table 8.1 – Electrical properties of materials used in mine construction.

8.2 Test site description

A picture of the test field is shown in Fig. 8.2 with arrows pointing to the lane where the targets are buried. A detailed layout of the test lane and test targets (red points) is displayed in the left side of the picture. Here the red squares correspond to the 1x1m area scanned in every survey. The targets in the left line (the red points with odd numbers) are buried approx. 10cm depth and the targets in the right line (the red points with even numbers) lie approx. 15cm depth. The bold lines with the numbers starting in 200 and 300 respectively, indicate the plastic rails at the borders of the area. These points will be our reference to measure the antenna offset of the different surveys. The zero point of the coordinates is located on the right corner of the left rail and it is marked by a red circle.

Time Domain Reflectometry (TDR) probes were used at each scanned area to determine the dielectric constant and soil water content. The theory behind TDR probes is very similar to ground penetrating radar. TDR probes measure the dielectric constant of the soil and use this measurement to calculate the soil water content using Topps equation (see Chapter 4). It is claimed that the volumetric water content of soils can be determined with this method to an accuracy of 2% and a precision of 1% [Hillel, 1998]. The texture of the mineral soil, which characterizes the distribution of the grain size at the test lane, was sandy (see Fig. 8.3) and highly inhomogeneous due to the presence of organic material and changing moisture content; hence, the electrical parameters and in particular the permittivity presented a substantial variability. The dielectric constant was measured at three different days in August and September with a TDR along 12m long line every 10cm. The average value oscillated between 4.6 in August to 10.1 in September with $\sim$ 15% standard deviation and a correlation length of $\sim$20cm. The days of the campaign the average permittivity was 7.3, a value that lies in the middle.

8.3 Methodology

The interpretation of GPR data can be significantly improved by the use of several data pre-processing algorithms as well as advanced postprocessing techniques adapted to the particular application.

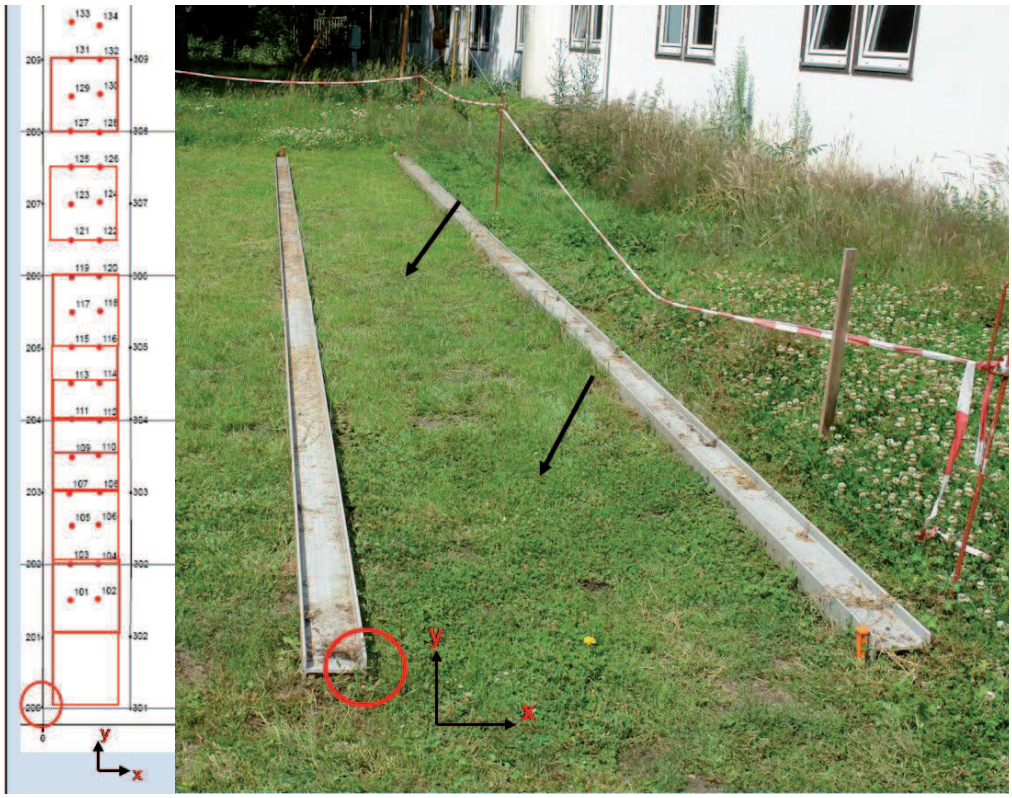

Figure 8.2 – Test area layout and targets' position (left) and test field with buried test mines indicated by arrows (right).

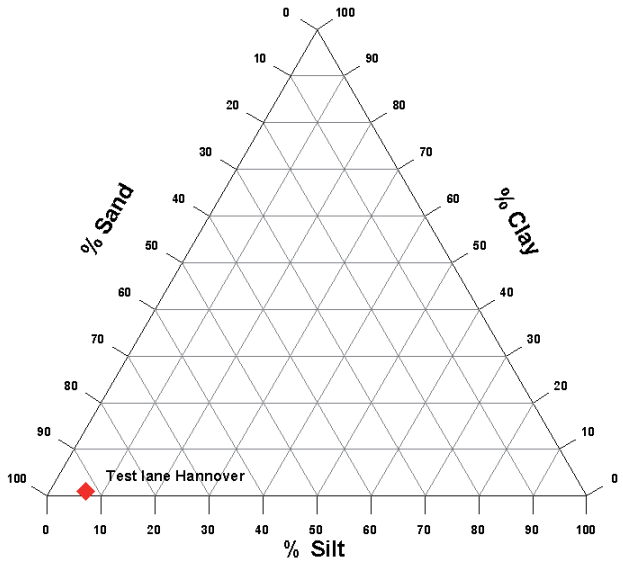

Figure 8.3 – Texture triangle set after laboratory analysis, clay=1%, silt=6.7%, sand=92.3%

8.3.1 Preprocessing

In the next sections we describe some basic preprocessing methods which are typically applied to the GPR data, either offline or in real time during the acquisition process.

i. Stacking

Averaging, or stacking is used to reduce the random noise and consequently increase the SNR, by averaging several samples (A-scans) together (10 or 20 for the ERA system).

ii. DC Component Removal

A common feature in commercial GPR systems is the presence of a continuous or low frequency component, namely DC component, in the recorded A-scans so that the averaged level of the signal amplitude is shifted to a value different from zero. The appearance of this component is usually linked with both inductive effects and limitations on the system's dynamic range [Annan, 2003]. DC levels often vary depending on the medium below the antenna and its height, so this component might change slightly from one trace to another along a continuous profile. The DC component removal is necessary for a correct visualization and for the subsequent data processing because otherwise, the results may be significantly distorted.

iii. Time-Varying Gain

It has been shown that EM waves can be rapidly attenuated as they propagate through different materials. The response from a target can therefore be much smaller in amplitude that the direct wave. To clearly display both these responses a time varying gain function is often applied to the GPR data. This method is usually only applied for visualization since it modifies the target response.

iv. Frequency Filtering

Frequency filtering is a common signal processing technique and when correctly applied can substantially enhance features present in GPR data. Typically, simple low and high-pass filters are used and can be applied vertically to each A-scan or horizontally across a B-scan. A "devow" high-pass filter is commonly applied to remove very low frequency components which can be related to antenna tilt and inductive phenomena [Annan, 2003]. Similarly, a low-pass filter can be run to reduce high-frequency noise. We will apply here a digital band-pass filter over the raw data, typically for the bandwidth 100MHz-5GHz.

v. Clutter suppression algorithms: background removal

As mentioned before, the main problem for detection of AP mines with GPR is the presence of clutter. The clutter, which is defined as any electromagnetic phenomenon not associated with targets, cannot in general be treated as white additive noise. This significantly complicates the issue of clutter suppression. Most of the algorithms for clutter removal are based on the background subtraction in various forms. The main idea of the algorithms of this type is the definition of a background model and its removal from the measured signals.
By far the most popular techniques are average and moving average background subtraction. However, these methods should be used carefully where features of interest are planar interfaces, since such responses can be removed by this sort of filtering [Daniels, 1996]. Other approaches that have shown good potential to take the target/background decision and reduce the clutter are for example the wavelet transform [Carevic, 2000], independent component analysis [Karlsen et al., 2002] or system identification [Brooks et al., 2000].

vi. Hilbert transform

Recorded amplitudes and arrival times of the reflected signals are the first information used to interpret GPR data. However, the phase information is sometimes more sensitive to subsurface changes than the amplitude and an equivalent complex-valued signal is desirable.
A Hilbert Transform can be applied to decompose the recorded real-valued signal into its magnitude (by envelope detection), local phase, or local frequency components (the derivative of phase), which allows the phase to be reconstructed from its amplitude. The figure below depicts an example of the original and the resulting signal after applying the Hilbert transform to measured 1D data.

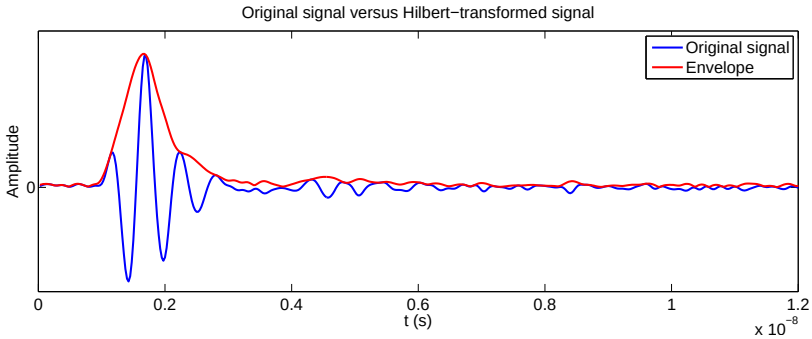

Figure 8.4 – Recorded 1D data before and after applying the Hilbert transform.

8.3.2 Postprocessing

To overcome the problem of landmine detection and classification in realistic scenarios there are several postprocessing techniques.
For the detection alone a model of the background can be defined and all the reflections that

clearly differ from the estimated background signal are declared as targets. Some algorithms that have shown good potential to localize anomalies and reduce the clutter are for example the already mentioned wavelet transform and related techniques [Carevic, 2000].
The approach followed in this thesis for the detection is, to establish a clutter level according to the average amount of scattered energy at each depth, and the detection is called when a cluster or a single pixel supersedes significantly this level. Another common method for target detection is based on performing a statistical binary hypothesis testing. However, it must be noted that such techniques are not capable of discriminating between a landmine and other reflectors present in soil (such as munition fragments, roots, stones, etc.), hence elevating the false alarm rate and becoming necessary additional processing to identify anomalies. A possible strategy relies on defining a target model given by a target feature vector and look for it in the data [Cosgrove et al., 2004], [Gader et al., 2001a], [Gader et al., 2001b], [Kovalenko et al., 2007]. The target feature vectors may be based on a single 1D waveform (A-scan) or on characteristic 2D or 3D target traces spread along several B-scans or C-scans (typically hyperboloid-like). The search of scattering features in the data can be implemented in different ways, including fuzzy logic approaches, neural networks, Markov models or Support Vector Machines.
In order to accelerate the detection process and make it real time, our recognition approach is based on the most simple feature vector, i.e., a single 1D waveform. Accordingly, the processing methodology presented here consists of an energy based detection algorithm which takes into account the amplitude information of the signatures and a target identification algorithm which considers the shape of the scattered waveforms. More specifically, we will see that a similarity measure (via cross-correlation) between measured and simulated temporal responses can be combined with the detection procedure to suppress image clutter and help in target recognition.
The complete procedure will be described in more detail in subsequent sections.

i. Energy based detection algorithm

The detection algorithm introduced in this section is based on scattered energy information. It is performed over the absolute value of the preprocessed 3D data (Hilbert transformed or not). Basically, it consists in normalizing the pixel energy per C-scan; then, we apply an energy threshold (required SCR constraint in dB) per pixel respect to the average amplitude value per C-scan and pixel (estimated clutter level at every depth) in order to find the most "brilliant" pixels and reject the ones below this level; finally, we sum all these energy contributions over an interval of the sampled time vector, thus obtaining the so called 2D detection map. This algorithm can be formulated as follows:

$$|I(x,y;t)| = \begin{cases} |I(x,y;t)| & \text{if } 10\log\left[\frac{|I(t)|}{E_\Omega(|I(t)|)}\right]^2 > \text{SCR} \\ 0, & \text{otherwise} \end{cases} \tag{8.1}$$

where $|I|$ is the absolute value of the recorded signal per pixel, x, y are the spatial coordinates and t the arrival times, SCR corresponds to the Signal-to-Clutter ratio in dB, $E(\cdot)$ is the expectation operator and $\Omega \subset (x, y)$ is the slice area.

Next, the aforementioned detection map can be calculated by the following sum over depth:

$$D(x, y; T) = \sum_{t=t_1}^{t_2} |I(x, y; t)|, \tag{8.2}$$

with $T = t_2 - t_1$ being the width of the time window considered for the detection.
It is possible to obtain 3D images of the detected targets if we perform the sum given by Eq. 8.2 for successive and very short time intervals along the whole desired investigation depth, so that we obtain a collection of detection maps for successive depth intervals which can be displayed in a 3D plot. This kind of representation would allow the viewer to localize the objects inside the whole imaging domain, giving him an impression of the target's real depth.
As an example, Fig. 8.5 displays the results after applying the detection algorithm to two of the surveys acquired in the LIAG Hannover test field. The preprocessing applied is simply a digital bandpass frequency filter and DC removal. No background removal by average subtraction is performed due to the high degree of inhomogeneity of the upper subsurface. Instead, we window the traces in time to eliminate partially the surface reflection and the antenna crosstalk. Nevertheless, in case of the PMA-2 simulants in survey SVY-151, the target scattering was enough strong to result in clear detections even when summing over the entire time axis without any windowing.
The performance of the energy-based detection algorithm can be improved using an Inverse Distance Weighted IDW averaging technique as shown in [Gonzalez-Huici & Giovanneschi, 2013]. In this way, the energy information within the neighbourhood of each individual pixel is considered before performing the energy thresholding given by Eq. 8.1.

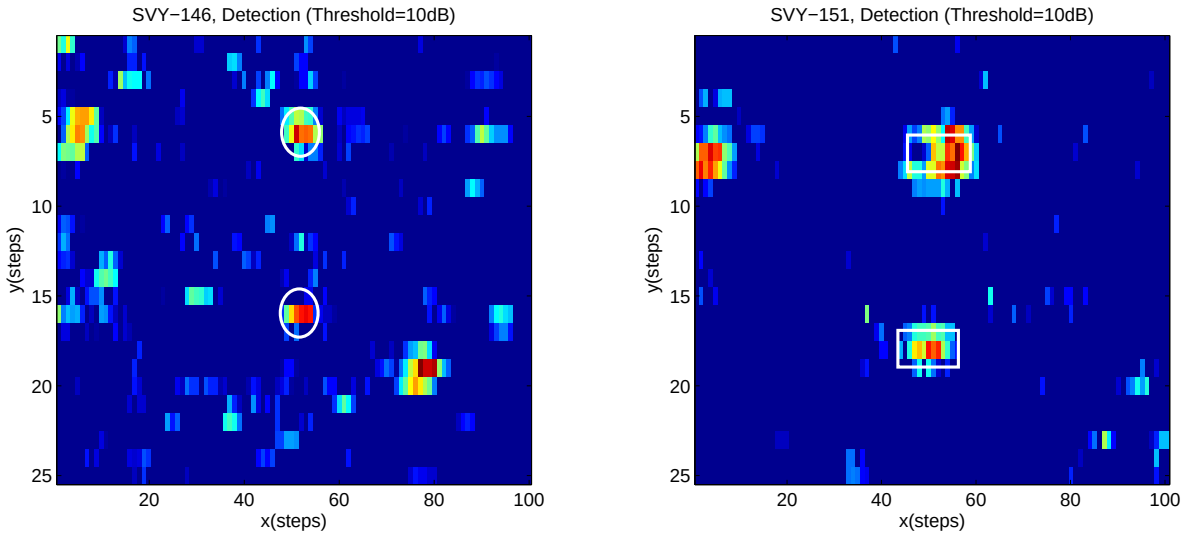

Figure 8.5 – Detection maps for the surveys 146 and 151. The targets in the middle are ERA test mines (left) and PMA-2 simulants (right).

As a measure of the detectability of the different test mines in the LIAG test field, we have also calculated the Receiver Operating Characteristic (ROC) curves related to the surveys with buried mines of the same class separately. The definition of a ROC curve within the landmine

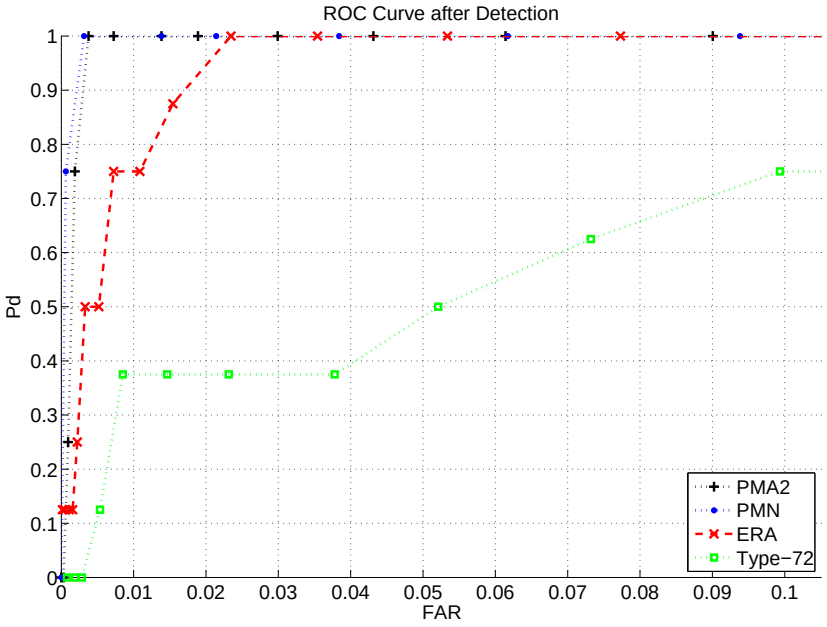

Figure 8.6 – ROC curves after applying the detection algorithm to the surveys with buried PMA-2, PMN, ERA and Type-72 targets respectively.

detection context was already presented in Chapter 2. The probability of detection (Pd) and the False alarm rate (FAR) are generated based on a pixel-wise calculation according to the following expressions:

$$\text{Pd} = \frac{\text{Number of detected mines}}{\text{Number of mines}} \tag{8.3}$$

$$\text{FAR} = \frac{\text{Number of false alarms}}{\text{Number of pixels outside halos}} \tag{8.4}$$

The target impact area assumed for a true detection was 12cmx12cm in all cases.
In Fig. 8.6 we show the obtained results. The points of the curves correspond to different SCR values for the detection algorithm. More detection results for other surveys are displayed in the following sections.

ii. Phase-shift and Stolt migration

As already stated in Chapter 2, due to the beam-width of transmit and receive antennas and the differences in round-trip travel time of the pulse caused by the movement of the antenna along the measurement line, the reflections from scatterers will appear as hyperbolic curves in the recorded data.
These hyperbolic structures can be migrated (focused) into the real position of the corresponding scatterer via different migration techniques [Gazdag, 1978], [Schneider, 1978], [Stolt, 1978]. To apply these algorithms successfully a correct estimation of the velocity structure of the propagation medium, i.e., the dielectric permittivity of the soil, needs to be done.
The phase-shift migration is a Fourier transform based technique which is also referred to as

frequency-wavenumber migration (f-k migration). It makes use of the wave equation to back-propagate the received signal into the soil back to the scattering source, and obtain an image of the subsurface reflectors. For the implementation a monostatic setting is assumed (which is a valid approximation when the transmitter and receiver are close to each other); and we will only consider the 2D case, but the extension to 3D is straightforward. In this procedure, a 2D Fourier transform over the spatial components and time is calculated first via FFT as formulated below:

$$D(k_x, z_0 = 0, \omega) = \int\int d(x, z_0 = 0, t) e^{-jk_x x} e^{-j\omega t} dx dt \tag{8.5}$$

where d is the data matrix, ω is the angular frequency, z_0 is the antenna vertical position and k_x is the horizontal wave number. Here, it is assumed that d satisfies the wave equation.
Then, to determine the field at a range of depths, a phase shift is applied, which is dependent on the propagation constant. This phase shift operation is an extrapolation along z-axis.

$$D(k_x, z_1, \omega) = D(k_x, z_0 = 0, \omega)\ exp\left(j\sqrt{\frac{4\omega^2}{v^2} - k_x^2}\Delta z\right), \tag{8.6}$$

being v the EM wave velocity which is given by Eq. 2.1. In this way, by recursively extrapolating the field in steps Δz and using the result of each step as input for the next iteration the frequency-wavenumber distribution of the field can be reconstructed [Gu et al., 2004].
Finally, the migrated data is obtained via the inverse Fast Fourier Transform iFFT of the wavenumber data over k_x and ω for the imaging condition t=0,

$$d(x, z = z_1, t = 0) = \frac{1}{4\pi^2}\int\int D(k_x, z = z_1, \omega) e^{jk_x x} dk_x d\omega, \tag{8.7}$$

where z_1 is the vertical length of the migrated scene. In order the iFFT to be applicable to solve the above integral, the data matrix D previously needs to be evenly mapped into the k-space via interpolation.
This technique can handle velocity variations with depth by making the propagation velocity a function of z and assuming it is constant for each step Δz. When the velocity is assumed constant along z, it is known as Stolt migration or Stolt mapping [Stolt, 1978]. This method does not account for lateral velocity changes. Several interpretations of the Stolt migration exist in seismic processing literature. A good overview is given in [Yilmaz, 2001].
For validation purposes, we first display the migration of the scattered energy by two of the considered test mines in free space (see Fig. 8.7). It is interesting to observe that for the case of the PMN on the right, we can even roughly recognize its shape, and the horizontal length is well reconstructed. The vertical length is a bit longer than the actual height of the simulant, but this is because the target, which is not a point scatterer, has a component material with a relative permittivity higher than 1 and the algorithm assumes constant permittivity in range equal to 1 for free space.
In Figures 8.8 to 8.11, we show processed images after applying Stolt migration to different B-scans measured in the field. In particular, in the middle of each image we can see four different buried test mines, from the most difficult to detect, the Type-72 in survey SVY-142, to the easiest one, the PMN in survey SVY-140. On the top of each figure, we represent the preprocessed raw data only for comparison; both plots in the middle illustrate the corresponding migrated data (original

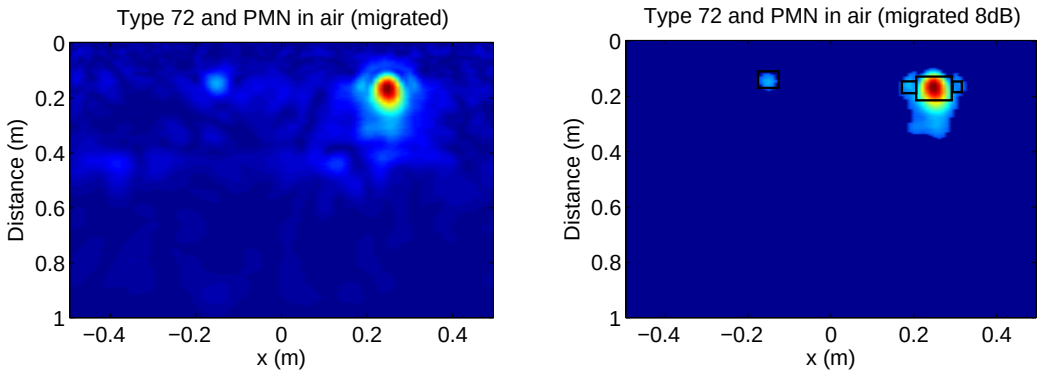

Figure 8.7 – Migrated image with two targets in free space. Left: Type 72 and PMN simulants; right: same as before with background noise removal (8dB). Survey SVY-188.

and filtered) and the plot on the bottom displays the energy contrast of the image for different permittivity values. For all these reconstructions in soil, the reason why we have selected different values of the background permittivity is because we are applying an adaptive Stolt migration algorithm that automatically estimates the permittivity which maximizes the energy contrast of the scene. Then, the resulting permittivities are different for each survey because the soil is highly inhomogeneous. A suitable quantitative measure of the above mentioned image contrast is given by [Cumming & Wong, 2005]:

$$C = \frac{E(\mid I \mid^2)}{[E(\mid I \mid)]^2}, \tag{8.8}$$

where I is the pixel magnitude and $E(\cdot)$ is the expectation operator. According to this definition we obtain the contrast curves illustrated on the bottom of each figure.

The adaptive algorithm used here, basically looks for the permittivity value which after the application of Stolt migration produces an image with a minimum number of pixels with energy above a given threshold. Thereby, it is not necessary to have a priori information about the permittivity of the soil. We explain this method in detail in [Gonzalez-Huici, 2011].

For the illustrated migration results the only preprocessing applied to the raw data has been again DC correction and bandpass filtering. By a subsequent time gating we have removed partially the antenna crosstalk and surface reflection, increasing the contrast to the object. To suppress some background clutter, a 8dB energy filter has been additionally applied to each survey.

In all the B-scans the targets are visible and their depth and size are quite well reconstructed. Moreover, the obtained permittivities are in agreement with the measured ones employing a TDR. Nevertheless, since the targets are shallowly buried, it is not possible to remove completely the surface and upper subsurface reflections, and these contributions are clearly visible in the migrated image. As the wavelength decreases in soil with respect to free space, we are able to distinguish top and bottom reflection for the biggest mine simulants, i.e., PMN and PMA-2. It must be noted that the Stolt migration assumes waves traveling through a homogeneous medium; hence, the obtained permittivity values correspond to the effective permittivity of the complete travel path, accounting not only for the soil propagation but also for the air propagation segment due to the antenna elevation.

It can be demonstrated that a preliminary migration of the input data for an energy-based

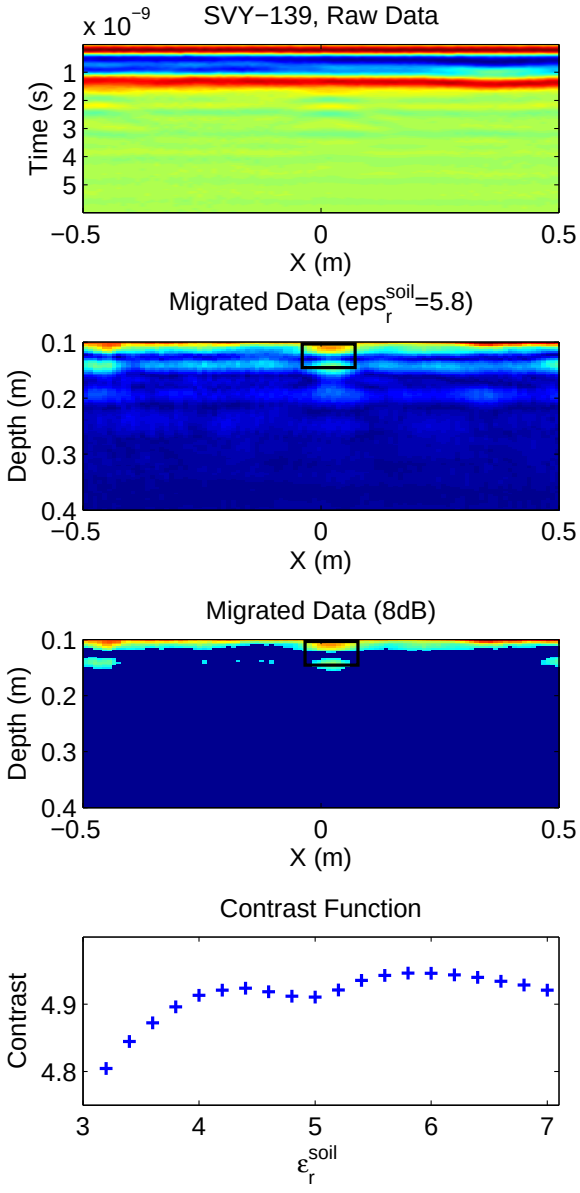

Figure 8.8 – From top to bottom: raw data with a PMA-2 simulant, migrated image, migrated image with background noise removal (8dB), contrast function. Survey SVY-139.

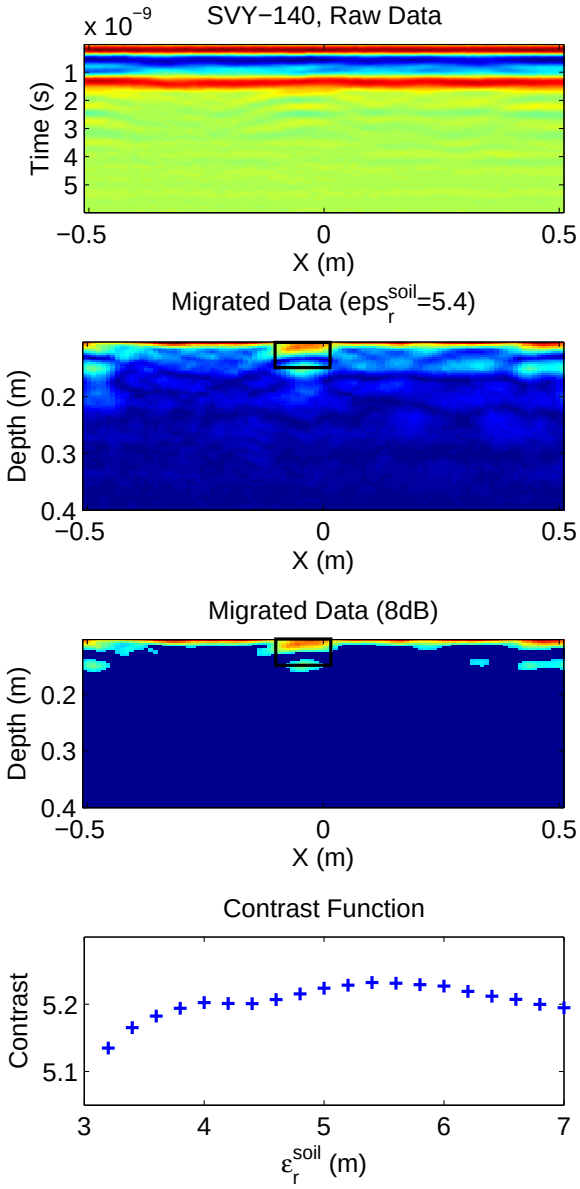

Figure 8.9 – From top to bottom: raw data with a PMN simulant, migrated image, migrated image with background noise removal (8dB), contrast function. Survey SVY-140.

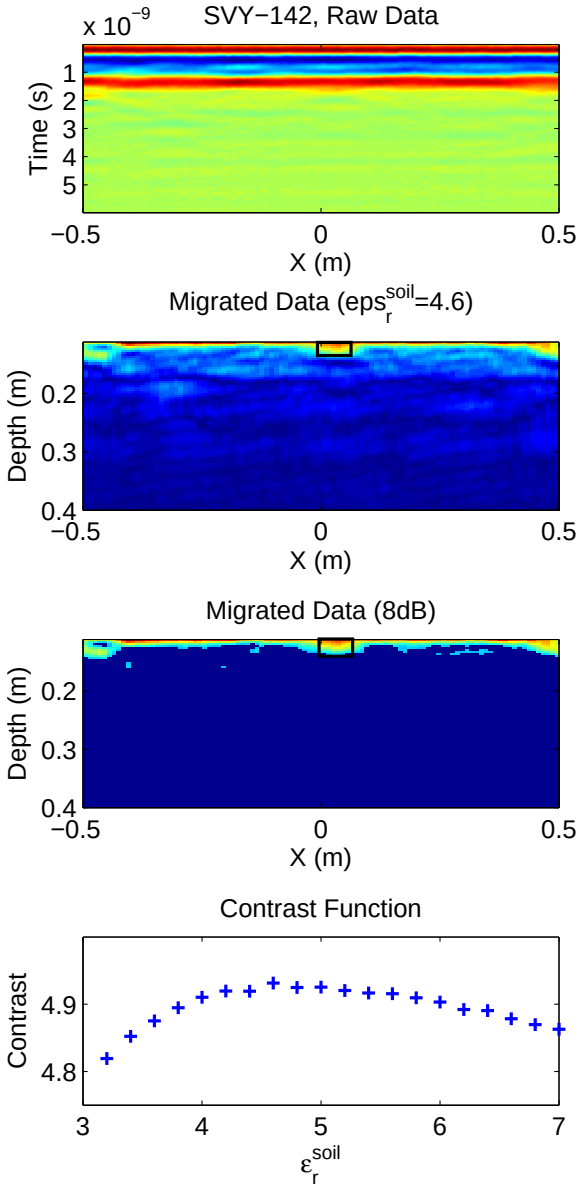

Figure 8.10 – From top to bottom: raw data with a Type-72 simulant, migrated image, migrated image with background noise removal (8dB), contrast function. Survey SVY-142.

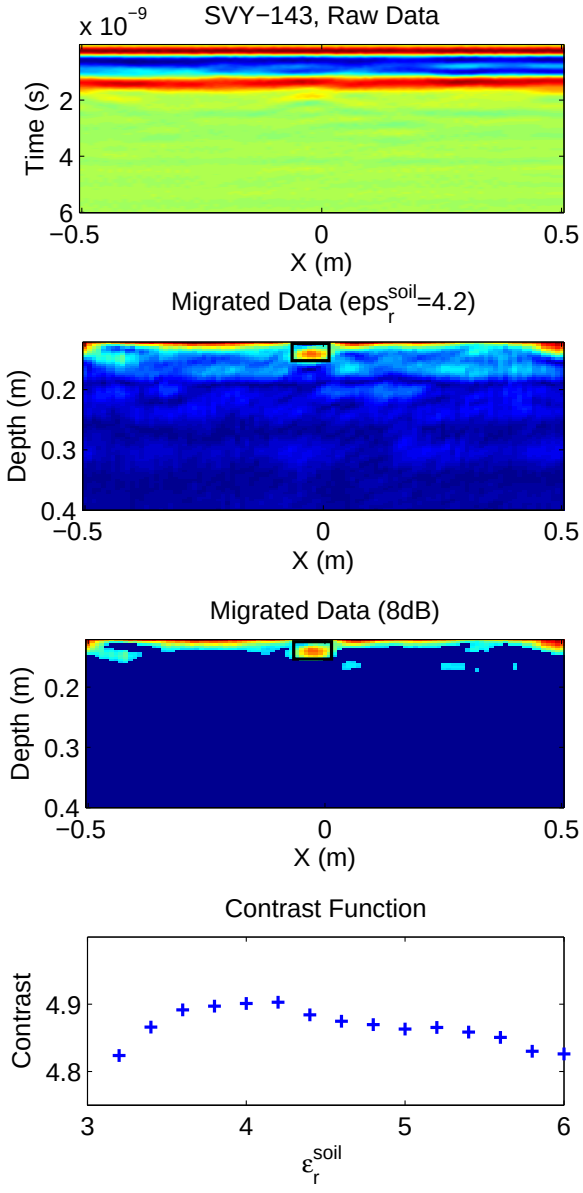

Figure 8.11 – From top to bottom: raw data with an ERA test target, migrated image, migrated image with background noise removal (8dB), contrast function. Survey SVY-143.

detection algorithm like the one presented before, may improve notably the detection rate of antipersonnel landmines (see for example [Feng & Sato, 2004]) but this is not the focus of this thesis.

iii. Cross-correlation based identification algorithm

A measure of the similarity between a given signal $u(t)$ and a reference $v(t)$ is well-known by means of their cross-correlation function,

$$R_{uv}(\tau) = \int u(t-\tau)v(t)dt = u(-t) * v. \tag{8.9}$$

This function shows the analogy between two non-identical waveforms as a function of the time shift τ between them and may reveal similarities undetectable by other techniques. The cross-correlation can be approximated by the sampling method:

$$R_{uv}(\tau) = \frac{1}{N}\sum_{n=1}^{N} u(n\Delta t - \tau)v(n\Delta t). \tag{8.10}$$

From the previous definition, we observe that the cross-correlation is essentially an averaged sum of the term by term product of one waveform and the delayed version of the second waveform. It depends linearly on the magnitude of the input signal $u(t)$. But, for our purpose, we are just interested in the shape information since the amplitude of the signal or its energy does not represent a feature for the target model. Then, a normalization of the input and reference waveforms needs to be performed before the comparison of the waveforms. However, to carry out the input signal normalization is not a trivial issue because the target response usually does not possess the highest amplitude in the trace, in particular if the direct coupling and the surface reflection are not removed. Then, as we only wish to keep the shape information, the input signal should be windowed in time and normalized before carrying out the similarity measure:

$$\bar{u}(t,T) = \begin{cases} \frac{u(T)}{max\{|u(T)|\}}, & \text{for} \quad t_1 \leq T \leq t_2 \\ 0, & \text{otherwise} \end{cases} \tag{8.11}$$

where $\bar{u}(t,T)$ is the new input signal for the cross-correlation calculation and T is the time window.

Applying this method, the discrete cross-correlation of a normalized portion of a measured A-scan and a high-quality normalized reference wavelet (which is obtained by accurate numerical modeling) is determined. Then, the maximum absolute value of the cross-correlation vector determines the correlation coefficient ρ_{uv} between both waveforms:

$$\rho_{uv} = \max\{|R_{uv}|\}. \tag{8.12}$$

Measurements vs. Simulations To test the achieved similarity degree between simulated echoes using accurate CAD models of the targets and actual measurements, we carry out some tests in laboratory with the test mines displayed in Fig. 8.1. The cross-correlation is computed

for a sequence 2N-1 time shifts $T(m-N)$ where $m = 1, ..., 2N-1$ and N is the length of the vectors u and v.

Figure 8.12 depicts the comparison of the normalized synthetic and recorded responses for the considered test mines in free space and the corresponding cross-correlation measure between both waveforms. The scattering signatures are obtained subtracting the simulated/measured signal without target from the scattered simulated/measured signal with target for each of the cases. The material electrical parameters to simulate the test mines are taken from [Hippel, 1995].

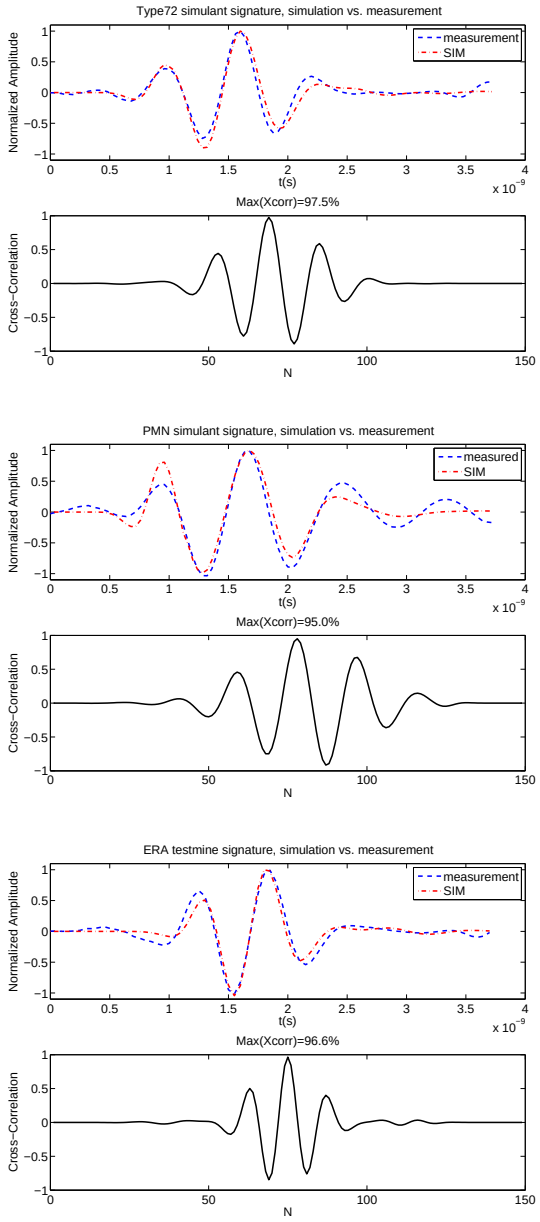

Figure 8.12 – Cross-correlation between measured and simulated signatures for a Type-72 simulant (top), a PMN simulant (middle) and an ERA test target (bottom).

The different plots reveal a high correlation coefficient between simulations and measurements for

all the three objects analyzed. Even for the PMN, which is the one with most complex internal structure, a correlation coefficient of 95% was achieved.

Class maps The class map is a classified image comprised of a mosaic of pixels, which are color-coded according to the target class they belong to. To elaborate this sort of map we perform the cross-correlation trace by trace with all the reference waveforms present in the database. The values of the correlation coefficient obtained for each reference signature in the survey area define a data level (slice) C^k for that survey area. Besides, the pixels where these coefficients are below a certain similarity threshold are set to zero, so that the data level for a reference target k (class) is given by:

$$C^k(x,y) = \begin{cases} \rho^k(x,y) & \text{if } \rho^k(x,y) > \text{Threshold} \\ 0, & \text{otherwise} \end{cases} \tag{8.13}$$

where k is the corresponding reference class for that data level. Each individual pixel of the final map is then classified based on this similarity information. For those samples with a zero in all the data levels, the corresponding cell is declared as empty, i.e., the assigned $Class$ is "No object". For the rest of pixels, the class declaration $Class$ corresponds to the most similar reference target, which is the object from the dataset whose synthetic signature has the highest correlation coefficient (maximum similarity) with the considered trace:

$$Class\ (x,y) = \max_k \{C^k(x,y)\}. \tag{8.14}$$

As an example, Figures 8.13 and 8.14 depict two of the computed class maps for one survey with buried PMA-2 simulants (not present in our database) and another one with buried ERA test targets. The computed detection maps are also illustrated for comparison purposes.

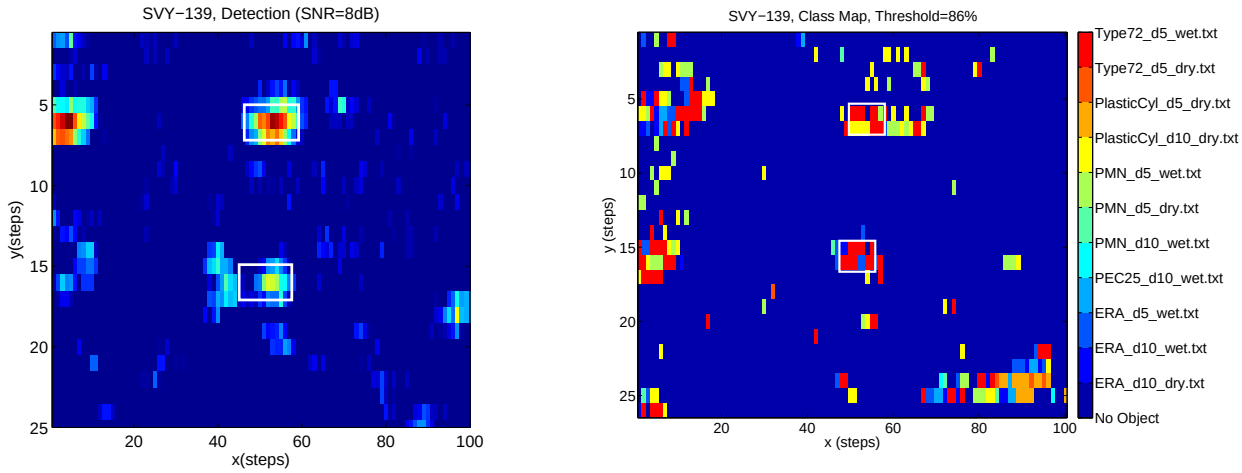

Figure 8.13 – Detection map (left) and class map of the survey SVY-139. The target in the middle is a PMA-2 simulant, which is a rectangular plastic mine (height=3.5cm, length-xwidth=6x14cm).

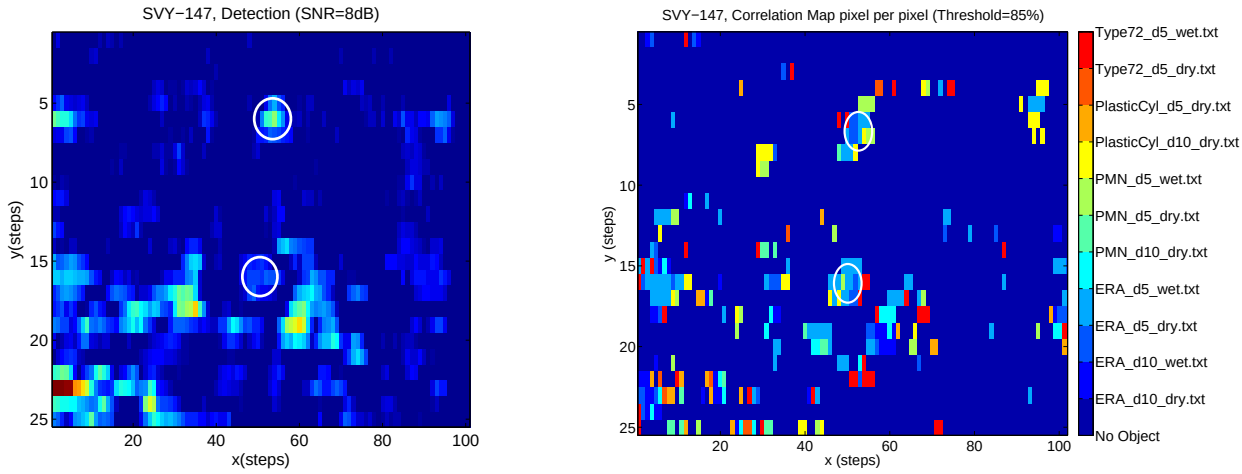

Figure 8.14 – Detection map (left) and class map of the survey SVY-147. The target in the middle is an ERAtest mine.

In the middle of both images there are aggregates of coloured pixels, which correspond with the position of the real targets. From the results, we can affirm that the class maps demonstrate the presence of buried objects and may be able to identify them correctly. In the directory of the database considered for the correlation calculation, there were 20 simulated waveforms for different landmine simulants and clutter objects buried in dry and wet soil at two different depths. For instance, none of the metallic objects in the dataset are declared in the maps, since their waveforms are not enough similar to any of the traces in the surveys. In the case presented in Fig. 8.13, there is no reference waveform in the synthetic dataset for the mine PMA-2 and the mine is wrongly declared but detected. This happens because the similar dimensions of the mines and all the clutter objects considered give rise to rather similar echoes. In particular, the bottom mine is identified as a Type-72 which has almost the same height as the actual PMA-2. Note the similarity of the detection for this survey and for the survey SVY-151 displayed in Fig. 8.5 (right). Both correspond to the same scanning area, but the measurements were taken in different days. In the second example, we have selected a survey with a particularly high noise level. As we can see in Fig. 8.14, after the detection algorithm alone, it is difficult to distinguish the bottom mine. However, in the correlation map an ERAtest mine is declared, which agrees with the reality.

iv. Detection-after-Recognition

Sometimes the energy-based detection algorithm alone does not work well since the backscattered energy by the landmine-like target is of the same order or below the clutter level. This will happen especially for very weak scatterers or for inhomogeneous soils where the clutter average value is high. The incorporation of a previous processing or filtering step, may help to improve this limitation, suppressing part of the clutter and hence, increasing the SCR. More specifically, we propose a combined Detection-after-Recognition strategy, that is illustrated in the block diagram below (see Fig. 8.15).

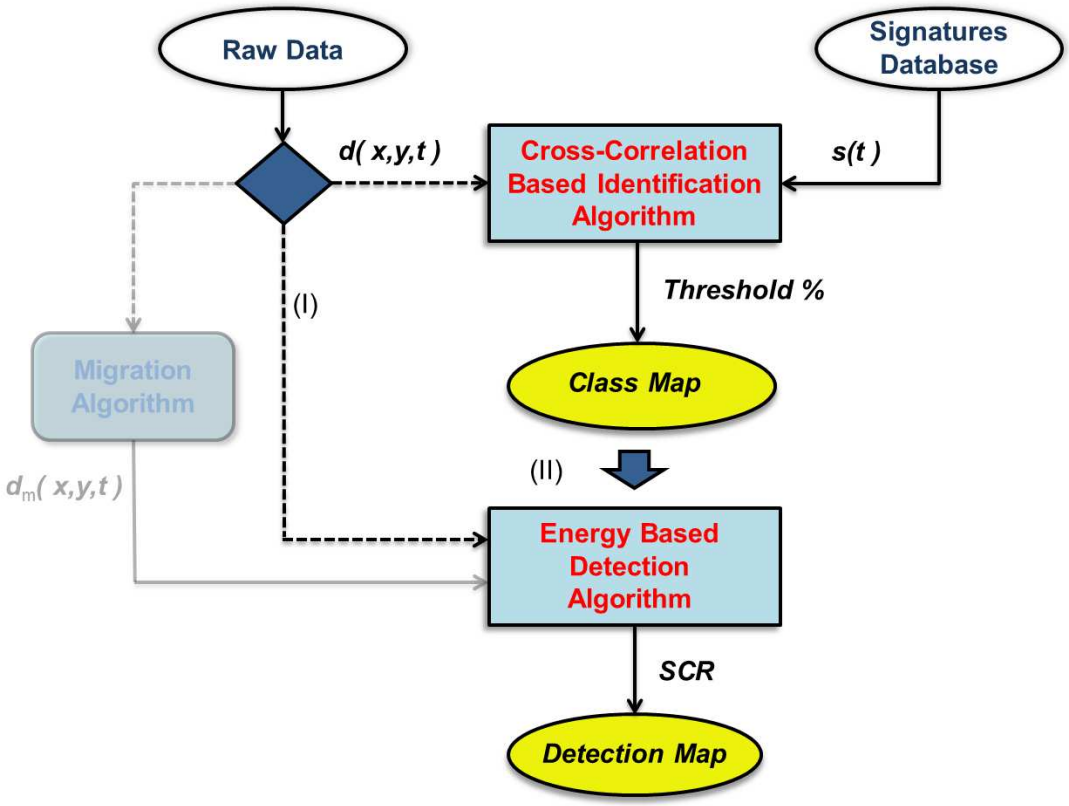

Figure 8.15 – Block diagram of the proposed methodology.

In this schematic overview of the combined approach, we see the input data on the top (measured d and simulated s), the main algorithms (for identification and detection) in blue and finally the resulting outputs, the class and detection maps, are highlighted in yellow. We observe that the input for the detection algorithm is either the raw or migrated data (only detection case), or the filtered (after the similarity constraint) data (Detection-after-Recognition case). In particular, the filter looks for the positions (x, y) in the input data matrix corresponding to those A-scans which show a correlation coefficient above a certain threshold. The rest of the traces in the data matrix are filled with zeros. Another possibility could be to take those coordinates (x, y) (already determined by computing the cross-correlation between the traces in the raw data and a given synthetic echo) and use them to filter the migrated data, i.e., to cancel all the migrated A-scans except for those at such positions. Afterwards, the detection algorithm will search in the filtered data for the pixels/clusters containing enough energy to be relevant according to Eq. 8.2. The similarity filter employed is defined as follows:

$$|I(x,y;T)| = \begin{cases} |I(x,y;T)| & \text{if } \rho^k(x,y) > \text{Threshold} \\ \mathbf{0}, & \text{otherwise} \end{cases} \tag{8.15}$$

where $|I(x,y;T)|$ represents again the absolute value of the time windowed recorded signal and $\rho^k(x,y)$ is the corresponding correlation coefficient with the reference waveform associated with the object k. In this way, we eliminate much of the clutter contributions and the estimated clutter level is accordingly lowered, resulting in a more efficient landmine detection performance.

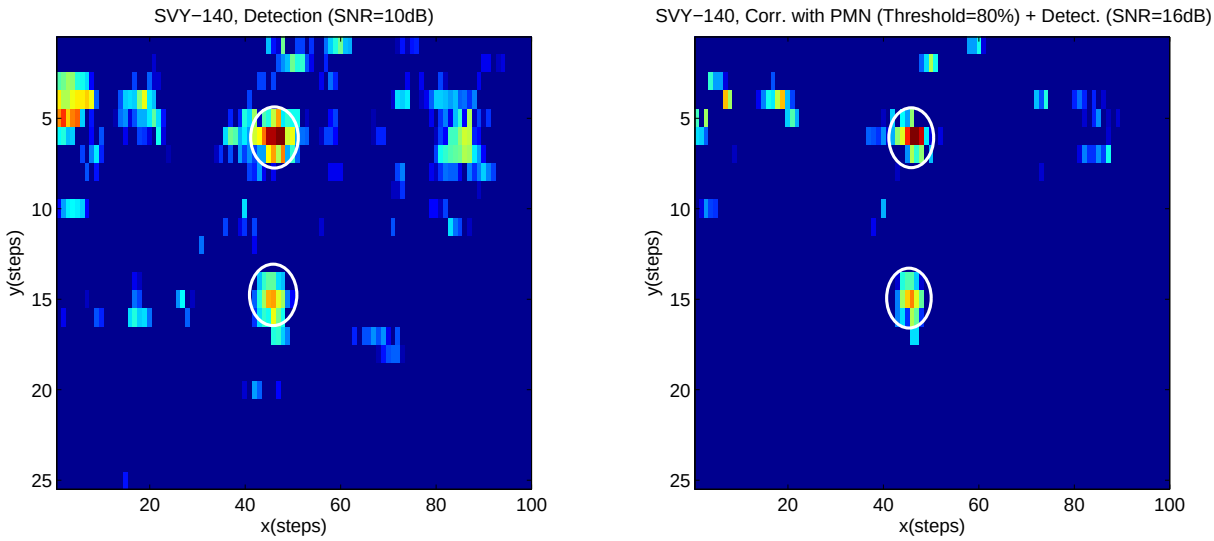

Figure 8.16 – Detection map without (left) and with similarity filtering (PMN) (right) over a survey area with buried PMN simulants.

Figures 8.16-8.22 display the improvement obtained by the combined strategy (right) in comparison with the application of the detection algorithm alone (left) for a collection of representative surveys carried out in LIAG Hannover. The selected time window for each survey remains the same as when we apply the detection alone. We can clearly appreciate that the clutter reduction is significant in all cases, even those with a buried Type-72. Moreover, the SCR, is now notably higher and the detection rate is not penalized. In difficult detection cases (weak scatterers), like the surveys SVY-147 and SVY-157, where the bottom test mines were hardly visible applying the detection algorithm alone, the performance of the combined algorithm is particularly satisfactory: the mines are now visible, i.e., the detection rate is notably enhanced. Furthermore, the achieved results are even more promising considering that the test field was highly inhomogeneous and the buried test mines were shallow and non-metallic. Finally, to evaluate the potential of this method to discriminate between targets we present below the ROC curves obtained after applying the combined strategy to the surveys with buried PMN, ERA and Type-72 mines respectively. Figures 8.26, 8.24 and 8.25 represent the ROC curves for each group of surveys. The discrimination threshold is the correlation coefficient. We also display the ROC curves after applying only detection for a better comparison.

In Fig. 8.26 we display the ROC curves for the biggest of the targets, the PMN simulant. In this case, since the mine contrast is high, the detection algorithm gives a very low false alarm rate ($< 1\%$) for a detection rate of 100 %. For such a situation, applying a similarity filter does not improve the curve in any case. This result makes sense since such a filter enhances certain samples, removing some others that don't fulfill the similarity criterion. But the cross-correlation calculation is done respect to a simulated reference wavelet in ideal conditions (homogeneous soil) for a CAD model of the target (which is not an exact copy) and for a given depth. As we have seen in a previous section, we never get a correlation coefficient between simulation and measurement above 99%. Then, the sensitivity of the similarity measure is below the true positive rate already achieved with the detection algorithm alone. However, applying the correlation filter we are able

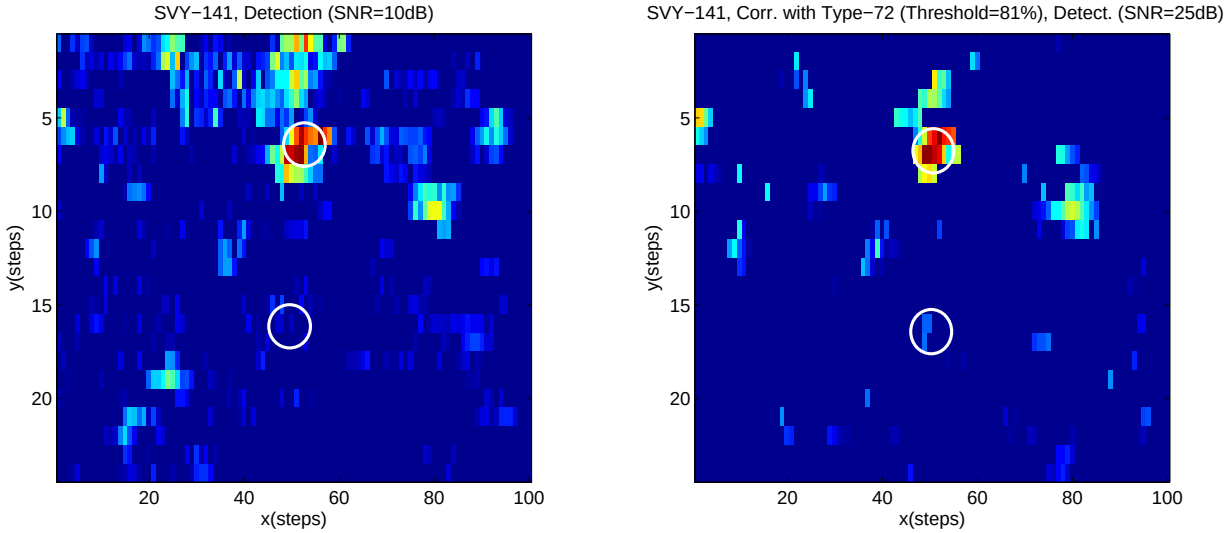

Figure 8.17 – Detection map without (left) and with similarity filtering (Type-72) (right) over a survey area with buried Type-72 simulants.

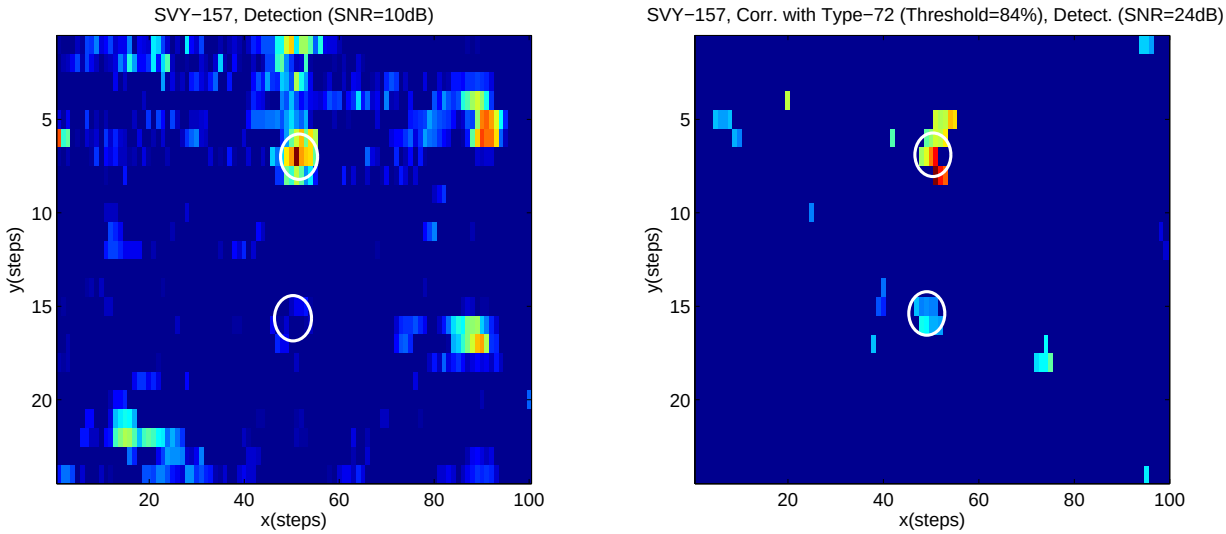

Figure 8.18 – Detection map without (left) and with similarity filtering (Type-72) (right) over a survey area with buried Type-72 simulants.

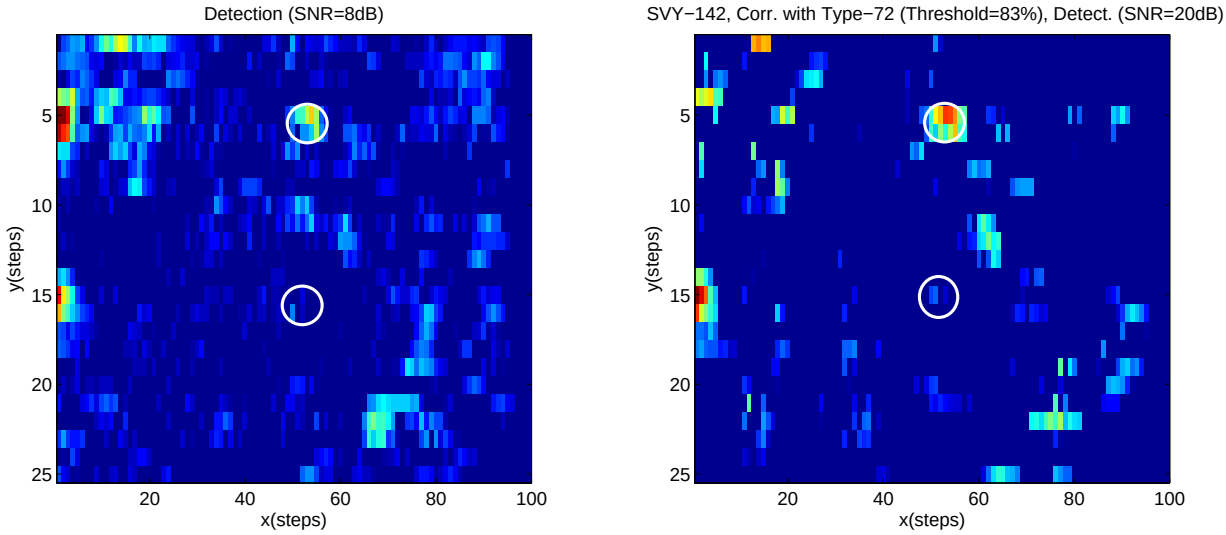

Figure 8.19 – Detection map without (left) and with similarity filtering (Type-72) (right) over a survey area with buried Type-72 simulants.

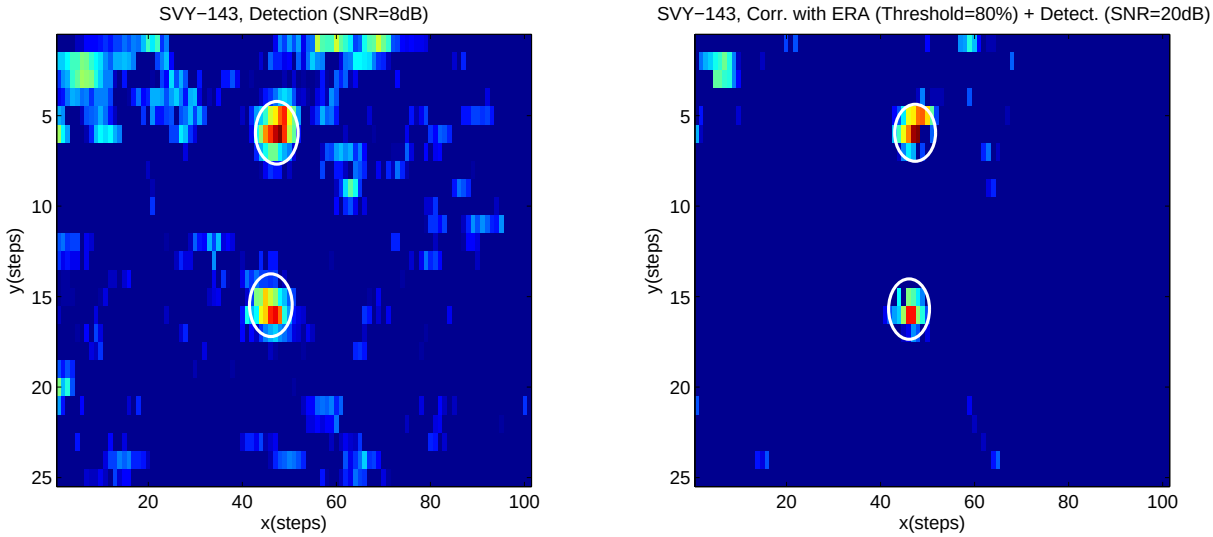

Figure 8.20 – Detection map without (left) and with similarity filtering (ERA) (right) over a survey area with buried ERA test targets.

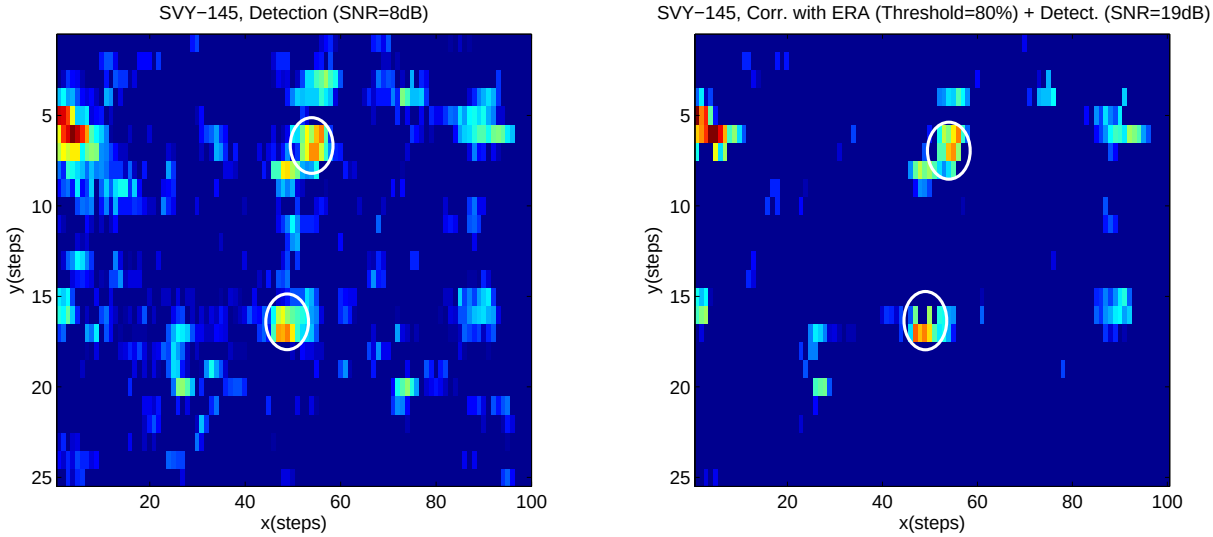

Figure 8.21 – Detection map without (left) and with similarity filtering (ERA) (right) over a survey area with buried ERA test targets.

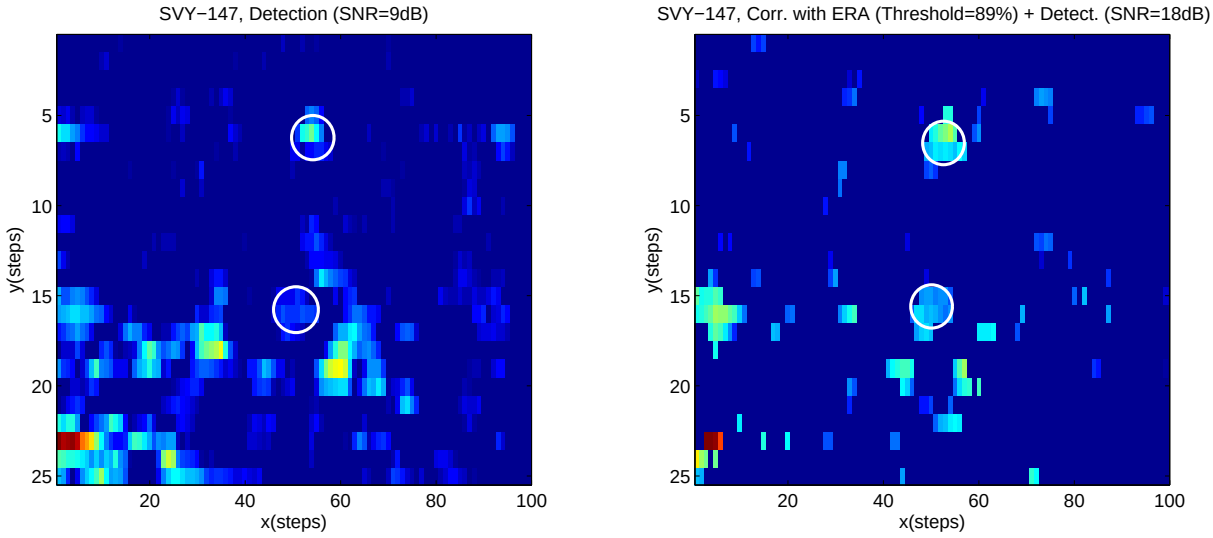

Figure 8.22 – Detection map without (left) and with similarity filtering (ERA) (right) over a survey area with buried ERA test targets.

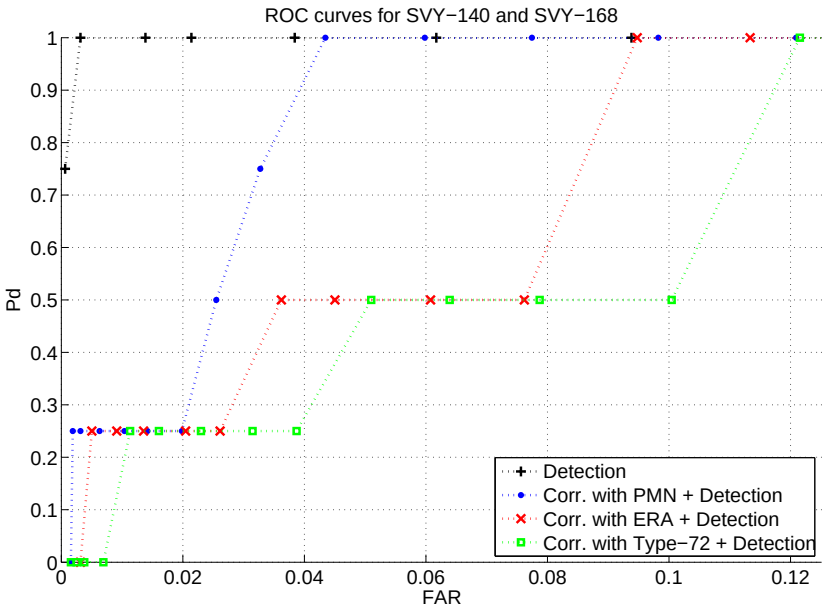

Figure 8.23 – ROC curves after applying the detection algorithm to the surveys with buried PMN simulant.

to classify the targets. We can clearly observe that the true positive rate is the highest for the PMN mine while for Type-72 the ROC curve shows the worst values, since the latter is the most dissimilar simulant.
A second example is illustrated in Fig. 8.24. Now, the true positive rate applying just the detection algorithm is still satisfactory but worse than in the case of the PMN mine, which is a logical result since the mine is smaller. In this case, after the application of the correlation filter, the true positive rate is improved when the comparison is made with an ERA test mine, which is the actual mine. For the other two simulants the curve gets slightly worse. In this case the mine discrimination is again successful.
The third example in Fig. 8.25 corresponds to the smallest and most difficult to detect simulant, the Type-72. We can see that in this particular case, the detection performance is very unsatisfactory. Applying energy-based detection exclusively, all the mines cannot be detected even for a low threshold (which gives rise to a high false alarm). On the other hand, when we perform the correlation step, the ROC curves are substantially improved even for a correlation with a false mine. This is because the mines are relatively similar (in size, shape and composition) objects whose signatures don't differ too much between each other. Then, when the energy detector performance is so bad, a similarity filtering with any little plastic cylindrical object will most probably improve the result. In particular, when we apply cross-correlation with the Type-72 reference waveform, the obtained ROC curve is the best one, achieving now 100% detection rate.

At this point, we must remark that the synthetic reference waveforms considered to carry out the comparison were just a first approximation and most probably not enough to be representative. They were computed for a few targets buried either 5cm or 10cm deep and antenna height of 5cm. The soil assumed for the simulation was homogeneous (either dry: $\epsilon_r = 5, \sigma = 0.001 S/m$ or wet:

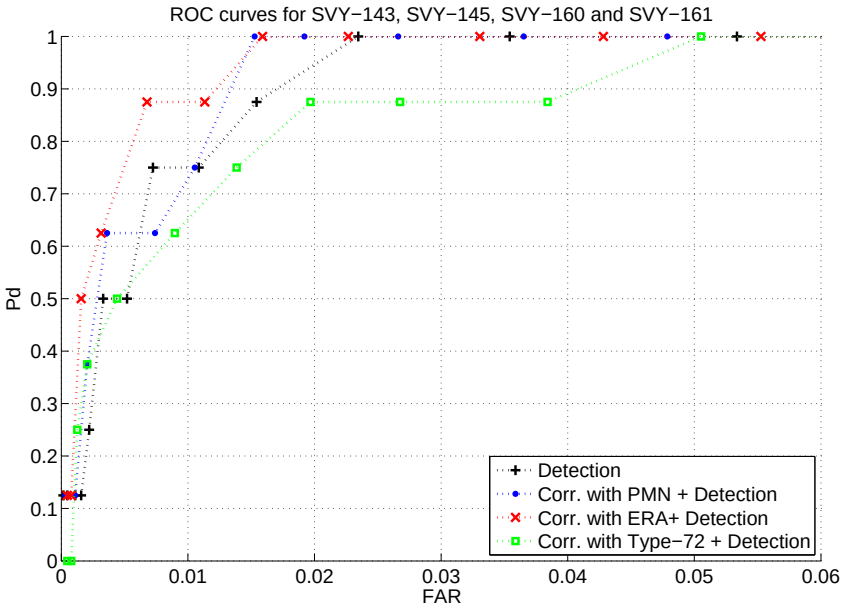

Figure 8.24 – ROC curves after applying the detection algorithm to the surveys with buried ERA test mine.

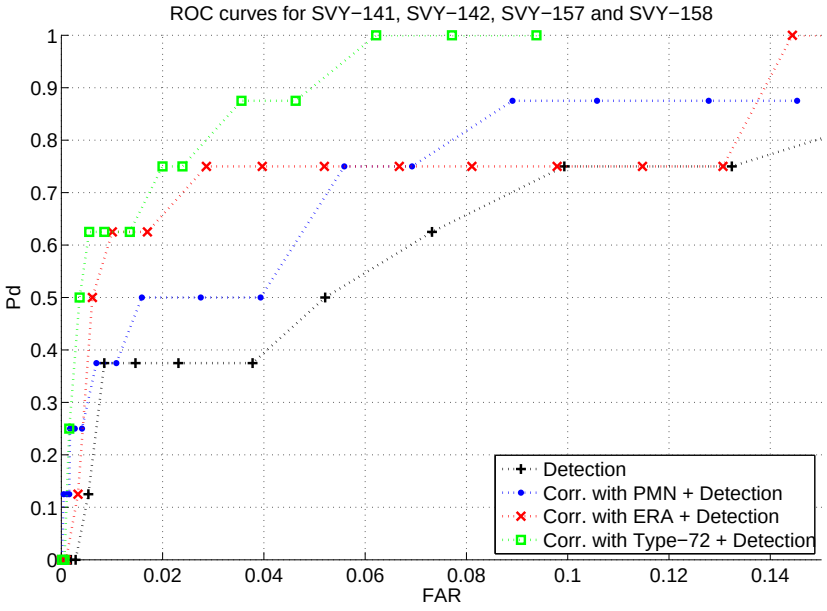

Figure 8.25 – ROC curves after applying the detection algorithm to the surveys with buried Type-72 simulant.

$\epsilon_r = 7, \sigma = 0.01 S/m$) while in the test field the soil permittivity values measured with the TDR sensor changed between 4.5 and 11. Moreover, the soil roughness made impossible to maintain a constant antenna height. Then, the obtained results could probably have been better if a more accurate and large collection of waveforms had been considered. Nevertheless, the goal here was not to build a complete database, but to demonstrate the potential of adding a similarity filter based on accurate simulations to reduce the false alarm rate and classify the targets.

Summarizing, the procedure presented seems to work well as classifier even for an inhomogeneous scenario like the one considered for the test. In particular, it achieves a clear false alarm reduction respect to only energy detection when the ROC curve from the latter lies above 2% false alarm for 100% detection rate, i.e., for those landmines that are most difficult to detect (small and low-contrast). These are the situations where more complicated GPR postprocessing algorithms become imperative and this method seems to bring at least part of the solution to the problem. The presented strategy and examples were also introduced in [Gonzalez-Huici & Uschkerat, 2010] and [Gonzalez-Huici, 2012]; in the aforementioned [Gonzalez-Huici & Giovanneschi, 2013], we have proposed an extension of the methodology to enhance the imaging results incorporating an IDW averaging technique.

8.4 A GUI for automatic landmine detection and recognition

A Graphical User Interface for target detection and recognition has been additionally developed. The GUI allows reading, visualizing and processing the GPR data in an automatic and user-friendly way. The interface is connected to a representative but still small database with the scattered waveforms by the previously presented landmine simulants and some canonical clutter objects made of metal or plastic. The echoes correspond to the scatterers in free space and buried in three different soils (dry, medium and wet soil) at three different depths (5cm, 10cm and 15cm). All the standard preprocessing methods along with the energy based detection algorithm, cross-correlation based identification technique and the combined Detection-after-Recognition strategy has been implemented, being possible to visualize the resulting detection and class maps for each survey. The similarity measure is performed with the reference objects included in the database folder selected by the user. Some other reconstruction (adaptive migration and tomographic inversion) algorithms are being incorporated. A screen shot of the GUI after the application of the combined methodology to one of the surveys acquired in LIAG Hannover is displayed below.

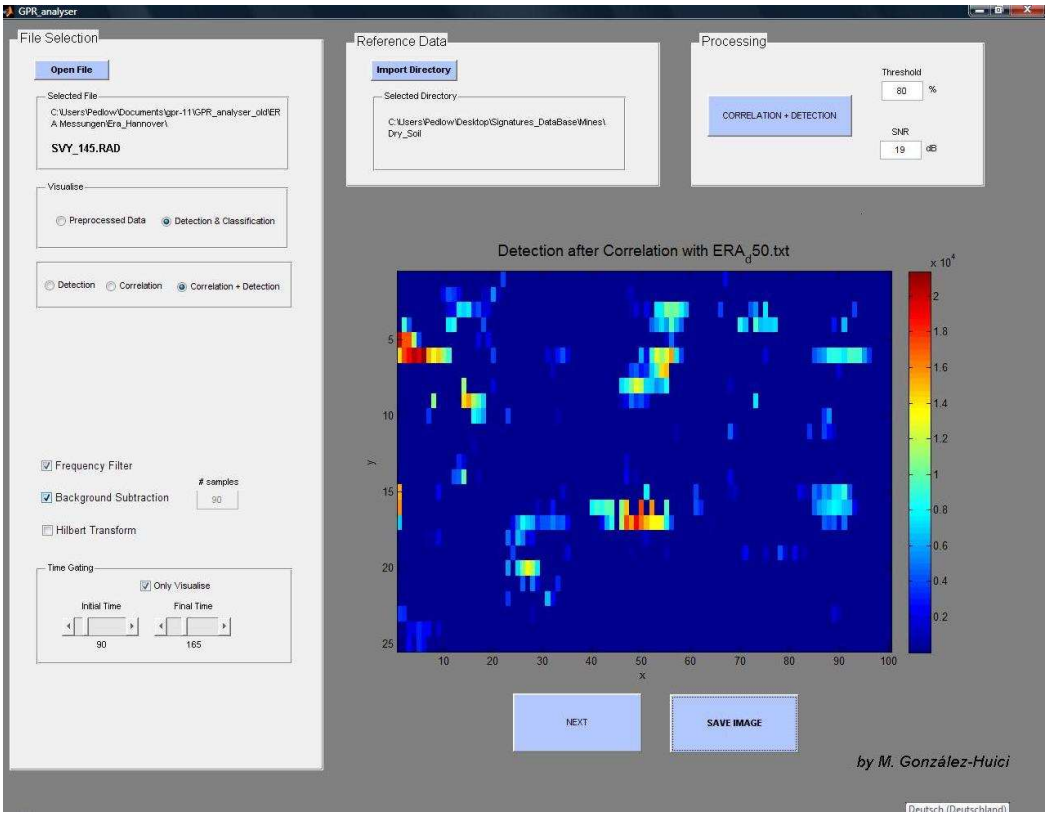

Figure 8.26 – Screen shot of the GUI.

9

Conclusions

When you reach the top of a mountain, keep climbing
Zen Proverb

In this thesis we have described the process of full forward modeling a real GPR scenario and have presented several simulations in the context of radar antenna characterization and target scattering signature retrieval and interpretation.
The modeling problem was firstly addressed in 2D, investigating several simple and more complex soil/target configurations and assuming ideal plane wave illumination. After this initial approach, we faced the task of accurately modeling a real UWB GPR antenna and we performed a comprehensive parametric study (in frequency domain) of the antenna radiation characteristic and performance for several antenna parameters/setups in free space and above different soil types. This analysis was helpful to explore the parameters that control the antenna directivity, gain and bandwidth. It may be also useful for setting an upper limit on the capability of a particular GPR system given a particular configuration. Based on the acquired knowledge, we were able to built an adequate model to simulate our commercial GPR system.
The above antenna model was optimized by comparing and fitting the simulated GPR responses in time domain with some free space laboratory measurements. Furthermore, the impact on the radar echoes of the antenna system characteristics, the target size and geometry, and the soil conditions were fully investigated, including an analysis of the effects of soil inhomogeneity as well as surface roughness. To finish this part of the investigation an overall summary along with some guidelines to elaborate a representative database were highlighted. Summarizing, this study supplied a deep physical understanding of the complex scattering phenomena involved and the influence of fundamental parameters on the soil and target radar response.
In the last and most practical part of this thesis and considering the model presented before, we simulated the scattering signatures of several test mines and clutter objects (in free space and buried in typical soils) in order to investigate the potential of accurate modeling to identify

the GPR returns and discriminate between scatterers. To do this, we defined a combined detection and recognition strategy based on the incorporation of a similarity filter with synthetic reference waveforms into an energy based detection scheme. This algorithm was applied to some experimental data acquired in a prepared test field and we demonstrated that this method can substantially reduce the clutter and increase the true detection rate for those mines most difficult to detect. The technique showed also satisfactory results in target recognition.

9.1 Future work

There is still much work to do in order to bring the acquired knowledge to a practical demining system that supersedes the performance of a single metal detector. The new system should be reliable, considerably faster and present a better detection characteristic than a standard sensor in order to compensate for the higher costs of the new system itself and operator training time/costs.

Possible future work would be to develop a complete and well-structured target database (with the corresponding synthetic reference signatures or some other characteristic features) that should be integrated in the GPR system together with an optimized detection/recognition algorithm to automatically search for the signatures/features of mine-like targets and detect/identify them. A k-nearest neighbour (K-NN) based approach could be also incorporated within the processing chain to reduce different mine declarations in neighboring pixels to a single mine type per cluster. Even if a complete and efficient classification of the detected objects would be the final goal to achieve, it is at least desirable to be able to discriminate correctly between mines and other clutter objects, which would reduce significantly the false alarms and accelerate the demining labors. For this task, self-learning techniques such as Support Vector Machines or Neural Networks could be considered [Yang & Bose, 2005], [Massa et al., 2005], [Parekh et al., 2000], even though these type of approaches usually require large training sets (and for this application are not easy to get).

Furthermore, to make the algorithm more robust and assist the classification of "difficult" targets, other recognition methods can be added to the main classification procedure, like algorithms for detecting specific shapes or materials that do not try to reconstruct or identify every anomaly in soil, but they just look for certain characteristic scattering patterns (1D or 2D) in the recorded signals.

As we have mentioned, data migration (via for example Stolt migration) applied prior to the detection algorithm may notably improve the detection rate of landmines. The Stolt migration can be made adaptive as shown in [Gonzalez-Huici, 2011] in order to avoid introducing a priori information (often unknown) about soil parameters into the algorithm. However, when considering migration for an homogeneous medium (as it is the case presented here) some artifacts and image blurring may happen due to the vertical velocity variations associated with the different material layers. Then, another task might be to extend the adaptive Stolt migration to a layered medium, making it adaptive for every single layer, where each layer thickness is jointly with the background permittivity automatically estimated and optimized to get a satisfactory focusing.

Other focusing techniques could be also further investigated in order to not only improve

the detection but also to approximately localize and reconstruct the object shape in 3D. Among them, presently we are paying special attention to the backprojection technique [Ribalta & Gonzalez-Huici, 2013a]. The 3D visualization of the focused information, may help the operator to interpret the recorded data and in general, enhance the detection and recognition of the scatterers.

Another possibility to identify or reconstruct the scatterers may be to build an efficient tomographic inversion algorithm, which would allow to obtain the electromagnetic contrast function of the subsurface through the measurements taken above the surface. In fact, inversion is the only technique capable of reconstructing not only the shape but also the electromagnetic parameters (and then, the composition) of the scatterers. However, this is a typical illposed problem (there are many possible solutions which satisfy the integral equation to be inverted) and the more data we collect (frequencies, illumination angles and traveling paths), the more we reduce the solution domain, i.e., the more accurate solution we will achieve.

There are a few approaches to this problem that employing certain approximations (Born Approximation) and making certain assumptions (antennas are Hertzian dipoles, the soil is nonmagnetic, either the conductivity contrast dominates over permittivity contrast or vice versa) can reach satisfactory solutions in some cases but in general this is a rather complex mathematical problem and is still open.

For obvious reasons this method cannot produce automatic results from single or small collection of A-scans, and it is hardly applicable in real time for demining labors.

All the topics discussed and investigated along this thesis are presented within the landmine detection and identification scope. Nevertheless, the proposed algorithm for detection-after-recognition of landmines may also be of interest in other application areas, like for instance in civil infrastructure sector (to recognize pipes, cables, and other utilities and their filling materials).

Appendices

Appendix A

Boundary Conditions in COMSOL

In the next sections we describe the formulation of the boundary conditions applied in the models presented in this thesis. The definition of the complete list of boundary conditions available in the Electromagnetic Module of COMSOL Multiphysics is out of the scope of this appendix. Such a description can be found in [COMSOL, 2005].

A.1 Absorbing Boundary Conditions

Truncating the computational domain without introducing large errors due to the reflections at the boundaries in one of the great challenges in numerical modeling.
When solving radiation problems with open boundaries, special low-reflecting or absorbing boundary conditions have to be applied at the borders of the model geometry, which should lie in the order of a few wavelengths away from any source. The Electromagnetic Module offers two closely related types of absorbing boundary conditions, the *scattering boundary condition* and the *matched boundary condition*. The former can handle plane, spherical and cylindrical waves and is perfectly absorbing for an incident plane wave, whereas the latter is perfectly absorbing for guided modes, provided that the correct value of the propagation constant is supplied. However, in many scattering and antenna modeling problems, you cannot describe the incident radiation as a plane wave with a well-known propagation direction. In such cases, the use of *Perfectly Matched Layers* (PMLs) may be considered. PMLs are pure mathematical constructs that are not physically realizable, and by a suitable choice of the PML parameters it is in principle possible to minimize the energy reflected at the borders of the modeling domain.

A.1.1 Perfectly Matched Layers

In the seminar work of Berenger (1994) a new type of material ABC was introduced, referred as perfectly matched layer (PML).

The original PML technique is based on a split-field formulation of the Maxwell's equations while other PML approaches like the Generalized Perfectly Matched Layer (GPML) presented by [Fang & Wu, 1996]GPML are based on more compact stretched-coordinate formulations [Chew & Weedon, 1994] or combinations of both formulations. A more physical approach is the uniaxial PML (UPML), which does not involve the splitting of fields. In this formulation the absorbing material is a uniaxial anisotropic material involving permittivity and permeability tensors.

The original PML formulation can be deduced from Maxwell's equations by introducing a complex-valued coordinate transformation under the additional requirement that the wave impedance should remain unaffected for any frequency and any angle of incidence. For the implementation, it is more practical to describe the PML as an anisotropic material with losses and for simplicity, it is assumed that the wave is entering the PML from an isotropic medium.

To define a PML, we have to add an additional modeling domain outside the boundaries that we would like to be absorbing. The PML can have arbitrary thickness and is specified to be made of an artificial absorbing material. The material has anisotropic permittivity and permeability that match the permittivity and permeability of the physical medium outside the PML in such a way that there are no reflections. The subdomain representing the PML has anisotropic material parameters:

$$\begin{aligned} \epsilon &= \epsilon_0 \epsilon_r \mathbf{L} \\ \mu &= \mu_0 \mu_r \mathbf{L} \end{aligned} \tag{A.1}$$

where $\mathbf{L}$ is a rank 2 tensor. The values of the relative permittivity and permeability are those of the physical domain. For a PML that is parallel to one of the Cartesian coordinates, $\mathbf{L}$ becomes diagonal

$$\mathbf{L} = \begin{bmatrix} L_{xx} & 0 & 0 \\ 0 & L_{yy} & 0 \\ 0 & 0 & L_{zz} \end{bmatrix}$$

where

$$L_{xx} = \frac{s_y s_z}{s_x}, \quad L_{yy} = \frac{s_z s_x}{s_y}, \quad L_{zz} = \frac{s_x s_y}{s_z}$$

. The parameters s_x, s_y and s_z are the complex-valued coordinate scaling parameters. By assigning suitable values to these, you can obtain a PML that absorbs waves traveling in a particular direction. The values below represent a PML that attenuates a wave traveling in the x direction:

$$s_x = a - bi, \quad s_y = 0, \quad s_z = 0,$$

where a and b are arbitrary positive real numbers. For an x PML, the attenuation of a propagating wave over a distance Δx is given by the x component of the wave vector k_x, and the imaginary part of s_x:

$$|\mathbf{E}| = |\mathbf{E}_0| e^{-bk_x \Delta x}. \tag{A.2}$$

The real part of s_x affects how fast an evanescent wave decays in the PML. From the practical viewpoint, it is necessary to resolve the e^{-1} attenuation length in the PML with at least a couple of elements since a poorly resolved PML give rise to unwanted reflections. In the absence of evanescent waves, an imaginary part of $-i$ for s_x in the PML results in approximately the same

requirement on the mesh density as that for a propagating wave outside the PML (10 linear elements per wavelength). In many cases, due to the problem geometry, it is more convenient to use cylindrical or spherical PML. This is the case for the 3D antenna radiation simulations presented in this thesis, where we have applied spherical PMLs. Because the basic coordinate system of COMSOL Multiphysics is Cartesian, we give the Cartesian tensor component for spherical PMLs. Using spherical coordinates (r, θ, ϕ), it takes the form:

$$\mathbf{L} = \begin{bmatrix} \frac{\tilde{r}^2 s_\theta s_\phi}{r^2 s_r}\sin^2\theta\cos^2\phi + s_r(\cos^2\theta\cos^2\phi + \sin^2\phi) & \left(\frac{\tilde{r}^2 s_\theta s_\phi}{r^2 s_r}\sin^2\theta + s_r(\cos^2\theta - 1)\right)\cos\phi\sin\phi & \left(\frac{\tilde{r}^2 s_\theta s_\phi}{r^2 s_r} - s_r\right)\sin\theta\cos\theta\cos\phi \\ \frac{\tilde{r}^2 s_\theta s_\phi}{r^2 s_r}\sin^2\theta\sin^2\phi + s_r(\cos^2\theta\sin^2\phi + \cos^2\phi) & \left(\frac{\tilde{r}^2 s_\theta s_\phi}{r^2 s_r}\sin^2\theta + s_r(\cos^2\theta - 1)\right)\cos\phi\sin\phi & \left(\frac{\tilde{r}^2 s_\theta s_\phi}{r^2 s_r} - s_r\right)\sin\theta\cos\theta\sin\phi \\ \left(\frac{\tilde{r}^2 s_\theta s_\phi}{r^2 s_r} - s_r\right)\sin\theta\cos\theta\cos\phi & \left(\frac{\tilde{r}^2 s_\theta s_\phi}{r^2 s_r} - s_r\right)\sin\theta\cos\theta\sin\phi & \frac{\tilde{r}^2 s_\theta s_\phi}{r^2 s_r}\cos^2\theta + s_r\sin^2\theta \end{bmatrix},$$

where

$$\tilde{r} = \int_0^r s_r(r')dr'$$

.

A.1.2 Scattering Boundary Condition

This boundary condition is used when we want a boundary to be transparent for a scattered wave. The boundary condition is also transparent for an incoming plane wave. The wave types that this boundary can handle are:

$$\mathbf{E} = \mathbf{E}_{sc}e^{-jk(\mathbf{n}\cdot\mathbf{r})} + \mathbf{E}_0 e^{-jk(\mathbf{k}\cdot\mathbf{r})} \qquad \text{Scattered plane wave}$$

$$\mathbf{E} = \mathbf{E}_{sc}\frac{e^{-jk(\mathbf{n}\cdot\mathbf{r})}}{\sqrt{r}} + \mathbf{E}_0 e^{-jk(\mathbf{k}\cdot\mathbf{r})} \qquad \text{Scattered cylindrical wave}$$

$$\mathbf{E} = \mathbf{E}_{sc}\frac{e^{-jk(\mathbf{n}\cdot\mathbf{r})}}{r_s} + \mathbf{E}_0 e^{-jk(\mathbf{k}\cdot\mathbf{r})} \qquad \text{Scattered spherical wave}$$

The field $\mathbf{E}_0$ is the incident plane wave which travels in the direction $\mathbf{k}$. Note that the boundary condition is transparent for plane waves with any incidence angle. For the boundary to be perfectly transparent it is important that the boundary represent an open boundary. If the wave enters a guided structure where only certain modes are excited, this boundary condition will give reflections. For such boundaries that do not represent a physical boundary, it is more adequate to use the so called matched boundary condition. This boundary was not applied in any of the models presented in this thesis and it will not be described here.

A.2 Interface Boundary Conditions

In order to minimize the problem size it is convenient to replace thin layers with boundary conditions. For example we have replaced materials with high conductivity, like the antenna

sheets, by the perfect electric conductor boundary condition.

A.2.1 Perfect Electric Conductor

The perfect electric boundary condition sets the tangential component of the electric field to zero:

$$\mathbf{n} \times \mathbf{E} = \mathbf{0}.$$

This is a special case of the electric field boundary condition, which allows to specify the tangential component of the electric field.
In the transient case this boundary condition is used to set the tangential component of the magnetic vector potential to zero. Since the perfect electric conductor boundary condition

$$\mathbf{n} \times \mathbf{E} = -\mathbf{n} \times \frac{\partial \mathbf{A}}{\partial t} = \mathbf{0}$$

implies that

$$\mathbf{n} \times \mathbf{A} = \mathbf{A}(t = 0)$$

Normally the initial condition for $\mathbf{A}$ on a perfect electric conductor is zero. In the cases where the initial boundary condition is different from zero the magnetic potential boundary condition can be used.

A.2.2 Continuity

The continuity boundary condition is the natural boundary condition ensuring continuity of the tangential components of the electric and magnetic fields:

$$\mathbf{n} \times (\mathbf{E}_1 - \mathbf{E}_2) = \mathbf{0}$$
$$\mathbf{n} \times (\mathbf{H}_1 - \mathbf{H}_2) = \mathbf{0}$$

Appendix B

Plane Wave Scattering by Simple Canonical Objects

In this Appendix we introduce the analytical solutions to some canonical scattering problems which are of interest for validation and comparison with some of the simulated results presented in Chapter 5. In particular, we will show the solution to the scattering by a metallic and a dielectric circular cylinder and by a metallic and a dielectric sphere for an incoming plane wave. The complete derivations can be found in [Balanis, 1989] and [Harrigton, 2001].

B.1 Scattering by Circular Cylinders

Many practical scatterers can be represented by cylindrical structures and due to its simplicity and well known solutions, circular cylinders correspond to one of the most important types of scattering geometries. For instance, they are widely employed to represent typical radar scatterers such as fuselage of airplanes and missiles. In particular, in cylindrical coordinates (z, ρ, ϕ) the solutions are expressed in terms of the products of Bessel and Hankel functions and exponential functions. In this section only infinite cylinders and two dimensional cases are considered; the scattered field from finite length cylinders is calculated by transforming the corresponding solutions for infinite length applying approximate relationships.
Assuming an uniform plane wave (with only one electric component in the z direction as defined in Section 5.2) normally incident upon a perfectly conducting cylinder of radius a, the scattered electric field takes the form [Harrigton, 2001]:

$$E_z^s = E_0 \sum_{n=-\infty}^{\infty} j^{-n} a_n H_n^{(2)}(k\rho) e^{jn\phi} \tag{B.1}$$

with the coefficient a_n given by

$$a_n = \frac{-J_n(ka)}{H_n^{(2)}(ka)}, \tag{B.2}$$

where k is the wavenumber of the free space, ρ is the distance to the measurement point, and n is the order of the Bessel function of first kind J_n and the Hankel function of the second kind $H^{(2)}$. In the more general case of a dielectric circular cylinder it can be demonstrated that the scattered field is equal to [Balanis, 1989]:

$$E_z^s = E_0 \sum_{n=-\infty}^{\infty} a_n H_n^{(2)}(k\rho) e^{jn\phi} \tag{B.3}$$

and now the coefficient a_n is of the form:

$$a_n = j^{-n} \frac{J_n'(ka)J_n(k_c a) - \sqrt{\epsilon_r/\mu_r} J_n(ka) J_n'(k_c a)}{\sqrt{\epsilon_r/\mu_r} J_n'(k_c a) H^{(2)}(ka) - J_n(k_c a) H_n^{(2)'}(ka)} \tag{B.4}$$

with k_c the wavenumber of the dielectric medium and $' = \frac{\partial}{\partial(ka)}$.
An example of the resulting analytical solutions is displayed in the next illustration. It represents the scattered fields by one metallic cylinder and two dielectric cylinders of different radius at a distance of 10cm from the top of the object (and the z-polarised plane wave propagating from top to bottom along the xy-plane).

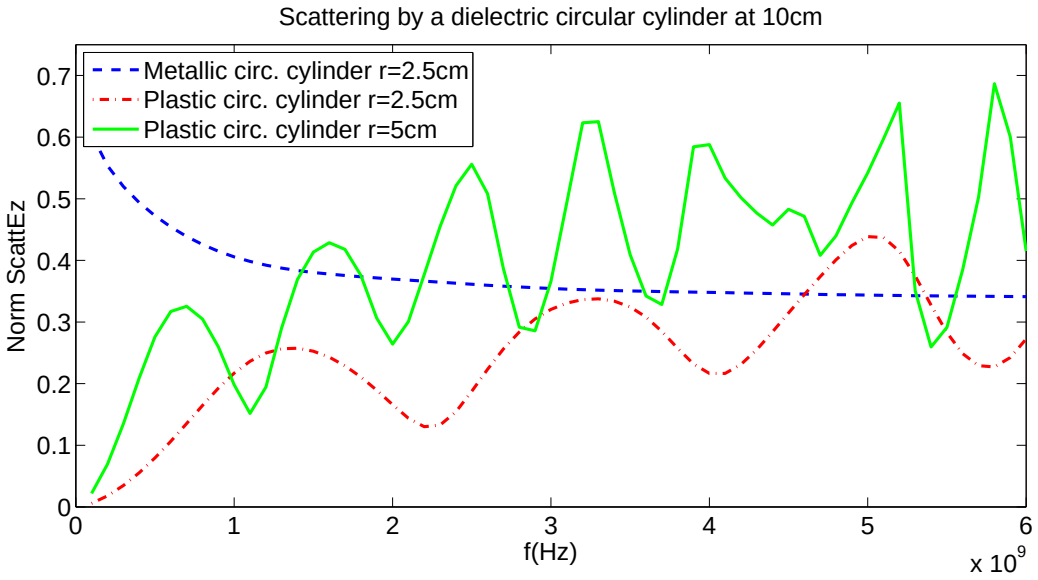

Figure B.1 – Analytical scattered field by different objects in free space and plane wave excitation; receiving point at a distance of 10cm.

The results represented in this figure can be directly compared with the simulated analogs previously displayed in Fig. 5.7 in Section 5.4. As we can observe, the agreement is very good.

B.2 Scattering by a sphere

Probably the most classic scattering problem if that of a plane wave scattering by a metallic sphere. Due to its symmetry, the sphere is often employed as a reference scatterer for calculating the scattering properties of other targets. The scattered fields are obtained through the

formulation of the radial components of the magnetic and vector potentials [Harrigton, 2001] and in spherical coordinates, the solutions are expressed in term of products of the Riccati-Bessel functions, associated Legendre polynomials, and exponential functions.
Assuming that the electric field of the impinging plane wave is polarized in the x direction and traveling along the z-axis, the scattered electric field components in spherical coordinates are given by:

$$\begin{aligned} E_r^s &= -jE_0\cos\phi\sum_{n=1}^{\infty} b_n[\hat{H}_n^{(2)''}(k\rho)+\hat{H}_n^{(2)}(k\rho)]P_n^1(\cos\phi) \\ E_\theta^s &= \frac{E_0}{k\rho}\cos\phi\sum_{n=1}^{\infty}\left[jb_n\hat{H}_n^{(2)'}(k\rho)\sin\theta P_n^{'1}(\cos\theta)-c_n\hat{H}_n^{(2)}(k\rho)\frac{P_n^1(\cos\theta)}{\sin\theta}\right] \\ E_\phi^s &= \frac{E_0}{k\rho}\sin\phi\sum_{n=1}^{\infty}\left[jb_n\hat{H}_n^{(2)'}(k\rho)\frac{P_n^1(\cos\theta)}{\sin\theta}-c_n\hat{H}_n^{(2)}(k\rho)\sin\theta P_n^{'1}(\cos\theta)\right] \end{aligned} \tag{B.5}$$

where $\hat{H}_n^{(2)}$ refers to spherical Hankel functions of the second kind, and

$$\begin{aligned} ' &= \frac{\partial}{\partial(k\rho)} \quad \text{for spherical Hankel functions} \\ '' &= \frac{\partial}{\partial(k\rho)^2} \quad \text{for spherical Hankel functions} \\ ' &= \frac{\partial}{\partial(\cos\theta)} = -\frac{1}{\sin\theta}\frac{\partial}{\partial\theta} \quad \text{for associated Legendre functions} \end{aligned} \tag{B.6}$$

When we have a conducting sphere the coefficients acquire the following form:

$$\begin{aligned} a_n &= j^{-n}\frac{(2n+1)}{n(n+1)} \\ b_n &= -a_n\frac{\hat{J}_n'(ka)}{\hat{H}_n^{(2)'}(ka)} \\ c_n &= -a_n\frac{\hat{J}_n(ka)}{\hat{H}_n^{(2)}(ka)} \end{aligned} \tag{B.7}$$

with $\hat{J}_n$ the spherical Bessel function.
For the general case of the dielectric sphere a_n does not change, and b_n and c_n become notably more complicated:

$$\begin{aligned} b_n &= \frac{-\sqrt{\epsilon_d\mu_0}\hat{J}_n'(ka)\hat{J}_n(k_da)+\sqrt{\epsilon_0\mu_d}\hat{J}_n(ka)\hat{J}_n'(k_da)}{\sqrt{\epsilon_d\mu_0}\hat{H}_n^{(2)'}(ka)\hat{J}_n(k_da)-\sqrt{\epsilon_0\mu_d}\hat{H}_n^{(2)}(ka)\hat{J}_n'(k_da)}a_n \\ c_n &= \frac{-\sqrt{\epsilon_d\mu_0}\hat{J}_n(ka)\hat{J}_n'(k_da)+\sqrt{\epsilon_0\mu_d}\hat{J}_n'(k_a)\hat{J}_n(k_da)}{\sqrt{\epsilon_d\mu_0}\hat{H}_n^{(2)}(ka)\hat{J}_n'(k_da)-\sqrt{\epsilon_0\mu_d}\hat{H}_n^{(2)'}(ka)\hat{J}_n(k_da)}a_n \end{aligned} \tag{B.8}$$

where a is now the radius of the sphere.
Below (see Fig. B.2) we illustrate some examples of the analytical Radar Cross Section for different size and material spheres at 50cm distance. As it was observed in the previous example for a cylindrical target, the number of resonances increases with the size of the scatterer.

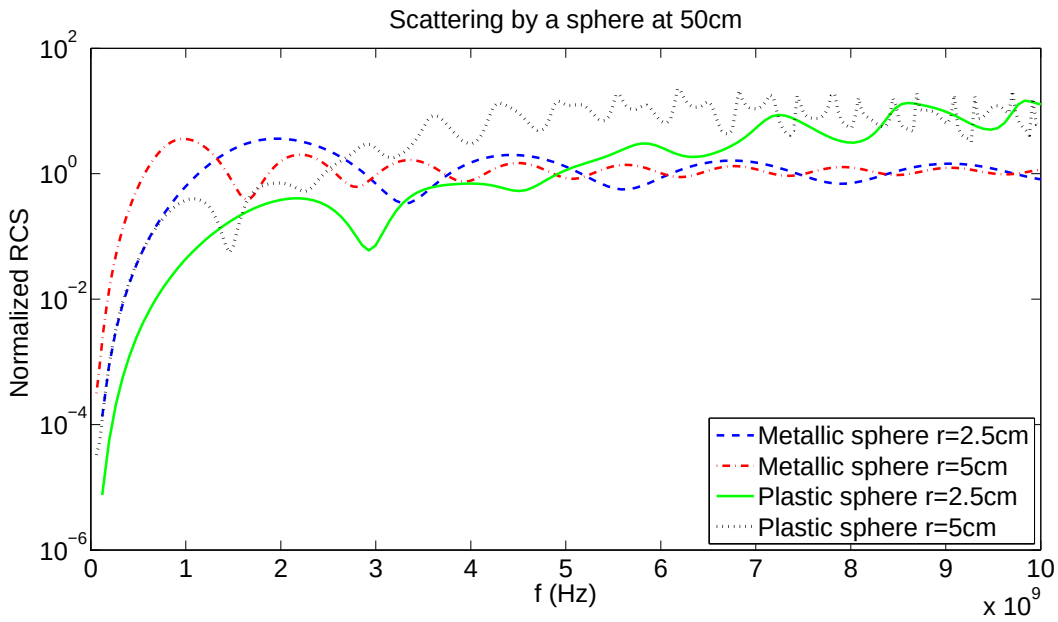

Figure B.2 – Radar Cross Section by different spheres in free space and plane wave excitation; receiving point at a distance of 50cm.

Definitions

- **Field Regions**
  The space surrounding an antenna is usually divided into three regions: reactive near-field, radiating near-field (Fresnel region) and far-field (Fraunhofer region). Although no abrupt changes in the fields are appreciated as the boundaries are crossed, there are remarkable differences among them. There boundaries between the regions are not unique but there are various criteria commonly used to separate the regions [Balanis, 2005].

  Reactive near-field region is defined as "the portion of the near-field region immediately surrounding the antenna wherein the reactive field predominates". For most antennas the outer boundary of this region is considered to be at a distance $R = \sqrt{0.62D^3/\lambda}$ from the antenna surface, where λ is the wavelength and D is the largest dimension of the antenna.

  Radiating near-field (Fresnel) region is "the region between the reactive near-field and the far-field wherein radiation fields predominate and wherein the angular distribution of the fields is dependent upon the distance from the antenna. If the antenna has a maximum dimension that is small compared to the wavelength, this field region may not exist". The inner boundary corresponds to the distance $R = \sqrt{0.62D^3/\lambda}$ and the outer is assumed to be at $R = 2D^2/\lambda$ where D is the largest dimension of the antenna (to be valid D must be large compared to the wavelength, $D > \lambda$). In this region the field pattern is, in general, a function of the radial distance and the radial field component may be significant.

  Far-field (Fraunhofer) region is "that region of the field of an antenna where the angular field distribution is practically independent of the distance from the antenna. If the antenna has a maximum overall dimension D, the far-field is usually assumed to be at distances greater than $2D^2/\lambda$. In physical media, if the maximum dimension D is large compared to $\pi/|\gamma|$, the far-field region can be assumed to start approximately at a distance $|\gamma|D^2/\pi$ from the antenna, γ being the propagation constant in the medium". In this region, the the E- and H-field components are perpendicular to each other and transverse to the radial direction of propagation, and the angular distribution is independent of the radial distance r, i.e., the r variations are separable from those of the angular directions (see Fig. 9.3).

- **Radiation Pattern, Power Density and Poynting Vector**
  An antenna *radiation pattern* is defined as a graphical representation of the radiation prop-

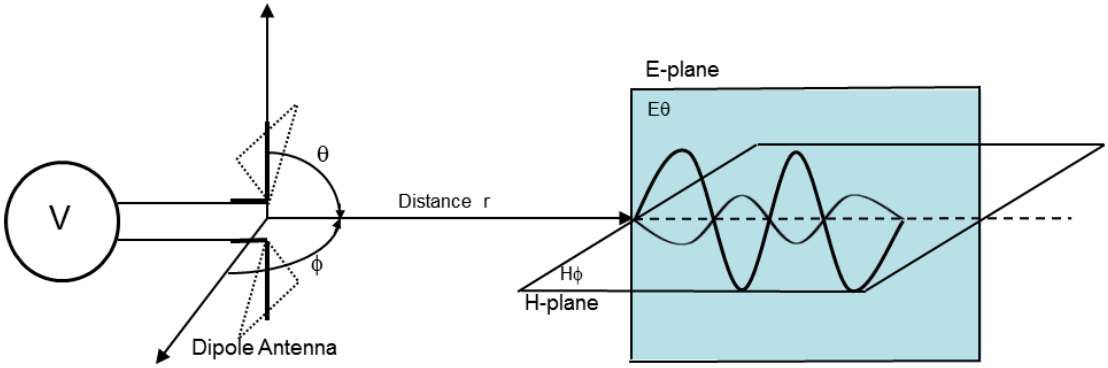

Figure 9.3 – Coordinate system and relationship between E and H in the far field.

erties of the antenna as a function of space coordinates [Balanis, 2005]. In most cases, the radiation pattern is determined in the far-field region. The most significant radiation property if the 2D or 3D spatial distribution of radiated energy as a function of the observer's position along a path or surface of constant radius. A trace of the received power at a constant radius is called the power pattern and a graph of the angular distribution of the electric (or magnetic) field is called an amplitude pattern.

The average *power density* radiated by an antenna is quantified by the time-averaged *Poynting vector*

$$\mathbf{W}_{av} = [\mathcal{W}(x,y,z;t)]_{av} = \frac{1}{2} Re[\mathbf{E} \times \mathbf{H}^*] \quad (W/m^2),$$

where $\mathcal{W}$ is the instantaneous Poynting vector defined as $\mathcal{W} = \mathcal{E} \times \mathcal{H}$ and for time harmonic variations, the complex fields $\mathbf{E}$ and $\mathbf{H}$ are related to their instantaneous counterparts $\mathcal{E}$ and $\mathcal{H}$ by

$$\mathcal{E}(x,y,z;t) = Re[\mathbf{E}(x,y,z)e^{j\omega t}],$$
$$\mathcal{H}(x,y,z;t) = Re[\mathbf{H}(x,y,z)e^{j\omega t}].$$

Since the Poynting vector is a power density, the average total power radiated by an antenna, P_{rad}, can be calculated by integrating the normal component of the Poynting vector over the entire close surface

$$P_{rad} = \iint \mathbf{W}_{av} \cdot \hat{\mathbf{n}} da = \frac{1}{2} \iint Re(\mathbf{E} \times \mathbf{H}^*) \cdot d\mathbf{s}.$$

In the above equation, while the real part of the expression inside parenthesis represents the average real power density, the imaginary part represents the reactive (stored) power density associated with the electromagnetic fields, i.e., the real part accounts for the radiative losses and the imaginary part for the resistive losses.

- **Directivity and Gain**

  The *directivity* of an antenna can be defined as the ratio of the radiation intensity in a given direction from the antenna to the radiation intensity averaged over all directions. The radiation intensity which is the power radiated by an antenna per unit solid angle can be obtained by just multiplying the above defined radiated power density W_{rad} by the

square of the distance. The average radiation intensity is equal to the total power radiated by the antenna divided by 4π. If the direction is not specified, the direction of maximum radiation intensity is implied. In mathematical form:

$$D = \frac{U}{U_0} = \frac{4\pi U}{P_{rad}},$$

where U is the radiation intensity in a given direction and U_0 if the radiation intensity of an isotropic source.

The *gain* of an antenna is closely related to the directivity, but it takes into account the antenna efficiency as well as its directional capabilities. Absolute gain of the antenna in a given direction is defined as the ratio of the intensity in that direction, to the radiation intensity that would be obtained if the power accepted by the antenna were radiated isotropically. The radiation associated to the isotropically radiated is equal to the power accepted by the antenna divided by 4π. However, in most cases we deal with relative gain, which is defined as the ratio of the power gain to the power gain of a reference antenna in a given direction. The power input must be then the same for both antennas. The reference antenna can a dipole, horn, or any other whose gain is known or can be calculated. But in most cases, the reference antenna is a lossless isotropic source. Thus

$$G(\theta, \phi) = \frac{4\pi U(\theta, \phi)}{P_{in}^{iso}},$$

which is often expressed in terms of decibels and stated dBi to indicate that the antenna is compared to an isotropic radiator.
Here again, when the direction is not indicated, the power gain is normally considered in the direction of maximum radiation.
In the above formula, the total input power P_{in} is directly related to the total radiated power P_{rad} by the antenna radiation efficiency η (dimensionless): $P_{rad} = \eta * P_{in}$. For an ideal lossless radiator the efficiency equals 1. Both directivity and gain are unitless measures.

- **Impedance**
  The input impedance (Z_{in}) is the ratio between the voltage and currents at the antenna port. It is a complex quantity that varies with frequency as

  $$Z_{in}(f) = R_{in}(f) + jX_{in}(f),$$

  where f is the frequency, the real part R_{in} is the antenna's total feed point resistance including both radiation (R_r) and loss (R_l) terms, and the imaginary part X_{in} is the antenna's feed point reactance. For efficient power transfer and antenna radiation the input impedance needs to be matched to the internal impedance of the rest of the network. The input impedance can be used to determine other related parameters such as the reflection coefficient (Γ) and the voltage standing wave ratio (VSWR).

- **Signal-to-Noise Ratio (SNR)** is defined as the power ratio between a signal (meaningful information) and the background noise (unwanted signal), where both the signal and the noise power must be measured at the same or equivalent point of a system:

  $$SNR = \frac{P_{signal}}{P_{noise}} = \left(\frac{A_{signal}}{A_{noise}}\right)^2,$$

where P is the average power and A the RMS amplitude (for example, in the energy based detection algorithm presented in Chapter 8, the RMS voltage). Because many signals have a very wide dynamic range, SNRs are often expressed using the logarithmic decibel scale. In decibels, the SNR is defined as:

$$SNR_{dB} = 10\log_{10}\left(\frac{A_{signal}}{A_{noise}}\right)^2 = 20\log_{10}\left(\frac{A_{signal}}{A_{noise}}\right).$$

In our case the amplitude of the noise is calculated as the average RMS amplitude of the voltage over a given scan area and the signal amplitude is evaluated pixel per pixel.

- **Dynamic range** is defined as the ratio between the peak transmitted signal power and the minimum detectable peak power entering the receiver antenna. This number quantifies the maximum amount of loss that the radar signal can have, and still be detectable in the receiver, being a key measure for the performance of the radar system. It is dependent on the radar integration time and it is normally given in dB [Hamran, 2010].

- **Adaptivity** is an active research area within FEM and it is particularly effective in fluid flow, heat transfer, and structural analysis. Generally, there are two types of adaptation: h-adaptation (mesh refinement), where the element size varies while the orders of the shape functions are kept constant; p-adaptation, where the element size is constant while the orders of the shape functions are increased (linear, quadratic, cubic, etc.). Adaptive remeshing (know as r-adaptation) employs a spring analogy to redistribute the nodes in an existing mesh without adding new nodes; the accuracy of the solution is limited by the initial number of nodes and elements. In mesh refinement (h-adaptation), individual elements are subdivided without altering their original position. The use of hp-adaptation includes both h- and p-adaptation strategies and produces exponential convergence rates. Both mesh refinement and adaptive meshing are present in COMSOL.

Acronyms

ABS	Absorbing Boundary Condition
AP	Antipersonnel
AT	Antitank
A/D	Analog to Digital
CO	Common Offset
dB	decibel
EM	Electromagnetic
FD	Finite Difference
FDTD	Finite Difference Time Domain
FEM	Finite Element Method
FFT	Fast Fourier Transform
GO	Geometrical Optics
GPR	Ground Penetrating Radar
GTD	Geometrical Theory of Diffraction
GUI	Graphical User Interface
GPML	Generalized Perfectly Matched Layers
IDW	Inverse Distance Weighted
LIAG	Leibniz Institute for Applied Geophysics
LNA	Low Noise Amplifier
MD	Metal Detector
MoM	Method of Moments
MS	Mie Scattering
MWR	Method of Weighted Residuals
PEC	Perfect Electric Conductor
PSD	Power Spectral Density
PML	Perfectly Matched Layer
RCS	Radar Cross Section
RF	Radio Frequency
ROC	Receiver Operation Characteristics
RS	Rayleigh Scattering
RMS	Root Mean Square
SAR	Synthetic Aperture Radar
SCR	Signal to Clutter Ratio
SNR	Signal to Noise Ratio
STT	Standard Test Target
TDR	Time Domain Reflectometry
TNT	Trinitrotoluene
UWB	Ultra Wideband
UXO	Undexploded Ordnance
VNA	Vector Network Analyser

Bibliography

[Acheroy, 2007] Acheroy, M. (2007). Mine action: status of sensor technology for close-in and remote detection of antipersonnel mines. *Near Surface Geophysics*, 5, 43–56.

[Annan, 2003] Annan, P. (2003). *Ground Penetrating Radar Principles, Procedures and Applications*. Mississauga, Canada: Sensors and Software, Inc.

[Balanis, 1989] Balanis, C. A. (1989). *Advanced Engineering Electromagnetics*. New York: John Wiley and Sons, Inc.

[Balanis, 2005] Balanis, C. A. (2005). *Antenna theory: analysis and design*. New York: John Wiley and Sons, Inc.

[Berenger, 1994] Berenger, J. P. (1994). A perfectly matched layer for the absorption of electromagnetic waves. *Journal of Computational Physics*, 114, 185–200.

[Beres & Haeni, 1991] Beres, J. & Haeni, F. (1991). Application of ground-penetrating-radar methods in hydrogeologic studies. *Groundwater*, 29(3), 375–386.

[Bergman et al., 1998] Bergman, T., Robertson, J., & Holliger, K. (1998). Finite-difference modeling of electromagnetic wave propagation in dispersive and attenuating media. *Geophysics*, 63(3), 856–867.

[Bohren & Huffman, 1983] Bohren, C. F. & Huffman, D. R. (1983). *Absorption and scattering of light by small particles*. New York: John Wiley and Sons.

[Born & Wolf, 1975] Born, M. & Wolf, E. (1975). *Principles of optics*. Pergamon Press.

[Borovikov & Kinber, 1994] Borovikov, V. A. & Kinber, B. Y. (1994). *Geometrical Theory of Diffraction*. London: The Institution of Electrical Engineers.

[Bourgeois & Smith, 1996] Bourgeois, J. M. & Smith, G. S. (1996). A fully three-dimensional simulation of a ground-penetrating-radar: Fdtd theory compared with experiment. *IEEE Trans. Geosci. Remote Sensing*, 34, 36–44.

[Brooks et al., 2000] Brooks, J., van Kempen, L., , & Sahli, H. (2000). A primary study in adaptative clutter reduction and buried minelike target enhancement from gpr data. *Proc. of SPIE, Detection and Remediation Technologies for Mines and Minelike Targets V*, 4038, 1183–1192.

[Brunzell, 1999] Brunzell, H. (1999). Detection of shallowly buried objects using impulse radar. *IEEE Trans. Geosci. Remote Sensing*, 37(2).

[Bruschini et al., 1998] Bruschini, C., Gros, B., Guerne, F., Pice, P., , & Carmona, O. (1998). Ground penetrating radar and imaging metal detector for antipersonnel mine detection. *Journal of Applied Geophysics*, 40, 59–71.

[Carevic, 2000] Carevic, D. (2000). Clutter reduction and detection of minelike objects in ground penetrating radar data using wavelets. *Subsurface Sensing Technologies and Applications*, 1(1).

[Cassidy, 2009] Cassidy, N. J. (2009). *Electrical and Magnetic Properties of Rocks, Soils and Fluids*, (pp. 41–72). Elsevier.

[Chew & Weedon, 1994] Chew, W. C. & Weedon, W. (1994). A 3-d perfectly matched medium from modified maxwell's equations with stretched coordinates. *IEEE Microwave and Optical Technology Letters*, 7, 599–604.

[Cloude et al., 1996] Cloude, S., Milne, A., Thornhill, C., & Crisp, G. (1996). Uwb sar detection of dielectric targets. *IEE Eurel International Conference on The Detection of Abandoned Land Mines*, (pp. 114–116).

[Clough, 1960] Clough, R. W. (1960). The finite element method in plane stress analysis. *Proc. 2nd ASCE Conf. on ELectronic Computation, Pittsburg*.

[COMSOL, 2005] COMSOL (2005). *Comsol Multiphysics 3.2, Electromagnetics Module User's Guide*.

[Conyers & Goodman, 1997] Conyers, L. & Goodman, D. (1997). *Ground-Penetrating Radar: An Introduction for Archaeologists*. Altamira Press, U.S.

[Cosgrove et al., 2004] Cosgrove, R., Milanfar, F., & Kositsky, J. (2004). Trained detection of buried mines in sar images via the deflection-optimal criterion. *IEEE Trans. Geosci. Remote Sensing*, 42(11), 2569–2575.

[Courant, 1943] Courant, R. (1943). Variational methods for the solution of problems of equilibrium and vibrations. *Bull. Am. Math. Soc.*, 49, 1–23.

[Cumming & Wong, 2005] Cumming, I. G. & Wong, F. H. (2005). *Digital Processing of Synthetic Aperture Radar Data*. MA: Artech House Nordwood.

[Daniels, 1996] Daniels, D. (1996). *Surface-penetrating radar*. London, UK: IEE Radar, Sonar, Navigations and Avionics Series 6, The Institution of Electrical Engineers, 1st edition.

[Daniels, 2004] Daniels, D. (2004). *Ground Penetrating Radar*. IEE Radar, Sonar, Navigation and Avionics Series, The Institution of Engineering and Technology, 2nd edition.

[Daniels, 2007] Daniels, D. (2007). *Ground Penetrating Radar*. IEE Radar, Sonar, Navigations and Avionics Series 15, The Institution of Engineering and Technology, 2nd edition.

[Davis & Annan, 1976] Davis, J. & Annan, A. (1976). Impulse radar sounding in permafrost. *Radio Science*, 11, 383–394.

[Davis & Annan, 1989] Davis, J. & Annan, A. (1989). Ground penetrating radar for high-resolution mapping of soil and rock stratigraphy. *Geophyisical Prospecting*, 37(5), 531–551.

[Debye, 1929] Debye, P. (1929). *Polar Molecules*. Mineola, NY: Dover Publications.

[Dobson et al., 1985] Dobson, M., Ulaby, F., Hallikainen, M., & El-Rayes, M. (1985). Microwave dielectric behaviour of wet soil - part ii: Dielectric mixing models. *IEEE Trans. Geosci. Remote Sensing*, 23(1), 35–46.

[Fang & Wu, 1996] Fang, J. & Wu, Z. (1996). Generalized perfectly matched layers for the absorption of propagating and evanescent waves in lossless and lossy media. *IEEE Trans. Microwave Theory Techn.*, 44, 2216–2222.

[Feng & Sato, 2004] Feng, X. & Sato, M. (2004). Pre-stack migration applied to gpr for landmine detection. *Inverse Problems*, 20(6), 99–115.

[Gader et al., 2001a] Gader, P., Keller, J., & Nelson, B. (2001a). Recognition technology for the detection of buried land mines. *IEEE Trans. Fuzzy Systems*, 9(1), 31–43.

[Gader et al., 2001b] Gader, P., Mystkowski, M., & Zhao, Y. (2001b). Landmine detection with ground penetrating radar using hidden markov models. *IEEE Trans. Geosci. Remote Sensing*, 39(6), 1231–1244.

[Gazdag, 1978] Gazdag, J. (1978). Wave equation migration with the phase shift method. *Geophysics*, 43, 1342–1351.

[Giannopoulos, 2002] Giannopoulos, A. (2002). Gprmax-fdtd based gpr simulation software, user manual.

[Gonzalez-Huici, 2011] Gonzalez-Huici, M. (Aachen, 2011). Adaptive stolt migration via contrast maximization for gpr applications. *Proceedings of the 6th International Workshop on Advanced Ground Penetrating Radar*.

[Gonzalez-Huici, 2012] Gonzalez-Huici, M. (Shanghai, 2012). A strategy for landmine detection and recognition using simulated gpr responses. *Proceedings of the 14th International GPR Conference*.

[Gonzalez-Huici & Giovanneschi, 2013] Gonzalez-Huici, M. & Giovanneschi, F. (2013). A combined strategy for landmine detection and identification using synthetic gpr responses. *Journal of Applied Geophysics (Submitted)*.

[Gonzalez-Huici & Uschkerat, 2010] Gonzalez-Huici, M. & Uschkerat, U. (Berlin, 2010). Gpr modeling for landmine detection (invited). *Proceedings of the 20th International Symposium on Electromagnetic Theory URSI/EMTS*.

[Groenenboom & Yarovoy, 2002] Groenenboom, J. & Yarovoy, A. (2002). Data processing and imaging in gpr system dedicated for landmine detection. *Subsurface Sensing Technologies and Application*, 3(4).

[Gu et al., 2004] Gu, K., Wang, G., & Li, J. (2004). Migration based sar imaging for ground penetrating radar systems. *IEE Proc.-Radar, Sonar and Navigation*, 151(5), 317–325.

[Gürel, 2001] Gürel, L. (2001). Simulation of ground-penetrating radars over lossy and heterogeneous grounds. *IEEE Trans. Geosci. Remote Sensing*, 39, 1190–1197.

[Gürel & Oğuz, 2000] Gürel, L. & Oğuz, U. (2000). Three dimensional fdtd modeling of a ground-penetrating radar. *IEEE Trans. Geosci. Remote Sensing*, 38, 1513–1521.

[Hamran, 2010] Hamran, S.-E. (2010). *Radar Performance of Ultra Wideband Waveforms, Radar Technology*, chapter Chapter 1. Guy Kouemou (Ed.), InTech.

[Harrigton, 1968] Harrigton, R. (1968). *Field computations by methods of moments*. New York: The Macmillan Company.

[Harrigton, 2001] Harrigton, R. (2001). *Time-Harmonic Electromagnetic Fields*. Piscataway NJ: IEEE Press.

[Hasted, 1973] Hasted, J. (1973). *Aqueous dielectrics*. London: Chapman and Hall.

[Hillel, 1998] Hillel, D. (1998). *Environmental Soil Physics*. San Diego, CA: Academic Press.

[Hippel, 1995] Hippel, A. (1995). *Dielectric materials and applications, Artech House*. Artech House.

[Hoekstra & Delaney, 1974] Hoekstra, F. & Delaney, A. (1974). Dielectric properties of soils at uhf and microwave frequencies. *Journal of Geophysical Research*, 79(11), 1699–1708.

[Holliger & Bergman, 1998] Holliger, K. & Bergman, T. (1998). Accurate and efficient fdtd modelling of ground-penetrating radar antenna radiation. *Geophysical Research Letters*, 25(20), 3883–3886.

[Huebner et al., 2001] Huebner, K. H., Dewhirst, D. L., Smith, D. E., & Byrom, T. G. (2001). *The Finite Element Method for Engineers*. New York: John Wiley and Sons.

[ICBL, 2009] ICBL (2009). *Landmine Monitor Report 2009, Toward a Mine-free World*. Canada: Mines Action Canada, Human Rights Watch.

[Igel, 2007] Igel, J. (2007). *On the Small-Scale Variability of Electrical Soil Properties and its Influence on Geophysical Measurements*. PhD thesis.

[ITOP, 1999] ITOP (20.05.1999). *Target Standarisation for Countermine and Demining Testing (ITOP 4-2-521)*. Interantional Test and Evaluation Program for Humanitarian Demining (ITEP).

[Jackson, 1999] Jackson, J. (1999). *Classical Electrodynamics*. John Wiley and Sons, 3rd edition.

[Jin, 2002] Jin, J. (2002). *The Finite Element Method in Electromagnetics*. Wiley-IEEE Press, 2nd edition.

[Karlsen et al., 2002] Karlsen, B., Sorensen, H. B., Larsen, J., & Jakobsen, K. B. (2002). Independent component analysis for clutter reduction in ground penetrating radar data. *Proc. SPIE*, 4742(378).

[Keller, 1962] Keller, J. B. (1962). Geometrical theory of diffraction. *Journal of the optical society of America*, 52(2).

[Knight & Endres, 2005] Knight, R. & Endres, A. (2005). *Introduction to Rock Physics Principles for Near-Surface Geophysics*. D.K. Butler, Ed. SEG.

[Kovalenko et al., 2007] Kovalenko, V., Yarovoy, A., & Ligthart, P. (2007). A novel clutter suppression algorithm for landmine detection with gpr. *IEEE Trans. Geosci. Remote Sensing*, 45(11).

[Lampe & Holliger, 2001] Lampe, B. & Holliger, K. (2001). Numerical modeling of a complete ground-penetrating radar system. *Proceedings of SPIE*, 4491, 99–110.

[Lampe & Holliger, 2005] Lampe, B. & Holliger, K. (2005). Resistively loaded antennas for ground penetrating radar antennas. *Geophysics*, 70.

[Liu & Chen, 1991] Liu, C. & Chen, L. C. (1991). Numerical simulation of subsurface radar for detecting buried pipes. *IEEE Trans. Geosci. and Remote Sensing*, 29(5), 795–798.

[MacDonald & R., 2003] MacDonald, J. A. & R., L. J. (2003). *Alternatives for Landmine Detection*. RAND Corporation.

[Massa et al., 2005] Massa, A., Boni, A., & Donelli, M. (2005). A classification approach based on svm for electromagnetic subsurface sensing. *IEEE Trans. on Geosci. and Remote Sensing*, 43(9).

[Mavko et al., 1998] Mavko, G., Mukerji, T., & Dvorkin, J. (1998). *The Rock Physics Handbook: Tools for Seismic Analysis of Porous Media*. Cambridge University Press, 1st edition.

[Mironov et al., 2004] Mironov, V., Dobson, C., Kaupp, V., Komarov, S., & Kleshchenko, V. (2004). Generalized refractive mixing dielectric model for moist soils. *IEEE Trans. Geosci. and Remote Sensing*, 42, 773–783.

[Mittra, 1973] Mittra, R. (1973). *Computer techniques for electromagnetics*. Pergamon.

[Moghaddam et al., 1991] Moghaddam, M., Yannakakis, E., Chew, W., & Randall, C. (1991). Modeling of the subsurface interface radar. *Journal of Electromagnetic Waves and Applications*, 5(1), 17–39.

[Parekh et al., 2000] Parekh, R., Yang, J., & Honavar, V. (2000). Constructive neural-network learning algorithms for pattern classification. *Trans. on Neural Networks*, 11(2).

[Peplinski et al., 1995] Peplinski, N., Ulaby, F., & Dobson, M. (1995). Dielectric properties of soils in the 0.3-1.3 ghz range. *IEEE Trans. Geosci. and Remote Sensing*, 33, 803–807.

[Pozar, 2005] Pozar, D. M. (2005). *Microwave Engineering*. New York Wiley, 3rd edition.

[Rial et al., 2009] Rial, F. I., Lorenzo, H., Arias, P., & Novo, A. (2009). Resolution of gpr bowtie antennas: An experimental approach. *Journal of Applied Geophysics*, 67(4).

[Ribalta & Gonzalez-Huici, 2013] Ribalta, A. & Gonzalez-Huici, M. A. (2013). Backprojection algorithm for subsurface radar imaging: Computing the round-trip time delay. *Proceedings of the IEEE International Geoscience and Remote Sensing Symposium (Submitted)*.

[Sabouroux & Ba, 2011] Sabouroux, P. & Ba, D. (2011). *Epsimu*, a tool for dielectric properties measurement of porous media: application in wet granular material characterization. *Progress in Electromagnetic Research B*, 29, 191–207.

[Savelyev et al., 2007] Savelyev, T., van Kempen, L., Sahli, H., Sachs, J., & M., S. (2007). Investigation of time-domain frequency features for gpr landmine discrimination. *IEEE Trans. Geosci. and Remote Sensing*, 45, 118–129.

[Scheers, 2001] Scheers, B. (2001). *Ultra-wideband ground penetrating radar with application to the detection of anti personnel landmines*. PhD thesis, Catholic University of Louvain-Royal Military Academy, Belgium.

[Schneider, 1978] Schneider, W. A. (1978). Integral formulation for migration in two and three dimensions. *Geophysics*, 43, 49–76.

[Smith, 1984] Smith, G. H. (1984). Directive properties of antennas for transmission into a material half-space. *IEEE Trans. on Antennas and Propagation*, 32(3), 232–246.

[Southwell, 1946] Southwell, R. V. (1946). *Relaxation Methods in Theoretical Physics*. Oxford University Press.

[Stolt, 1978] Stolt, R. H. (1978). Migration by transform. *Geophysics*, 43(1), 23–48.

[Taflove & Hagness, 2005] Taflove, A. & Hagness, S. (2005). *Computational Electromagnetics: The Finite-Difference Time-Domain Method*. MA: Artech House Norwood, 3rd edition.

[Texeira & Chew, 2000] Texeira, F. & Chew, W. (2000). Finite difference computation of transient electromagnetic waves for cylindrical geometries in complex media. *IEEE. Trans. Geosci. Remote Sensing*, 38(4), 1530–1543.

[Texeira et al., 1998] Texeira, F., Chew, W., Straka, M., Oristaglio, M. L., , & Wang, T. (1998). Finite-difference time domain simulation of ground penetrating radar on dispersive, inhomogeneous and conductive soils. *IEEE. Trans. Geosci. Remote Sensing*, 36(6), 1928–1937.

[Topp et al., 1980] Topp, G., Davis, J. D., , & Annan, A. (1980). Electromagnetic determination of soil water content: Measurements in coaxial transmission lines. *Water Resources Research*, 16, 574–582.

[Uduwawala et al., 2005] Uduwawala, U., Norgren, M., , & Fuks, P. (2005). A complete fdtd simulation of a real gpr antenna system operating above lossy and dispersive grounds. *Progress In Electromagnetics Research*, 50, 209–229.

[Uduwawala & Norgren, 2004] Uduwawala, U. & Norgren, M. andand Fuks, P. (2004). A deep parametric study of resistor-loaded bow-tie antennas for ground-penetrating radar applications using fdtd. *IEEE Trans. Geosci. Remote Sensing*, 42(4), 732–742.

[Ufimtsev, 2007] Ufimtsev, P. Y. (2007). *Fundamental of the Physical Theory of Diffraction*. New Jersey: John Wiley and Sons.

[van de Hulst, 1957] van de Hulst, H. (1957). *Light scattering by small particles*. New York: John Wiley and Sons.

[van den Bosch, 2006] van den Bosch, I. (2006). *Accurate Modeling of Ground-Penetrating Radar for Detection and Signature Extraction of Mine-like Targets buried in Stratified Media*. PhD thesis, Universit Catholique de Louvain, Facult Polytechnique, cole Rayale Militaire.

[van der Kruk, 2004] van der Kruk, J. (2004). Three-dimensional gpr imaging in the horizontal wavenumber domain for different heights of source and receive antenna. *Near Surface Geophysics*, 2(1), 25–31.

[Wackernagel, 2003] Wackernagel, H. (2003). *Multivariate Geostatistics: an introduction with applications*. Springer Verlag, 3rd edition.

[Wang, 1990] Wang, J. (1990). Generalized moment methods in electromagnetics. *IEEE Proceedings Microwaves, Antennas and Prop.*, 137(2).

[Wang & Schmugge, 1980] Wang, J. & Schmugge, T. (1980). An empirical model for the complex dielectric permittivity of soils as a function of water content. *IEEE. Trans. Geosci. Remote Sensing*, 18, 574–582.

[Wang & Tripp, 1996] Wang, T. & Tripp, A. (1996). Fdtd simulation of em wave propagation in 3d media. *Geophysics*, 61(1), 110–120.

[Warren & Giannopoulos, 2009] Warren, C. & Giannopoulos, A. (Granada, 2009). Optimising models of commercial gpr antennas. *Proceedings of the 5th International Workshop of Advanced Ground Penetrating Radar*.

[Wobschall, 1977] Wobschall, D. (1977). A theory of the complex dielectric permittivity of soil containing water, the semidisperse model. *IEEE Trans. Geosci. Electronics*, 15(1), 49–58.

[Yang & Bose, 2005] Yang, C.-C. & Bose, N. K. (2005). Landmine detection and classification with complex-valued hybrid neural network using scattering parameters dataset. *IEEE Trans. on Neural Networks*, 16(3), 743–750.

[Yee, 1966] Yee, K. (1966). Numerical solution of initial boundary value problems involving maxwell's equations in isotropic media. *IEEE Trans. Antennas and Propagation*, 14, 302–307.

[Yilmaz, 2001] Yilmaz, O. (2001). *Seismic data analysis.* Tulsa, Okla: Society of Exploration Geophysicists.

List of Figures

List of Tables

Declaration

I hereby declare that the present work was done by myself and no other than the cited sources were employed.

Ich erkläre hiermit, die vorliegende Arbeit selbständig und nur mit den angegebenen Hilfsmitteln angefertig zu haben.

Bonn, November 2012.

María A. Gónzalez Huici